A STUDY OF MYOELECTRIC SIGNAL PROCESSING

by

Lukai Liu

A Dissertation
Submitted to the Faculty
of the
Worcester Polytechnic Institute
in partial fulfillment of the requirements for the
Degree of Doctor of Philosophy

in

Electrical and Computer Engineering

January 14, 2016

APPROVED:

_____

Professor Edward A. Clancy, Major Advisor, WPI ECE

_____

Professor Xinming Huang

_____

Paolo Bonato, Ph.D.
Dept. Phys. Med. Rehabil., Harvard Medical School

Abstract

This dissertation of various aspects of electromyogram (EMG: muscle electrical activity) signal processing is comprised of two projects in which I was the lead investigator and two team projects in which I participated. The first investigator-led project was a study of reconstructing continuous EMG discharge rates from neural impulses. Related methods for calculating neural firing rates in other contexts were adapted and applied to the intramuscular motor unit action potential train firing rate. Statistical results based on simulation and clinical data suggest that performances of spline-based methods are superior to conventional filter-based methods in the absence of decomposition error, but they unacceptably degrade in the presence of even the smallest decomposition errors present in real EMG data, which is typically around 3–5%. Optimal parameters for each method are found, and with normal decomposition error rates, ranks of these methods with their optimal parameters are given. Overall, Hanning filtering and Berger methods exhibit consistent and significant advantages over other methods.

In the second investigator-led project, the technique of signal whitening was applied prior to motion classification of upper limb surface EMG signals previously collected from the forearm muscles of intact and amputee subjects. The motions classified consisted of 11 hand and wrist actions pertaining to prosthesis control. Theoretical models and experimental data showed that whitening increased EMG signal bandwidth by 65–75% and the coefficients of variation of temporal features computed from the EMG were reduced. As a result, a consistent classification accuracy improvement of 3–5% was observed for all subjects at small analysis durations (< 100 ms).

In the first team-based project, advanced modeling methods of the constant posture EMG-torque relationship about the elbow were studied: whitened and multi-channel EMG signals, training set duration, regularized model parameter estimation and nonlinear models. Combined, these methods reduced error to less than a quarter of standard techniques. In the second team-based project, a study related biceps-triceps surface EMG to elbow torque at seven joint angles during constant-posture contractions. Models accounting for co-contraction estimated that individual flexion muscle torques were much higher than models that did not account for co-contraction.

Acknowledgement

I am truly grateful to all my dissertation committee and I cannot possibly thank them enough. I extend my sincere appreciation to Dr. Edward Clancy, my research advisor, for all his guidance, knowledge shared and enthusiasm helping me to complete this dissertation. Your inspirations, enthusiasm and patience exposed to me responsibilities of true research. Dr. Xinming Huang your sharp observations, keen suggestions and feedback were all most valuable. Dr. Paolo Bonato, thank you for your patient exposition of the state of art, the Motion Analysis Laboratory in Spaulding Hospital to me, and for kindly offering me the collaboration opportunity.

I would like to express my gratitude to others who helped me towards the completion of this dissertation: Pu Liu and Chenyun Dai, my laboratory partners; Daniel V. Moyer my team project fellow; Giacomo Severini and Patrick Kasi, who kindly shared with me clinical datasets they collected.

Finally, special thanks go to my parents, whose financial and emotional support and encouragement nurtured my dissertation work, and my lovely fiancée Sijia Wu, for her efforts to help me finish this dissertation.

Table of Contents

List of Figures Found in the Introduction and Appendices

List of Tables Found in the Introduction and Appendices

Chapter 1

Introduction

1.1 Background

1.1.1 Motor unit action potential

A motor unit (MU) consists of an α-motorneuron originating in the spinal cord and the skeletal muscle fibers it innervates. Repeated (albeit not periodic) MU activation leads to subsequent mechanical twitches. The summed mechanical activity of many concurrently active (typically unsynchronized) MUs produces gross muscle tension. MU recruitment refers to increasing the number of those MUs that are active at a specific time. Recruitment and average firing rate of individual MUs (discharge frequency, or rate coding) are the two schemes used by the central nervous system to control the gross tension produced by a muscle. Rate encoding refers to the precise spike timing and firing rate describes the time-varying properties of spike timing.

At the cellular level, cell bodies of α-motorneurons are found in the central nervous system (CNS) and their axons extend to the periphery to innervate skeletal muscles. In healthy MUs, activation of an α-motorneuron leads to activation of each innervated muscle fiber, inducing a brief mechanical twitch. Upper motor neurons send input to α-motorneurons, which propagate to extrafusal muscle fibers. The corticonuclear tract, one pathway between the upper motor neurons and α-motorneurons, connects between the cerebral cortex and α-motorneurons. It is found that many parameters associated with movement within a body region—such as force, angle and velocity—are represented in the motor cortex [Aflalo 2007, Georgopoulos 1982, 1988]. The net membrane current induced in an α-motorneuron by various innervation sites determines the firing pattern of the MU [Merletti 2004]. All muscle fibers in a MU are of the same fiber type, which is defined by biochemical, histochemical and contractile characteristics. Three types of motor units [Burke 1971] are found: slow-twitch fatigue-resistant (type I), fast-twitch fatigue-resistant (type IIa) and fast-twitch fatigable (type IIb). The activation of a motor nerve leads to activation of all associated motor fibers.

The motor unit action potential (MUAP) is an all-or-none phenomenon: once the recruitment threshold, the stimulus intensity at which a MU begins to fire, is reached, it fires fully. In voluntary contractions, force generated is modulated by MU recruitment and firing rate [Kukulka 1981]. For small loads requiring less force in healthy subjects, slow-twitch low-force fatigue-resistant muscle fibers are recruited earlier and dismissed later than fast-twitch high-force or less fatigue-resistant muscle fibers. Henneman's size principle [Henneman 1965] states that MUs are recruited in order of increasing size of motorneuron and MU. This size principle, however, has been challenged in observations of complex task requirements [Bolhuis 1997], and is considered applicable for tasks with little dynamics with isometric contractions.

1.1.2 Electromyogram

Electromyogram (EMG) is a technique used for evaluating and recording the electrical signal generated by skeletal muscles. It detects the electrical potential generated by muscle cells when these cells are electrically or neurologically excited, and is used in a variety of applications including prosthesis control, ergonomics, movement and gait analysis and sports medicine [Sörnmo 2005]. There are two kinds of EMG in widespread use: intramuscular EMG (iEMG) and surface EMG (sEMG).

The iEMG is a standard clinical tool that uses needle (or wire) electrodes inserted into the contracting muscle and can be used to study the morphological properties of motor unit action potentials (MUAPs) and distinguish between normal and abnormal activity. Studies of recruitment patterns and firing rates of iEMG require high temporal and spatial resolution in order to differentiate MU types, among other issues. It provides wide band, localized descriptions of the muscle's electrical activity, utilizing useful spectrum up to 5 kHz and RMS signal values typically below 1.5 mV. Simulation methods for generating EMG signals consistent with clinical observations have been proposed [Hamilton-Wright 2005], and study of firing pattern statistics associated with muscle fatigue [Kristina 2008] have been made.

EMG decomposition is used to separate the iEMG signal into its constituent MUAP trains based on MUAP shapes. Decomposition algorithms use manual and automated methods, composed of segmentation and classification stages, possibly followed by MUAP classification into pathological situations [Katsis 2006]. Error rates of about 2–5% are common [Nawab 2008, Negro 2009, Farina 2001].

Various measurements based on EMG decomposition can be derived. Among them are MU firing rate and MU synchronization, both containing important information related to the brain or CNS. Synchronization occurs when firing times from two or more MUs coincide in time more frequently than expected from independent random processes and lead to an increase of power at lower frequencies and a relative decrease of power at higher frequencies [Weytjens 1984]. Exercise and training may increase the level of synchronization of certain muscles [Milner-Brown 1975].

The sEMG is a non-invasive standard procedure to obtain EMG signal with electrodes mounted on the skin surface. It has primary frequency content below 500 Hz and the standard deviation of sEMG usually contains the desired information. The sEMG measurements sacrifice spatial resolution to gain a gross estimate of a large number of MUs. MU firings from a large portion of muscle under surface electrodes are recorded simultaneously, making individual MUAPs indiscernible (although closely-spaced, high-density arrays of electrodes are solving this limitation [Holobar 2009]). Parameters used to quantify sEMG signal include mean absolute value (MAV—an estimate of the standard deviation), absolute signal length (ASL) and mean spike amplitude. Each EMG firing has a similar shape in the time domain (at least for healthy subjects whose muscles are not fatigued). Therefore, the sEMG measurements can be considered as a superposition of numerous independent, identically distributed (i.i.d.) MU firings, with tissue between the site of activation and the skin surface acting as a temporal (lowpass) and spatial filter. By virtue of the central limit theorem of probability, sEMG can be modeled as amplitude-modulated correlated random noise.

Neuropathic or myopathic diseases such as hemiparesis [Gemperline 1995, Stålberg 1997], neuromyotonia [Torbergsen 1996], Parkinson disease [Dietz 1974, Kasi 2009] and multiple sclerosis [Rice 1992, Dorfman 1989] may increase firing rate variability, lower firing rate or present as bursts of spontaneous firings. They may also change recruitment of MUs [Stålberg 1991] or MUAP amplitude [Kuntzer 2004]. Some early attempts have been made to differentiate neuromuscular diseases from the EMG signal [Garrault 1987].

1.1.3 EMG firing rate analysis

The MUAP train is modeled as the convolution of firing times and MUAP wave shape. In this case, the neural transmission can be modeled as a linear system, with its synaptic inputs derived from the summation of all chemical/electrical stimulus from contacting neurons and system response the typical temporal neural firing shape. Studies of mechanisms of intracellular potential profile have parameterized the sEMG shape [Roeleveld 1997, Ruijven 1990] and iEMG [Monsifrot 2013]. Figure 1.1 shows the temporal shape of MUAP and fiber AP from a type FF (fast fatigable, IIb) MU recorded during stimulation by 40-Hz trains and 30 min recovery period [Sandercock 1985] using an iEMG monopolar electrode. Zhou [Zhou 2004] found the average duration of MUAP from sEMG to be 5.3±0.63 ms for FDI muscles.

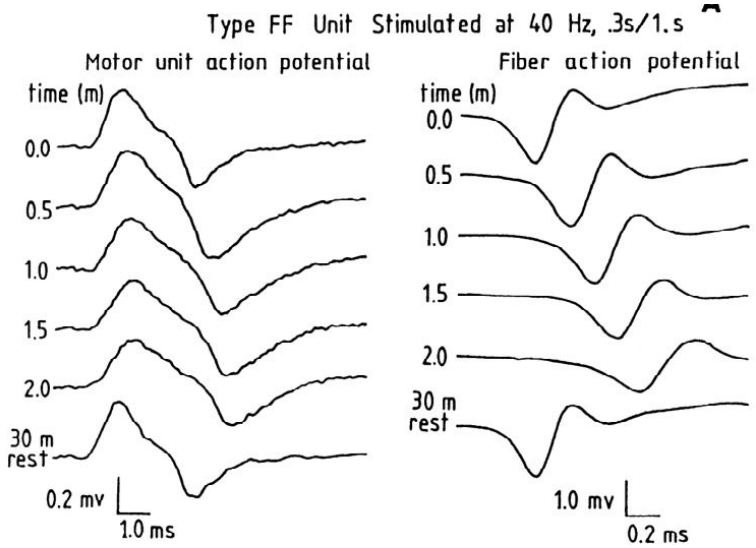

Figure 1.1. Representative of MUAP and fiber AP from a type FF (fast fatigable) MU recorded stimulation 40-Hz trains and following 30-min recovery period. Taken from [Sandercock 1985].

During voluntary muscle contraction, a MU normally begins firing at 4–5 pulses per second (pps) when initially recruited; with increasing isometric force, the average firing rate of bicep brachii increases to a maximum of 20 pps at 100% maximal voluntary contraction (MVC) [Clamann 1970, DeLuca 1979].

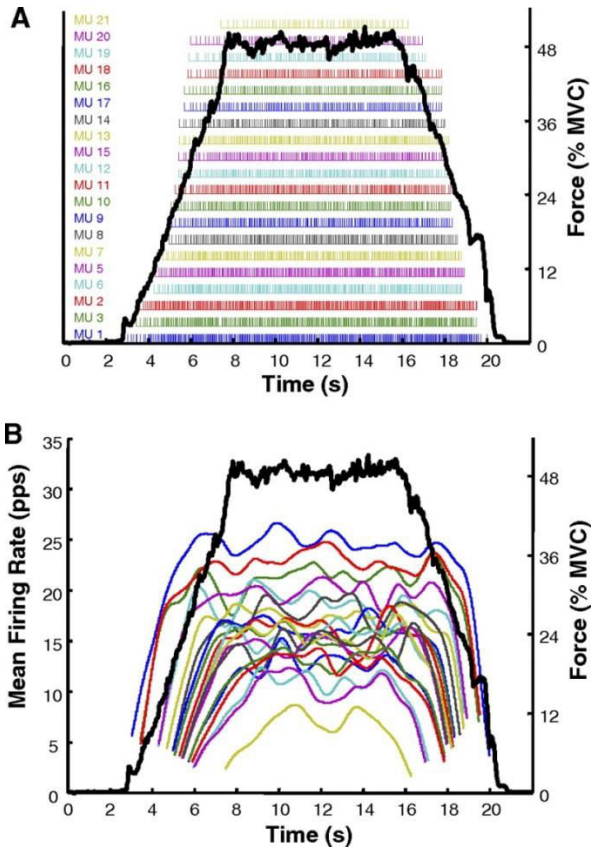

Figure 1.2. Example of the incidences of firing of 21 motor units decomposed from the surface EMG signal obtained from the first dorsal interosseous muscle (FDI). Each bar represents the firing time of an action potential. The dark solid line represents the force output of the FDI muscle. The force in percentage of maximal voluntary contraction (MVC) level is scaled on the *right* and the motor unit number in order of recruitment order is listed on the *left*. *B*: these are the averaged time-varying firing rates for each of the 21 motor units calculated from the timing data above. Note the hierarchical relationship of the firing rates of each motor unit. The earlier recruited motor units (lower-threshold) have greater firing rates. Note that the firing rate values at recruitment and de-recruitment are influenced by the filter used to smoothen the firing rate values. Taken from [DeLuca 2010].

It has been shown [DeLuca 1982] that rate encoding plays a dominant role in first dorsal interosseous muscle up to 80% MVC, while recruitment was the major mechanism for generating extra force between 40%–80% MVC in deltoid. At a low voluntary contraction level, more MUs are recruited asynchronously to generate a larger contraction force whereas at a high contraction level, more frequent firings are generated and muscle twitches are fused. It was found that the firing rates of active motor units increase monotonically with increasing force output [Milner-Brown 1973] and the change of firing rate was correlated to the recruitment threshold [Erim 1996].

The firing rate pattern is represented as firing times of each decomposed MU, and the property for coherent behavior between firing rates and MU is called common drive—the degree to which a single source controls the activities of all MUs in a given pool [DeLuca 1994]. The "onion skin" pattern refers to the fact that lower-threshold action potentials (i.e., those recruited first) always tend to fire at a higher rate than MUs that are recruited later, and is interpreted as evidence in favor of common drive shown in Figure 1.2. The "onion skin" pattern also implies that for the same increase in force, MUs recruited earlier increase their firing rate faster than those recruited later.

The maximum firing rate measured for clinical usage under constant force contraction for healthy subjects is usually below 30 pps [Bigland-Ritchie 1983]. The firing rate of a MU in the first dorsal interosseus of the index finger varies between 4–40 pps with variation in firing rate below 10 pps/sec for clinical uses [Moritz 2004].

Subsequent firings of a MU have timing that is well modeled as an independent random process. Neural responses in rate coding are typically treated statistically because stimuli are repeated [Basmajian 1985]. Clamann [1967], Perkel [1967] and Masland [1969] observed that the majority of inter-pulse intervals (IPIs) of a MUAP train are independent during voluntary isometric constant-force non-fatiguing contractions. Persen and Kudina [Persen 1972] found no correlation between adjacent IPIs for MUs firing below 10 pps, and a negative correlation above 10–13 pps, but DeLuca [DeLuca 1973] showed that for MUAP trains recorded from the middle fibers of the deltoid muscle, the assumption of IPI independence cannot be rejected.

The purpose of firing rate calculation is to estimate a time-continuous function from the individual timing of firings of a MU. The continuous rate $r(t)$ reflects the change of underlying CNS command. Christova [1998] showed that increased firing rates of biceps brachii muscle at some elbow angles compensate for the reduction of twitch duration of evoked contraction at short muscle lengths. Sinex [1988] showed that the average firing rates of auditory-nerve fiber that was tuned to the frequency region near the first formant increase at the onset of voicing, closely related to spectral amplitude changes at onset of voicing and activation of first formant. In these cases, the CNS uses firing rate to mediate functionality of muscle.

Kamen [Kamen 1995] calculated average firing rate from the five shortest IPIs during a steady-state portion of contraction, excluding possible doublets (IPI<10ms) and very

long IPIs (>200ms) from the IPI sequence. Gerdle [Gerdle 2008] used median firing rate to make the estimate of the mean firing rate less sensitive to possible missed MUAPs. Azevedo and Lepora [Azevedo 2005, Lepora 2009] counted the number of spikes in 50 ms intervals with a sliding window that moves by 10% for electroneurograph (ENG) firing rate calculation. Weber [Weber 2011] convolved spike times with a Gaussian kernel and resampled at longer intervals. DeLuca [DeLuca 1982] applied a 400 ms Hanning filter to a MUAP train to estimate EMG firing rate fluctuation. Berger [Berger 1986] calculated the heart beat variability by convolving the instantaneous heart rate with a rectangle window. Maeto [Maeto 2000] used the integral pulse frequency modulation model (IPFM) for simulating electrocardiograph (ECG) variability and Bailón [Bailón 2011] extended the model to allow for a time-varying threshold parameter in the IPFM.

1.1.4 EMG-amplitude and signal whitening

The standard deviation (a.k.a., amplitude) of sEMG waveform has been observed to increase with the level of muscle contraction, and has been used as control input of proportional control myoelectric prosthesis and in ergonomic studies [Mathiassen 1995]. Factors such as temperature [Petrofsky 1980], subcutaneous fat layer thickness [Nordander 2003], muscle contraction level [Olson 1968], torque [Karlsson 2001], gender and muscle difference [Pincivero 2000], and muscle fatigue [Moritani 1986] each affect EMG amplitude. Normalization of sEMG amplitude is needed to enable inter-subject [Yang 1984], and inter-muscle [Burden 1999] comparisons. EMG amplitude has been widely used for prosthesis control [Mann 1981], ergonomics analysis [Dietz 1989, Yang 1985] and clinical evaluation [Barry 1990, Ferri 2008]. The relationship between EMG amplitude and joint torque has been modeled using neural networks [Song 2005] and polynomials [Clancy 1991], and is studied in ergonomics [Jamison 1993] and prosthetic control [Luh 1999, Morita 2000].

A whitening transformation is a decorrelation transformation that transforms a set of random variables with some covariance matrix into a set of new random variables whose covariance matrix is the identity matrix. A wide range of methods exists for temporal signal whitening, from simple high-pass filtering of sEMG [Potvin 2004] to signal detection [Barton 1988]. In general, signal whitening techniques orthogonalize the data samples, allowing subsequent analysis to operate on each output sample individually. For samples acquired periodically in the time domain, whitening broadens the spectrum of

discrete samples and increases statistical bandwidth by decreasing the linear dependency of adjacent data samples. This technique had been applied in EMG amplitude estimation [Prakash 2005] and EMG to torque estimation [Clancy 2006]. EMG amplitude estimation incorporating signal whitening and multiple channel combination was shown to improve signal to noise ratio (SNR) by 187% compared with conventional EMG amplitude estimation during constant-posture, constant-force, non-fatiguing contractions [Clancy 1995], and the techniques reduce EMG-torque error by one third [Clancy 1997].

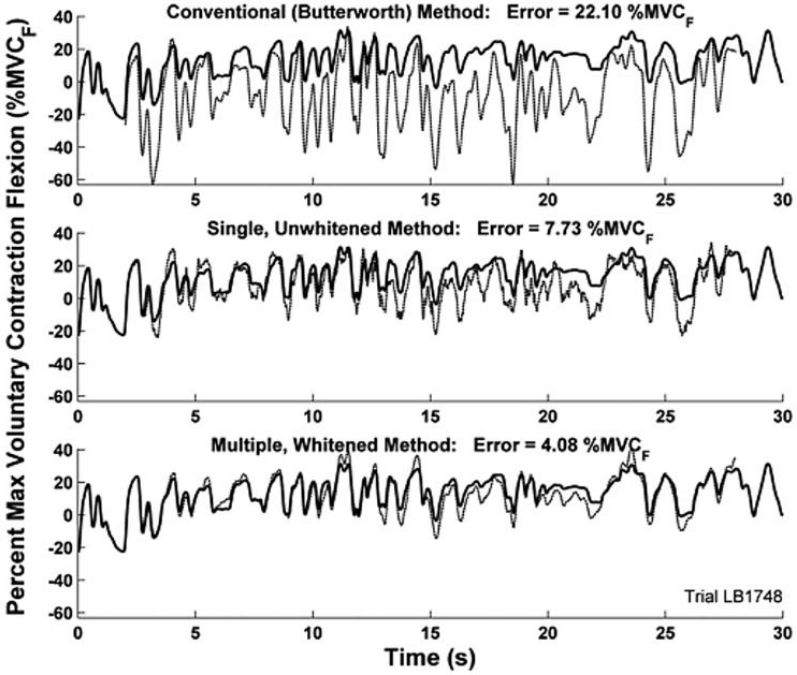

Figure 1.3. Representative sample of actual and estimated elbow-torque as a function of time. Solid line in each graph is actual torque, scaled to percent maximal voluntary contraction flexion (%MVC$_F$), for the same 30-s contraction period. Positive values denote flexion torque. Dotted line in each plot shows the torque estimated by training a model to distinct trials, then using EMG to estimate torque from this trial. (Top) Estimates from the best "conventional"method. (Middle) Best single-channel unwhitened method. (Bottom) Best multiple-channel whitened method. Taken from [Clancy 2012].

Figure 1.3 shows a representative sample of actual and estimated elbow-torque as a function of time [Clancy 2012]. Combination of multiple-channel, EMG whitening and advanced processor has reduced torque estimation error from 22.10% MVC of conventional method to 4.08% MVC.

1.2 Contributions of this dissertation

This dissertation is organized in a compendium form, with each of Chapter 2–12 being a published (or in preparation) journal/conference manuscript. Thus, each chapter is devoted to an independent aspect of EMG study. Chapter 13 (Appendix) provides more background and details of methods / results mentioned in Chapters 2–12. The Introduction serves as a brief introduction of background and per-subject overview; the body of studies in Chapter 2–12 is published or drafted journal / conference papers; and the Appendix elaborates on any data and material not used in the publications of Chapter 2–12.

1.2.1 EMG firing rate calculation

The first investigator-led project resulted in the manuscripts provided in Chapter 2–3. This project takes a step back to evaluate the current state of art for calculating EMG firing rate (from the EMG firing times), and methods to calculate neural firing rates in general. Only the simplest temporal filter with fixed window type and size had been used for EMG firing rate estimation, while some more sophisticated methods give more accurate depictions of heart rate calculation for electrocardiogram (ECG), and neural firings in electroneurogram (ENG). Simulations for generating realistic firing patterns are used to evaluate conventional EMG rate methods and those methods previously applied to ECG/ENG. Based on these evaluation results, optimal methods with optimal parameters are given.

Chapter 2–3 address how neural firing rates calculated for other types of bioelectric signals can be used to calculate firing rate from the firing sequence of iEMG decomposition, comparing both their advantages and limitations. In this chapter, methods used to obtain a time-varying firing rate from decomposed EMG signals are investigated. These methods are applied to both simulated firing times and firing times from decomposed clinical data. For simulation, both sinusoidal firing rate modulation and more realistic stochastic rate modulation are investigated, using the known “true” firing rate from the IPFM model. The rate calculation methods are evaluated within the physiological range of firing rates, variation range and variation bandwidth, with iEMG decomposition errors representative of the state of the art. Optimal parameters of each

method are found under these physiological conditions and their performances are cross-compared with respect to different decomposition error percentage.

Formal proofs of a few simple properties of those methods are presented in Appendix. The iEMG decomposition error is typically much higher than the error found in ECG detection, therefore some preliminary analysis of how missed/spurious firing can affect accuracy of firing rates are given in the Appendix, i.e. the difference between a presumptuous firing rate that results in missed/spurious firing and the actual firing rate based on when the missed/spurious firings take place, ignoring the refractory period. Given the mathematical model of the firing times of MUs, we also show approaches to estimate more realistic firing patterns such that the resulting IPIs satisfy well established properties [DeLuca 1973].

Methods for firing rate estimation are evaluated using sinusoidal simulated rate modulation spanning from 5 pps to 20 pps, and with stochastic modulation with a statistical bandwidth of 1 Hz. Decomposition error ranged from 0–4%. The results show that: DeLuca and Berger methods are more applicable to EMG firing rate calculation than simple instantaneous method and spline-based methods (Mateo and instantaneous spline). The RMS error performances of Berger/DeLuca methods using optimal parameters are much lower than the other methods, and spline-based methods perform poorly in presence of decomposition errors. Each of these methods smooth the firing rate to some extent. Spline-based methods are much more sensitive to smaller errors than LTI-filtering based methods, and therefore are unsuitable for EMG analysis since substantial decomposition errors (<10% [DeLuca 2006, Holobar 2013]) are standard.

1.2.2 sEMG whitening for prosthesis control

The second investigator-led project resulted in the manuscripts provided in Chapter 4–7. In these chapters, signal whitening techniques are applied as a preprocessing stage to pattern classification of motion types of sEMG data collected from intact and amputated subjects. Pattern classification of the EMG signal is used as a control mechanism for powered, upper-limb prostheses and is under investigation for use in lower-limb prostheses. We showed that sEMG classification accuracy is improved due to signal whitening.

EMG classification has long been applied to upper-limb prosthesis control [Saridis 1982]. Typically a few temporal features are extracted using a sliding window and some

frequency measures such as auto-regressive model coefficients are fit to a segment of sEMG data, assuming that the properties of the underlying signal are unchanged during a short period of time (up to a few hundred milliseconds) when performing some given tasks. A classifier based on these features is then trained to determine the user's intention.

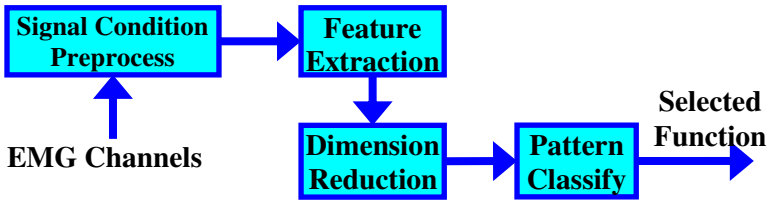

Figure 1.4 sEMG-based motion classification diagram

Signal whitening had been used for EMG amplitude estimation and EMG to torque estimation. It has also been used in lab for proportional control and assessed in constant-force and various EMG-torque settings [Hogan 1980]. However, whitening has not previously been applied to upper-limb prosthesis classification. In Chapter 4–7, we apply electromyogram whitening to upper-limb prosthesis classification. We use signal whitening as a preprocessing stage to sEMG-based motion classification as shown in Figure 1.4. Whitening decreases the variation for temporal features used: mean absolute value, average signal length and zero-crossing rate; thereby increasing feature discrimination and making the classification task more accurate. In Appendices, approaches to estimate statistical bandwidth from sEMG and simulated data in an accurate and unbiased way are shown.

In a study of ten intact subjects and five amputee subjects with up to 11 motion classes and ten-electrode channels, we show that using signal whitening as a preprocessing stage improves motion classification accuracy by approximately 5%, especially at smaller window sizes. This improvement allows for a faster response of prosthesis control and higher recognition accuracy.

1.2.3 Other contributions

Chapter 8–9 describe a team-based study of advanced models of constant posture EMG-torque relationship about the elbow. Advanced EMG amplitude estimation (signal whitening and multiple-channel combination), longer duration training sets, regularized least squares (pseudo-inverse and ridge regression) and nonlinear models (Wiener model and Hammerstein model) are used. When combined, these methods reduce the average

estimation error from 19.15±11.5% MVC using conventional methods to 4.65±3.6% MVC.

Chapter 10–12 document another team-based project in which an experimental study relating biceps-triceps surface EMG of 12 subjects to elbow torque at seven joint angles (spanning 45º-135º) during constant-posture, quasi-constant-torque contractions was conducted. Advanced EMG amplitude estimation processors and three nonlinear EMG-amplitude-torque models were used. The best model that interpolates across angles using a parameterized angle dependence achieved an error of 4.17±1.7% MVC, and models that accounted for co-contraction estimated individual extension muscle torques ~29% higher and individual flexion muscle torques ~68% higher.

The Appendix of Chapter 13 gives explanations and justifications for certain methods used in the previous chapters. Specifically, Section 13.1 gives a brief introduction of firing rate calculation methods, Section 13.2 shows firing rate estimations used in Chapter 2–3 for constant firing rate conditions; Section 13.3 discusses practical methods to estimate statistical bandwidth of a given EMG signal segment; Section 13.4 associates the output of the IPFM model with multi-tone input with its true firing instants and Section 13.5 takes a brief look at approaches to calculating firing rate when the IPIs are stochastic.

1.3 Summary of Contributions

In Chapter 2–3, we are the first to quantitatively compare different methods to calculate neural firing rate and apply them to the EMG field. Only rudimentary methods have been used for EMG firing rate before, presumably because of iEMG's high decomposition error that is absent in other neural firing measures (especially ECG). We generalized methods used in other fields as well as EMG firing rate, adapted a method to simulate realistic EMG firing sequences and evaluated various firing rate calculation methods using both sinusoidal and stochastic simulation rate modulations.

In Chapter 4–7, we applied signal whitening to the sEMG motion classification framework. Signal whitening has been extensively used in information and communication theory, and in EMG-amplitude estimation and EMG-force processing; but has not been used for pattern recognition within the application of prosthesis control. We showed that the coefficient of variation of some temporal features decreased as statistical bandwidth increased due to whitening, which supports the observation that

motion classification accuracy improves when signal whitening is applied as a preprocessing stage.

In Chapter 8–9, a team-based project relating constant-posture EMG amplitude to joint torque, using advanced dynamic models is described that effectively reduces estimation error to 4.65±3.6% of MVC flexion, which is less than a quarter of that of standard techniques used before.

In Chapter 10–12, a team-based project relating constant-posture EMG amplitude to joint angles, a combination of advanced EMG amplitude estimation processor and a dynamic polynomial regression model accounting for co-contraction, are used that reduces estimation error below 5% MVC.

1.4 Summary

This compendium of studies describes various aspects of electromyogram theory and applications. We evaluated methods for firing rate estimation used in the fields of EMG/ECG/ENG, in the presence of realistic EMG decomposition errors using simulation and clinical EMG data. Our results showed that the simple linear filtering methods of Berger/DeLuca are best over a wide range of firing rate conditions and decomposition errors. In a different project, we applied signal whitening as a preprocessing stage to upper-limb prosthesis control and showed that it decreased the variability of temporal features and improved classification accuracy by about 5%. Advanced dynamic/nonlinear models for constant-posture EMG amplitude-torque were used and average estimation error was reduced by more than 75%. Advanced models for relating biceps/triceps surface EMG to elbow torques parameterizing angle dependency achieved lower error.

Chapter 2

Calculation of Surface Electromygram Discharge Rate

Lukai Liu[1], Edward A. Clancy[1], Paolo Bonato[2]

[1]ECE Dept., Worcester Polytechnic Institute, Worcester. MA, USA.

[2]Dept. Phys. Med. & Rehab., Harvard Medical School, Boston. MA, USA

This chapter has been published as: **Lukai Liu**, **Edward A. Clancy** and **Paolo Bonato**. "Calculation of Surface Electromyogram Discharge Rate", *2013 39th Annual Northeast Bioengineering Conference*, Syracuse University, pp. 187–188, 5–7 April, 2013. Available: http://ieeexplore.ieee.org/xpl/login.jsp?reload=true&tp=&arnumber=6574421&url=http%3A%2F%2Fieeexplore.ieee.org%2Fxpls%2Fabs_all.jsp%3Farnumber%3D6574421

Abstract—The discharge rate of motor unit action potential sequences has been related to fatigue and neuromuscular diseases, but typically simple methods are used to do so. We adapted more advanced methods used to calculate heart rate to fit in the context of surface electromyogram discharge rate calculation. Simulation results with a deterministic discharge rate modulation model suggest that parameter fine-tuning is necessary to accurately and robustly estimate discharge rate.

Keywords—surface electromygram; discharge rate; IPFM.

2.1 Introduction

The motor unit action potential firing sequence contains information about the central nervous system and several neuromuscular diseases have been reported to correlate with firing variability [Gemperline 1995, Dietz 1974, Rice 1992 and Dorfman 1989]. Simple methods such as filtering the discharge sequence [DeLuca 1982] and calculating the average discharge rate [Kamen 1995] have been used for estimating electromyogram (EMG) discharge rate. More sophisticated models and methods had been used for calculating heart rate [Bayly 1986, Berger 1986 and Maeto 2000], but have not been adapted to the EMG application. This omission may be partially due to the fact that detection accuracy of ECG complexes is much higher than that of EMG, with effective decomposition methods for EMG being an active area of research [Nawab 2008, McGill 2005 and Erim 2008]. Missed and false-detected EMG pulses of about 2–5% are common [Erim 2008], even with the best decomposition schemes. The

consequences of inaccurate EMG decomposition must be taken into consideration when EMG discharge rate is interpreted.

In this study, we modify methods used to calculate heart rate variability for EMG discharge rate estimation. We used the integral pulse frequency modulation (IPFM) model [Bayly 1968] to generate discharge sequences from a known deterministic model and evaluated the performance using various proposed rate calculation methods. We also artificially introduced missed and false detections into our evaluation.

2.2 Methods

The IPFM model mimics the dynamic properties of the neural system and has been used to model heart rate variation. It can be similarly applied to EMG firing rate. A zero-mean process specifies the underlying rate variation. For simplicity, a sinusoidal modulation is used in (2.1):

$$x(t) = \int_0^t \frac{1 + a\cos(\omega\tau)}{T} d\tau \tag{2.1}$$

where T is the average inter-pulse interval (s), a/T is the amplitude of discharge rate variation (pps) and ω is the variation velocity of discharge rate (radians/s). The discharge sequence comprising of impulses at $\{t_k, k \in \mathrm{N}\}$ satisfies $x(t_k) = k$, and the sampled sequence is one at $\{[t_k]\}$ and zero elsewhere, where the notation "$[t_k]$" denotes discrete sampling instant closest to t_k. Following this model, the discharge rate is given by its derivative $x'(t)$. [Maeto 2000]

The instantaneous rate is defined in (2.2a) with step changes at $\{t_k\}$, which suffers from high frequency artifacts. The LeFever method (2.2b) [DeLuca 1982] convolves a 400ms Hanning window with the discrete sequence $\{[t_k]\}$, and the Berger method (2.2c) convolves a rectangular window of duration T_c with the instantaneous rate before it is discretized. The Berger method reduces high frequency artifacts, but still permits aliasing. Thus we introduce the Berger-variant that convolves a temporal sinc function with cut-off bandwidth f_c (2.2d) with the instantaneous rate before it is discretized.

$$R_{\mathrm{inst}}(t) = \frac{1}{t_k - t_{k-1}} \quad t_{k-1} \le t < t_k \tag{2.2a}$$

$$R_{\mathrm{Maeto}}[nT] = \frac{\delta[nT - [t_k]]}{t_k - t_{k-1}} \otimes \mathrm{Hann}_{Th}[nT] \tag{2.2b}$$

$$R_{\mathrm{Berger}}(t) = R_{\mathrm{inst}}(t) \otimes \mathrm{rect}_{T_c}(t) \tag{2.2c}$$

$$R_{\mathrm{BergerV}}(t) = R_{\mathrm{inst}}(t) \otimes \mathrm{sinc}_{f_c}(t) \tag{2.2d}$$

$$y_{\mathrm{Maeto}}(t) = \begin{cases} k, & t = t_k \\ 0, & \text{otherwise} \end{cases} \tag{2.2e}$$

The Maeto method [Maeto 2000] transforms impulse sequence $\{t_k\}$ to (2.2e) and then spline interpolates to obtain continuous function $\hat{y}_{\text{Lag}}(t)$ which approximates (2.1). Discharge rate is obtained by taking its derivative $R_{\text{Lag}}(t) = \hat{y}'_{\text{Lag}}(t)$. We define the instantaneous spline method by sampling (2.2a) at instants $\{t_k\}$ and spline fitting these values. All these methods are viewed as lowpass filtering, with spline interpolation viewed as a time-varying filter whose frequency response depends on the duration between interpolated samples.

2.3 Results

All methods given except instantaneous rate have one parameter: filter order, cut-off frequency or interpolation degree of freedom. The sinusoid IPFM model has three parameters: amplitude, frequency of discharge rate variation, and average inter-pulse interval.

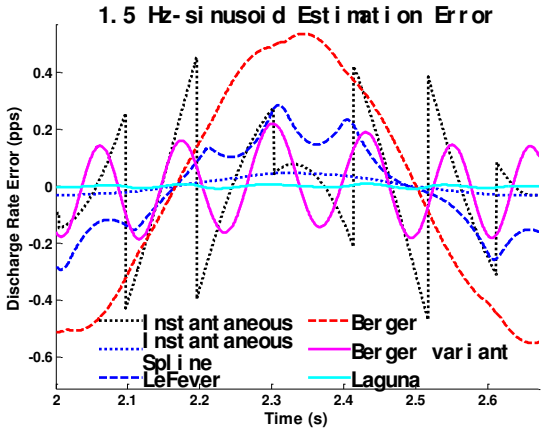

Figure 2.1. Simulation discharge rate estimation error $\hat{r}(t) - r(t)$ using 1.5 Hz sinusoid IPFM model with average discharge rate of 8 pps and a=0.1. LeFever and Berger methods use 400ms window; Berger-variant uses f_c=10 Hz; Maeto and instantaneous-spline methods use cubic spline.

Figure 2.1 shows the discharge rate error vs. time, when average discharge rate is 8 pps, a=0.1 and 1.5 Hz modulation frequency. The LeFever and Berger methods used 400ms windows, the Berger-variant method used 10 Hz cutoff frequency and a cubic spline was used for the Maeto and instantaneous spline methods. We see that the Laguna rate perfectly follows the true rate, followed by the instantaneous spline method that exhibits smaller amplitudes when the discharge rate is changing rapidly. The Berger-variant and LeFever methods are capable of following fast-changing portions but fluctuate at peaks with these parameters, and the Berger method barely reaches the peak.

In the presence of missed/false detections, however, the spline-based methods drastically deteriorate where these errors take place, due to their capability of tracking fast transients. Figure 2.2 shows the

estimation error vs. detection error rate up to 5% error, with average discharge rates varying up to 10 pps. Spline-based methods are more sensitive to detection error than temporal-filtering methods.

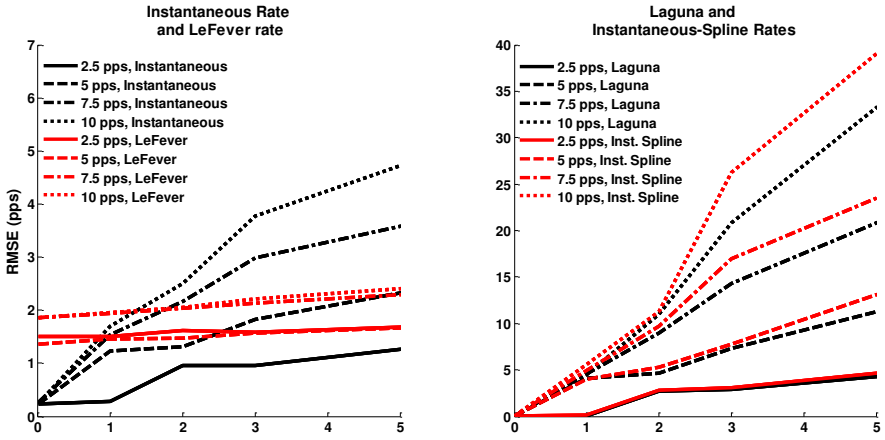

Figure 2.2 Average RMSE with different average discharge rate in presence of detection error.

2.4 Conclusion

We introduced several methods to calculate EMG discharge rates. While spline-based methods are capable of accurately tracking fast rate transitions, they perform poorly in the presence of detection errors. Ongoing studies include the use of a stochastic modulation model, variations in method parameters, and validation of our methods on clinical data.

Chapter 3

Comparison of methods for estimating motor unit firing rate times series from firing times

Lukai Liu[1], Paolo Bonato[2] and Edward A. Clancy[1],

[1]ECE Dept., Worcester Polytechnic Institute, Worcester. MA, USA.

[2]Dept. Phys. Med. & Rehab., Harvard Medical School, Boston. MA, USA, pbonato@partners.org

Abstract—The central nervous system regulates recruitment and firing of motor units to modulate muscle tension. Estimation of continuous firing rate is typically performed by decomposing the electromyogram (EMG) signal into its constituent firing times, then lowpass filtering a constituent train of impulses. Little prior work has examined the performance of different estimation methods, particularly in the inevitable presence of decomposition errors. The study of electrocardiogram (ECG) and electroneurogram (ENG) firing rate presents a similar problem, and has applied novel simulation models and firing rate estimation techniques. In this study, we adapted an ENG/ECG simulation model to generate realistic EMG firing times derived from known rates, and then assessed various firing rate estimation methods. ENG/ECG-inspired rate estimation worked exceptionally well when EMG decomposition errors were absent, but degraded unacceptably with decomposition error rates of 1% and higher. Typical expert EMG decomposition error rates are 3–5%. At realistic decomposition error rates, more traditional EMG smoothing approaches performed best—when optimal smoothing window durations are selected. This duration decreased as the modulation frequency of firing rate increased, average firing rate increased and decomposition errors decreased. Examples of these rate estimation methods on physiologic data are also provided.

Keywords—Electromyogram, decomposition, firing rate, EMG signal processing.

3.1 Introduction

It has long been known that the central nervous system regulates recruitment and firing rates of motor units (MUs) in order to modulate overall muscle tension [Henneman 1965 and Milner-Brown 1972, 1973a, 1973b]. For active MUs, firing rate—and other measures derived from firing rate—have been studied during many healthy physiologic states, including: constant-force contractions [DeLuca 1996],

slowly increasing force contractions [DeLuca 1982a and Milner-Brown 1973b], fatigue [Bigland-Ritchie 1983], muscle pain [Farina 2004], physical training [Duchateau 2006] and aging [Kallio 2012 and Christie 2009]); and during many disease states [Dietz 1974, Dorfman 1989, Gemperline 1995, Kasi 2009 and Rice 1992]. This research remains ongoing.

In using the term "firing rate," we are referring to the firing rate *time series* as it evolves in time. To study firing rate, indwelling electrodes are typically used to record the electromyogram (EMG). This EMG is decomposed into its constituent MU firing times, from which individual MU firing rate information is extracted. Recently, surface arrays have also been used to identify MU firing times [Holobar 2004 and 2007]. In either case, the firing times are generally modeled as a stochastic point process, formed as a result of the underlying time-varying firing rate. Most commonly, rather simple information extraction techniques have been used and they have been limited to estimating statistical *parameters* of the EMG firing rate time series. Kamen et al. [Kamen 1995] estimated average firing rate during maximum-effort contractions from the five shortest inter-discharge intervals (IDIs) during a steady-state portion of contraction, excluding possible doublets (IDI < 10 ms) and very long IDIs (> 200 ms). Gerdle et al. [Gerdle 2008] used the median firing rate of constant-force contractions to produce an estimate that was less sensitive to possible missed MU action potential (MUAP) detections. Navallas et al. [Navallas 2014 and 2015] used maximum likelihood estimation to improve computation of the mean and standard deviation of the IDI during constant-force contractions. Some researchers have developed estimators of the complete (time-varying) firing rate time series. Estimates of the complete time series facilitate more advanced characterization of its evolution, beyond what is available in the mean and standard deviation values, e.g. the "onion skin" effect, inter-unit synchronization and common drive [DeLuca 1982a, DeLuca 1985 and Stashuk 1989]. Lepora et al. [LePora 2009] estimated firing rate from the number of firings in contiguous 50 ms time intervals, pooling data across ensemble trials to assure a sufficient number of firings per interval. Stashuk [Stashuk 2001] estimated firing rate at each firing time as the inverse of a Hamming weighted average of 10 IDIs centered about the firing time, excluding outlier intervals. DeLuca et al. [DeLuca 1982a] estimated firing rate by convolving an impulse train corresponding to the MU firing times with a non-causal (zero phase) 400 ms duration Hanning filter. Physiologically, however, no underlying firing rate time series actually exists; rather, multiple central nervous system factors contribute to motor nerve excitation and the resulting MU firing times. Thus, the absence of a physiological "gold standard" makes it difficult to objectively assess the accuracy of firing

rate time series (and parameter) estimates. We are not aware of rigorous assessment of firing rate time series estimation methods within the EMG field.

More sophisticated models and methods of firing rate time series analysis have been applied to studies of the nervous system and heart rate [Bayley 1968, Berger 1986 and Mateo 2000], but have not been applied to the EMG application. In particular, the continuous-time integral pulse frequency modulation (IPFP) model, adapted for implementation in discrete time, can be used to simulate firing times from a firing rate time series. These firing times can be supplied to a firing rate time series estimation algorithm, and then the estimated rate compared directly against the known "true" rate at each discrete time. Within the ECG literature, robust performance comparisons have been made between advanced firing rate estimators using this model: Berger et al. [Berger 1986] estimated heart rate by analytically convolving the continuous-time instantaneous heart rate with a rectangular window function and then sampling the result, while Mateo and Laguna [Mateo 2000] used spline functions to smooth the instantaneous heart rate (directly in discrete time). In each case, the instantaneous rate was defined as the inverse of the IDI throughout the duration of each IDI.

In this study, we used the IPFM model to simulate MUAP firing times from various firing rate profiles and then quantitatively evaluated several firing rate time series estimators drawn from both the EMG and ECG literature. Existing firing rate estimators drawn from the EMG literature have not been previous evaluated in such a manner, while the more advanced ECG firing rate estimators have not previously been applied to the EMG field. Our goal was to rigorously cross-compare these estimators. Of particular interest was the performance of each rate estimator in the presence of firing detection/classification errors. In the ECG field, detection errors are quite low (particularly during recording at rest), certainly under 0.7% [Pan 1985]. In contrast, detection errors in EMG decomposition are much higher; errors of 3–5% are common even when automated decomposition is augmented by exhaustive manual editing [Erim 2008], and considerably higher errors (10–20% or more) occur when automated decomposition is used alone or if low amplitude MUAP trains are included [Nawab 2008]. Hence, our simulations compared performance across a range of false positive and missed detection rates. Lastly, examples drawn from physiologic recordings are used to illustrate the performance of the different firing rate estimation algorithms.

3.2 Methods

3.2.1 Integral pulse frequency modulation (IPFM) model and firing rate estimators

All processing was performed in discrete timebut, as described, may be based on initial continuous-time steps. Firing timesin our simulations were generated as the output of the IPFM model, given afiring rate as input.In acontinuous-valued IPFM model, every two consecutive firing times t_k and t_{k+1} are related as [Bayly 1968]:

$$1 \text{ pulse} = \int_{t_k}^{t_{k+1}} [f_0 + f_{Mod}(t)]\, dt \tag{3.1}$$

where $f_0 > 0$ is the average firing rate in pulse/s (pps) and $f_{\text{Mod}}(t) \geq -f_0$ is the zero-mean rate modulation as a function of time, *t*, in pps. Thus, the instantaneous firing rate equals $f_0 + f_{\text{Mod}}(t)$. This model is constrained so that the instantaneous firing rate is non-negative. Essentially, the integral sums the instantaneous rate until a threshold of 1 pulse is achieved, a simulated firing then occurs and the integral resets for accumulation during the next IDI. For a constant firing rate, $f_{\text{Mod}}(t) = 0$. We implemented this model in discrete time using a discrete sum (rather than an integral) with a sampling interval of 1/40960 s. Firing times were rounded to the nearest 1/4096 s, to correspond to the sampling rate of the firing rate estimators. For one simulation, this model produced a set of *N* time-increasing firing times $\vec{t}_F = \{t_1, t_2, \ldots, t_N\}$.

Firing rate estimators (in pps) were compared using asampling rate of F_s=4096Hz. Rate estimation was made from a N-length firing time vector $\vec{t}_F$, which was output from the IPFM model. The "instantaneous" rate, $r_{Inst}[n]$, was computed at each discrete time sample *n* as the inverse of the IDI in which the sample was located. Short duration IDIs correspond to large firing rates; long duration IDIs correspond to small firing rates. The rate is constant between firing times and changes in a step fashion at the next firing time. If sample *n'* falls between firing times t_k and t_{k+1}, then the instantaneous rate at this sample is:

$$r_{Inst}[n'] = \frac{1}{t_{k+1} - t_k} \tag{3.2}$$

This estimator has no parameters.

The "Berger" rate [Berger 1986] begins by considering the continuous-time instantaneous rate, defined as above but in continuous-time. Berger et al. show that the continuous-time instantaneous rate can be analytically convolved with a rectangular (a.k.a. gate) function and then sampled, producing $r_{Berger}[n]$. They note that the discrete-time instantaneous rate $r_{Inst}[n]$ is actually a sampled version of the continuous-time instantaneous rate $r_{Inst}(t)$, and thus will suffer aliasing at the step transitions occurring

at each firing time. Convolution in continuous time with a gate function is a form of lowpass filtering that limits the aliasing. Their rate calculation can be thought of as:

$$r_{Berger}[n] = r_{Inst}(t) \otimes \mathrm{Rect}_{T_B}(t)\big|_{t=2nT_B} \tag{3.3}$$

where $\mathrm{Rect}_{T_B}(t) = \begin{cases} \frac{1}{2T_B}, & -T_B \le t < T_B \\ 0, & \text{otherwise} \end{cases}$. Parameter T_B was varied between 20 and 800 ms in increments of 20 ms. Note that the lowpass analytic convolution windows the spectrum of the firing rate. Berger et al. applied a multiplicative frequency-domain correction (inverse window) at low frequencies only—which happen to be the only frequencies applicable to their ECG application. Since we were computing a time-domain quantity (firing rate), we did not apply their correction.

The "DeLuca" rate [DeLuca 1982a] is formed directly in discrete-time. Let time-series $\delta_F[n]$ equal one at sample location closest to each firing rate, and zero otherwise. Then,

$$r_{DeLuca}[n] = \delta_F[n] \otimes \mathrm{Hann}_{T_D}[n] \tag{3.4}$$

where $\mathrm{Hann}_{T_D}[n]$ is a non-causal (zero-phase) Hanning window. The window duration T_D varied between 20 and 800 ms in increments of 20 ms.

Mateo and Laguna [Mateo 2000] created a smoothed firing rate by initially assembling the previously defined *N*-length vector of firing times, t_F, as the *x*-axis vector; and the staircase vector $\{1,2,\dots,N\}$ as the *y*-axis vector. A cubic spline fit was made between these non-periodically sampled points, and the resulting fit was periodically resampled at F_s=4096 Hz. This signal was differentiated in discrete time (first backward difference) to form $r_{Mateo}[n]$.

Finally, we implemented a simplified "spline" version of the method of Maeto and Laguna that avoided the derivative. The continuous-valued instantaneous rate was sampled at the mid-point of each IDI. These non-periodically sampled time (*x*-axis) and rate (*y*-axis) value-pairs were cubic spline-fit and then resampled periodically at F_s=4096 Hz, forming $r_{spline}[n]$.

3.2.2 Simulation methods

A simulation was performed in which the firing rate was modulated in a (zero-mean) sinusoidal fashion, i.e., $f_{Mod}[n] = a\sin(2\pi f_{Sine} n/F)$, where a sets the sine wave magnitude and f_{Sine} sets the modulation frequency. Sinusoidal evaluation is common in engineering analysis and is relevant to repetitive motion profiles. Average firing rates studied were: f_0 = 5, 10, 15 and 20 pps. Modulatin frequencies studied were: f_{Sine} = 0, 0.25, 0.5 and 1 Hz. Modulation magnitude was set to 40% of the average firing rate. Each combination of f_0, f_{Sine}, a and rate estimator parameter was simulated. This

sinusoidal modulation was studied in the presence of simulated decomposition errors. Decomposition error rates studied were: 0, 1, 2, and 4%, with half of the errors assigned as false negatives ("misses") and half as false positives (extraneous detections). For each simulation, the instantaneous firing rate time series, $f_{Inst}[n] = f_0 + f_{Mod}[n]$, was used by the IPFM model to produce an initial vector of firing times. Errors were then inserted. The number of false positives was computed from the error rate and the average firing rate, and these many firings were randomly deleted (each firing having equal probability of being deleted). The false positive detections were then inserted randomly into sample times that did not already contain detection, again with each time sample having the same probability of insertion. The resulting firing times were used by each firing rate algorithm to estimate the firing rate time series. The RMS error between the actual and estimated firing rate, excluding firing startup and tail transients, was used as the measure of performance. Each simulation was 100 s in duration. For non-zero error rates, each simulation was iterated 2000 times, with independent errors generated each iteration.

Another simulation was performed in which the firing rate was modulated in a zero-mean random fashion with predefined average firing rate about the average firing rate. This evaluation is relevant to both constant-effort contractions (random IDI variation about an average rate) and more generalized motion. A challenge was to design a random firing sequence that is non-negative band-limited and, when input to the IPFM model, produced output IDI distribution similar to those found experimentally [Clamann 1969, DeLuca 1973 and Englehart 1994]. Most band-limited random signals are produced as a Gaussian probability density function. However, the Gaussian PDF includes a tail with negative values (out to -∞) that violates the requirements that the instantaneous rate be non-negative. In addition, we observed IDI density results that were too clustered about the mean firing interval, perhaps due to rapid decay of the Gaussian PDF. A truncated Gaussian PDF fared little better. Alternatively, the uniform PDF limits its range of values to appropriately provide only non-negative instantaneous firing rates, but similarly limits positive values such that the resulting IDI skewness did not match that of experimental data. Thus, we informally evaluated several rate-modulation PDFs. In each case, independent identically distributed random variables were generated at a rate sufficient to produce the desired statistical bandwidth [Bendat 1971] of 1 Hz, then upsampled to 4096 Hz using spline interpolation. This upsampled rate signal was thresholded (the upsampling could produce signal values slightly outside of the original region) to arrive at a non-negative instantaneous rate. This upsampling process produces limited distortion in the rate signal PDF prior to being input to the IPFM model. We settled on a firing

rate modulation PDF mixture with uniform density for negative rates and exponential density for positive rates, with equal probability of negative and positive rates (yielding zero-mean modulation):

$$p_x(x) = \begin{cases} 0, & x < -a \\ \frac{1}{2a} & -a \le x < 0 \\ \frac{1}{2a} e^{\frac{-x}{a}} & x \ge 0 \end{cases} \tag{3.5}$$

where x (pps) is the firing rate modulation (it is added to the average firing rate to form the instantaneous rate) and parameter a ($0<a<1$) sets the range of the modulation. This PDF is continuous at $x=0$. A parameter value of $a=0.9$, corresponding to a modulation range equal to 90% of the mean firing rate, was selected to best match experimental distributions. The same average firing rates and decomposition error rates as with the sinusoidal analysis were used, as well as the RMS error measure between the actual and estimated firing rates. For each case, 2000 iterations of a 200 s trial duration were evaluated. Statistical evaluation utilized ANOVA and two-tailed, pairwise and paired t-tests (with Bonferroni adjustment for multiple comparisons).

3.2.3 Experimental examples

Experimental EMG data and their expert decomposition from a prior study of patients with amyotrophic lateral sclerosis (ALS) [Kasi 2009] were used as examples to contrast firing rate estimation techniques on actual data. This data-reuse was approved by the WPI Institutional Review Board. In brief, quadrifilar needle electrode data were acquired from the first dorsal interosseous muscle during constant-posture trials at 20% maximum voluntary contractions (MVC; 15 s duration) and 50% MVC (5 s). These data were passband filtered between 300 and 10k Hz, then sampled at 25 kHz using 16-bit resolution. EMG data were decomposed, including full manual editing, using the publicly-available EMGLAB toolbox [McGill 2005]. The toolbox produces an annotation file with the firing times for each decomposed MU.

3.3 Results

3.3.1 Results contrasting all methods

Figure 3.1 shows sample firing rate estimators for the Berger, Mateo and spline methods, as well as the true firing rate (for simulated data only). For the simulated data, note that the Berger rate—with T_B=400 ms—follows the lower frequency rate changes well and is not substantially affected by error (missed or extra) detections; but has difficulty following rapid rate changes. Alternatively, the Mateo and spline methods follow rapid *and* slow true changes in the simulated firing rate, but produce very large errors in the local time region of error detections. These trends seemed characteristic. Although

not shown in these plots, the instantaneous and DeLuca estimators showed performance most similar to the Berger method.

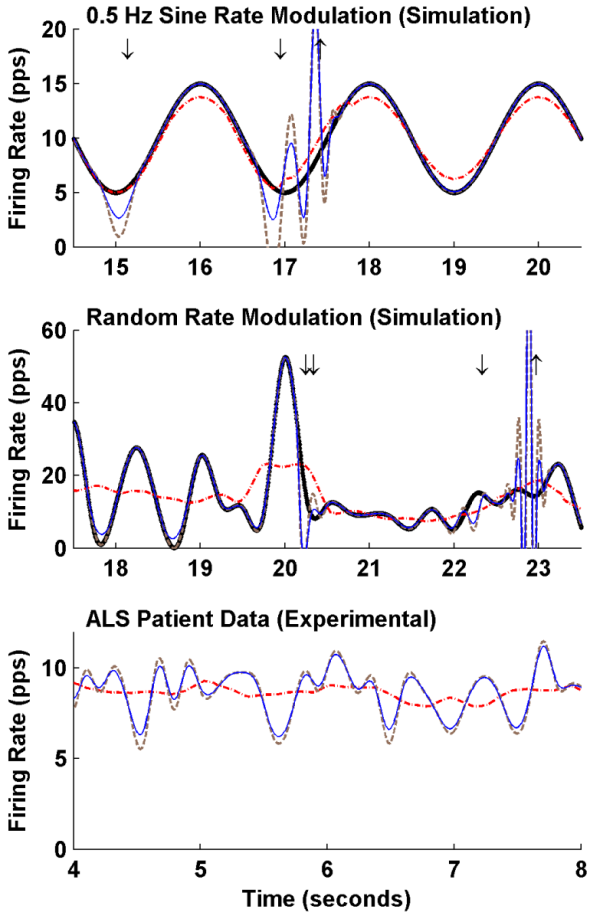

Figure 3.1: Sample firing rate estimators shown for the simulated sine wave modulated firing rate (top), simulated random modulated firing rate (middle) and ALS patient data (bottom). In plots of simulated data, up arrows show the error insertion location of extra firing detections, down arrows show the error location of missed firing detections and thick solid black lines show the true firing rate vs. time. In all plots, dashed red line is the Berger method (T_B=400 ms), dotted brown line is the Mateo method and thin blue line is the spline method.

Table 3.1 tabulates a complete set of results for the sinusoidal simulations. Note that the Berger and DeLuca methods have tunable smoothing parameters which influence performance. Only one parameter per method is shown in the table, selected as 400 ms within this table to be consistent with the most common selection in the literature [DeLuca 1982a]. The role of these parameters will be described in more detail subsequently. The Mateo and spline techniques do not have parameters. In Table 3.1, the trend was for average errors to increase with

decomposition error rate, average firing rate and modulation frequency. A three-factor ANOVA was conducted for each of the five methods shown in the table, using the factors of: four decomposition error rates, three average firing rates and three modulation frequencies. For each comparison, each of the three main effects was significant ($p<10^{-5}$), but there were significant interactions. For the instantaneous, Mateo and spline methods, there was one significant interaction—a two-way interaction between decomposition error rate and average firing rate ($p<10^{-6}$). For the Berger and DeLuca methods, all two-way interactions and the three-way interaction were significant ($p<10^{-6}$). The interactions confound the statistical interpretation. Hence, comparison between methods was next evaluated. When there were no decomposition errors, the Mateo and spline methods were clearly superior to the other three, with errors consistently near 0 pps for all conditions. (No statistical test is appropriate, as these results are deterministic.) At decomposition error rates of 1% and above, the Mateo and spline methods exhibited much higher errors than each of the other three methods; in fact, all average errors for the Mateo and spline methods exceeded their corresponding average firing rate. Within each table row, a paired t-test compared results between the Mateo (or spline) method and, separately, each of the instantaneous, Berger and DeLuca methods. Each of these six paired comparisons was significant ($p<0.001$).

Table 3.2 tabulates a complete set of results for the random simulations, again using 400 ms smoothing windows for the Berger and DeLuca methods. Average errors tended to increase with decomposition error rate and average firing rate. A two-factor ANOVA was conducted for each of the five methods shown in the table, using the factors of: four decomposition error rates and three average firing rates. For each comparison, each of the two main effects was significant ($p<10^{-6}$); but so was the two-way interaction ($p<10^{-6}$), except for the Berger method. Thus, comparison between targeted pairs of methods was next evaluated. When there were no decomposition errors, the Mateo and spline methods exhibited lower average errors than the other three methods, else they exhibited higher average errors. Thus, within each table row, a paired t-test compared these observations between the Mateo (or spline) method and, separately, each of the instantaneous, Berger and DeLuca methods. Each of these six paired comparisons was significant ($p<10^{-6}$).

The simulation results of Figure 3.1 and Tables 3.1 and 3.2 show that the Mateo and spline methods are superior when there are no decomposition errors, but greatly inferior at

decomposition error rates of 1% or more. As noted previously, error-free decomposition is not realistic for EMG decomposition. Decomposition error rates are reported to be 3–5% after exhaustive manual editing [Erim 2008] and well above that (10–20%) otherwise [Nawab 2008]. Thus, we conclude that the excellent performance of the Mateo and spline methods on error-free decompositions is not applicable to firing rate computation for EMG. Our remaining results will, therefore, concentrate on the other three methods.

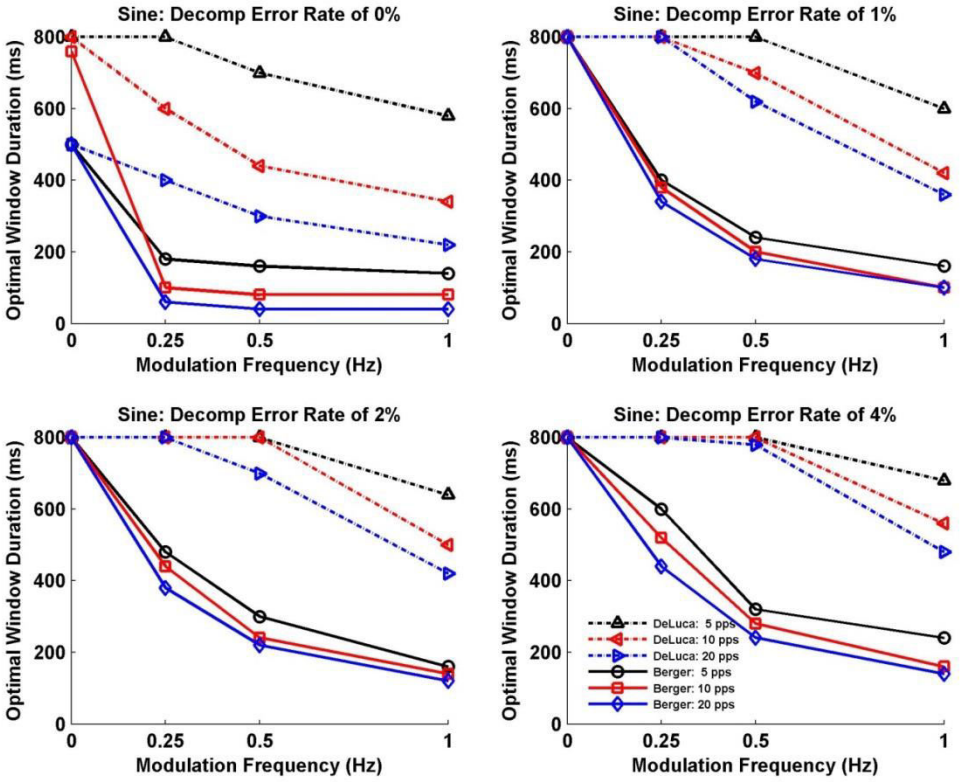

Figure 3.2 Optimal window duration for Berger and DeLuca methods for sinusoidal simulations. Results for a different decomposition error rate, as titled, are shown in each of the four plots. Each plot shows results as a function of modulation frequency. Key at lower right delineates each average firing rate.

Decomp Err Rate (%)	Ave Firing Rate (pps)	Modulate Freq (Hz)	Error Mean ± Standard Deviation (pps) for Firing Rate Estimator: Instantaneous (r_{Inst})	Berger (r_{Berger}) T_B = 400 ms	DeLuca (r_{DeLuca}) T_D = 400 ms	Mateo (r_{Mateo}) Cubic Spline	Spline (r_{Spline}) Cubic Spline
0	5	0	**0.00**	**0.00**	0.00	**0.00**	**0.00**
		0.25	0.14	0.10	0.76	**0.00**	0.01
		0.5	0.27	0.38	0.75	**0.00**	0.04
		1	0.53	1.13	0.74	**0.01**	0.14
	10	0	**0.00**	**0.00**	0.01	**0.00**	**0.00**
		0.25	0.14	0.19	0.11	**0.00**	0.01
		0.5	0.27	0.71	0.12	**0.00**	0.02
		1	0.54	2.19	0.29	**0.00**	0.08
	20	0	**0.00**	**0.00**	0.01	**0.00**	**0.00**
		0.25	0.14	0.37	0.04	**0.01**	**0.01**
		0.5	0.27	1.38	0.14	**0.01**	**0.01**
		1	0.55	4.35	0.56	**0.01**	0.04
1	5	0	1.07 ± 0.79	**0.26 ± 0.01**	0.47 ± 0.02	6.86 ± 20.9	5.83 ± 18.2
		0.25	0.86 ± 0.72	**0.24 ± 0.01**	0.85 ± 0.01	5.08 ± 17.5	4.22 ± 14.4
		0.5	1.12 ± 0.81	**0.47 ± 0.02**	0.88 ± 0.01	6.85 ± 18.9	5.61 ± 15.5
		1	1.03 ± 0.70	1.15 ± 0.00	**0.83 ± 0.01**	5.36 ± 19.5	4.44 ± 16.0
	10	0	2.00 ± 1.20	**0.34 ± 0.02**	0.61 ± 0.02	12.1 ± 23.1	10.2 ± 19.2
		0.25	1.99 ± 1.19	**0.40 ± 0.02**	0.62 ± 0.02	12.8 ± 26.5	10.7 ± 22.0
		0.5	1.99 ± 1.18	0.79 ± 0.02	**0.62 ± 0.02**	12.8 ± 27.4	10.6 ± 22.6
		1	2.1 5± 1.36	2.22 ± 0.01	**0.68 ± 0.02**	14.9 ± 31.3	12.2 ± 25.5
	20	0	4.01 ± 1.62	**0.49 ± 0.03**	0.86 ± 0.03	25.4 ± 30.8	21.3 ± 25.6
		0.25	4.00 ± 1.64	**0.63 ± 0.03**	0.87 ± 0.03	25.5 ± 32.3	21.4 ± 26.9
		0.5	3.98 ± 1.53	1.49 ± 0.03	**0.88 ± 0.03**	25.3 ± 30.2	21.1 ± 25.0
		1	4.13 ± 1.79	4.38 ± 0.01	**1.04 ± 0.03**	27.0 ± 34.9	22.4 ± 28.8
2	5	0	1.47 ± 1.00	**0.33 ± 0.01**	0.61 ± 0.02	10.3 ± 25.0	8.62 ± 20.8
		0.25	1.46 ± 1.00	**0.35 ± 0.02**	0.96 ± 0.01	11.9 ± 40.4	9.81 ± 33.0
		0.5	1.48 ± 0.93	**0.51 ± 0.02**	0.96 ± 0.01	11.7 ± 30.0	9.56 ± 24.2
		1	1.62 ± 1.34	1.18 ± 0.01	**0.96 ± 0.02**	12.8 ± 34.0	10.5 ± 27.5
	10	0	2.94 ± 1.45	**0.48 ± 0.03**	0.86 ± 0.03	20.3 ± 32.8	17.0 ± 27.2
		0.25	3.03 ± 1.60	**0.53 ± 0.03**	0.87 ± 0.03	24.4 ± 46.0	20.3 ± 38.3
		0.5	3.02 ± 1.53	**0.87 ± 0.03**	0.87 ± 0.03	23.3 ± 37.8	19.3 ± 31.1
		1	3.06 ± 1.53	2.25 ± 0.01	**0.92 ± 0.03**	25.5 ± 66.6	20.8 ± 56.8
	20	0	5.80 ± 1.73	**0.69 ± 0.04**	1.22 ± 0.04	40.9 ± 40.6	34.3 ± 33.8
		0.25	5.75 ± 1.79	**0.81 ± 0.04**	1.22 ± 0.04	43.0 ± 143	36.0 ± 121
		0.5	5.84 ± 1.79	1.58 ± 0.05	**1.23 ± 0.04**	41.7 ± 38.7	34.8 ± 32.0
		1	5.86 ± 2.14	4.41 ± 0.02	**1.36 ± 0.04**	42.9 ± 41.8	35.5 ± 34.2
4	5	0	2.25 ± 4.79	**0.47 ± 0.03**	0.86 ± 0.02	18.6 ± 42.1	15.5 ± 35.3
		0.25	2.22 ± 1.67	**0.48 ± 0.03**	1.14 ± 0.02	19.4 ± 42.1	16.0 ± 34.5
		0.5	2.15 ± 1.08	**0.62 ± 0.03**	1.13 ± 0.02	19.5 ± 36.2	15.8 ± 29.1
		1	2.22 ± 1.16	1.23 ±0.01	**1.13 ± 0.02**	21.2 ± 59.7	17.3 ± 49.7
	10	0	4.34 ± 2.29	**0.68 ± 0.04**	1.22 ± 0.04	36.0 ± 41.4	29.9 ± 34.2
		0.25	4.38 ± 1.73	**0.72 ± 0.04**	1.22 ± 0.04	38.9 ± 52.7	32.4 ± 43.6
		0.5	4.34 ± 2.30	**1.01 ± 0.04**	1.23 ± 0.04	39.8 ± 57.3	32.8 ± 46.4
		1	4.42 ± 3.51	2.31 ± 0.02	**1.26 ± 0.04**	40.5 ± 69.1	33.0 ± 55.9
	20	0	8.48 ± 3.03	**0.98 ± 0.05**	1.72 ± 0.05	69.7 ± 64.4	58.0 ± 53.2
		0.25	8.45 ± 2.07	**1.08 ± 0.06**	1.72 ± 0.05	70.7 ± 69.3	58.9 ± 57.5
		0.5	8.49 ± 3.19	1.76 ± 0.06	**1.74 ± 0.05**	69.8 ± 62.6	57.9 ± 52.1
		1	8.53 ± 2.50	4.48 ± 0.02	**1.84 ± 0.06**	72.6 ± 60.9	59.6 ± 49.8

Table 3.1 Mean ± standard deviation RMS errors from sinusoidal simulations. Results when the decomposition error rate was 0% show no standard deviations, as these results are deterministic (no random errors). Lowest average error bolded within each row.

Decomp. Error Rate (%)	Ave. Firing Rate (pps)	Mean ± Std. Dev. Error (pps) for Firing Rate Estimator: Instantaneous (r_{Inst})	Berger (r_{Berger}), T_B = 400 ms	DeLuca (r_{DeLuca}), T_D = 400 ms	Mateo (r_{Mateo}), Degree = 2	Spline (r_{Spline}), Degree = 2
0	5	1.30 ± 0.06	3.32 ± 0.19	1.15 ± 0.04	**0.50 ± 0.07**	0.74 ± 0.04
	10	1.54 ± 0.08	6.64 ± 0.37	1.44 ± 0.08	**0.21 ± 0.06**	0.65 ± 0.04
	20	1.74 ± 0.10	13.3 ± 0.77	2.66 ± 0.16	**0.21 ± 0.07**	0.66 ± 0.05
1	5	1.84 ± 0.60	3.33 ± 0.23	**1.26 ± 0.04**	15.8 ± 38.3	12.3 ± 32.2
	10	2.96 ± 1.08	6.66 ± 0.37	**1.61 ± 0.08**	37.6 ± 77.5	27.2 ± 52.3
	20	5.28 ± 1.63	13.3 ± 0.76	**2.87 ± 0.16**	68.1 ± 350	51.2 ± 290
2	5	2.29 ± 0.96	3.34 ± 0.19	**1.34 ± 0.04**	33.2 ± 87.3	24.9 ± 62.7
	10	4.02 ± 1.31	6.67 ± 0.37	**1.77 ± 0.08**	68.4 ± 146	50.4 ± 107
	20	7.35 ± 1.75	13.4 ± 0.76	**3.07 ± 0.16**	109 ± 140	79.9 ± 97.7
4	5	3.12 ± 1.50	3.37 ± 0.19	**1.51 ± 0.04**	60.4 ± 111	45.5 ± 83.9
	10	5.56 ± 2.49	6.72 ± 0.64	**2.04 ± 0.08**	114 ± 164	83.2 ± 129
	20	10.4 ± 2.87	13.4 ± 0.76	**3.44 ± 0.17**	194 ± 348	140 ± 227

Table 3.2 Mean ± standard deviation RMS errors from stochastic simulations. Lowest average error bolded within each row.

3.3.2 Optimal selection of window duration for the Berger and DeLuca methods

Next, selection of the optimal smoothing window duration is reported for the Berger and DeLuca methods. For each simulation case, the window duration exhibiting the lowest average RMS error was considered optimal. Figure 3.3 shows optimal window duration results for the sinusoidal simulations and Figure 3.4 for the random simulations. We can see that under the same conditions, the optimal Berger window duration is about half that of the DeLuca method. For example, with a sinusoidal modulation frequency of 0.5 Hz, 2% decomposition error rate and 20 pps average firing rate, a 700 ms window duration is optimal for the DeLuca method, while a 220 ms window duration is optimal for the Berger method. This ratio is expected since in (3.3), Berger method parameter T_B is defined as the half-window duration.

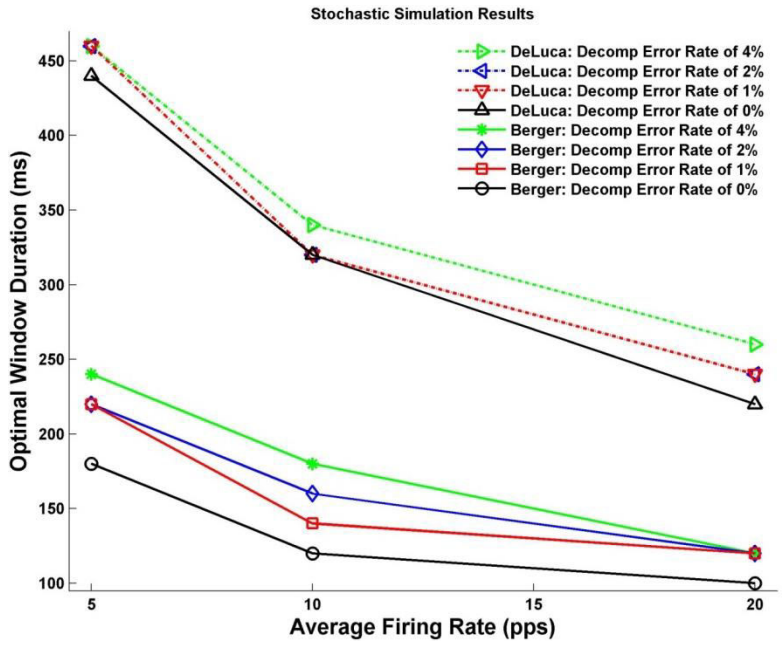

Figure 3.3 Optimal window duration for Berger and DeLuca methods for random simulations. Results shown as a function of average firing rate and decomposition error rate.

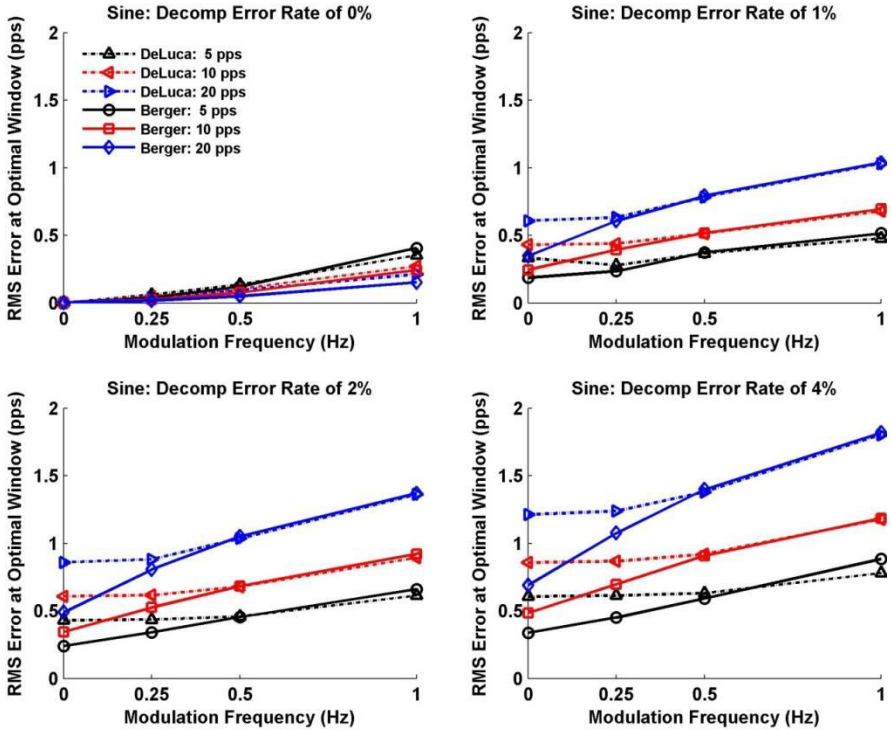

Figure 3.4 Mean RMS errors for Berger and DeLuca methods from sinusoidal simulations when the optimal window duration is selected for each combination of decomposition error rate, average firing rate and modulation frequency. Corresponding results for instantaneous method shown in Table 3.1.

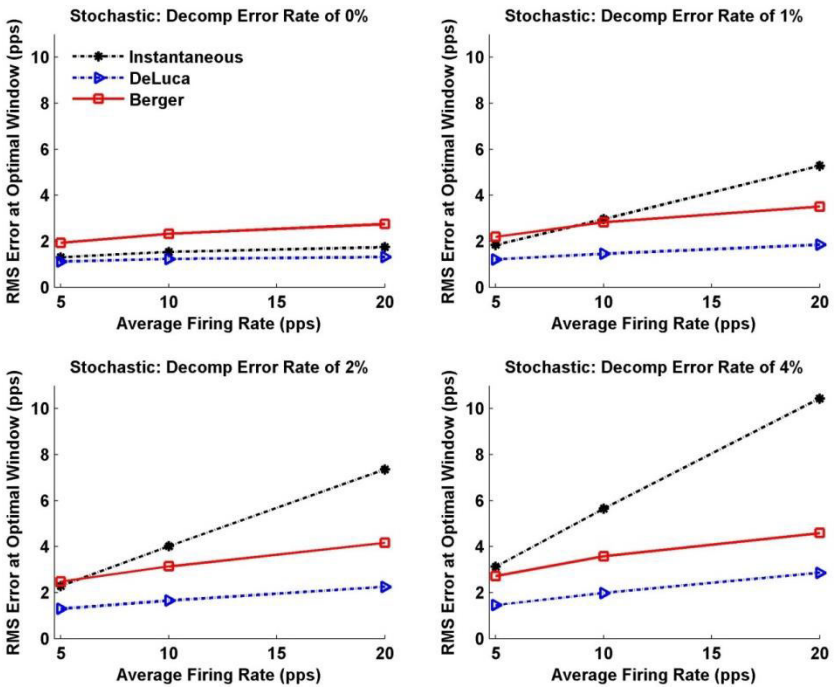

Figure 3.5 Mean RMS errors for instantaneous, Berger and DeLuca methods from stochastic simulations when the optimal window duration (for Berger and DeLuca methods) is selected for each combination of decomposition error rate and average firing rate. The instantaneous method does not have a selectable parameter.

Figure 3.4 shows the mean RMS errors for the Berger and DeLuca methods from the sinusoidal simulations when the optimal window duration is selected for each combination of decomposition error rate, average firing rate and modulation frequency. Table 3.1 lists the corresponding errors for the instantaneous method, which has no parameters. Again, statistical comparisons were not performed on the results using a decomposition error rate of 0%, as these results are not random. For the remaining decomposition error rates, RMS errors for the instantaneous method (Table 3.1) were always statistically higher than each of the Berger and DeLuca methods (Figure 3.4) for each condition ($p<10^{-6}$ for each paired comparison). We next statistically tested differences between the Berger and DeLuca method (Figure 3.4) using paired t-tests. All mean differences were significant ($p<10^{-6}$ for all but two comparisons, whose p-values were significant at 0.017 and 0.005). The actual mean differences were rather small at modulation frequencies of 0.5 and 1 Hz. Figure 3.5 shows the mean RMS errors for the Berger and DeLuca methods from the random simulations when the optimal window duration is selected for each combination of decomposition error rate and average firing frequency, as well as the corresponding results for the instantaneous method. Paired comparisons between the three methods for each case were each significant ($p<10^{-5}$ for all but two comparisons, whose p-values were significant at

0.01 and 0.001). Note that the large number of simulation iterations likely resulting in all result mean differences being statistically significant.

3.3.3 Implications for firing rate applications of physiological data

Figure 3.6 shows sample normalized power spectral density (PSD) estimates of firing rate, computed using Welch periodograms, when the algorithms studied herein were each applied to an identical set of MU detections from a patient with ALS. The Mateo, spline and instantaneous methods produce similar spectral estimates, which are distinct from the estimate produced by each of the Berger and DeLuca methods. This example supports the need for accurate firing rate time series estimates.

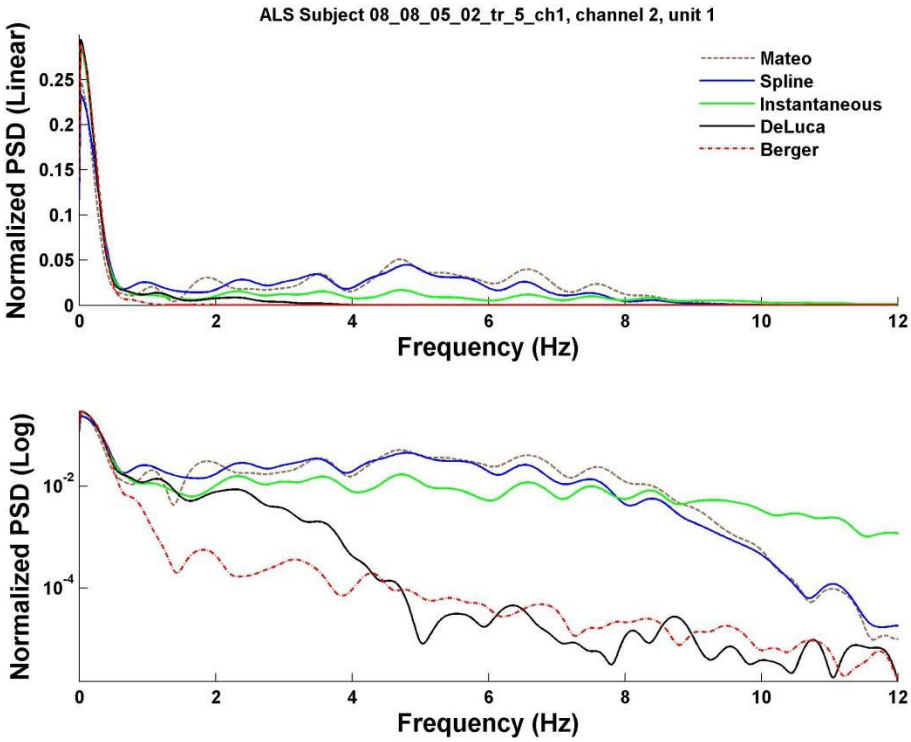

Figure 3.6. Example firing rate power spectrum (top=linear scale, bottom=log scale) derived from ALS patient data using five different methods of estimating the firing rate time series from identical EMG detections.

3.4 Discussion

This chapter provides a rigorous model-based comparison of methods for estimating the firing rate *time series* from decomposed EMG signals. In other fields such as nerve signals and ECG, formal comparisons have been useful in the development of more accurate rate estimators [Bayley 1968, Berger 1986 and Mateo 2000]. Within the EMG field, detailed evaluation has been presented when studying the mean, median or standard deviation of the firing rate of constant-force contractions [Gerdle 2008, Navallas 2014 and 2015]. However, knowledge of the time series allows subsequent estimation of

parameters such as firing rate mean, median and standard deviation, while facilitating further general analysis of how firing rates evolve in time throughout a contraction, e.g., power spectral analysis, the "onion skin" effect, inter-unit synchronization and common drive [DeLuca 1982a, DeLuca 1985 and Stashuk 1989].

Model-based evaluation of firing rate estimators within the ECG field has led to two spline-based algorithms that we evaluated herein within the context of EMG signals. Mateo and Laguna [Mateo 2000] fit a spline function to a staircase function, whose step locations correspond to the locations of the firing events. The derivative of this fit provides a firing rate estimate. We also implemented a direct "spline" interpolator, which was simpler in form and avoided the discrete-time derivative computation. When EMG decomposition errors were absent, the performance of these two estimators was excellent—significantly better than all of the other methods. The spline techniques provided smoothing when the rate was slowly modulated and the ability to change rapidly when the rate changed quickly. These initial results were quite encouraging in the early stages of our investigation. However, each of these rates was far inferior once decomposition errors were simulated. These rate estimates reacted too abruptly to the missing/extra detections, as shown in the simulation and patient results of Figure 3.1 (as well as the detailed results of Tables 3.1 and 3.2, and Figure 3.6). Within the ECG field, error detections are rare [certainly under 0.7% [Pan 1985]] and typically associated with artifact regions of an ECG recording. During many such regions, accurate rate estimation is either not expected or artifact is detected and alternative rate smoothing/interpolation is employed. For EMG, however, missed detections are common, especially when the motor unit firing times of multiple units overlap in time. Erim and Lin [Erim 2008] reported decomposition error rates of 3–5% after exhaustive manual editing, while Nawab et al. [Nawab 2008] reported error rates as high as 10–20% in the absence of manual editing. Hence, it is clear that the advanced spline-based methods that excel in ECG applications are simply not appropriate for the EMG decomposition problem—at least until decomposition error rates can be brought well below 1%.

For the three remaining firing rate estimation methods, our results (Tables 3.1–3.2 and Figures. 3.4–3.5) found that the Berger and DeLuca methods consistently produced lower RMS errors than that of the instantaneous method—so long as optimal window durations were selected for the Berger and DeLuca methods. We examined this performance in simulation. While simulations do not perfectly match the firing times of physiologic data, they have the advantage of having a known true firing rate time series for comparison. Figure 3.4 shows that the Berger and DeLuca methods (using optimal window

durations) had similar performance during sinusoidal modulation at frequencies of 0.5 and 1 Hz. At lower modulation frequencies (0 and 0.25 Hz), our implementation of the Berger method produced lower errors. However, we limited the window duration of the DeLuca method to a maximum of 800 ms [twice the duration recommended by DeLuca et al. [DeLuca 1982a]]. Figure 3.2 shows that the DeLuca method utilized this maximum duration at these lower modulation frequencies. Hence, the DeLuca method might have produced errors as low/lower than the Berger method at the lower modulation frequencies if even longer window durations had been examined. When the firing rate varied in a random fashion over a statistical bandwidth of 1 Hz, the DeLuca method produced consistently lower errors than the Berger method (each utilizing optimal windows).

In general, Figures. 3.2–3.3 show that optimal window duration for the Berger and DeLuca methods decreased as modulation frequency increased, as average firing rate increased and as decomposition error rate decreased. These results elucidate the balance between longer window durations that reduce undesired abrupt transitions due to stochastic variation in firing times and/or decomposition errors ("variance" errors) vs. shorter window durations which are more capable of following true changes in rate ("bias" errors). Window length selection in EMG amplitude estimation makes these same considerations, choosing a longer window duration when the amplitude is more constant (e.g., slowly-varying contractions) and a shorter window duration when the amplitude varies quickly (e.g., rapidly-varying contractions). In this context, a few researchers developed time-adaptive window length smoothing algorithms [Clancy 1999, D'Alessio 1984, Park 1995 and Sanger 2007]. A similar concept might help in firing rate time series estimation, so as to choose longer window durations when the rate is changing slowly and shorter window durations when the rate is changing rapidly.

3.5 Conclusion

Several different techniques for calculating the EMG firing rate *time series* were compared quantitatively, using the integral pulse frequency modulation simulation model. Sinusoidal and random rate variation models with artificial decomposition errors were used to assess performance of various proposed methods. We found that the Mateo and spline methods outperformed other estimation methods in the absence of decomposition errors, but deteriorated rapidly in the presence of even 1% decomposition errors; actual errors are typically 3–5% when manually reviewed by experts. Of the remaining methods evaluated, the instantaneous rate consistently exhibited higher errors than either of the Berger and DeLuca methods—so long as the optimal window duration was selected for the Berger and DeLuca methods. When firing rate was modulated as a sinusoid, the Berger method (with optimal

window durations selected) exhibited lower error than the DeLuca error, but only at the lowest modulation frequencies (0 and 0.25 Hz). However, the DeLuca method may have produced lower error had its window duration been permitted to extend beyond 800 ms. When firing rate was modulated randomly over a 1 Hz bandwidth, the DeLuca method (with optimal window durations selected) exhibited lower error than the Berger method. Overall, each of the Berger and DeLuca methods performed well, so long as the optimal window duration was selected. Figures 3.2 and 3.3 provide a mechanism for selecting the optimal window length for these methods, based on the characteristics of the modulation in firing rate for a particular application. These figures show that optimal window duration for the Berger and DeLuca methods decreased as modulation frequency increased, as average firing rate increased and as decomposition error rate decreased.

3.6 Acknowledgements

Our thanks to Patrick Kasi for access to the experimental data and their expert decompositions.

Chapter 4

Electromyogram whitening for improved classification accuracy in upper-limb prosthesis control

Lukai Liu[1], Pu Liu[1], Edward A. Clancy[1], Erik Scheme[2] and Kevin B. Englehart[2]

[1]ECE Dept., Worcester Polytechnic Institute, Worcester. MA 01609, USA.

[2]BME Inst., University of New Brunswick, Frederiction NB E3B 5A3, Canada.

This chapter has been published as: **Lukai Liu**, **Pu Liu**, **Edward A. Clancy**, **Erik Scheme** and **Kevin B. Englehart**, "Electromyogram Whitening for Improved Classification Accuracy in Upper-limb Prosthesis Control," *IEEE Transactions on Neural System and Rehabilitation Engineering*, pp. 767–774, vol. 21(5), 2013. Available: http://ieeexplore.ieee.org/xpls/abs_all.jsp?arnumber=6471832

Abstract—Time and frequency domain features of the surface electromyogram (EMG) signal acquired from multiple channels have frequently been investigated for use in controlling upper-limb prostheses. A common control method is EMG-based motion classification. We propose the use of EMG signal whitening as a preprocessing step in EMG-based motion classification. Whitening decorrelates the EMG signal, and has been shown to be advantageous in other EMG applications including EMG amplitude estimation and EMG-force processing. In a study of ten intact subjects and five amputees with up to 11 motion classes and ten electrode channels, we found that the coefficient of variation of time domain features (mean absolute value, average signal length and normalized zero crossing rate) was significantly reduced due to whitening. When using these features along with autoregressive power spectrum coefficients, whitening added approximately five percentage points to classification accuracy when small window lengths (<100 ms) were considered.

Keywords—coefficient of variation, electromyography, EMG, myoelectric, prosthesis, whitening

4.1 Introduction

Approximately 1.5 million people in the U.S. are living with upper or lower limb loss, with 230, 000 new cases occurring each year [Adams 1999, Dilingham 2002]. Surface electromyogram (EMG) controlled powered hand/wrist/elbow prostheses are used by some of these amputees to return partial upper-limb function. Conventional transradial prostheses, for example, can use surface EMG amplitudes from the residual forearm flexors and extensors to control hand opening and closing. Additional degrees of freedom (e.g., wrist rotation) cannot currently be controlled simultaneously in commercial systems. Rather, prostheses apply EMG-based or mechanical mode switching, so that the same EMG sites sequentially control the additional function(s) [Parker 2006, Varol 2010]. It is reported that control of more degrees of freedom is the greatest desired prosthetic improvement for below-elbow amputees [Atkins 1996]. Accordingly, a pattern recognition approach has been emerging over the past several years in which EMG signals in the forearm are used to discern desired movements of the hand and wrist [Parker 2006, Hudgins 1993, Hargrove 2009, Ahsan 2010, Li 2010, Graupe 1975 and Boostani 2003]. Continuous control of multiple degrees of freedom is achieved by applying the pattern recognition algorithm in a continuous manner along the EMG signal stream. The approach consists of four sequential steps: EMG signal conditioning and preprocessing, feature extraction, dimension reduction and pattern classification.

Common time-domain features that are extracted include the EMG mean absolute value (MAV), signal length and zero crossing rate [Hudgins 1993]. Frequency-domain features have also been used, e.g. the coefficients of autoregressive power spectral modeling of the EMG [Graupe 1975]. In both cases, features are extracted from an epoch/window of the EMG signal stream for classification. The extent to which these features—or their dimensionally reduced representations—distinguish the different motion classes directly relates to the accuracy of the classifier. Limitations in class separation in the feature space represent a *systematic* error (i.e., bias) in the classifier. Because the EMG signal presents itself as a stochastic process, a distinct *random* error (i.e., variance) also exists. That is, even if amputees produce a repeatable force pattern in their residual limb, the EMG-derived features will vary trial-to-trial due to the inherent variations in the EMG signal.

Errors due to the stochastic component of the EMG signal are also problematic in the related areas of EMG amplitude estimation and EMG-force processing [Clancy 2000, Clancy 2002, Hogan 1980a and Hogan 1980b]. In these applications, signal whitening has been used to reduce the random error of the processed EMG, with substantial performance improvements resulting. Whitening temporally decorrelates the EMG signal, increasing the effective number of signal samples (a.k.a., statistical degrees of freedom) and reducing the variance in the amplitude estimate.

Whitening has not previously been applied to the EMG multifunction classification problem. In this report, we investigate the hypothesis that EMG signal whitening prior to feature extraction will similarly reduce the random error in EMG-based features and lead to improved classification accuracy. This effect should be most prominent at short window durations, since long window durations already experience high classification accuracy (often above 95%, for which little improvement is either available or needed). Shorter window durations are relevant, because they reduce the delay between user command and prosthesis actuation, permitting higher speed (bandwidth) movement and more realistic motion [Farrell 2007]. A preliminary report of this work appeared in [Liu 2011].

4.2 Analytic time-domain feature performance

For purposes of classification analysis, the random variation of an EMG feature can be quantified as the standard deviation of the feature (σ) relative to its mean value (μ), i.e., the feature's coefficient of variation: $\mathrm{CoV} = \frac{\sigma}{\mu}$. Lower CoVs should facilitate higher classification accuracy. An analysis of the CoV of common EMG time-domain classification features does not appear to have been previously reported. Thus, we do so here.

A common model of the EMG samples, $m[n]$, from one window is that of a wide sense stationary, correlation-ergodic, zero-mean, Gaussian random process [Clancy 2002, Hogan 1980a and Kwatny 1970], where n is the sample index and $m[\cdot]$ is measured in millivolts. Without loss of generality, assume that successive model samples are independent [Hogan 1980b, Kwatny 1970 and Clancy 1997]. In fact, these samples are correlated due to the limited bandwidth of the EMG signal. However, let window length N_{Eq} represent the equivalent number of independent samples within a window, given by

[Bendat 1971]:

$$N_{Eq} = 2B_sT \tag{4.1}$$

where B_s is the statistical bandwidth of the EMG (Hz) and T is the window length (seconds). Since whitening increases N_{Eq} via an increase in statistical bandwidth [Hogan 1980a and Hogan 1980b], the relevant analytic relationship is to determine the CoV vs. N_{Eq} for each time-domain feature.

The MAV of an EMG window of N_{Eq} samples is defined as:

$$\mathrm{MAV}_{N_{Eq}} = \frac{1}{N_{Eq}} \sum_{n=0}^{N_{Eq}-1} |m[n]| \tag{4.2}$$

Its CoV is the inverse of the SNR, which has been previously analyzed [Clancy 1999]. Inverting the SNR results gives:

$$\mathrm{CoV}_{\mathrm{MAV}}[N_{Eq}] = \sqrt{\frac{\pi-2}{2N_{Eq}}} \cong \frac{0.755}{\sqrt{N_{Eq}}} \tag{4.3}$$

The average signal length of N_{Eq} samples, in millivolts per second per sample, is defined as:

$$\mathrm{SL}_{N_{Eq}} = \frac{f_s}{N_{Eq}-1} \sum_{n=1}^{N_{Eq}-1} |m[n] - m[n-1]| \tag{4.4}$$

The gain factor $\frac{f_s}{N_{Eq}-1}$, not normally included in the definition of signal length, normalizes its values across sampling rates and window lengths. Since the $m[n]$ are zero-mean Gaussian, so is each difference term in the sum, but with a doubled variance. An analytic form for the sum was not readily apparent due to the correlation between adjacent differences, which share a common EMG sample. Hence, the CoV of average signal length was approximated numerically in MATLAB by creating 10^6 replicates of Gaussian vectors of size N_{Eq} and computing the sample mean and standard deviation of the average signal length, across these replica. Window length N_{Eq} was varied from 2–2000. The resulting CoV values vs. N_{Eq} closely fit the model:

$$\mathrm{CoV}_{SL}[N_{Eq}] \cong \frac{0.911}{\sqrt{N_{Eq}}} \tag{4.5}$$

The normalized zero crossing rate of N_{Eq} samples is defined as the number of adjacent samples with different polarity, normalized by the ratio between sampling rate

and the number of samples:

$$\mathrm{ZC}_{N_{Eq}} = \frac{f_s}{N_{Eq}-1}\sum_{n=1}^{N_{Eq}-1}[1-\mathrm{sgn}(m[n]m[n-1])] \tag{4.6}$$

The gain factor $\frac{f_s}{N_{Eq}-1}$ normalizes the zero-crossing values across sampling rates and window lengths, so that its unit is Hz, and $\mathrm{sgn}(t) = \begin{cases} 1, & t > 0 \\ 0, & t \leq 0 \end{cases}$. For independent identically distributed Gaussian samples, the probability of a sign change between a pair of samples is 0.5. Thus, the number of sign changes in N_{Eq} samples follows a Binomial distribution with (N_{Eq}–1) trials, and its coefficient of variation is [Drake 1967]:

$$\mathrm{CoV}_{ZC}[N_{Eq}] = \frac{\sigma_{ZC}}{\mu_{ZC}} = \frac{\frac{f_s}{N_{Eq}-1}\sqrt{\frac{N_{Eq}-1}{4}}}{\frac{f_s}{N_{Eq}-1}\frac{N_{Eq}-1}{2}} = \frac{1}{\sqrt{N_{Eq}-1}} \cong \frac{1}{\sqrt{N_{Eq}}} \tag{4.7}$$

We see that the CoV for each time-domain feature is (asymptotically) a univariate function of the number of equivalent independent samples, in the form of a constant divided by $\sqrt{N_{Eq}}$, where N_{Eq} represents the equivalent number of independent samples. We expect that signal whitening will increase N_{Eq}, thereby reducing CoVs for any given window duration, with better classification accuracy hypothesized to result. An experimental trial evaluated this hypothesis.

4.3 Methods

4.3.1 Experimental methods

Experimental data from two prior studies were analyzed. The Worcester Polytechnic Institute (WPI) Institutional Review Board (IRB) approved and supervised this analysis. Data from ten intact-limbed subjects, aged 19–32 years, had been collected at the University of New Brunswick [Hargrove 2009]. Briefly, ten adhesive Duotrode® electrodes (manufactured by 3M) were applied about the circumference of the forearm of each intact subject. Twelve equally-spaced locations were marked along the entire forearm circumference at 1/3 the distance from the elbow to the wrist, beginning at the palmar aspect (see [Hargrove 2009], Fig. 2). The most medial and lateral locations were omitted (leaving ten locations). Bipolar electrodes had a contact diameter of 1.4 cm and a center-to-center distance of 2 cm. A subject began and ended each trial at rest (fixed posture with no motion attempted, muscle effort minimized) with their elbow supported

on an armrest. Each trial consisted of two repetitions of the 11 motion classes: 1, 2) wrist pronation/supination; 3, 4) wrist flexion/extension; 5) hand open; 6) key grip; 7) chuck grip; 8) power grip; 9) fine pinch grip; 10) tool grip; and 11) no motion. Each motion class within a trial was maintained for 4 s, and the subject returned to the rest posture for a specified inter-motion delay period prior to producing the next motion class. Trials 1–4 used an inter-motion delay of 3, 2, 1 and 0 s respectively, and trials 5–8 used an inter-motion delay of 2 s. The eight trials were performed twice and a minimum of two minutes inactivity was given between each trial. A general familiarization session was provided prior to data collection, typically lasting approximately 15 minutes in duration. The EMG data were collected using a custom-built pre-amplification system (Liberating Technologies, Inc., Holliston, MA) with a frequency response from 30–350 Hz, and sampled at 1000 Hz using a 16-bit ADC.

The Rehabilitation Institute of Chicago collected EMG data from five subjects aged 28 to 77 years, who had received unilateral transradial amputation three months to 21 years prior [Li 2010]. Three subjects were myoelectric prosthesis users, one subject used a body-powered prosthesis and one subject had not yet received a prosthesis. A total of 12 self-adhesive Ag/AgCl snap bipolar electrodes with a 1.25-cm-diameter circular contact and center-to-center distance of 2 cm (Noraxon USA, Inc) were used. Eight of the 12 electrodes were placed around the proximal portion of the forearm over the apex of the muscle bulge and the other four on the distal end (see [Li 2010], Fig. 1a). In this study, we used only the first ten electrodes, to most closely match the electrode placement of the intact-limbed subjects. Only data from the amputated side was used. The experiment protocol was the same as that of the intact subjects, including subject posture, the general familiarization session and the motion trials. Identical motion trial data were available for analysis. The EMG data were transduced using Liberating Technologies preamplifiers, bandpass filtered between 5–400 Hz and sampled at 1000 Hz using a 16-bit ADC.

4.3.2 Methods of analysis

Feature Computation: The trials were segregated into training and testing data, as described below. The inter-trial delay segments were removed from data recordings, resulting in 22 four–second segments per electrode per trial (two repetitions of 11 motion

classes). Each segment was zero-phase notch-filtered (0.4 Hz bandwidth) at the power-line frequency and its harmonics. When desired, each four–second segment was also whitened. To do so, each segment was highpass filtered at 15 Hz, then adaptively whitened using an algorithm that was tuned to the power spectrum of each EMG channel [12], [23]. Whitening filters were calibrated from a training trial by manually selecting, subject-by-subject for each electrode, the trial with the largest MAV. A no motion trial was also used to represent resting EMG in the whitening calibration. Prior to feature extraction, 0.5 seconds of data were truncated from the beginning and end of each segment to account for filter start-up transients. Contiguous, non-overlapping windows were formed from the remaining three-second epochs.

Feature sets were extracted in each window within an epoch. The time-domain feature set consisted of the three features described earlier: MAV, average signal length and normalized zero-crossing rate. Hysteresis as described in [Hudgins 1993] was applied to normalized zero-crossing rate. Specifically, a zero-crossing was not counted if the absolute difference between the two adjacent samples did not exceed a fixed threshold value. The threshold value was set to approximately $1/6^{th}$ the average RMS value of the no-motion class of all subjects and all electrodes. A frequency domain feature set consisted of the estimated AR coefficients of a seventh order AR model [Graupe 1975 and Neumaier 2001]. A third (combined) feature set concatenated the seven AR coefficients and MAV. It has been shown that linear classification models give different weights to each feature, and the MAV feature alone tends to have a large amount of motion classification power.

Coefficient of Variation Analysis: CoV values were computed for each of the three time-domain EMG features. Because CoV is the ratio between standard deviation and the mean of a feature, EMG signals with a small mean value can lead to unstable CoV estimates (due to dividing two small numbers in the presence of noise). Thus CoV was calculated using only two training trials per channel by manually selecting, subject-by-subject for each channel, the two trials with the largest MAV. All motion classes were considered when searching for the maximum MAV. The sample standard deviation divided by the sample mean of the contiguous feature values from a 3 s epoch formed a CoV value. The average CoV from the two trials per channel served as the CoV estimate

for that channel. Data from the intact subjects were studied separately from those of the amputee subjects. CoV values that compared unwhitened to whitened signals were computed for the following window durations: 25, 50, 75, 100, 150, 200, 250 and 300 ms. Once the CoV had been determined as a function of sample length *N*, we fit these results to the power decay model: $\mathrm{CoV}[n] = a/\sqrt{n}$.

We defined *N* as the number of samples corresponding to the window duration. The number of samples (*N*) is always greater than the equivalent number of independent samples (N_{eq}) due to signal correlation. In practice, this correlation cannot be entirely eliminated via whitening. A more direct measure of whitening performance is to assess the statistical bandwidth of the EMG before and after whitening. The same 3 s epochs as above were used to do so. The discrete-time power spectrum, $S_{mm}(k)$, of each epoch was estimated using Welch's method (window length of 150 ms, Hamming window, 50% overlap), where *k* is the frequency index. The statistical bandwidth was then estimated as [Bendat 1971]:

$$B_s = \frac{\Delta f\left[\sum_{k=0}^{K-1} S_{mm}(k)\right]^2}{\sum_{k=0}^{K-1} S_{mm}^2(k)} \tag{4.8}$$

where *K* specifies the range of positive-valued frequencies and Δf = 6.67 Hz is the frequency increment. Values from the two trials per channel were averaged.

Classification Analysis: A linear discriminant classifier was employed. Trials 1–4 of the two repetitions were used to train the coefficients of the classifier, and trials 5–8 to test classifier performance. The model was trained and tested for each individual subject using all features of a feature set, and only test results are reported. Eight window durations were used: 25, 50, 75, 100, 150, 200, 250 and 300 ms. We repeated the analysis after the EMG signal had been whitened.

Two global processing variants were also considered. First, the entire analysis was repeated using only seven preselected motion classes (the classes denoted above as numbers 1–5, 8 and 11), and again using only nine preselected motion classes (1–8 and 11), thereby giving three motion variations. Second, the entire analysis was repeated using a preselected set of six of the electrode channels (channels 1–6, spread around the arm circumference), giving two channel variations.

4.4 Results

Coefficient of Variation Results: Figure 4.1 shows a sample 3 s raw EMG epoch, the same epoch after whitening, and the spectrum of each of these two signals (normalized to the total power in each spectrum). The spectra show how whitening equalizes the contributions across frequency, increasing the statistical bandwidth of the signal. Figure 4.2 shows all CoV results, averaged across subjects, for the three time-domain features, together with the standard errors. Lines within the figure show the best fit power decay model and the inset tables list the fit errors. The sample size for calculating the CoV and standard error was 100 for intact subjects (10 subjects x 10 EMG channels/subject) and 50 for amputees (5 subjects x 10 EMG channels/subject). The CoV for each feature improved (i.e., decreased) with window length and due to whitening, although the MAV and SL results were a poor fit to the power decay model. The normalized zero crossing rate exhibited substantially lower CoV values than the other two features and fit well to the power decay model. CoV values for intact subjects were consistently lower than those of amputee subjects. Paired sign tests were conducted between whitened and unwhitened features at each window duration and for each of the intact and amputee data sets. All comparisons were significant for MAV ($p<10^{-4}$) and for average signal length ($p\leq 0.006$ for intact subjects, $p<10^{-4}$ for amputees). For normalized zero crossing rate, whitened features only differed from unwhitened features in intact subjects when the window length was ≤50 ms ($p<0.002$), and in amputees when the window length was ≤ 200 ms ($p<0.008$).

Table 4.1 shows the results of the statistical bandwidth computations. Whitening increased the statistical bandwidth by 65–75%, on average. Statistically, the ten statistical bandwidth values per subject (one per electrode) were averaged. These values for unwhitened vs. whitened processing were compared using a paired t-test. Results were significant for both the intact and amputee subjects ($p<10^{-4}$).

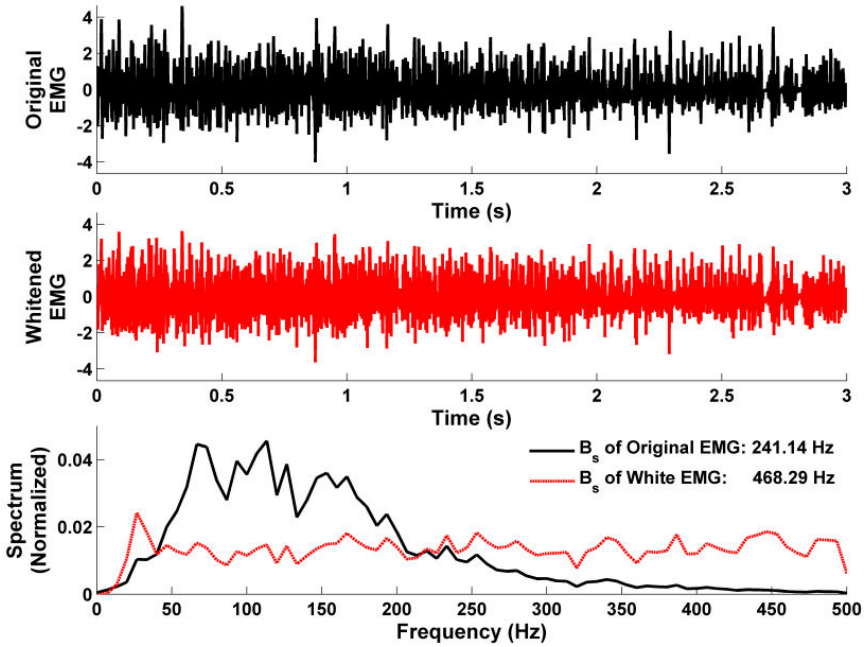

Figure 4.1. Sample original EMG epoch (top), the same epoch after whitening (middle) and the normalized spectrum of each (bottom). The statistical bandwidth, B_s, of each signal is listed. Data from healthy subject 6, channel 3, fine pinch grip motion, epoch 2.

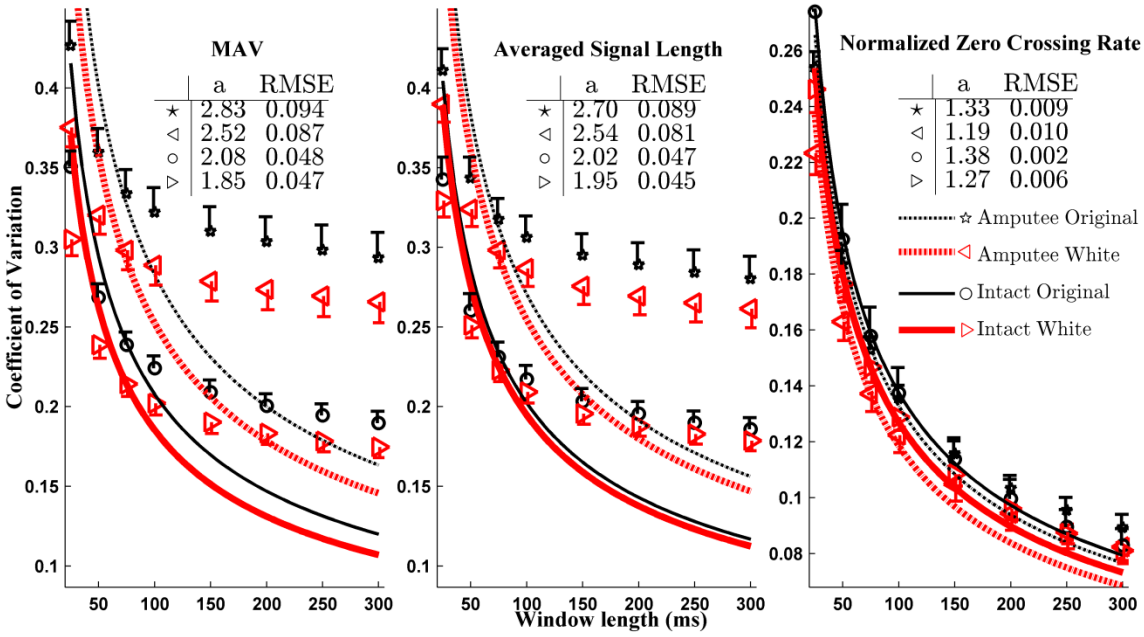

Figure 4.2. Average coefficient of variation (plus or minus one standard error) for the time-domain features from ten intact and (separately) five amputee subjects. The two recordings per channel per subject with the largest MAV EMG were used for this analysis. Lines show fit to power decay model: $\mathrm{CoV}[N] = a/\sqrt{N}$. Inset tables show fit parameter "a" and fit rms error (RMSE). Scale of y-axis differs for normalized zero crossing rate. Sample size is 100 for intact subjects, 50 for amputee subjects.

Subjects	Condition	
	Unwhitened	Whitened
Intact	238.0 ± 49.8 Hz	413.2 ± 73.0 Hz
Amputee	254.1 ± 53.4 Hz	423.1 ± 52.7 Hz

Table 4.1 Average ± standard deviation statistical bandwidths. Sample size is 100 for intact subjects, 50 for amputee subjects.

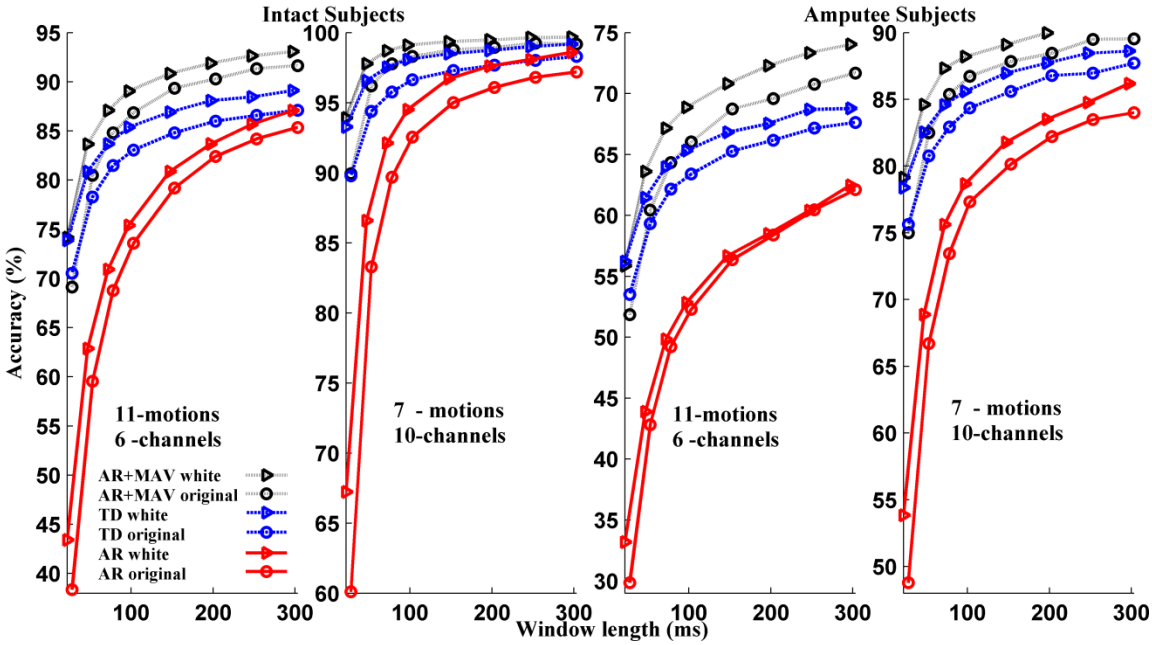

Figure 4.3. Average classification accuracies from ten intact (left) and five amputee (right) subjects for each of the three feature sets, with and without whitening. The motion-channel combinations shown represent the lowest accuracies (fewest channels and most motion classes) and highest (most channels and fewest classes). Note the different y-axis scale for each plot.

Classifications Results: Complete classification results were produced for six classifier variants (11 or 9 or 7 motion classes vs. 10 or 6 electrodes). Higher accuracies were found when fewer motions and/or more electrode channels were included in the classifier. Hence, our presentation of results will be limited to the highest (7-motion, 10-channel) and lowest (11-motion, 6-channel) performing classifiers—all four remaining result variants fell between these two extremes. Figure 4.3 shows the average test accuracies for intact and amputee subjects, for window lengths between 25 and 300 ms, for each feature set with and without whitening. The combined AR-MAV feature set gave the highest overall accuracy in each case, and the AR features the lowest. For all feature sets, accuracy was generally improved by approximately 5% at shorter window durations

(<100 ms) due to whitening. The improvement was smaller as window duration increased further. Accuracy values for intact subject were consistently higher than those of amputee subjects. Because sample sizes were small (DoF=9 for ten intact subjects, DoF=4 for five amputees) paired t-tests compared unwhitened to whitened processors at each window duration. For the AR-MAV feature set and intact subjects, differences were significant for: the 7-motion, 10-channel case when the window length was ≤ 300 ms (p<0.009), and the 11-motion, 6-channel case for all window lengths except 400 ms (p<0.005). For the AR-MAV feature set and amputees, differences were significant for: the 7-motion, 10-channel case when the window length was ≤ 50 ms (p<0.006), and the 11-motion, 6-channel case when the window length was ≤ 100 ms (p<0.008). For the TD feature set, results were only significant for intact subjects with the 7-motion, 10-channel case when the window duration was ≤ 300 ms (p<0.01); and in amputee subjects in the 11-motion, 6-channel case when the window duration was 25 ms (p=0.004). For the AR feature set of amputees, unwhitened vs. whitened result differences were significant in all cases when the window length was 25 ms (p<0.006); and in intact subjects with the 7-motion, 10-channel case when the window duration was ≤ 400 ms (p<0.003).

4.5 Discussion

We studied the use of EMG signal whitening in classification algorithms for prosthesis control. Signal whitening methods have existed for several years [Clancy 2000, Clancy 2002, Hogan 1980a and Hogan 1980b], having been shown in the laboratory to improve EMG amplitude estimation [Clancy 2000] as well as EMG-force estimation [Hogan 1980b]. They had not previously been applied to the EMG multifunction classification problem. Whitening decorrelates the EMG signal in time—increasing its statistical bandwidth—resulting in a larger number of effective degrees of freedom in the data [Bendat 1971]. Essentially, whitening increases the effective sample size (N_{Eq}) of each individual data epoch, making each epoch more representative of the entire sequence.

Theoretically, the influence of epoch sample size on the MAV feature had been previously studied via the SNR (inverse of the CoV) [Clancy 1997]. The CoV decreases in a square root fashion with sample size. We extended this analysis to the other two time-domain features. The CoV of the average signal length and normalized zero

crossing rate also each decrease in a square root relationship with sample size. Our theoretic model for normalized zero crossing rate did not include hysteresis. However, this effect is generally considered small when an appropriate (small) level of hysteresis is applied [Hudgins 1993].

In practice, whitening increased statistical bandwidth by 65–75% (Table 4.1) and CoV was reduced for each of the three time-domain features (Figure 4.2). However, the MAV and average signal length features produced CoV values that did not fit the power decay model. Further, our CoV values were consistently much higher than the model predictions, based on the statistical bandwidth. For example, for whitened data from intact subjects (average bandwidth of 413 Hz from Table I) using a 300 ms window, (4.1) and (4.2) can be used to compute an anticipated CoV_{MAV} of 0.048. Our result of ~0.175 shown in Figure 4.2 is well above this value. Visual inspection of the calibration data from both intact and amputee subjects found substantial modulations in EMG amplitude *within* each 3 s epoch. For the MAV and average signal length features, such modulations would greatly increase the standard deviation of the contiguous features extracted from an epoch, resulting in the observed CoV increase. Recall that intact subjects were not provided force feedback; amputee subjects cannot be provided such feedback. While such feedback could be provided to the intact subjects, it is generally considered best to train classifiers using the same conditions representative of their use—which would *exclude* feedback.

Consistent with these observations, consider the SNR results of St-Amant *et al.* [26], which were produced by intact subjects utilizing force feedback. The inverse of their SNR calculation provides a CoV estimate. Figure 4.4 plots the inverse of their average SNR measurements vs. window length, as well as fits to our power decay model. Excellent model fits result. Although the St-Amant *et al.* data are from different muscles using a smaller inter-electrode distance, they are supportive of the role of EMG amplitude modulation in artificially increasing estimated CoV values. Conversely, the zero crossing feature *did* follow a power decay model as a function of window length and had CoV values that followed theoretic expectations. So long as the crossing signal does not have a peak or trough near zero voltage, even a modest amount of amplitude modulation will not

alter proper identification of the crossing. Hence, zero crossings would not be substantially affected by amplitude modulations, as observed in our results.

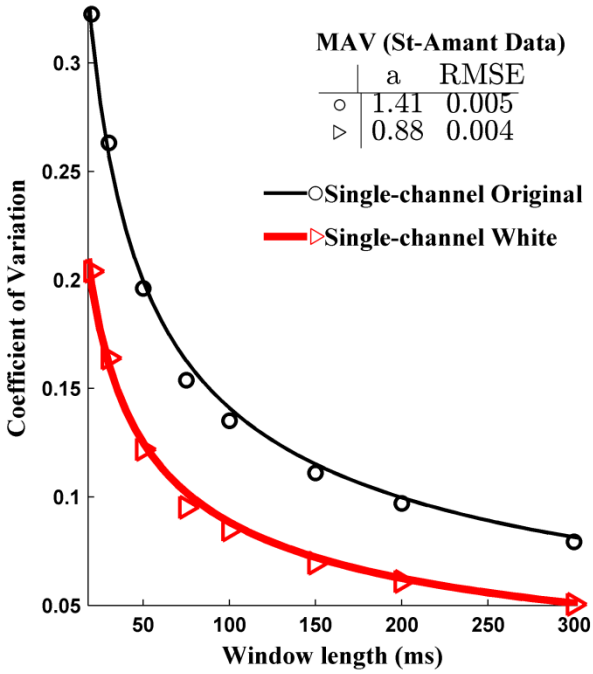

Figure 4.4. Inverse of average SNR gives an estimate of average coefficient of variation, with and without whitening for MAV feature, from the data of St-Amant *et al.* [St-Amant 1998]. Lines show fit to power decay model $\mathrm{CoV}[n] = a/\sqrt{N}$. Inset table shows fit parameter "a" and fit RMS error (RMSE).

In any case, the experimental CoV for whitened features was consistently better (smaller) than that of unwhitened features for MAV and average signal length, and better at shorter epoch lengths for normalized zero crossing rate. Thus, the variability of the time-domain features was generally reduced by preprocessing the signal with a whitening filter.

Features with less variability would be expected to lead to more accurate classification. However, classification analysis does not solely rely on the CoV of the features. Individual features may be weighted differently in the linear classifier, giving a larger impact to some features than others; and small changes in the classification model space can have varied influence on classification accuracy.

The classification accuracy results consistently showed an improvement due to whitening, when the shorter epoch durations were considered. The shortest epoch durations of 25–100 ms generally experienced the greatest improvement—an

approximate 4–5% increase in accuracy. It is not surprising that the improvement diminishes with increased epoch length, since all accuracies are improving, but cannot exceed 100%. Larger sample sizes might be useful in demonstrating significant improvements due to whitening at these longer epoch lengths. Consistent with prior research [Hargrove 2009 and Li 2010], our results also found that higher accuracies resulted when fewer motions and/or more electrode channels were included in the classifier.

Because the performance improvements due to whitening are modest, its inclusion in a prosthesis controller should be weighed vs. its costs. Disadvantages/challenges of using whitening include its substantial added computation and memory requirements, the need to collect calibration data, and possible robustness issues in the presence of high frequency noise. Advantages include that whitening is implemented as a stand-alone preprocessing step whose output can be feed into all further EMG processing steps, accuracy improvements at the shorter epoch durations may facilitate the use of shorter epochs thereby reducing prosthesis response time, and that modern signal processing hardware is increasingly capable of the required processing demands. A logical next step to all of this work is to evaluate whitening within a myoelectric-controlled prosthesis.

We considered only simple feature vectors and classifiers in this analysis. Many more complex features/classifiers have appeared in the literature [Hargrove 2009 and Ahsan 2010], although their classification performance is not markedly distinct from those reported herein. Nonetheless, one would expect that EMG signal whitening would similarly improve the performance of those classifiers. Note that the data available to this research was collected from EMG electrodes with bandwidth out to 350–400 Hz. This bandwidth is common. However, whitened signals have been shown to take advantage of a wider bandwidth (out to nearly 2000 Hz in some cases [Clancy 1994 and Liu 2011]), with additional performance improvement provided. Future work may wish to utilize a wider band EMG data acquisition system. In addition, we calibrated the whitening filters from available functional contractions that contained visible amplitude modulations. It may be better to collect dedicated calibration contractions at 0% and 50% MVC [12], [27].

In conclusion, we have shown that whitening the EMG signal leads to time-domain

features with an increased statistical bandwidth and concomitantly smaller CoV, leading to a consistent increase in classification accuracy in both intact and amputee subjects in a laboratory evaluation. Whitening added approximately five percentage points to classification accuracy at the shortest epoch durations (~25–100 ms). Improvement in classification accuracy at these shortest epoch durations is important, as it may allow prosthesis control systems to use shorter epochs, thereby improving response time.

4.6 Acknowledgement

The authors thank Guanglin Li and the Neural Engineering Center for Artificial Limbs, Rehabilitation Institute of Chicago, Chicago, IL 60611 USA, for providing the amputee data for this study. This work was supported in part by NSERC Discovery Grant 217354-10.

Chapter 5

Signal whitening processing for improved classification accuracy in myoelectric control

Lukai Liu[1], Pu Liu[1], Edward A. Clancy[1], Erik Scheme[2] and Kevin B. Englehart[2]

[1]ECE Dept., Worcester Polytechnic Institute, Worcester. MA 01609, USA.

[2]BME Inst., University of New Brunswick, Frederiction NB E3B 5A3, Canada.

This chapter has been published as: **Lukai Liu**, **Pu Liu**, **Edward A. Clancy**, **Erik Scheme** and **Kevin B. Englehart**, "Signal Whitening Processing for Improved Classification Accuracy in Myoelectric Control," *2011 IEEE 37th Annual Northeast Bioengineering Conference*, Rensselaer Polytechnic Institute, April, 2011. Available: http://ieeexplore.ieee.org/xpls/abs_all.jsp?arnumber=5778636

Abstract—The surface electromyogram (EMG) signal collected from multiple channels has frequently been investigated for use in controlling upper-limb prostheses. One common control method is EMG-based motion classification. Time and frequency features derived from the EMG have been investigated. We propose the use of EMG signal whitening as a preprocessing step in EMG-based motion classification. Whitening decorrelates the EMG signal, and has been shown to be advantageous in other EMG applications. In a ten-subject study of up to 11 motion classes and ten electrode channels, we found that whitening improved classification accuracy by approximately 5% when small window length durations (<100ms) were considered.

5.1 Introduction

The surface EMG has often been used in prosthesis control, ergonomics analysis and clinical biomechanics. Whitening has been used as a preprocessor to decorrelate the EMG signal. In the context of EMG-based motion selection for prosthetic control, we hypothesized that whitening would provide a decrease in the in-class variation of features leading to improved classification accuracy. The present study examined the influence of whitening on classification using time and frequency features of the EMG, in particular at

shorter time durations. Three time domain features: mean absolute value (MAV), signal waveform length and zero-crossing rate; and 7th order autoregressive (AR) coefficients as frequency features, were used in our study. We observed an accuracy improvement of about 5% at smaller window lengths (less than 100 ms) with diminishing returns at longer window durations.

5.2 Methods

5.2.1 Experimental data and methods

Data from a prior study [Hargrove 2009] were reanalyzed. The WPI IRB approved and supervised this reanalysis. Briefly, ten electrodes were applied transversely about the entire circumference of the proximal forearm. A custom electrode amplifier system provided a frequency response spanning approximately 30–450 Hz. Ten subjects with intact upper limbs began and ended each trial at "rest" with their elbow supported on an armrest. Each trial consisted of two repetitions of 11 sequential motion classes: 1, 2) wrist pronation/supination; 3, 4) wrist flexion/extension; 5) hand open; 6) key grip; 7) chuck grip; 8) power grip; 9) fine pinch grip; 10) tool grip; and 11) no motion. Each motion within a trial was maintained for 4 s, after which the subject returned to no motion for a specified inter-motion delay period. Trials 1–4 used an inter-motion delay of 3, 2, 1 and 0 s, respectively, and trials 5–8 used an inter-motion delay of 2 s. A minimum 2-min rest was given between trials. EMG data were sampled at 1000 Hz with a 16-bit ADC. Notch filters were used to attenuate power-line interference at the fundamental frequency and its harmonics.

5.2.2 Methods of analysis

The inter-trial delay segments were removed from the data recordings, resulting in 22, four-second epochs per electrode, per trial (two repetitions of 11 motion classes). For all features, 0.5 seconds of data were truncated from the beginning and end of each epoch. Contiguous, non-overlapping windows were formed from the remaining 3-second epoch segments.

Feature sets were computed for each window within an epoch. A time-domain feature set consisting of three features per window—MAV, signal length and zero-crossing [Hudgins 1993] rate—was evaluated. A frequency domain feature set consisted of seven features per window, comprised of the coefficients of a seventh order autoregressive

(AR) power spectral density estimate [Neumaier 2001]. A third feature set concatenating the seven frequency domain features and the MAV was also evaluated.

Trials 1–4 were used to train the coefficients of the classifier, and trials 5–8 were used to test classifier performance. Initially, all channels and all motions were included in the classifier. The models were trained and tested for each individual subject. Only the test results are reported.

Ten window durations were used: 25, 50, 75, 100, 150, 200, 250, 300, 400 and 500 ms. The analysis was then repeated after the data had been whitened. When doing so, each epoch was high-pass filtered at 15Hz, then adaptively whitened using an algorithm that is tuned to the power spectrum of each EMG channel [Clancy 2000]. Two global variants were also considered. First, the entire analysis was repeated using only nine pre-selected motion classes (the classes denoted above as numbers 1–8 and 11), and again using only seven pre-selected motion classes (1–5, 8 and 11). Second, the entire analysis was repeated using a preselected set of six of the electrode channels. A linear discriminant classifier was used for the recognition task.

5.3 Results

Figure 5.1 shows the averaged test accuracies for the motion–channel combinations with lowest (left) and highest (right) overall performance. Classifying with more channels and fewer motion types (right) produced better overall performance. The concatenated (AR-MAV) feature set gave the highest overall classification accuracy, and the frequency domain feature set the lowest. A consistent 4–5% classification performance increase can be seen at shorter window durations for all three feature sets due to whitening, although the improvement decreases with longer window duration. Paired t-tests ($p<0.05$) at all window lengths suggest that use of whitening as a preprocessing stage provides a statistically significant performance improvement.

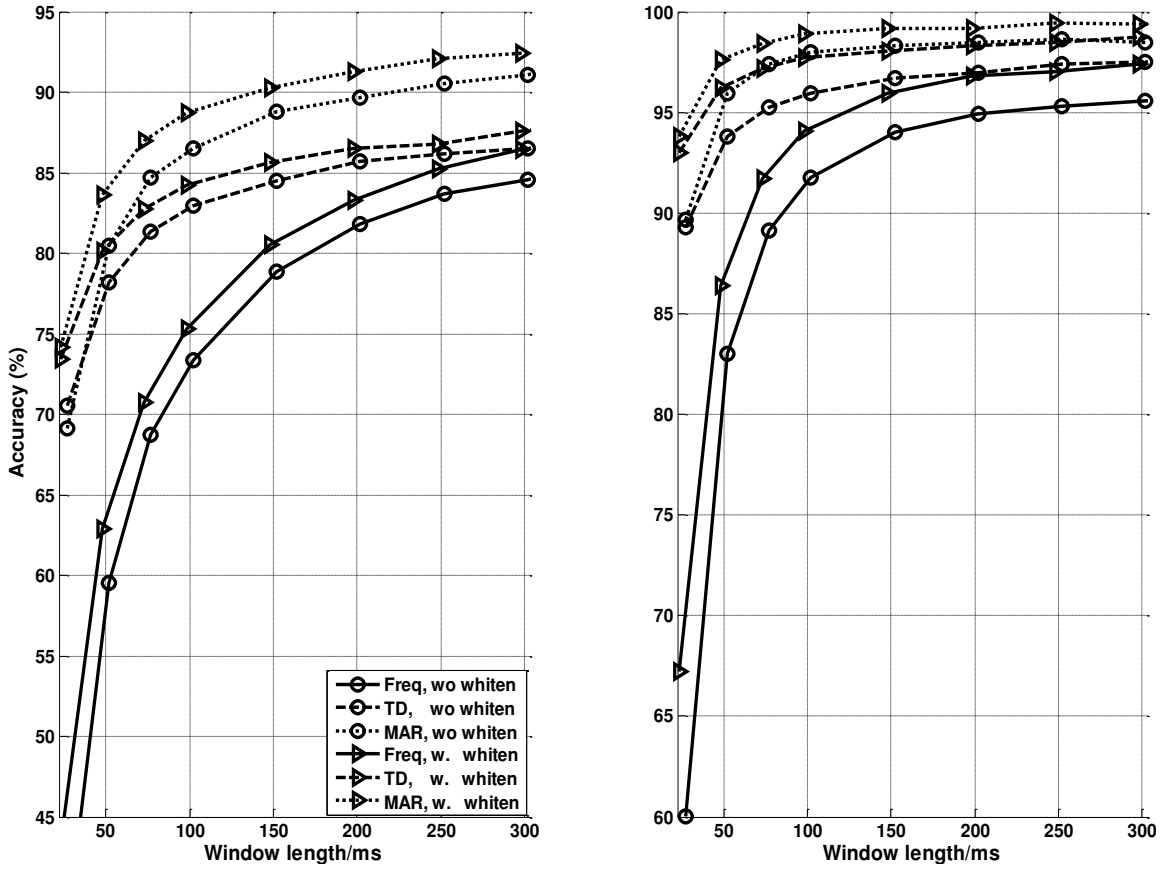

Figure 5.1. Classification accuracies for intact subjects with (triangle)/without (circle) whitening used for pre-processing. The frequency feature set (Freq) is comprised of the seven AR coefficients. The time domain feature set (TD) is comprised of three features, and the concatenated feature set (MAR) uses the AR coefficients and MAV. Window durations up to 300 ms are shown. Note the different y-axis scale for each plot.

5.4 Discussion

We have shown that the use of signal whitening prior to classification analysis of the EMG system consistently improves the recognition accuracy, especially at shorter time durations. This improvement is modest (~5% for window durations less than 100 ms), but may help improve the accuracy of EMG-based artificial limb controllers. The fact that the most substantial improvement is seen with small window lengths is important, as it may allow a control system to use less data, and therefore improve response time.

Further work may apply to other EMG processing techniques, such as universal principal components analysis [Hargrove 2009] and more sophisticated classifiers to further improve classification performance.

Chapter 6

Whitening of the electromyogram for improved classification accuracy in prosthesis control

Lukai Liu[1], Pu Liu[1], Edward A. Clancy[1], Erik Scheme[2] and Kevin B. Englehart[2]

[1]ECE Dept., Worcester Polytechnic Institute, Worcester. MA 01609, USA.

[2]BME Inst., University of New Brunswick, Frederiction NB E3B 5A3, Canada.

This chapter has been published as: **Lukai Liu**, **Pu Liu**, **Edward A. Clancy**, **Erik Scheme** and **Kevin B. Englehart**, "Whitening of the Electromyogram for Improved Classification Accuracy in Prosthesis Control," *Engineering in Medicine and Biology Society (EMBC), 2012 Annual International Conference of the IEEE*, pp. 2627–2630, 28 Aug 2012. Available: http://ieeexplore.ieee.org/xpls/abs_all.jsp?arnumber=6346503

Abstract—The electromyogram (EMG) signal has been used as the command input to myoelectric prostheses. A common control scheme is based on classifying the EMG signals from multiple electrodes into one of several distinct classes of user intent/function. In this work, we investigated the use of EMG whitening as a preprocessing step to EMG pattern recognition. Whitening is known to decorrelate the EMG signal, with improved performance shown in the related applications of EMG amplitude estimation and EMG-torque processing. We reanalyzed the EMG signals recorded from 10 electrodes placed circumferentially around the forearm of 10 intact subjects and 5 amputees. The coefficient of variation of two time-domain features—mean absolute value and signal length—was significantly reduced after whitening. Pre-whitened classification models using these features, along with autoregressive power spectrum coefficients, added approximately five percentage points to their classification accuracy. Improvement was best using smaller window durations (<100 ms).

6.1 Introduction

Traditional myoelectric-controlled upper limb prostheses provide one degree of freedom of proportional control, often by subtracting the EMG amplitudes of an antagonist pair of muscles. The amputee uses manual mode switches to cycle between distinct functions (e.g., hand-wrist-elbow) in order to sequentially control different devices [Parker 2006 and Varol 2010]. More natural control of multiple degrees of freedom is greatly desired by below-elbow amputees [Atkins 1996]. One emerging method for such advanced control is based on EMG pattern recognition [Parker 2006, Hudgins 1993, Hargrove 2009, Li 2010, Graupe 1975 and Boostani 2003]. A window ("epoch") of data from multiple electrodes is used to discriminate between a set of distinct hand/wrist/elbow actions. For continuous control, classification can be performed on the EMG signal stream at a periodic rate.

Pattern recognition consists of the sequential steps of EMG signal conditioning/ preprocessing, feature extraction, dimension reduction and pattern classification. Classification errors are due both to a systematic component (e.g., inability of the available features to distinguish all investigated motions) and a random component. In the related areas of EMG amplitude estimation and EMG-torque modeling, whitening has been shown to reduce the variation (i.e., random component) in the EMG signal and improve performance [Clancy 2010 and Hogan 1980b]. Physiologically, whitening may counteract, in part, the lowpass filter effect imposed on the signal as it propagates from its origin along the muscle fiber membranes; through intervening muscle, fat and skin; before being recorded at the electrodes. From a stochastic processing standpoint, whitening temporally decorrelates the EMG signal, increasing the effective number of signal samples (a.k.a., statistical degrees of freedom), which reduces the variance in the amplitude estimate. Thus, we hypothesized that pre-whitening of the EMG signal would reduce the random variation of the EMG features used in classification, resulting in improved classification performance. This effect should be more evident at small window durations, since classification accuracy already approaches 100% when long epoch lengths are used. A preliminary report of this work appeared in [Liu 2011].

6.2 Methods

6.2.1 Experimental methods

Data from two prior experiments with similar protocols were available for reanalysis. The reanalysis was approved and supervised by the WPI IRB. The original data collection was approved by the human studies boards of the respective institutions and written informed consent was received from each subject. Data from ten intact-limbed subjects were collected at the University of New Brunswick [Hargrove 2009]. Data from five unilateral transradial amputees were collected at the Rehabilitation Institute of Chicago [Li 2010]. Distinct EMG acquisition systems were available at each site. In each case, ten disposable bipolar electrodes (3M Duotrode for intacts; Noraxon 1.25cm diameter Ag/AgCl for amputees) were secured about the circumference of the proximal forearm, oriented along the presumed direction of action potential conduction. EMG data were bandpass filtered (30–350 Hz for intacts; 5–400 Hz for amputees) and sampled at 1000 Hz.

Subjects completed two repetitions of eight trials. Each trial was initiated and terminated at rest with the subject's elbow supported on an armrest. Each trial was comprised of the sequential performance (or, for amputees, *attempted* performance) of 11 motion classes: 1, 2) wrist pronation/supination; 3, 4) wrist flexion/extension; 5) hand open; 6) key grip; 7) chuck grip; 8) power grip; 9) fine pinch grip; 10) tool grip; and 11) no motion. Each motion within a trial was maintained for 4 s, and the subject returned to the rest posture for a specified inter-motion delay period. Trials 1–4 used an inter-motion delay of 3, 2, 1 and 0 s respectively, and trials 5–8 used an inter-motion delay of 2 s. A minimum of two minutes rest was given between trials.

6.2.2 Computation of EMG features

The inter-motion delay portions of the data were removed, leaving epochs 4 s in duration. Each epoch was notch filtered at the power line frequency and each of its harmonics. When whitening was desired, each epoch was highpass filtered at 15 Hz, then adaptively whitened using the algorithm of [Clancy 2010 and Prakash 2005]. This algorithm initially whitens the complete signal (EMG signal plus noise) based on an estimate of the noise-free spectrum of the EMG signal. Unfortunately, this fixed filter also accentuates the high-frequency portion of the noise spectrum. Hence, an adaptive Weiner

filter (optimal linear filter to attenuate additive noise) is cascaded after the fixed whitening filter. This filter adapts its shape based on the spectra of the background noise and the EMG signal. The EMG signal spectrum is amplitude modulated with muscle effort, while the background noise spectrum is fixed. In practice, the Weiner filter is lowpass in shape, with a higher cutoff location occurring when muscle effort is high. Adaptive whitening requires calibration to a rest and an active contraction, for each electrode. The "no motion" class was used as the rest contraction. One active class was manually selected per electrode per subject, corresponding to the class with the largest EMG amplitude. After this filtering, the first and last 0.5 seconds of the epoch were discarded, to account for filter start-up transients.

Features were then extracted from each trimmed (3 s) epoch by segregating the epoch into contiguous windows. The following window durations were investigated: N = 25, 50, 75, 100, 150, 200, 250 and 300 ms. The time-domain feature set consisted of the three features: mean absolute value (MAV), average signal length (SL) and normalized zero crossing rate (ZC) (see [Hudgins 1993] for definitions). Our ZC feature used a noise threshold of approximately $1/6^{th}$ the average RMS value of the "no motion" class. The frequency-domain feature set consisted of the coefficients of a seventh-order autoregressive (AR) model [Graupe 1975 and Neumaier 2001]. The "combined" feature set used the AR coefficients along with MAV.

6.2.3 Analysis of coefficient of variation of EMG features

Since the mechanism of improvement due to signal whitening is hypothesized to be a reduction in the variation of feature values, we computed the coefficient of variation (CoV) of the features. We limited this analysis to the three time-domain features. For each electrode for each subject, we identified two classes with the largest EMG amplitudes. The CoV was computed for each epoch as the standard deviation of the features divided by their mean. Low amplitude recordings were avoided, since the CoV calculation is erratic when the mean feature value and its standard deviation are both small numbers. These CoV values were averaged across the two selected trials and across all subjects. Results were computed both with and without whitening, separately for intact-limbed subjects and amputees, and for each window duration N. Thereafter, a modified power decay model

was fit to the mean values, using the model: $\mathrm{CoV}[N] = a + b/\sqrt{N}$.Lower CoV values denote less variability in the features.

6.2.4 Analysis of classification performance

Linear discriminant classification was used with an exhaustive search over all possible electrode combinations. For ten electrode channels, there were 1023 possible electrode combinations evaluated. Both repetitions of data trials 1–4 were used for training and both repetitions of data trials 5–8 were used for testing. The results from the best test result per subject are reported. The entire analysis was repeated using a preselected set of six electrodes spread evenly about the circumference of the forearm. For six electrode channels, there were 63 possible electrode combinations evaluated. The analysis was repeated again using only a preselected set of nine motion classes (classes 1–8 and 11); and again using a preselected set of seven motion classes (classes 1–5, 8 and 11). Results for intact-limbed subjects and amputees are reported separately for each of the window durations.

6.3 Results

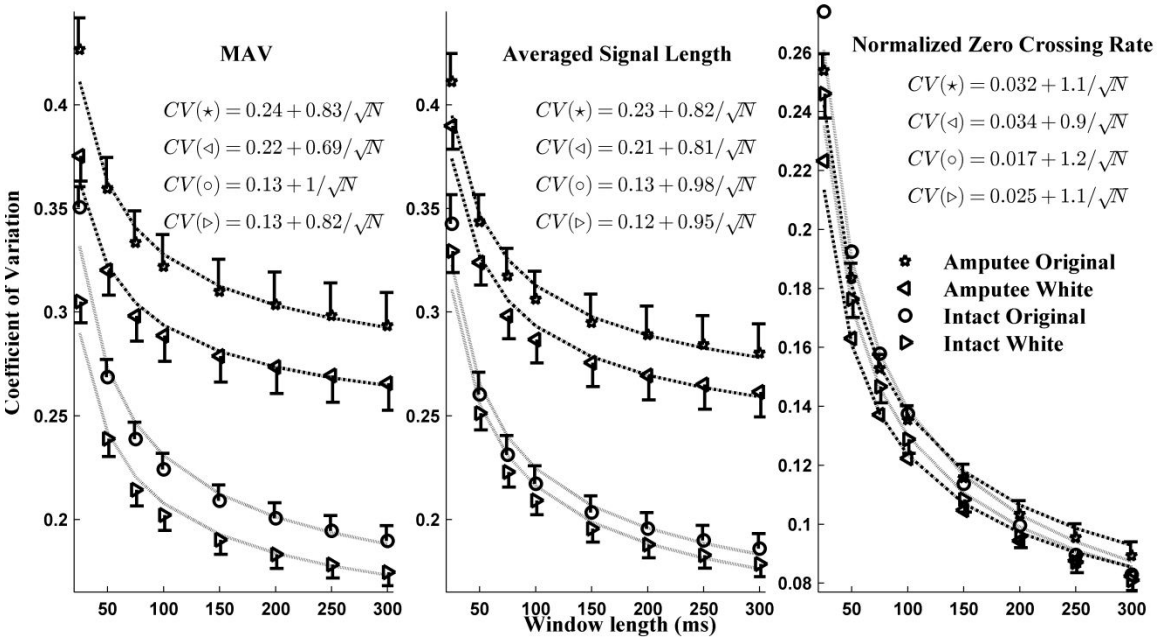

Figure 6.1. Average coefficient of variation (plus or minus one standard error) for the time-domain features from ten intact and (separately) five amputee subjects, with and without whitening. Lines show fit to the model: $\mathrm{CoV}[N] = a + b/\sqrt{N}$. Scale of y-axis differs from normalized zero crossing rate. Sample size is 100 for intact subjects, 50 for amputee subjects.

Figure 6.1 shows the average plus/minus standard error CoV results for the three time-domain features, with and without whitening, plotted separately for intact-limbed and amputee subjects. Whitening substantially reduced feature variation at all window durations for the MAV and SL features. There was rather limited affect due to whitening for the ZC feature. The CoV values were lower in the intact-limbed subjects. All plots fit well to the offset power law model.

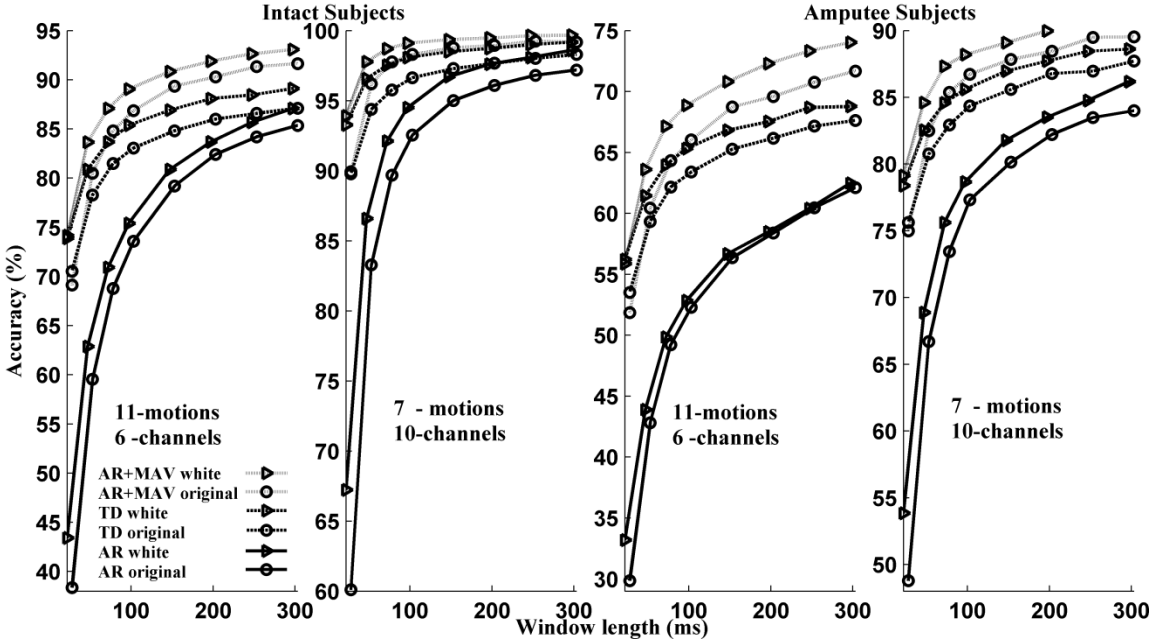

Figure 6.2. Exhaustive selection average classification accuracies from ten intact (left) and five amputee (right) subjects for each of the three feature sets, with and without whitening. The motion-channel combinations shown represent the lowest accuracies (fewest channels and most motion classes) and highest (most channels and fewest classes). Window durations vary from 25 to 300 ms. Note the different y-axis scale for each plot.

Classification accuracy results were higher when the number of EMG channels was larger and when the number of motion classes was lower. Thus, results will only be presented for the best (10-channel, 7-motion) and worst (6-channel, 11-motion) combination. Figure 6.2 shows the across-subject average classification accuracy for these channel-motion combinations, with and without whitening, for each of the three feature sets (time-domain, frequency-domain and combined), plotted separately for intact-limbed and amputee subjects. Whitening provided a consistent increase in performance. At low window durations, the performance increase is as much as five percent. The "combined" feature set (AR coefficients along with MAV) consistently provided the highest average

classification accuracy. Accuracy was higher in the intact-limbed subjects than in the amputees.

6.4 Discussion

Although signal whitening methods have been available for several years, they do not seem to have been applied to the EMG pattern recognition problem. When computing EMG MAV, the signal to noise ratio (SNR) of the amplitude estimate has been shown to increase with window duration in a square root fashion [Clancy 1999], with whitening improving the SNR. Since CoV is defined as the reciprocal of the SNR, it follows that the CoV of the MAV feature should decrease with window length as the reciprocal of a square root; thus our use of the power law model for fitting to the CoV values. Further, whitened MAV features should have lower CoV values than unwhitened MAV features. We found, however, that an offset term was needed in the power law model in order to achieve an acceptable fit (Figure 6.1). Manual inspection of the epochs used to calculate the CoV showed that many subjects did not maintain a constant effort level across the 3 s used to form features. If the feature values are changing *within* a 3 s epoch, then a larger sample standard deviation will be found for that mean feature value. A larger CoV estimate will result. The inflated MAV CoV values fit better to a power law model that included an offset term than to the theoretically expected model that is absent an offset.

Although not described here, analytic and simulation analysis also predicted an inverse square root relationship with window duration for the SL and ZC features. Fig.1 shows that the SL feature also required substantial offset values in the power law fit, but the ZC feature did not. As effort varied *within* an epoch, the CoV of the SL feature would be expected to inflate, again due to the increased within-epoch variance. But, zero crossings are not substantially influenced by modulations in EMG amplitude within an epoch—so long as the EMG amplitude remains above the noise floor. Hence, the ZC features exhibited the lowest overall CoV values (and the lowest standard errors).

One would expect much lower CoV values for the MAV and SL features if the subject contractions were held more constant. However, acquisition of such data is only relevant to this intermediate evaluation of CoV. For training classifiers, it is better to collect data with the full range of within-epoch modulation that is representative of actual prosthesis control use. The classifier will then optimize for that realistic condition.

Regardless of this inter-epoch modulation concern, whitening decreased the CoV, making the features more repeatable. As shown in Figure 6.2, an improvement in classification accuracy resulted. The improvement was most prominent at the shorter window durations. This result was expected, since classification performance increases towards 100% at the longer window durations. No further increase is possible.

6.5 Conclusion

We investigated whitening as a preprocessing step to EMG pattern recognition in intact-limb and amputee subjects. Whitening was shown to decrease the average CoV for MAV and SL features, with less influence on the ZC feature. Whitening was shown to consistently improve the average classification accuracy when distinguishing up to 11 distinct motion classes using up to 10 different electrodes. Improvement due to whitening was also found using fewer motion classes and fewer electrode channels.

6.6 Acknowledgement

The authors thank Guanglin Li and the Neural Engineering Center for Artificial Limbs, Rehabilitation Institute of Chicago, Chicago, IL 60611 USA, for providing the amputee data for this study.

Chapter 7

EMG whitening improves pattern recognition in prosthesis control

Lukai Liu[1], Pu Liu[1], Edward A. Clancy[1], Erik Scheme[2] and Kevin B. Englehart[2]

[1]ECE Dept., Worcester Polytechnic Institute, Worcester. MA 01609, USA.

[2]BME Inst., University of New Brunswick, Frederiction NB E3B 5A3, Canada.

This chapter has been published as: **Lukai Liu**, **Pu Liu**, **Edward A. Clancy**, **Erik Scheme** and **Kevin B. Englehart**, "EMG Whitening Improves Pattern Recognition in Prosthesis Control," *Proceedings of the Twentieth Congress of the International Society of Electrophysiology and Kinesiology*, Rome, Italy, July 15-18, 2014.

7.1 Introduction

A common method for controlling powered upper-limb prostheses is via EMG-based motion classification. We improved classification accuracy by applying whitening as an EMG preprocessing step. Whitening decorrelates the EMG signal and has been shown to be advantageous in related problems such as EMG-force processing.

7.2 Methods

Previously collected EMG data from ten intact subjects and five amputees were reanalyzed, with and without EMG signal whitening. A linear discriminant classifier was employed. Up to 11 motion classes and ten electrode channels were examined, using both time- and frequency-domain EMG features.

7.3 Results

Whitening increased the statistical bandwidth of the EMG signal, on average, by 65–75%. Whitening significantly reduced the coefficient of variation of time-domain features (mean absolute value, average signal length and normalized zero crossing rate). Whitening increased classification accuracy approximately five percentage points at small window lengths (< 100 ms), with smaller gains found at longer window lengths.

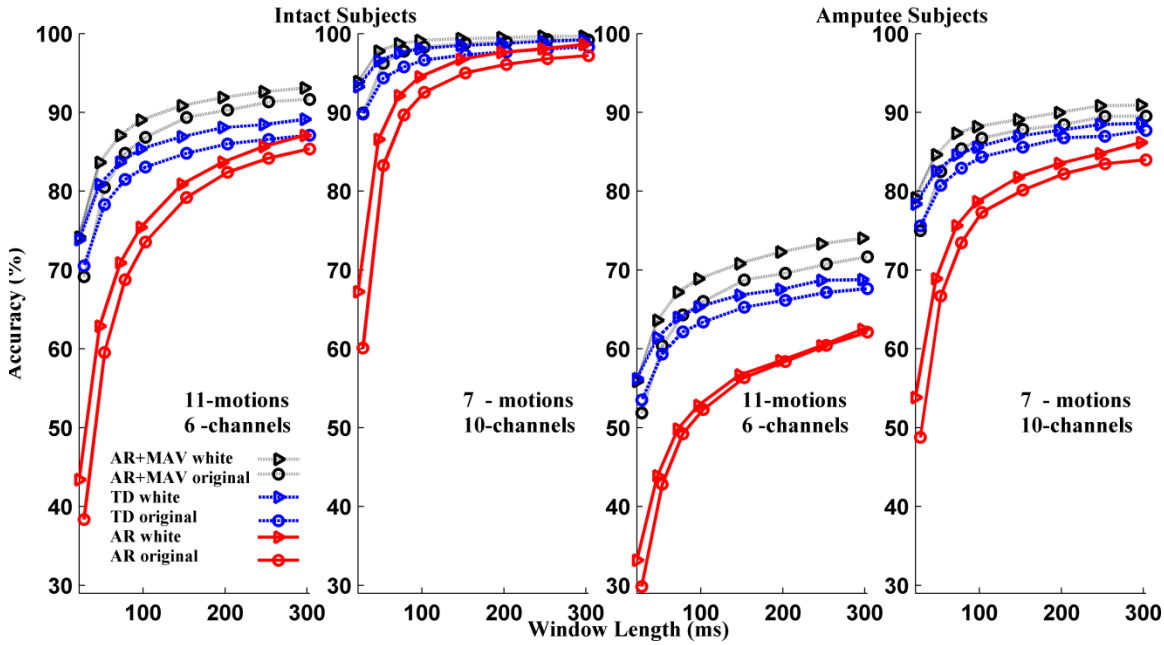

Figure 7.1. Average classification results with vs. without EMG signal prewhitening.

7.4 Conclusion

Whitening the EMG signal prior to its use in classification analysis increased the statistical bandwidth of the signal, decreased the coefficient of variation of extracted features and increased classification accuracy at short window lengths.

7.5 Acknowledgement

Amputee data provided by G. Li and the Neural Engineering Center for Artificial Limbs, Rehabilitation Institute of Chicago.

Chapter 8

Identification of constant-posture EMG-torque relationship about the elbow using nonlinear dynamic models

Edward A. Clancy[1], Lukai Liu[1], Pu Liu[1] and Daniel V. Moyer[2]

[1]ECE Dept., Worcester Polytechnic Institute, Worcester. MA, USA.

[2]Genasys Inc., Menlo Park, CA, USA.

This chapter has been published as: **Edward A. Clancy**, **Lukai Liu**, **Pu Liu** and **Daniel V. Moyer**, "Identification of Constant-posture EMG-torque Relationship about the Elbow using Nonliear Dynamic Models," *IEEE Transactions on Biomedical Engineering*, pp. 205–212, vol. 59 (1), 2012. Available: http://ieeexplore.ieee.org/xpls/abs_all.jsp?arnumber=6032732

Abstract—The surface electromyogram (EMG) from biceps and triceps muscles of 33 subjects was related to elbow torque, contrasting EMG amplitude (EMGs) estimation processors, linear/nonlinear model structures and system identification techniques. Torque estimation was improved by: advanced EMGs processors (i.e., whitened, multiple-channel signals); longer duration training sets (52 s vs. 26 s); and determination of model parameters via pseudo-inverse and ridge regression methods. Dynamic, nonlinear parametric models that included second- or third-degree polynomial functions of EMGs out-performed linear models and Hammerstein/Weiner models. A minimum error of 4.65±3.6% maximum voluntary contraction (MVC) flexion was attained using a third-degree polynomial, 28th-order dynamic model, with model parameters determined using the pseudo-inverse method with tolerance 5.6x10^{-3} on 52 s of four-channel whitened EMG data. Similar performance (4.67±3.7% MVC flexion error) was realized using a second-degree, 18th-order ridge regression model with ridge parameter 50.1.

Keywords—Biological system modeling, biomedical signal processing, EMG amplitude estimation, EMG signal processing, electromyography

8.1 Introduction

The surface electromyogram (EMG) reflects the neural activity of the underlying musculature, and has often been used to estimate torque produced about joints. Typically, EMG amplitude (EMGs)—the time-varying standard deviation of the EMG waveform—is estimated and then related to joint torque through parametric models determined via system identification techniques. Both agonist and antagonist muscles are included in these models to account for co-contraction (particularly at higher contraction levels) [An 1983, Solomonow 1986 and Brown 2008]. Low error EMG-torque estimation has several applications. In prosthesis control [Parker 2006], it would be expected to provide more accurate emulation of the natural command relationship between the central nervous system and peripheral joints/muscles. In ergonomics [Kumar 1996, Mathiassen 1995 and Hagg 2004] and clinical biomechanics [Disselhorst-Klug 2009 and Doorenbosch 2003], it should lead to better estimates of joint loading and muscle tension in studies of worker tasks and biomechanical evaluations. Other applications include investigation of motor control [Ostry 2003] and control of powered exoskeletons [Fleischer 2008, Rosen 2001 and Khokhar 2001].

Numerous studies, concentrating on various aspects of the EMG-torque problem, have been conducted over the years (see [Staudenmann 2010] for a recent review). Study conditions have ranged from constant-posture, constant-torque (the simplest) to posture-varying, torque-varying (the most complete case, representing unconstrained movement). The latter condition is most representative of the full range of application tasks, but can be too complex when studying methodological improvements (such as those presented herein). To reduce EMG-torque estimation error, some research has applied advanced EMGs estimation methods [Hogan 1980a, Hogan 1980b, Clancy 1994, Clancy 1995, Clancy 1997a, Clancy 2001, Clancy 2002, Clancy 2006, Sanger 2007, Staudenmann 2007 and Potvin 2004] or advanced/nonlinear system identification methods relating EMGs to torque [An 1983, Solomonow 1986, Brown 2008, Mathiassen 1995, Gottlieb 1971, Thelen 1994, Mountjoy 2010 and Koo 2005].

Based on past research results, we hypothesized that incorporating nonlinear model structures into the EMG-torque problem—along with advanced EMGs processors—would further reduce joint torque error. However, nonlinear models typically require

additional parameters, which can lead to over-fitting [Ljung 1999]. There exists a complex interplay between the number of fit parameters in the model, training data duration, the SNR of the training data and the system identification method [Ljung 1999].

Accordingly, this study compares system identification methods for nonlinear EMG-torque models using advanced EMGs processors (whitening and multiple-channel combination), explicitly addressing model over-fitting. Hammerstein and Weiner models were specifically examined because their smaller number of model parameters is expected to alleviate over fitting [Ljung 1999]. We investigated the fitting of model parameters through the singular-value-decomposition-based least squares pseudo-inverse approach, in which certain linear combinations of the training data—those that likely provide little information but contain considerable noise—are omitted from the training solution [Press 1994]. We evaluated least squares estimation of the training parameters using ridge regression [Jones 1972, Hoerl 1970, Marquardt1975 and Clancy 1999a]. Additionally, we studied the effect of training data duration, as longer training data sets support models with more parameters.

8.2 Methods

8.2.1 Experimental data and methods

A subset of experimental data from 33 subjects (18 male and 15 female, ranging in age from 18 to 65 years) from two prior studies of the upper arm (fully described in [Clancy 1999a] and [Clancy 2000]) were reanalyzed. Because these data had been de-identified and unlinked, the WPI IRB stipulated that supervision of this reanalysis was not required. In these studies, each subject was secured into the seat of a Biodex exercise machine with his/her shoulder abducted 90^{o}, forearm oriented in a parasaggital plane, wrist fully supinated and elbow flexed 90^{o}. The subject was rigidly attached to the Biodex dynamometer with a cuff at the styloid process. The skin above the muscles under investigation was cleaned with an alcohol wipe. An array of four Liberty Technology MYO115 EMG electrode-amplifiers was placed transversely across each of the biceps and triceps muscles, midway between the elbow and the midpoint of the upper arm, centered on the muscle midline. Each electrode-amplifier had a pair of 4-mm diameter, stainless steel, hemispherical contacts separated by 15 mm (center to center), oriented along the muscle's long axis. The distance between adjacent electrode-amplifiers

was approximately 1.75 cm. A single ground electrode was gelled and secured above the acromion process. Custom electronics amplified and filtered each EMG signal (CMRR of approximately 90 dB at 60 Hz; second-order, 10–2000 Hz bandpass filter) before being sampled at 4096 Hz with 16-bit resolution.

Each subject was provided a warm-up period, after which MVC torque was measured in both elbow extension and flexion. Five-second duration, constant-posture constant-force contractions at 50% MVC extension, 50% MVC flexion and rest were recorded. These contractions were used to calibrate the advanced EMGs estimation algorithms [Clancy 2000 and Prakash 2005]. Then, a real-time feedback signal consisting of one of four EMGs processors (formed by subtracting the extensor EMGs from the flexor EMGs) was provided on a computer screen. The processors were: single-channel unwhitened, single-channel whitened, multiple-channel unwhitened and multiple-channel whitened. Thirty-second duration, constant-posture force-varying contraction trials were then recorded. The subjects used the feedback signal to track a computer-generated target that moved on the screen in the pattern of a band-limited (1 Hz) uniform random process, spanning 50% MVC extension to 50% MVC flexion. Twelve trials (three per feedback signal) were collected in a randomized order. Additional tracking trials not used in this study were also collected. Rest was provided between trials to prevent cumulative fatigue.

8.2.2 Methods of analysis

All analysis was performed offline in MATLAB. Two distinct EMGs processors were created from each of the extension and flexion muscle groups for each 30 s trial using our open-source MATLAB toolbox [Clancy 2010]. The estimates were either single-channel unwhitened (using an electrode located centrally on the muscle) or four-channel whitened [19]. Each estimator utilized a 15 Hz high pass filter (5^{th}-order Butterworth applied in the forward and reverse time directions to achieve zero phase) and a first-order demodulator (rectifier). Whitened channels used the non-causal adaptive whitening algorithm of Clancy and Farry [Clancy 2000 and Prakash 2005]. After demodulation, signals were decimated by a factor of 100 to a sampling rate of 40.96 Hz, using a low pass filter with cut-off frequency of 16.4 Hz (which also served as the smoothing stage of the amplitude estimate). The torque signal was similarly decimated, producing a data set with a

bandwidth approximately 10 times that of the torque signal being estimated [Clancy 2006 and Ljung 1999].

Extension and flexion EMGs were related to joint torque using four parametric, dynamic model structures. For each structure: $T[m]$ was the measured torque at the m^{th} decimated sample; a_0 was an offset parameter (not used in all system identification techniques); e_q and f_q were the extension and flexion fit parameters, respectively; and $s_E[m]$ and $s_F[m]$ were the extension and flexion EMGs estimates, respectively. The model structures were:

1) Linear, time invariant (LTI) system of dynamic order Q:

$$T[m] = a_0 + \sum_{q=0}^{Q} e_q \sigma_E[m-q] + \sum_{q=0}^{Q} f_q \sigma_F[m-q] \quad (8.1)$$

2) Polynomial nonlinear model of degree D, dynamic order Q:

$$T[m] = a_0 + \sum_{d=1}^{D} \sum_{q=0}^{Q} e_{q,d} \sigma_E^d[m-q] + \sum_{d=1}^{D} \sum_{q=0}^{Q} f_{q,d} \sigma_F^d[m-q] \quad (8.2)$$

3) Hammerstein model: This model was comprised of a D^{th}-degree polynomial static nonlinearity cascaded with a Q^{th}-order, LTI, FIR system, for each of the extension and flexion EMG inputs. The sum of the extension and flexion outputs was related to joint torque.

4) Weiner model: This model was comprised of a Q^{th}-order, LTI, FIR system cascaded with a D^{th}-degree polynomial static nonlinearity, for each of the extension and flexion EMG inputs. The sum of the extension and flexion outputs was related to joint torque.

In these four model structures, the LTI system order ranged from $1 \leq Q \leq 30$ and the polynomial degree ranged from $1 \leq D \leq 4$. Two seconds of data were excluded from the beginning and end of each 30 s signal to mitigate filter start-up transients.

The parameters of the LTI and polynomial models were estimated using linear least squares. Three approaches were evaluated to reduce over-fitting during parameter estimation. First, the singular value decomposition-based pseudo-inverse was used, in which the reciprocals of small singular values were replaced with the value zero [Press 1994]. The tolerance for replacement was based on the ratio of each singular value to the maximum singular value, ranging over 40 values spanning 10^{-16} to 0.5 in logarithmic increments. The pseudo-inverse model did not include an offset term a_0. Second, ridge regression [Jones 1972, Hoerl 1970 and Marquardt 1975] was investigated, including an

offset term a_0 in the model. The ridge parameter, k, ranged from 10^{-7} to 10^{4} in 112 logarithmic increments. Third, we examined the effect of increasing the duration of data available to train the least squares, as described in detail below. Parameters of the Hammerstein and Weiner models were determined via nonlinear least squares using the MATLAB System Identification Toolbox.

As noted above, each subject completed 12 tracking trials, consisting of three repetitions each of four different feedback options. Each set of three repetitions (representing one feedback style) was used to produce one test result. In the single-trial calibration method, the first trial was used as training data and the second as a test set. Then, the third trial was used as training data and the second was again used as the test set. The average mean absolute value error (between the actual torque and that predicted by the EMG-torque model) of these two test results is reported as the test error value. In the dual-trial calibration method, the first and third trials were simultaneously used to train one set of parameters (effective sequence duration of 52 seconds), and then tested on the second trial. Since all of this analysis was performed post-experiment, tracking performance during data collection was not directly relevant. Rather, the recorded EMG was related to the recorded joint torque from the load cell—the real-time feedback signal was not considered. In general, each of the feedback options produced torque with a similar characteristic (uniform random signal bandlimited to 1 Hz). Nonetheless, all training and testing remained within a feedback style. In all cases, error is reported as a percent of the MVC flexion torque. Only test trial results are presented. For statistical analysis, the four test trial results from each subject were averaged, and these average values subjected to a paired sign test [Miller 1977].

Lastly, it was desired to compare the results using these advanced EMG processors and models to a "conventional" EMG-torque estimator. A conventional estimator was formed by filtering the single-channel unwhitened EMGs from each of the biceps and triceps muscles through a second-order, Butterworth, low-pass filter; gain scaling these outputs based on their respective 50% MVC contractions (achieved by using the 50% MVC contractions to calibrate a zero-order linear model using the pseudo-inverse approach with the default tolerance in MATLAB); and then subtracting them to form the torque estimate. Typically, the cutoff frequency of the low-pass filter in conventional

estimators is set at a few Hz [Koo 2005, Lloyd 2003 and Doorenbosch 2004]. In our case, selection of the appropriate cut-off frequency was unclear. Thus, we repeated conventional torque estimation 40 times with cut-off frequencies ranging from 0.1 Hz to 4.0 Hz, in increments of 0.1 Hz. The best of these 40 results is reported. Note that the cut-off frequency was not adapted to individual subjects; only one flexion and one extension gain was subject-specific (based on the 50% MVC contractions). Training and testing proceeded as described previously.

8.3 Results

EMG-torque performance was studied as a function of two EMG processors, four model structures and three system identification techniques. Figures 8.1–8.4 graphically depict representative aspects of the overall test results. Figure 8.1 concentrates on results from the pseudo-inverse approach, Figure 8.2 on ridge regression results, Figure 8.3 on Hammerstein/Weiner model results and Figure 8.4 on results using the longer-duration training data (52 s). Figures 8.1, 8.2 and 8.4 show results only from dynamic model orders Q=5, 8, 15, 20 and 30, which form a representative sub-set of the 30 model orders evaluated. Table 8.1 lists the lowest test error, along with the corresponding model parameters, for the pseudo-inverse approach results. Overall, models which utilized a low model order (e.g., $Q \leq 5$) exhibited high error, presumably because this low model order did not sufficiently capture the system's true dynamic behavior. Exceptionally high dynamic model order often also led to higher error, particularly for high polynomial model degrees and with single-channel unwhitened EMG processors (or their combination), presumably due to over-fitting. Excessively large pseudo-inverse tolerance values or ridge k values exhibited poor performance, and should be avoided.

Figures 8.1 and 8.2 each provide direct comparison between the EMG processors. Excluding tolerance values above ~10^{-2} (Figure 8.1) and ridge k values below ~1 (Figure 8.2)—regions that users would avoid due to very high error—multiple-channel whitened processors consistently performed better than single-channel unwhitened. Statistically, the results for parameters of best performance (see Table 8.1) for the pseudo-inverse method, 26 s training duration, were compared between the two EMG methods for each polynomial degree. This comparison was repeated for the ridge regression results and for the 52 s training duration. Each comparison was significant ($p \leq 6.8 \times 10^{-3}$).

EMG⌐	Polynomial Degree (*D*)			
	D = 1 (Tol, *Q*)	*D* = 2 (Tol, *Q*)	*D* = 3 (Tol, *Q*)	*D* = 4 (Tol, *Q*)
26 s Training				
Single Channel, Unwhitened	7.10±5.9% (5.6e-4, 25)	7.06±5.7% (1.8e-3, 15)	7.43±6.2% (5.6e-3, 14)	7.97±7.0% (1.0e-2, 20)
Multiple Channel, Whitened	5.93±4.5% (5.6e-3, 30)	5.55±4.5% (1.0e-2, 16)	5.56±4.6% (5.6e-3, 16)	5.62±4.6% (5.6e-3, 14)
52 s Training				
Single Channel, Unwhitened	6.38±5.4% (3.2e-4, 30)	5.86±4.0% (5.6e-3, 18)	5.92±4.0% (5.6e-3, 16)	6.29±5.1% (5.6e-3, 14)
Multiple Channel, Whitened	5.15±3.8% (5.6e-3, 30)	4.69±3.6% (1.0e-2, 15)	4.65±3.6% (5.6e-3, 28)	4.70±3. 6% (5.6e-3, 16)

Table 8.1. Lowest EMG-torque error (mean ± standard deviation absolute %MVC flexion) with corresponding tolerance (*tol*) and dynamic model order (*Q*) for pseudo-inverse method. Each result from 33 subjects.

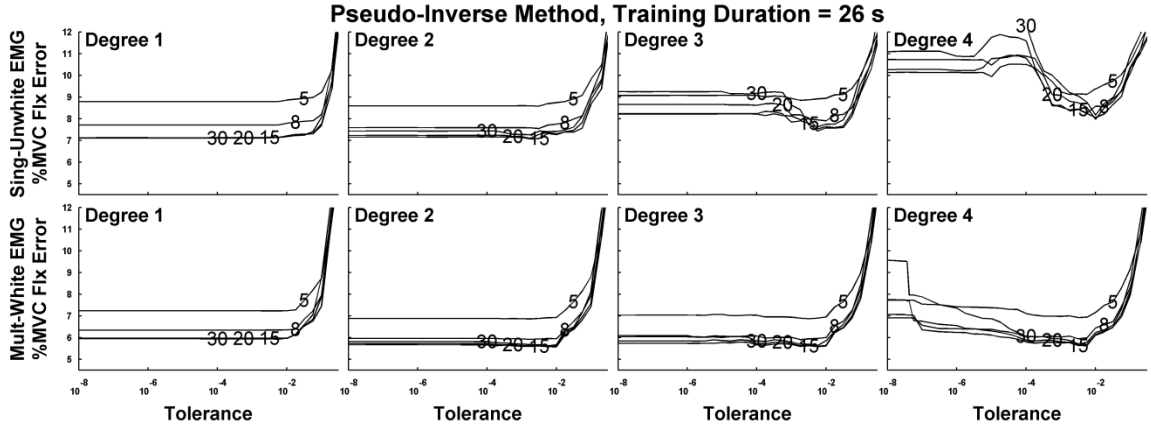

Figure 8.1. EMG-torque error as a function of tolerance value, using the **pseudo-inverse** system identification method, with **26 s of training data**. Results for tolerance values below 10^{-8} not shown, but follow similar trend. Each row shows results from the two EMG processors; columns distinguish the different polynomial model degrees (*D*). Each plot shows the results for representative dynamic model orders (*Q*) 5, 8, 15, 20 and 30, as labeled. Each result is the average from 33 subjects.

Figure 8.3 shows that the Weiner models were clearly inferior to the best polynomial nonlinear model. The results for parameters of best performance for the Weiner model (*D*=2, *Q*=18, multiple whitened EMG) were statistically different from those of the best pseudo-inverse-based polynomial nonlinear model ($p<10^{-8}$). The Hammerstein model's performance was closer to that of the pseudo-inverse and ridge regression methods. Comparing the results for parameters of best performance for the Hammerstein model (*D*=2, *Q*=10, multiple whitened EMG) to results from the best pseudo-inverse-based polynomial nonlinear model was marginally significant (p=0.0175). With the available

MATLAB toolbox, it was not possible to produce results that combined two training trials into a 52 s training duration for the Hammerstein and Weiner models.

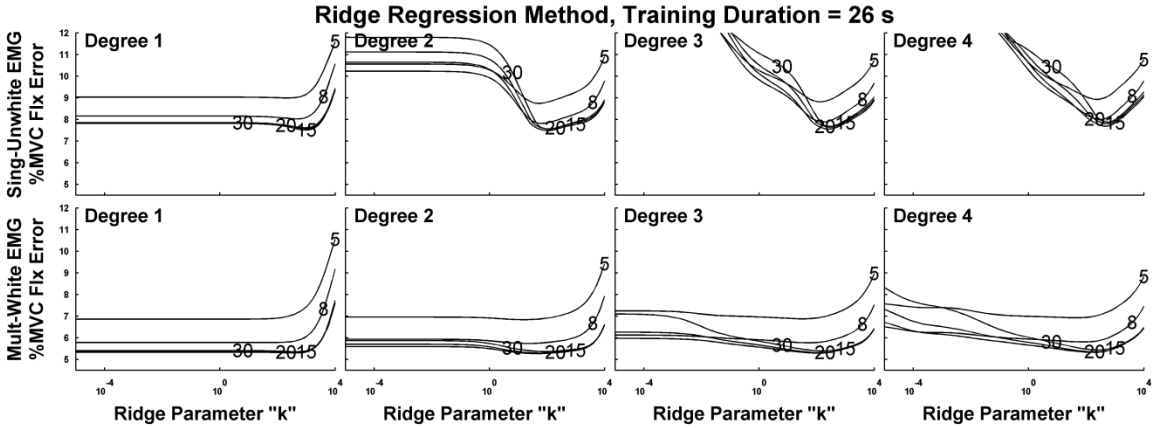

Figure 8.2. EMG-torque error as a function of ridge "k" value, using the **ridge regression** system identification method, with **26 s of training data**. Results for "k" values below 10^{-5} not shown, but follow similar trend. Each row shows results from the two EMG processors; columns distinguish the different polynomial model degrees (D). Each plot shows the results for representative dynamic model orders (Q) 5, 8, 15, 20 and 30, as labeled. Each result is the average from 33 subjects.

The best pseudo-inverse results (4.65±3.6% MVC flexion; D=3, Q=28, Tol=5.6×10^{-3}, 52 s training set, multiple whitened EMG) were not statistically different (p=0.5) from the best ridge regression results (4.67±3.7% MVC flexion; D=2, Q=18, k=50.1, 52 s training set, multiple whitened EMG). Differences between results were most consistent when using multiple-channel whitened EMG processing. The pseudo-inverse results for a linear model (D=1) differed from each of the three nonlinear degrees (D=2, 3, 4) when using either single unwhite or multiple white EMG processors ($p \leq 1.8\times10^{-3}$). Results were less consistent with the 26 s training duration.

Comparison of the results shown in Figure 8.4 to those in Figure 8.1 clearly demonstrates that error is reduced by a longer duration training set (52 s). Statistically, the results for parameters of best performance for the pseudo-inverse method, single-channel unwhitened EMG were compared between the two training durations for each polynomial degree. This comparison was repeated for the ridge regression results and for the multiple-channel whitened EMG method. All differences were significant ($p<1.6\times10^{-4}$).

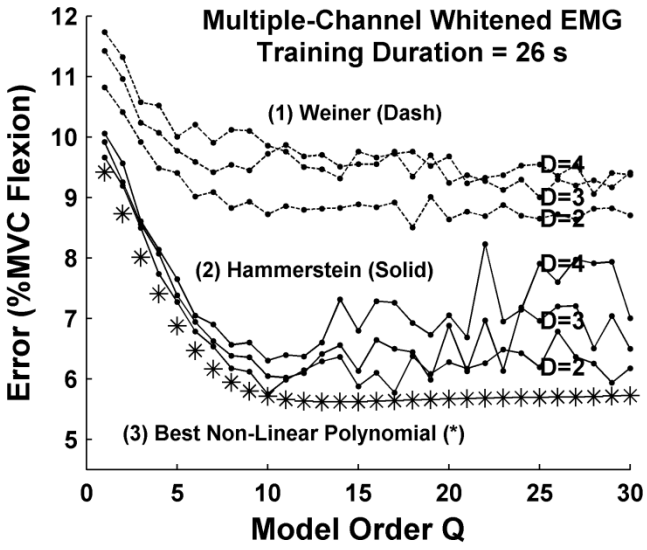

Figure 8.3. EMG-torque error as a function of dynamic model order (Q), using the **Hammerstein and Weiner** system identification methods, with **26 s of training data** and multiple-channel whitened EMG processor. Polynomial degree (D) is labeled on each plot. (Degree one not shown, since it is equivalent to the linear model, shown elsewhere.) For comparison, asterisks show the best results using the pseudo-inverse method (polynomial degree D=2, tolerance = $5.6\text{x}10^{-4}$). Each result is the average from 33 subjects.

Finally, results for the "conventional" processor varied as a function of the low-pass filter cut-off frequency of the Butterworth filter. The best cut-off frequency was 1.3 Hz, with considerably poorer performance at both lower and higher frequencies. At this cut-off frequency, the error was 19.15±11.15% MVC flexion. Statistically, the best "conventional" torque estimator was compared to the single-channel unwhitened results using a 26 s training duration (D=2, Q=15, Tol=$1.8\text{x}10^{-3}$). This comparison was significant ($p<10^{-5}$), showing that "conventional" modeling performed poorer than our more advanced single-channel models (and, by statistical inference, also poorer than our multiple-channel models and models that utilized 52 s training durations). Figure 8.5 displays a representative elbow torque profile, along with the torque predicted using the best "conventional" method, best single-channel unwhitened method and best multiple-channel whitened method.

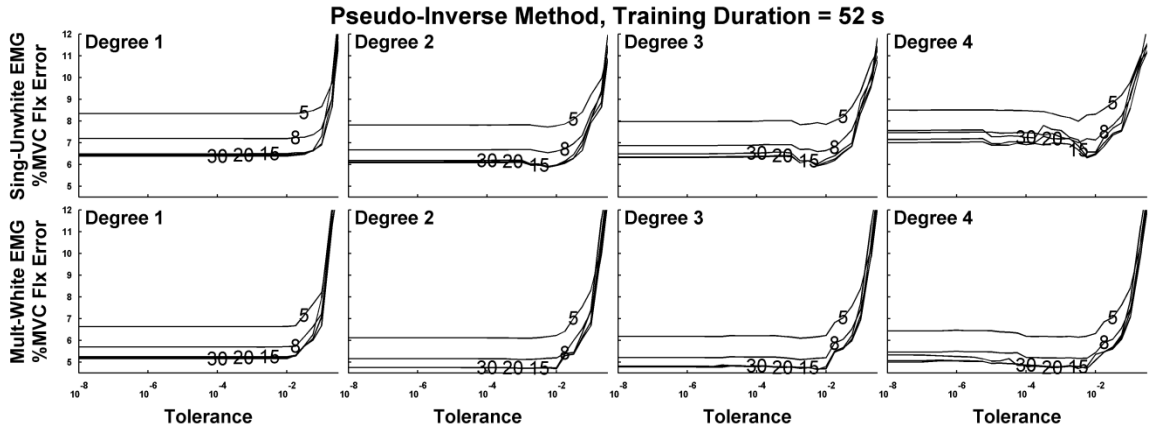

Figure 8.4. EMG-torque error as a function of tolerance value, using the **pseudo-inverse** system identification method, with **52 s of training data**. Results for tolerance values below 10^{-8} not shown, but follow similar trend. Each row shows results from the two EMG processors; columns distinguish the different polynomial model degrees (*D*). Each plot shows the results for representative dynamic model orders (*Q*) 5, 8, 15, 20 and 30, as labeled. Each result is the average from 33 subjects.

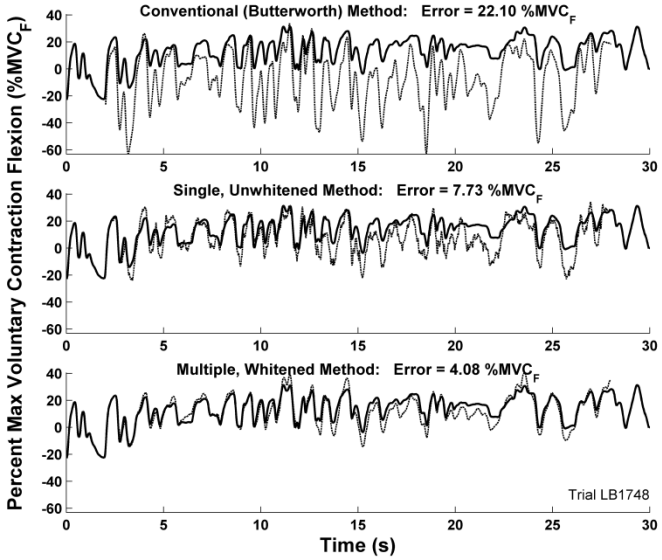

Figure 8.5. Representative sample of actual and estimated elbow torque as a function of time. Solid line in each graph is the actual torque, scaled to percent maximum voluntary contraction flexion (%MVC$_F$), for the same 30 s contraction trial. Positive values denote flexion torque. Dotted line in each plot shows torque estimated by training a model to distinct trials, then using EMG to estimate torque from this trial. Top: estimate from best "conventional" method (1.3 Hz cutoff frequency); Middle: Best single-channel unwhitened method (2^{nd}-degree polynomial, 18^{th}-order dynamic model, pseudo-inverse tolerance of 5.6×10^{-3}, 52 s training); Bottom: Best multiple-channel whitened method (3^{rd}-degree polynomial, 28^{th}-order dynamic model, pseudo-inverse tolerance of 5.6×10^{-3}, 52 s training). Estimated torques omit approximately 2 s from beginning and end of trial to account for filter start-up transients.

8.4 Discussion

Though models with a small number of parameters risk missing significant relationships in the data, over-fitting poses an obstacle to parameter identification in models with a large number of parameters. Factors known to decrease the severity of over-fitting include: training sets with higher SNR, larger training sets, model structures with fewer parameters, and system identification techniques that are robust with respect to training set noise and correlated features. In this study, several clear trends emerged from the methodological comparisons performed.

First, the multiple-channel whitened EMG processor was again demonstrated to improve EMG-torque estimation. It is well established that these methods decrease the variability of the EMG estimate [Hogan 1980a, Hogan 1980b, Clancy 1994a, Clancy 1994b, Clancy 1997, Clancy 2001, Clancy 2002, Clancy 2006, Clancy 2007, Staudenmann 2007 and Potvin 2004], hence increasing the SNR in the training and testing sets. Anecdotally, whitening seemed to provide the clearest performance improvement in this study. While multiple-channel EMG processors offer improved performance in many situations, problems can arise if even one of the raw EMG signals contains a large amount of noise [Clancy 1994b]. In addition, in less constrained contractions, multiple electrodes placed longitudinally across a muscle group might need to be modeled as separate electrical sources (rather than being combined into one EMG) [Staudenmann 2009 and Vieira 2010].

Second, increasing the training set duration from 26 s to 52 s provided a clear improvement, with considerably lower test errors and reduced sensitivity to the number of model parameters. A larger data set helps to reduce the influence of training set noise, because parameter estimates are averaged over more training samples. Training from multiple trials can also help average trial-to-trial variations in posture, since joint angle affects the EMG-torque relation [Hassan 1985, Doheny 2008 and Vrendenbregt 1973]. For example, the single-channel unwhitened results based on a 26 s training duration (Figure 8.1) show that test set error grows as dynamic model order is increased above approximately 15^{th}-order, for nonlinear polynomial degrees of D=3 and 4. However, when a 52 s training duration was used with the single-channel unwhitened data (Figure 8.4), the error was lower and remained so at higher model orders. Interestingly, the

multiple-channel whitened results for first- and second-degree polynomial models with 26 s training duration (Figure 8.1) do not exhibit the upward trend in error at high model orders. Thus, one might be convinced that adequate training had occurred without over-fitting. However, the corresponding 52 s training set results shown in Figure 8.4 still exhibit substantially lower errors. Thus, the fact that error ceases to vary as model order increases does not necessarily indicate that an optimal model has been found. Further reduction in EMG-torque error might be realized using even longer training sets or more training trials.

Third, the Weiner model results were consistently poorer than those of the nonlinear polynomial models. The Hammerstein models exhibited performance close to, but not as good as, the best nonlinear polynomial models. Because the Hammerstein and Weiner models contain fewer coefficients, it is possible that they simply did not capture the full complexity of the true EMG-torque relationship. These reduced parameter models might be advantageous in situations where only short durations of training data (i.e., less than 26 s) are available.

Fourth, with the nonlinear polynomial model (D=2 or 3), system identification using the best pseudo-inverse tolerance gave performance similar to that of the best ridge method. However, the range of pseudo-inverse tolerances over which a nearly optimal fit occurred ($\sim 10^{-16} < Tol < 10^{-2}$) was much wider than the range of ridge k values for its near-optimal fit ($1 < k < 10^{3}$). Hence, the pseudo-inverse method may be less sensitive and easier to tune. Results also indicate tolerance/ridge k value tuning is more critical when the data are more susceptible to over-fitting, i.e., for short duration training sets, single-channel unwhitened EMG processing, high nonlinear degree and high dynamic model order. Note that the tolerance value and ridge *k* value were fixed in this analysis, then studied as a function of the fixed value. It is possible that better performance is available by adapting the tolerance/ridge *k* value based on information within each training set. Anecdotal analysis suggests that the optimal ridge *k* value for individual subjects ranged across five orders of magnitude. Indeed, selection of a ridge *k* value is often performed based on case-by-case (graphical) evaluation of a "ridge trace" [Jones 1972, Hoerl 1970 and Marquardt 1975]. Herein, manual evaluation of the ridge trace was not compatible with

automated calibration of the EMG-torque relationship. But, automated algorithms for ridge trace evaluation might be considered in the future.

Note that our experimental situation is limited (constant-posture) and does not mimic fully dynamic, unconstrained motion. In addition, most daily movement activities of the upper limb encompass a smaller range of effort levels [Kern 2001] and may not mimic the bandwidth investigated herein. However, improvement due to advanced EMG□ processing should apply to the more complex movement cases since a lower variance signal is produced. In addition, there is considerable evidence of inter-subject variability in EMG-torque/force relationships as, for example, a function of joint angle [Hassan 1985, Doheny 2008 and Vredenbregt 1973]. Hence, attention to system identification methods for calibrating to these differences should also be useful. Nonetheless, most EMG-torque applications will require that the results of this study be appropriately translated to, and verified with, more dynamic and unconstrained motions. The relative impact of reducing EMG amplitude variance and improving model accuracy can vary between applications.

Taken together, the several techniques utilized in this study provide a substantial improvement over typical EMG-torque performance. The best "conventional" estimator provided an error of 19.15±11.15% MVC flexion. The merging of advanced EMG□ processors (whitening and multiple-channel combination), more complex EMG-torque models (e.g., nonlinear polynomial model) and robust system identification techniques (pseudo-inverse/ ridge regression, longer duration training sets) reduced the EMG-torque error in these constant-posture, torque-varying contractions to 4.65±3.6% of MVC flexion, a substantial performance improvement. These results should be informative to applications such as clinical biomechanics, EMG/neural control of powered prostheses, ergonomic analyses, motor control and powered exoskeletons.

Chapter 9

System identification of non-linear, dynamic EMG-torque relationship about the elbow

Lukai Liu[1], Pu Liu[1], Daniel V. Moyer[2] and Edward A. Clancy[1]

[1]ECE Dept., Worcester Polytechnic Institute, Worcester. MA, USA.

[2]Genasys Inc., Menlo Park, CA, USA.

This chapter has been published: **Lukai Liu**, **Pu Liu**, **Daniel V. Moyer** and **Edward A. Clancy**, "System Identification of Non-linear, Dynamic EMG-torque Relationship about the Elbow," *2011 IEEE 37th Annual Northeast Bioengineering Conference*, Rensselaer Polytechnic Institute, 1–3 April, 2011. Available: http://ieeexplore.ieee.org/xpls/abs_all.jsp?arnumber=5778638

Abstract—The surface electromyogram (EMG) from biceps/triceps muscles of 33 subjects was related to elbow torque, contrasting EMG amplitude (EMGσ) estimation processors, linear/non-linear model structures and system identification techniques. EMG-torque performance was improved by: advanced (i.e., whitened, multiple-channel) EMGσ processors; longer duration training sets (52 s vs. 26 s); and determination of model parameters via the use of the pseudo-inverse and ridge regression methods. Best performance provided an error of 4.65% maximum voluntary contraction (MVC) flexion.

9.1 Introduction

The surface EMG has often been used in prosthesis control, ergonomics analysis and clinical biomechanics. We applied advanced EMGσ estimates (whitening, multiple-channel combination) and different parametric model structures to the EMG-torque problem to reduce torque estimation error. The present study examined system identification methods for non-linear, dynamic EMG-torque models which utilized advanced EMGσ processors and explicitly addressed model over-fitting. Four system identification concepts were compared. First, Hammerstein and Weiner model structures were specifically selected to have a small number of parameters [Ljung 1999]. Second,

we investigated the fitting of model parameters via least squares, utilizing the singular value decomposition-based pseudo-inverse approach [Press 1994]. Third, we evaluated least squares estimation using ridge regression [Jones 1972]. Fourth, we increased the duration of the training data.

9.2 Methods

9.2.1 Experimental data and methods

Experimental data from 33 subjects from two prior studies ([Clancy 1999 and Clancy 200]) were reanalyzed. The WPI IRE stipulated that supervision was not required. A subject was secured into the seat of a Biodex exercise machine with their right shoulder abducted 90^0, their forearm oriented in a parasaggital plane, the wrist fully supinated and the elbow flexed 90°. The subject was rigidly attached to the Biodex dynamometer with a cuff at the styloid process. An array of four EMG electrode-amplifiers was placed transversely across each of the biceps and triceps muscles. Signals were sampled at 4096 Hz at 16-bit resolution. Twelve force-varying contraction trials of 30 s duration were recorded during which the subjects used a feedback signal to track a computer-generated target that moved on a screen as a band-limited (1 Hz) uniform random process, spanning 50% MVC extension to 50% MVC flexion. Eight trials per subject were used to fit model coefficients and four distinct trials were used for testing. Only test trial results are presented.

9.2.2 Methods of analysis

Two distinct EMGσ processors were created from each of the extension and flexion muscle groups for each 30 s trial-single-channel unwhitened and four-channel whitened [5]. EMGσ and torque signals were decimated by a factor of 100 to a sampling rate of 40.96 Hz.

Extension and flexion EMGσs were related to joint torque using four parametric, dynamic model structures. For each structure, m was the decimated discrete-time sample index, $T[m]$ was the measured torque; a_0 was an offset parameter; e_q and f_q were the extension and flexion fit parameters, respectively; and $\sigma_E[m]$ and $\sigma_F[m]$ were the extension and flexion EMGσ estimators, respectively. The model structures were:

1. Linear time invariant (LTI) FIR system of order Q.
2. Polynomial non-linear model of degree D, order Q:

$$T[m] = a_0 + \sum_{d=1}^{D}\sum_{q=0}^{Q} e_{q,d}\sigma_E^d[m-q] + \sum_{d=1}^{D}\sum_{q=0}^{Q} f_{q,d}\sigma_F^d[m-q] \qquad (9.1)$$

3. Hammerstein model (D^{th}-order polynomial static nonlinearity cascaded with a Q^{th}-order, LTI, FIR system).
4. Wiener model (Q^{th}-order, LTI, FIR system cascaded with a D^{th}-order polynomial static non-linearity).

The LTI system order ranged from $1 \leqslant Q \leqslant 30$ and the polynomial degree ranged from $1 \leqslant D \leqslant 4$. Two seconds of data were excluded from the beginning and end of each 30 s trial.

Three approaches were evaluated to reduce least squares over-fitting. First, the singular value decomposition-based pseudo-inverse was used, in which the reciprocals of small singular values were replaced with zero. Forty tolerance values ranged logarithmically from 10^{-16} to 0.5. The offset term a_0 was not used. Second, ridge regression [3] was used and the offset term a_0 was included in the model. Ridge parameter k ranged logarithmically from 10^{-7} to 10^{4} in 112 values. Third, the duration of data available to the least squares fit was altered between 26 s or 52 s.

9.3 Results

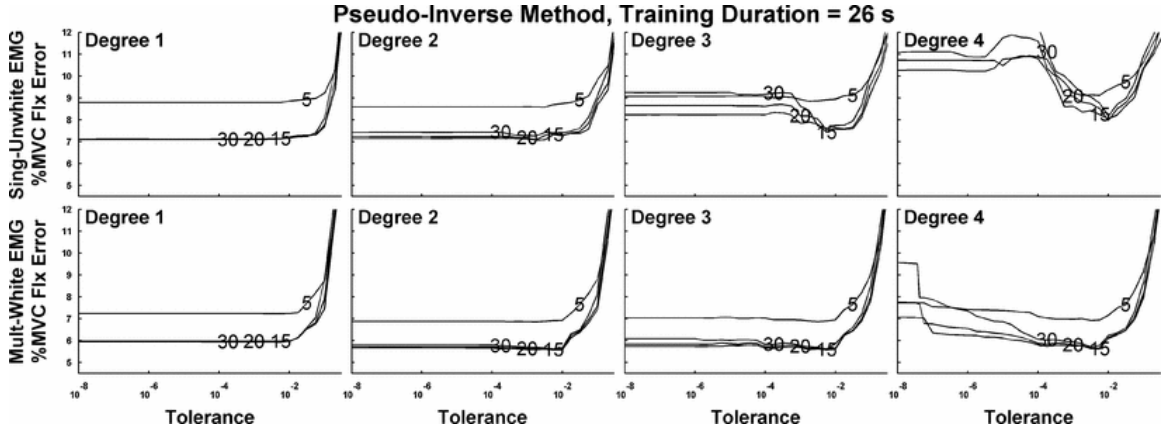

Figure 9.1. EMG-torque errors vs. tolerance value for **pseudo-inverse** system identification method, **26 s of training data**. Results for tolerance values below 10^{-8} not shown, but follow similar trend. Rows plot results from the two different EMGσ processors; columns distinguish polynomial model degrees (D). Each plot shows the results for representative model orders (Q) 5, 15, 20 and 30, as labeled. Each result is average of 132 test trials (33 subjects × 4 test trials/subject)

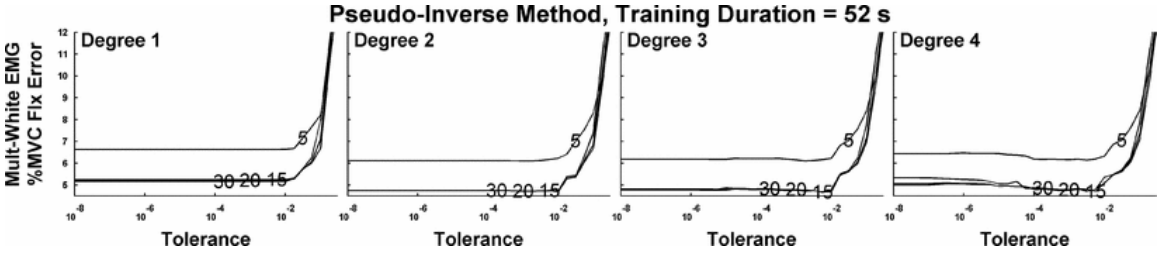

Figure 9.2. EMG-torque errors vs. tolerance value for pseudo-inverse system identification method, 52 s of training data. Plot details similar to Figure 9.1, except only results from the multiple-channel, whitened EMGσ processor are shown

Figures 9.1–9.2 show representative aspects of the overall results. Models which utilized a low linear model order (e.g. $Q \leq 5$) exhibited high error. High model order often also led to higher error, particularly for high polynomial model degrees and with single-channel unwhitened EMGσ processors (or their combination). Excessively large pseudo-inverse tolerance values and ridge k values exhibited poor performance.

Although results are not shown here, the Weiner models were clearly inferior to the polynomial non-linear model. Hammerstein model results were also inferior to the pseudoinverse and ridge regression results, but only mildly so. The best pseudo-inverse results (4.65% MVC flexion; D=3, Q=28, Tol=5.6×10^{-3}, 52 s training set, multiple whitened EMGσ) were not statistically different (p=0.5; paired sign test) than the best ridge regression results. Error was consistently reduced by fitting with a longer duration training set (52 s).

9.4 Discussion

The multiple-channel whitened EMGσ processor was again demonstrated to improve EMG-torque estimation. Increasing training set duration from 26 s to 52 s provided a clear improvement, with less sensitivity to the number of model parameters. Surprisingly, this improvement occurred even if the corresponding 26 s duration error did not vary much as a function of model order. Even though Weiner models contained the same number of coefficients as equivalent Hammerstein models, their results were consistently poorer. Hammerstein models exhibited performance close to that of the non-linear polynomial models. With the non-linear polynomial model, the best pseudo-inverse tolerance gave performance similar to that of the best ridge method. However, the range of pseudo-inverse tolerances over which a nearly optimal fit occurred (~$10^{-16} < Tol < 10^{-2}$) was wider than the range of ridge values for its near optimal fit ($1 < k < 10^3$).

The merging of advanced EMGσ processors (whitening, multiple-channel combination), more complex EMG-torque models (e.g., non-linear polynomial model) and robust system identification techniques (pseudo-inverse/ ridge regression, longer duration training sets) has reduced the EMG-torque error to 4.65% of MVC flexion-a substantial improvement over previous EMG-torque models.

Chapter 10

Influence of joint angle on EMG-torque model during constant-posture, quasi-constant-torque contractions

Pu Liu[1], Lukai Liu[1], Francoise Martel[2], Denise Rancourt and Edward A. Clancy[1]

[1]ECE Dept., Worcester Polytechnic Institute, Worcester. MA, USA.

[2]Sherbrooke University, Quebec J1K2R1, Canada.

This chapter has been published: **Pu Liu**, **Lukai Liu**, **Francoise Martel**, **Denise Rancourt** and **Edward A. Clancy**, "Influence of Joint Angle on EMG-Torque Model during Constant-Posture, Quasi-Constant-Torque contractions," *Journal of Electromyography and Kinesiology*, vol. 23 (5), pp. 1020-1028, 2013. Available: http://www.sciencedirect.com/science/article/pii/S1050641113001661

Abstract—Electromyogram (EMG)–torque modeling is of value to many different application areas, including ergonomics, clinical biomechanics and prosthesis control. One important aspect of EMG–torque modeling is the ability to account for the joint angle influence. This manuscript describes an experimental study which relates the biceps/triceps surface EMG of 12 subjects to elbow torque at seven joint angles (spanning 45–135°) during constant-posture, quasi-constant-torque contractions. Advanced EMG amplitude (EMGσ) estimation processors (i.e., whitened, multiple-channel) were investigated and three non-linear EMGσ–torque models were evaluated. When EMG–torque models were formed separately for each of the seven distinct joint angles, a minimum "gold standard" error of 4.23 ± 2.2% MVC_{F90} resulted (i.e., error relative to maximum voluntary contraction at 90° flexion). This model structure, however, did not directly facilitate interpolation across angles. The best model which did so (i.e., parameterized the angle dependence), achieved an error of 4.17 ± 1.7% MVC_{F90}. Results demonstrated that advanced EMGσ processors lead to improved joint torque estimation. We also contrasted models that did vs. did not account for antagonist muscle co-contraction. Models that accounted for co-contraction estimated individual flexion muscle

torques that were ~29% higher and individual extension muscle torques that were ~68% higher.

Keywords—Biological system modeling; Electromyography; EMG amplitude estimation; EMG signal processing; Joint angle influence

10.1 Introduction

The surface electromyogram (EMG) provides a non-invasive measure of muscle activation and hence has been used to estimate muscle tension and joint torque (see [Staudenmann 2010] for a recent review) [An 1983, Clancy 2006, Clancy 2012, Clancy 1997, Doheny 2008, Gottlieb 1971, Hasan 1985, Heckathorne 1981, Hof 1981, Hogan 1980b, Lawrence 1983, Messier 1971, Potvin 2004, Sanger 2007, Shin 2009, Solomonow 1986, Staudenmann 2009, Thelen 1994 and Vredenbregt 1973]. EMG–torque models have application in ergonomics, clinical biomechanics and prosthesis control [Disselhorst-Klug 2009, Doorenbosch 2003, Hagg 2004, Kumar 1996, Mathiassen 1995 and Parker 2006]. These models aim to emulate the natural relationship between the central nervous system and peripheral joints/muscles. This relationship must account for changes in muscle length/joint angle for several reasons, including the muscle length-tension relationship, muscle moment arms and the relative positioning of recording electrodes with respect to the underlying muscle and innervation zone [Martin 2006, Messier 1971, Rack 1969 and Zajac 1989].

Limited studies have been conducted over the years to model the influence of joint angle on the EMG–torque relationship. Vredenbregt and Rau's [Vredenbregt 1973] classic single-subject study of biceps muscles (more recently supported by the work of Doheny et al. [Doheny 2008]) suggests that this EMG–torque relationship may only change by a multiplicative gain factor as a function of joint angle. That is, the *shape* of the EMG–torque relationship is the same at each joint angle, but a distinct gain scales this shape for each angle. Vredenbregt and Rau did not account for agonist-antagonist co-contraction, although Solomonow et al. [Solomonow 1986] have shown antagonist muscle activity to be considerable (antagonist EMG amplitude levels often 10–20% that of the agonist). An additional modeling concern is that Hasan and Enoka [Hasan 1985] have shown that the EMG–torque variation across angle changes considerably person-to-

person, with the angular location of the force peak varying up to 50°. Each of the above three studies utilized constant-posture, constant-torque contractions. These results suggest that EMG–torque models should account for both individual subject differences, as well as agonist and antagonist muscles.

Advanced EMG amplitude (EMGσ—the time-varying standard deviation of the EMG waveform) processing techniques have been developed over the last few years, incorporating multiple-channel combination and whitening. Improved EMGσ estimates produce decreased EMG–torque error, as do improvements to system identification (i.e., model selection and fitting procedures) [Clancy 2002, Clancy 2006, Clancy 2012, Clancy 2000, Clancy 1995, Clancy 1997, Hogan 1980a, Hogan 1980b, Potvin 2004, Sanger 2007, Staudenmann 2010 and Thelen 1994]. These advances have not been incorporated into EMG–torque modeling when multiple joint angles are considered. The purpose of this study was to systematically investigate the influence of elbow joint angle on EMG–torque modeling during constant-posture, quasi-constant-torque contractions, while incorporating advanced EMGσ processors and muscular co-activation.

10.2 Methods

10.2.1 Experimental data and methods

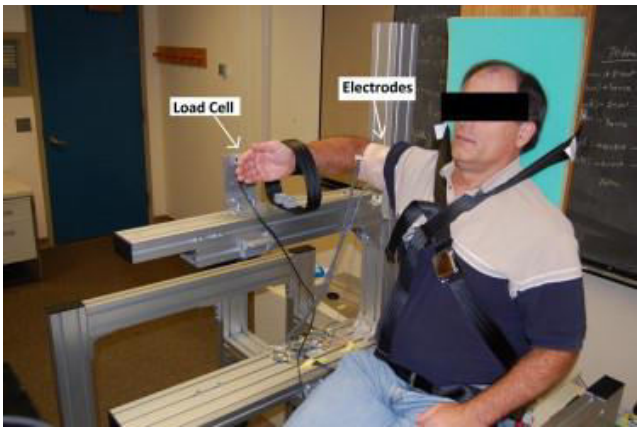

Figure 10.1 Experimental apparatus. The subject's right arm is oriented in a plane parallel to the floor, the upper arm is directed laterally outward from the shoulder, and the angle between the upper arm and the forearm is selectable, but fixed (shown here at 90°). EMG electrodes are mounted over the biceps and triceps muscles. The wrist is tightly cuffed to a load cell at the level of the styloid process.

Experiments were approved and supervised by the WPI IRB. All subjects provided written informed consent. Experimental data were acquired from 12 healthy subjects (9

male, 3 female; aged 18–52 years). Subjects were strapped into a custom-built straight-back chair (shown in Figure 10.1) with their right shoulder abducted 90°, their forearm oriented in a parasaggital plane, the wrist fully supinated (palm perpendicular to the floor) and the wrist tightly cuffed to a load cell (Vishay Tedea–Huntleigh Model 1042, 75 kg full scale). The angle between the upper arm and the forearm was selectable, but fixed. Skin above the muscles under investigation was cleaned with an alcohol wipe and a small bead of electrode gel was massaged into the overlying skin. Six bipolar EMG electrode-amplifiers were placed transversely across each of the biceps and triceps muscle groups, midway between the elbow and the midpoint of the upper arm, this positioning being intended to avoid the tendon distally and the innervation zone proximally. Subjects were instructed to tense their muscles at both angular extremes (45°, 135°) to aid in visualizing the distal tendon and the muscle midpoint locations. EMG recording over the tendon is discouraged as it is not electrically active tissue and because our own experience finds this location prone to motion artifacts. Recording over the innervation zone (typically located near the muscle mid-point for the biceps and triceps) can lead to large swings in EMGσ values with small changes in location [Rainoldi 2000]. The electrodes were also centered on the muscle midline, to best avoid crosstalk from adjacent muscles. Each electrode-amplifier had a pair of 8 mm diameter, stainless steel, hemispherical contacts separated by 1 cm edge-to-edge, oriented along the muscle's long axis. The distance between adjacent electrode-amplifiers was ~1.75 cm. A ground electrode was gelled and secured on the upper arm. Custom electronics amplified and filtered each EMG signal (CMRR greater than 90 dB at 60 Hz; 8th-order Butterworth highpass at 15 Hz; 4th-order Butterworth lowpass at 1800 Hz) before being sampled at 4096 Hz with 16-bit resolution. The RMS EMG signal level at rest (representing equipment noise plus ambient physiological activity) was on average 2.9 ± 4.3% of the RMS EMG at 50% maximum voluntary contraction (MVC) at 90°.

All contractions were constant-posture, with the elbow angle selectable. Subjects were provided a warm-up period, then rested four minutes. MVCs were then measured. Subjects took 2–3 s to slowly ramp up to MVC and maintained that force for two seconds. The average load cell value during the contraction plateau was taken as the MVC. Both elbow extension and flexion MVC were measured at a joint angle of 90°. Ten second

duration, constant-force contractions at 50% MVC extension, 50% MVC flexion and at rest (arm removed from the wrist cuff) were next recorded at a joint angle of 90°. These contractions were used to calibrate advanced EMGσ estimation algorithms [Clancy 2000 and Prakash 2005]. Then, a sequence of constant-posture, quasi-constant-torque contractions was conducted at randomized elbow angles of 45°, 60°, 75°, 90°, 105°, 120° and 135°. Elbow angle was the included angle between the forearm and upper arm. At each angle, MVC torque was measured in both elbow extension and flexion. The average of these two MVC torques was denoted the torque range midpoint. Then, three tracking trials of 45 s duration were recorded during which the subjects used the load cell as a feedback signal to track a computer-generated torque target ramping at a constant absolute torque rate from the torque range midpoint, to 50% MVC flexion, to 50% MVC extension, back to 50% MVC flexion, and then back to the torque range midpoint. Two-three minutes of rest was provided between trials to avoid cumulative fatigue.

10.2.2 Methods of analysis

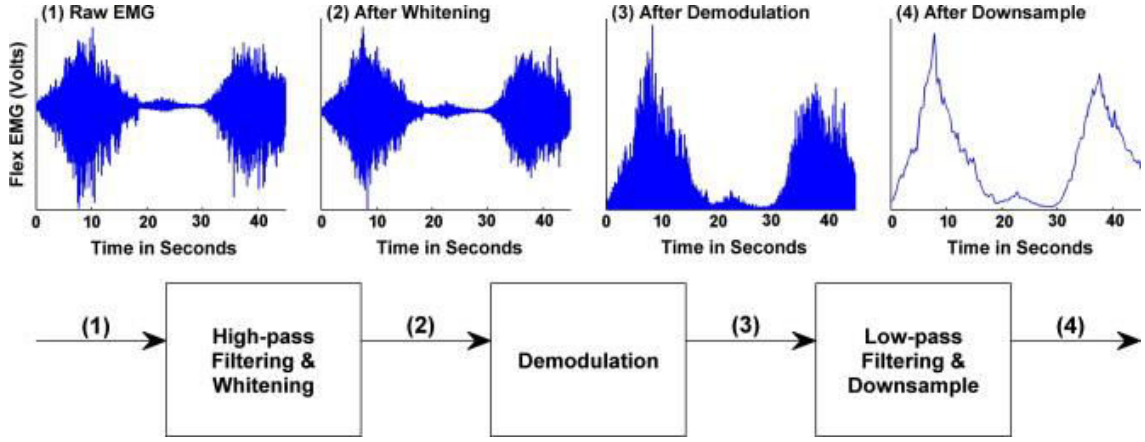

Figure 10.2 A single channel EMG signal (top plots) passing through various steps of EMGσ estimation (bottom plot). Data (45 s in duration) were collected from a biceps muscle channel at a joint angle of 90° for subject WY01. For simplicity, only one whitened channel is shown however, in practice, four channels were combined after demodulation whenever whitening was applied.

All analysis was performed offline in MATLAB. The sampled EMG data were notch filtered at the power line frequency and all harmonics (2nd-order IIR filter, notch bandwidth $\leqslant$0.5 Hz). Small amounts of power line interference, which can be larger in magnitude than the EMG signal power at high frequencies, can be inappropriately

accentuated due to the high gain of whitening filters at these frequencies. The narrow bandwidth of these notch filters eliminated this interference source, with limited decrease in the overall statistical bandwidth of the signal [Bendat 1971]. Next, two distinct EMGσ processors were created for each of the extension and flexion muscle groups for each 45 s trial. Estimators were either single-channel, unwhitened (using a centrally located electrode) or four-channel whitened (using the four centrally located electrodes). As depicted in Figure 10.2, each estimator utilized a 15 Hz highpass filter (5th-order Butterworth applied in the forward and reverse time directions to achieve zero phase) and a first-order demodulator (e.g., rectifier). Whitened channels used the non-causal adaptive whitening algorithm of Clancy and Farry [Clancy 2000]. After demodulation, signals were lowpass filtered at 1.6 Hz while being decimated by a factor of 1000, producing a resampled frequency of 4.096 Hz. The torque signal was similarly decimated, producing an EMG data set with a bandwidth approximately 10 times that of the torque signal being estimated [Ljung 1999]. This decimated sampling rate is best for system identification, being large enough to capture the system dynamics (the fundamental period of force variation was 45 s) and small enough to avoid noise existing out of the signal band [Clancy 2006 and Ljung 1999]. The original sampling rate of 4096 Hz is necessary for acquiring the raw EMG, but is not appropriate once an EMGσ estimate has been formed. The first and last 7.5 s of data were excluded from each 45 s trial to account for filter start-up transients.

The decimated extension and flexion EMGσ inputs were related to joint torque (output) using three non-linear polynomial model structures:

(1) Angle-specific model:

$$T[m] = \sum_{d=1}^{D} f_{d,\theta}\sigma_F^d[m] - \sum_{d=1}^{D} e_{d,\theta}\sigma_E^d[m] \tag{10.1}$$

(2) Flex-extend multiplicative model:

$$T[m] = \left(\sum_{a=0}^{A} g_{a,F}\theta^a[m]\right)\left(\sum_{d=0}^{D} f_{d,F}\sigma_F^d[m]\right) - \left(\sum_{a=0}^{A} g_{a,E}\theta^a[m]\right)\left(\sum_{d=0}^{D} e_{d,E}\sigma_E^d[m]\right) \tag{10.2}$$

(3) Single multiplicative model:

$$T[m] = \left(\sum_{a=0}^{A} g_a\theta^a[m]\right)\left(\sum_{d=1}^{D} f_d\sigma_F^d[m] - \sum_{d=1}^{D} e_d\sigma_E^d[m]\right) \tag{10.3}$$

where m was the decimated discrete-time sample index; T[m] was the measured torque; e_d and f_d were the extension and flexion fit parameters (which specified the *shape* of the EMGσ–torque relationship), respectively; $\sigma_E[m]$ and $\sigma_F[m]$ were the extension and

flexion EMGσ estimates, respectively; g_a were the angle fit parameters (which specified the multiplicative gain vs. joint angle); and θ was the elbow joint angle. The EMGσ polynomial degree was varied from $1 \leqslant D \leqslant 5$. The angle polynomial degree was varied from $1 \leqslant A \leqslant 5$. Both "*A*" and "*D*" were always the same for extension and flexion portions within any one model.

The "angle-specific" model estimated the extension and flexion fit parameters at the seven elbow joint angles separately, using linear least squares. The "flex-extend multiplicative" model contained two sets of gains (one each for extension and flexion activities) which were polynomial functions of elbow joint angle, and simultaneously estimated the extension and flexion fit parameters across the seven elbow angles. The multiplicative gain functions account for *all* factors associated with EMGσ–torque changes across angle, including muscle moment arms, muscle length–tension relationships, and movement of the electrodes with respect to the underlying muscles and innervation zones. The "single multiplicative" model was similar, except that it contained only one multiplicative gain function. Parameters of the flex-extend and single multiplicative models were estimated using non-linear least squares. For the multiplicative models, the inclusion of both EMGσ and angle polynomials resulted in one redundant overall scaling parameter. Anecdotally, this additional degree of freedom seemed to aid the least squares minimization, thus was retained. However, for consistency across angles, the angle polynomial was rescaled to a gain of one at 90° after the fit was complete, with a compensatory inverse scaling applied to the EMGσ polynomial.

Each subject completed three tracking trials at seven distinct angles. Seven trials, one per angle, were combined to form an analysis record (three per subject). The first analysis record was used as training data and the second as a test set. Then, the third record was used as training data and the second again used as the test set. The mean absolute difference between the actual torque and that predicted by the EMG–torque model was computed while the actual torque was between 40% MVC extension and 40% MVC flexion. Limiting the evaluation range reduces extrapolation errors due to trial-to-trial differences in actual torque [Clancy 1997]. The average of these two mean absolute difference values was reported as the test error value. All error values were normalized to

twice the torque at 50% flexion MVC at angle 90° (MVC_{F90}). Only test trial results are presented. For statistical analysis, test error values were subjected to a paired sign test [Miller 1977]. Eighty four values contributed to each sign test (seven angles × 12 subjects).

10.3 Results

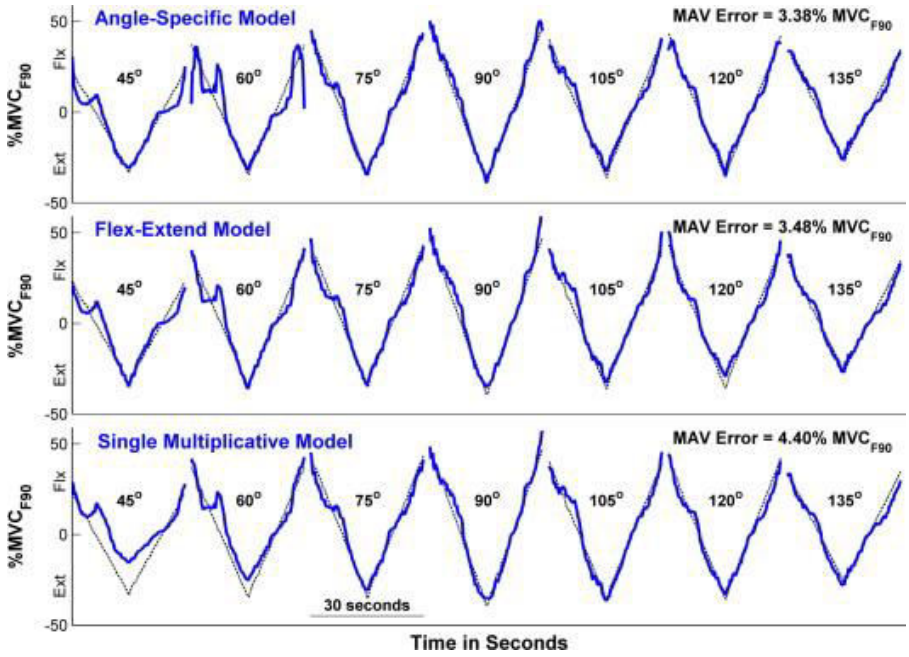

Figure 10.3. EMGσ–torque test results of estimated (solid line) and actual torque (dotted line) vs. time for seven elbow angles using three model structures (subject WY01). Data for each angle (30 s in duration, after exclusion of filter transients) were collected during distinct trials, then concatenated in the figure. Results use multiple-channel whitened EMGσ processing, the best EMGσ polynomial degree ($D = 3$ for the angle-specific model and $D = 2$ for the other two models) and an angle polynomial degree of $A = 2$.

Joint angle/	**Polynomial degree (*D*)**				
EMGσ	***D* = 1**	***D* = 2**	***D* = 3**	***D* = 4**	***D* = 5**
45°/					
Single, unwhite	8.43 ± 6.1	7.22 ± 7.2	7.12 ± 7.5	7.88 ± 11	9.92 ± 18
Multiple, white	7.44 ± 6.2	6.76 ± 7.2	6.34 ± 6.6	6.40 ± 7.3	7.12 ± 10
60°/					
Single, unwhite	7.52 ± 2.6	6.21 ± 3.1	5.96 ± 3.3	5.80 ± 3.3	5.84 ± 3.5
Multiple, white	6.94 ± 4.1	6.33 ± 5.8	6.18 ± 5.5	13.2 ± 30	35 ± 105
75°/					
Single, unwhite	6.64 ± 2.1	5.11 ± 1.8	4.83 ± 1.9	5.77 ± 5.4	11.1 ± 23
Multiple, white	5.45 ± 2.2	4.21 ± 1.7	3.99 ± 1.9	4.07 ± 2.5	4.73 ± 4.8

Joint angle/	Polynomial degree (D)				
EMGσ	$D = 1$	$D = 2$	$D = 3$	$D = 4$	$D = 5$
90°/					
Single, unwhite	5.89 ± 2.6	4.70 ± 1.8	4.59 ± 1.8	4.55 ± 1.8	4.61 ± 1.8
Multiple, white	5.14 ± 2.5	3.90 ± 1.6	3.63 ± 1.5	3.63 ± 1.5	3.71 ± 1.5
105°/					
Single, unwhite	5.04 ± 1.4	4.26 ± 1.3	4.16 ± 1.3	4.14 ± 1.2	4.14 ± 1.2
Multiple, White	4.32 ± 1.7	3.33 ± 1.5	3.29 ± 1.4	3.34 ± 1.5	3.32 ± 1.4
120°/					
Single, unwhite	5.46 ± 2.2	4.56 ± 2.0	4.58 ± 2.0	4.58 ± 2.2	4.65 ± 2.3
Multiple, white	4.12 ± 2.0	3.37 ± 1.6	3.35 ± 1.6	3.32 ± 1.6	3.45 ± 1.8
135°/					
Single, unwhite	3.94 ± 1.2	3.80 ± 1.1	3.79 ± 1.2	3.91 ± 1.4	4.05 ± 1.7
Multiple, white	2.95 ± 1.5	2.69 ± 1.3	2.80 ± 1.6	2.94 ± 2.0	3.69 ± 4.3
Overall/					
Single, unwhite	6.13 ± 2.1	5.12 ± 2.2	5.00 ± 2.2	5.23 ± 3.1	6.32 ± 6.6
Multiple, white	5.19 ± 2.4	4.37 ± 2.3	4.23 ± 2.2	5.27 ± 5.2	8.66 ± 16

Table 10.1. Angle-specific model: mean ± std. dev. EMG–torque error (% mean absolute MVC flexion at 90° from 12 test trials).

Figure 10.3 shows an example of the estimated torque and actual torque vs. time for seven elbow angles using the three different model structures. The angle-specific model was considered the "gold standard," since it optimized the model coefficients at each particular joint angle. It does not interpolate across angles. Table 10.1 gives the mean plus/minus standard deviation test error results for the angle-specific model for each combination of angle, model order and EMGσ processor. The bottom rows of the table list overall errors that collapse results across angle. Error was averaged across the seven angles for each subject, then the mean and standard deviation of these 12 values reported. The best overall performance was found using the multiple white EMGσ processor and polynomial degree $D = 3$, giving an error of $4.23 \pm 2.2\%$ MVC_{F90}. For all angles and EMGσ polynomial degrees, multiple-channel whitened processors consistently performed better than single-channel unwhitened, except for $D \geqslant 2$ at 60°. Statistically, results between the two EMGσ processors were compared for each EMGσ polynomial degree $1 \leqslant D \leqslant 5$. The multiple whitened processor was significantly better in all cases

($p < 0.001$). Note that the "Overall" results for $D \geqslant 2$ in Table 10.1 obscure this difference, due to the large errors associated with one subject at 60°. However, the *nonparametric* statistical analysis (paired sign test) confirms the difference. We next statistically compared the best ($D = 3$) multiple whitened processor results to the other multiple whitened processor results. Results for polynomial orders $D = 1$ and 2 were statistically inferior ($p < 0.001$), while results for $D = 4$ and 5 did not differ ($p > 0.07$).

A.P.D. (*A*)/	**EMGσ polynomial degree (*D*)**				
Model	***D* = 1**	***D* = 2**	***D* = 3**	***D* = 4**	***D* = 5**
A = 1/					
Flex-extend	5.55 ± 2.0	4.66 ± 1.5	4.94 ± 2.0	4.67 ± 1.9	5.26 ± 2.9
Single	6.90 ± 1.9	6.14 ± 1.7	6.67 ± 2.5	6.00 ± 1.7	6.92 ± 3.3
A = 2/					
Flex-extend	5.15 ± 2.2	4.17 ± 1.7	4.97 ± 2.9	4.85 ± 2.3	6.52 ± 3.7
Single	6.34 ± 2.2	5.65 ± 1.9	5.78 ± 2.1	6.11 ± 2.7	6.87 ± 2.9
A = 3/					
Flex-extend	5.26 ± 2.3	4.35 ± 1.8	6.25 ± 5.2	4.79 ± 2.8	28 ± 58
Single	6.50 ± 2.7	5.73 ± 2.0	7.06 ± 5.1	7.15 ± 4.3	15.6 ± 13
A = 4/					
Flex-extend	6.27 ± 2.4	5.24 ± 2.1	7.13 ± 5.4	28 ± 44	47 ± 118
Single	7.37 ± 3.1	6.41 ± 2.1	6.55 ± 2.5	9.67 ± 6.2	38 ± 74
A = 5/					
Flex-extend	14.7 ± 9.7	12.3 ± 7.4	12.0 ± 7.1	64 ± 154	282 ± 727
Single	9.31 ± 8.3	6.81 ± 2.9	8.08 ± 3.4	28 ± 62	33 ± 46

Table 10.2. Multiplicative models: mean ± std. dev. EMG–torque error (% mean absolute MVC flexion at 90° from 12 test trials). "A.P.D" = Angle Polynomial Degree.

Table 10.2 gives the mean plus/minus standard deviation test error results for the two multiplicative models, for only the multiple-channel whitened EMGσ processor. For each cell, error was averaged across the seven angles for each subject, then the mean and standard deviation of these 12 values reported. For both multiplicative models, when both D and A were high ($\geqslant 4$), the error became extremely large, likely due to over-fitting. Some over-fitting also may have occurred when only one of the two polynomial degrees was high (e.g., $D = 5$, $A = 3$). The best flex-extend model ($D = 2$, $A = 2$) had an error of 4.17 ± 1.7% MVC_{F90} and did not differ significantly from the best angle-specific model

($p = 0.29$). Figure 10.4 graphs an example set of flex-extend model fits for $D = 2$ and $A = 2$. Figure 10.5 graphs the gain functions for the flex-extend model (one per subject), again for $D = 2$ and $A = 2$. Considerable gain variation (exceeding a factor of two) exists across the span of angles studied. The best performance of the single multiplicative model ($D = 2$, $A = 2$) was 5.65 ± 1.9% MVC_{F90}, which was statistically different (poorer) than the best angle-specific model ($p < 0.001$) and the best ($D = 2$, $A = 2$) flex-extend model ($p < 0.001$).

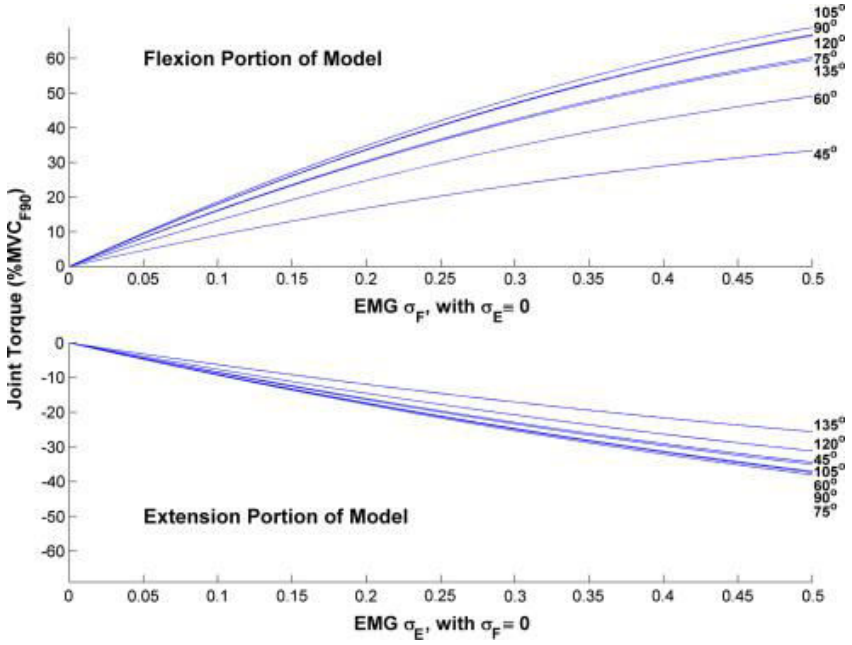

Figure 10.4. Flex-extend multiplicative model fits at each angle (subject WY04), using multiple white EMGσ processing, an EMGσ polynomial degree of $D = 2$ and an angle polynomial degree of $A = 2$. Plots provided for each of the seven joint angles (as labeled). Top plots formed from Eq. (10.2), while setting σ_E to zero and the multiplicative gains to one. Bottom plots formed from Eq. (10.2) while setting σ_F to zero and the multiplicative gains to one.

We also statistically compared EMGσ processors for the flex-extend model. The multiple white processor consistently produced lower errors ($p < 0.006$) when both polynomial degrees were three or less. For other polynomial degree combinations, results were either equivocal or not significant. However, these parameter combinations corresponded to higher errors and would not be utilized. Similarly, comparison between the two EMGσ processors with the single multiplicative model gave equivocal results particularly when the error was high.

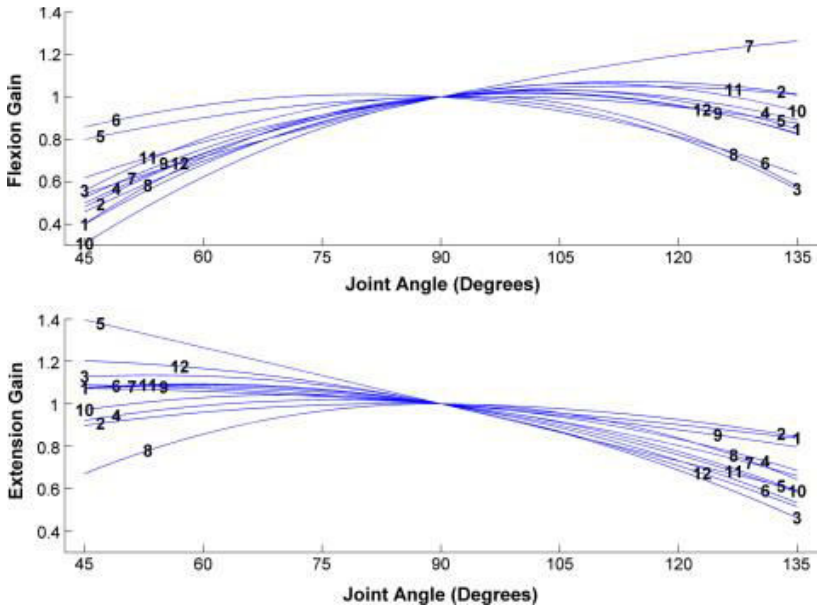

Figure 10.5. Flexion (top) and extension (bottom) gain functions vs. angle for the twelve subjects (numbered 1–12) with the flex-extend multiplicative model, using multiple white EMGσ processing, an EMGσ polynomial degree of $D = 2$ and an angle polynomial degree of $A = 2$. Note that the model requires a gain of one at joint angle 90°.

Model	EMGσ value			
	0.1	**0.2**	**0.3**	**0.4**
Flexion				
Co-contract	11.8 ± 2.5	22.7 ± 4.4	32.7 ± 5.8	41.8 ± 6.6
No co-contract	9.1 ± 3.0	17.6 ± 5.2	25.3 ± 6.6	32.3 ± 7.3
Extension				
Co-contract	14.2 ± 5.2	26.5 ± 9.6	37.0 ± 13.3	45.5 ± 16.5
No co-contract	8.2 ± 2.5	15.6 ± 4.3	22.2 ± 5.4	28.0 ± 6.2

Table 10.3. Mean ± std. dev. EMG-estimated muscle torque using models with and without co-contraction (% mean absolute MVC flexion at 90°). Results computed over all angles for 12 subjects.

Finally, we also produced flex-extend model EMGσ–torque relationships *without* accounting for muscular co-contraction by ignoring the antagonist muscle term in Eq. (10.2). Only parameters $D = 2$, $A = 2$ were considered. Within the flexion-dominant range of a tracking trial, we related flexion EMGσ to joint torque; and similarly for the extension-dominant portion of a tracking trial. Figure 10.6 shows an example result ($D = 2$ and $A = 2$). At every angle, *each* subject's model (flexion or extension) that accounted for co-contraction estimated higher muscle torques at every EMGσ value. We

then computed the model-estimated EMGσ–torque with vs. without modeling co-contraction at normalized EMGσ values of 0.1, 0.2, 0.3 and 0.4 (where 1.0 denotes the EMGσ value at MVC), separately for each of the flexion and extension portions of the models. For each subject, results were averaged across the seven angles. Table 10.3 gives the mean plus/minus standard deviation results, computed across the 12 subjects. For flexion, the models with co-contraction estimated ~29% more torque. For extension, the models with co-contraction estimated ~68% more torque.

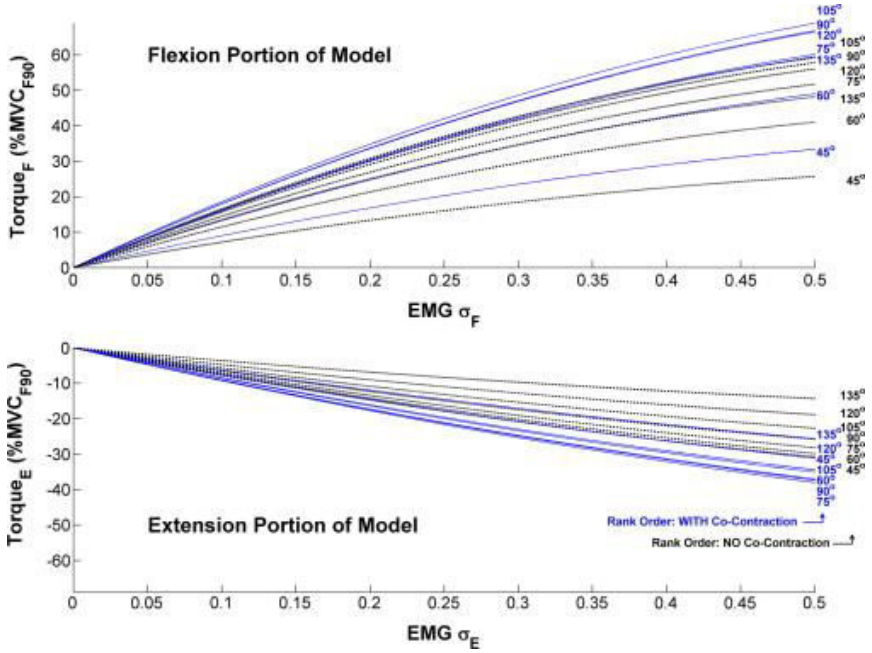

Figure 10.6. EMGσ–torque relationship with (solid lines) and without (dotted lines) accounting for muscle co-contraction. An EMGσ polynomial degree of $D = 2$ and an angle polynomial degree of $A = 2$. Plots provided for each of the seven joint angles (subject

10.4 Discussion

We examined three non-linear models for relating EMGσ to joint torque at different joint angles during constant-posture, slowly-torque-varying (quasi-constant-torque) contractions, as well as the role of advanced EMGσ processors and muscular co-activation. Rather clear distinctions emerged. The advanced EMGσ processing technique that combined whitening and multiple channels consistently provided an approximate 15–20% performance improvement, compared to unwhitened single-channel performance, for the better model structures. Although EMG performance differences were equivocal for the poorer performing model structures, these models would not be selected for use. These improvement results are consistent with past experimental evaluations [Clancy

1995, Clancy 1997, Clancy 2012, Hogan 1980b, Potvin 2004 and Prakash 2005], reflecting that a lower variance EMGσ signal used as the input to system identification produces lower modeling errors. There are, however, some possible drawbacks to using multiple recording channels, including: increased hardware costs; the risks that artifacts on only one channel can greatly degrade the entire EMGσ estimate [Clancy 1995]; and the possibility during less constrained contractions that the many electrodes should not be combined into one EMGσ, but should be represented as distinct electrical sources/muscle compartments [Staudenmann 2009 and Vieira 2010].

The particular model structures chosen for evaluation in this study were strongly influenced by prior literature in this field. Vredenbregt and Rau [Vredenbregt 1973] suggested that the constant-posture EMGσ–torque relation only varies by a multiplicative gain as a function of angle. These prior experiments, however, did not account for possible muscle co-activation and could not benefit from more recent advances in EMGσ processing. Thus, we selected two models that included multiplicative gain as a function of angle. Angle-dependent gain was implemented via a polynomial, consistent with the expectation of a singly-peaked function [Hasan 1985]. The EMGσ–torque relationship at a given angle was also implemented via a polynomial [Clancy 1997 and Vredenbregt 1973]. These models considered muscular co-activation and were calibrated from contraction trials that included both flexion-dominant and extension-dominant contraction.

The optimal EMGσ polynomial degree for the angle-specific model was $D = 3$, consistent with prior work [Clancy 1997]. The EMGσ–torque relationship shown in Figure 10.4, however, is much closer to a straight line than that typically plotted in the literature, at least for the biceps muscles [Lawrence 1983 and Vredenbregt 1973]. One reason for this difference is that we only used efforts up to 50% MVC. Past studies have shown the relationship to be mostly straight over this region, with a more curved (non-linear) shape at higher effort levels. The dependence of gain on joint angle (Figure 10.5) did not consistently exhibit a singly-peaked function as might have been anticipated [Hasan 1985]. Modeling muscle co-contraction likely influenced this shape, e.g., flexion gain was calibrated from both flexion-dominant and extension-dominant torques. In addition, subjects generally produced lower absolute torque at the extreme joint angles

(see Figure 10.3). Thus, the least squares parameter fit criterion would have given more influence to those joint angles closest to 90°, perhaps reducing the influence of the more extreme angles.

Figure 10.6 and Table 10.3 show the constant-posture EMGσ–torque relationship with and without consideration of muscle co-contraction. As expected, models that do not account for co-contraction estimate lower flexion and extension muscle torque contributions, likely underestimating true muscle torque contributions. This error is substantial: for flexion, the models with co-contraction estimated ~29% more torque; for extension, the models with co-contraction estimated ~68% more torque. Unfortunately, studies that ignore co-contraction are generally blind to this error. Least squares selection of the fit coefficients will reliably match agonist EMG to agonist-direction torque (e.g., biceps EMG to flexion-direction torque). *Net* joint torque will be appropriately estimated, but internal torques (i.e., the flexion and extension muscle torque contributions) will not—in fact, no antagonist torque is even considered. Of course, such models render large errors if the antagonist muscle activity changes from that which was experienced during calibration of the model. In most EMGσ–torque studies, subjects are asked to minimize muscle co-contraction. Doing so is advantageous from a system identification perspective, so as to most independently excite all modes of a system. But, real-life contractions will not always preserve the same level of co-contraction. If joint impedance were to be volitionally increased by subjects, one would expect even larger errors. For example, purposeful co-contraction to increase impedance is common in many tasks wherein the endpoint limb segment must be stabilized [Rancourt 2001]. Hence, modeling of muscular co-contraction is essential for generalization of an EMGσ–torque model.

It is not surprising that high degree multiplicative gain functions performed significantly poorly, particularly when the EMGσ polynomial model order was high. Data from only seven distinct angles were acquired experimentally. Hence, high angle polynomial degrees (A) would be expected to lead to over-fitting. One interesting solution to this problem would be to separately calibrate the angular dependence and the EMGσ dependence. That is, an angle-specific EMGσ–torque polynomial model might be calibrated at one reference angle (e.g., 90°) and these coefficients fixed. Thereafter, data could be collected while the joint angle was slowly varied across angle (quasi-constant-

torque). The coefficients of the angle function could then be independently calibrated. In doing so, many more angle values would be available, perhaps leading support to a higher degree angle polynomial. This calibration technique would also require far less data collection. The reduced number of required contractions might further permit repeated training trials for each contraction, which might lead to even lower model error [Clancy 2012]. Note that many subjects found it awkward to orient their elbow to the 45° joint angle and related difficulty in producing torque at this angle. This orientation might be outside the range of angles that need be considered in future research.

The fixed posture and avoidance of dynamic force changes in these experiments simplified study of the EMGσ–torque relationship versus joint angle, but may require caution when applying the results in less constrained application areas. Our intent was to limit the number of variables studied and concentrate on the role of joint angle. It would, therefore, be appropriate to reduce these postural and force limitations in future studies, transitioning towards EMGσ–torque models in more dynamic, unconstrained contractions. For example, when joint angle is allowed to vary dynamically (not the case in this study), EMGσ–torque models will likely need to differ as a function of eccentric vs. concentric contraction [Komi 2000]. Also, our sample size in this study was limited (12 subjects) and predominantly male. Larger and more diverse subject pools can aid in the development of EMGσ–torque models that are representative of different body types (e.g., height, weight, arm strength) as well as differences that are more specific to EMG signal acquisition and processing (e.g., arm circumference, amount of subcutaneous fat, relative composition of fast- vs. slow-twitch fibers).

These results extend the classic results of Vredenbregt and Rau [Vredenbregt 1973] by considering muscular co-activation, applying optimized EMGσ estimates, evaluating alternative models, quantifying the angular dependence and providing rigorous statistical support of all results from multiple subjects. In practice, the results provide strong support that the constant-posture, constant-torque EMGσ–torque relationship about the elbow maintains the same *shape* across angles, differing only by a multiplicative gain factor as a function of angle. Further, a polynomial function is sufficient to model the necessary gain vs. angle. Figure 10.5, for example, could be used to develop normative gain vs. angle functions, or better results would be expected if these functions are fit to

each subject (as performed in this work). In prosthetics, these results suggest that more natural control of a powered elbow might be provided if the gain between EMG and motor torque were adjusted as a function of the elbow angle. In ergonomic and biomechanical analyses, these results provide a model form in order to account for the angle dependence, which should lead to better tracking of predicted joint torques.

Lastly, this work quantifies the differences in estimated internal muscle tensions with vs. without consideration of muscular co-contraction. The differences are quite large, suggesting that co-activation about the joint must be considered in musculoskeletal models. Formally, doing so is best approached by quantifying joint mechanical impedance. That is, net torque about the joint is related to the *difference* between flexion and extension torques, while impedance about the joint is related to the *sum* of the flexion and extension torques. Simultaneously quantifying both joint torque and impedance provides a more complete mechanical description of the joint. Rigorous methods for relating EMG to joint impedance are just now emerging in the literature [Pfeifer 2012].

In summary, EMGσ–torque models were formed during constant-posture, slowly force-varying contractions ranging in joint angle from 45° to 135°, while modeling muscular co-activation. Advanced EMGσ processing, including signal whitening and multiple channel combination, provided consistent performance improvements for the better models. A gold standard model was calibrated at each specific angle using a polynomial EMGσ–torque relationship. A third-degree polynomial produced the lowest estimation error of 4.23 ± 2.2% MVC_{F90}. Models were also formed in which the angular dependence was parameterized via a multiplicative gain function written as a polynomial. When distinct gains were applied to each of flexion and extension, the best performance (EMGσ polynomial degree of two, angle polynomial degree of two) was 4.17 ± 1.7% MVC_{F90}. Models which did not account for co-contraction were compared to those that do so. Flexion torque was ~29% higher and extension torque was ~68% higher in the models which included co-contraction. Thus, failure to account for antagonist muscle activity can considerably underestimate individual muscle torques.

10.5 Conflict of interest

None of the authors is aware of any conflict of interest associated with this work or its submission to the Journal of Electromyography and Kinesiology.

Chapter 11

EMG-torque estimation of constant-posture, quasi-constant-torque contractions at varied joint angles

Pu Liu[1], Lukai Liu[1], Francoise Martel[2], Denise Rancourt and Edward A. Clancy[1]

[1]ECE Dept., Worcester Polytechnic Institute, Worcester. MA, USA.

[2]Sherbrooke University, Quebec J1K2R1, Canada.

This chapter has been published: **Pu Liu**, **Lukai Liu**, **Francoise Martel**, **Denise Rancourt** and **Edward A. Clancy**, "EMG-torque Estimation of Constant-posture, Quasi-constant-torque Contractions at Varied Joint Angles," *2011 IEEE 37th Annual Northeast Bioengineering Conference*, Rensselaer Polytechnic Institute, 1–3 April, 2011. Available: http://ieeexplore.ieee.org/xpls/abs_all.jsp?arnumber=5778635

Abstract—This paper describes an experimental study which relates the simultaneous biceps/triceps surface electromyogram (EMG) of 12 subjects to elbow torque at seven joint angles during constant-posture, quasi-constant-torque contractions. Advanced EMG amplitude (EMGσ) estimation processors were investigated, and an EMG-torque model considering agonist and antagonist co-contractions was evaluated at each joint angle. Preliminary results show that advanced (i.e., whitened, multiple-channel) EMGσ processors lead to improved joint torque estimation and that the EMGσ torque relationship may only change by a scaling factor as a function of joint angle.

11.1 Introduction

A significant literature has developed around the problem of relating the surface EMG to muscle tensions and joint torque. However, most investigators have not accounted for muscle co-contractions by assuming that an agonist muscle can be contracted while the antagonist muscle is inhibited [Vredenbregt 1973 and Woods 1983]. Also, there are clear advances in EMGσ processing techniques over the last few years [Clancy 2000], yet little have been incorporated into EMG-torque estimation. The present study investigated the EMG-torque problem by modeling agonist-antagonist co-

contractions over a wide range of joint torques at seven different angles, and also applied advanced EMGσ processing techniques (whitening, multiple-channel combination).

11.2 Methods

11.2.1 Experimental data and methods

Similar experimental apparatus and methods are described in detail elsewhere [Clancy 1997 and Clancy 2000]. Briefly, experimental data from 12 healthy subjects (9 male, 3 female; aged 18–52 years) were analyzed. A subject was secured into a custom-built straight-back chair with their right shoulder abducted 90^0, their forearm oriented in a parasaggital plane, the wrist fully supinated (palm perpendicular to the floor) and the wrist tightly cuffed to a load cell (Vishay Tedea-Huntleigh Model 1042). The angle between the upper arm and the forearm was selectable, but fixed. An array of six EMG electrode-amplifiers was placed transversely across each of the biceps and triceps muscle groups to record EMG signals. Signals were sampled at 4096 Hz at 16-bit resolution. A sequence of constant-posture, quasi-constant-torque contractions was conducted at elbow angles of 45°, 60°, 75°, 90°, 105°, 120° and 135°. The order of the angles was randomized. At each angle, three tracking trials of forty-five second duration were recorded during which the subjects used a feedback signal to track a computer-generated target linearly ramping slowly in time between 50% MVC flexion and 50% MVC extension. Additionally, subjects performed ten second duration 50% MVC and rest trials (0% MVC), used to calibrate the advanced EMGσ processors.

11.2.2 Methods of analysis

The sampled EMG data were notch filtered at the power line frequency and all harmonics, and then two different EMGσ processors were contrasted. Processor 1 was the "conventional" single-channel, unwhitened processor which used EMG recordings from a centrally located electrode. The EMG signal was high-pass filtered at 15 Hz and then rectified. Processor 2 was a four-channel, whitened processor. Each channel was similarly high-pass filtered, adaptively whitened prior to rectification [Clancy 2000], and then normalized and ensemble averaged. Prior to use in model fits, EMGσ and torque signals were effectively low-pass filtered at 3.3 Hz and decimated by a factor of 1000 (resulting sampling rate of 4.096 Hz).

The decimated extension and flexion EMGσ (inputs) were related to joint torque (output) using a degree *D* polynomial non-linear model:

$$T[m] = \sum_{d=1}^{D} e_{d,\theta}\sigma_E^d[m] + \sum_{d=1}^{D} f_{d,\theta}\sigma_F^d[m] \quad (11.1)$$

A train-test paradigm was utilized in which the model coefficients were determined using linear least squares from a training trial and then used to "predict" the torque from a distinct test trial [Ljung 1999]. An error signal was obtained from the difference between the predicted and actual test trial torque. All errors were normalized to twice the torque at 50% flexion MVC at joint angle 90°. To quantify these errors, we used the mean absolute error (MAE) computed for each testing trial, and took the median of 24 MAEs (12 subjects × 2 test trials per angle) at each joint angle.

11.3 Preliminary Results

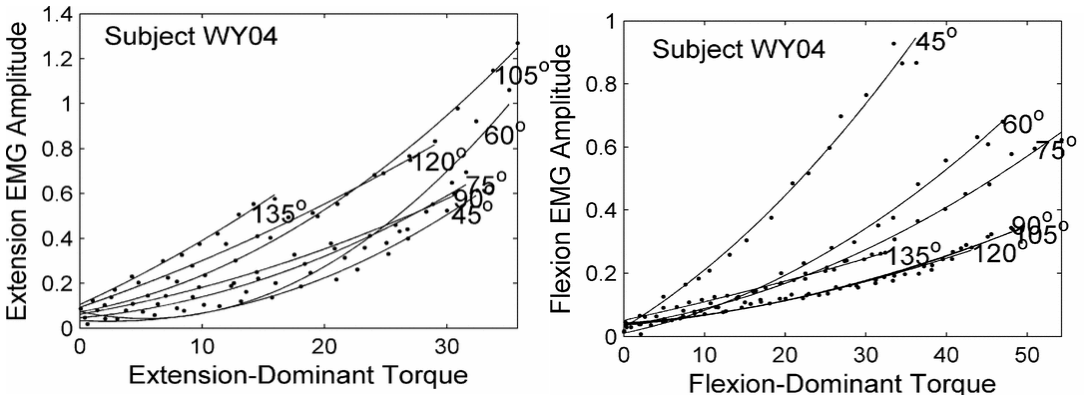

Figure 11.1. EMGσ estimation shown as a function of normalized extension (left) and flexion (right) dominant joint torque at seven joint angles for subject WY04. The dots are real data and the solid lines are the second-degree polynomial fits, using multiple-channel, whitened EMGσ processor

Figure 11.1 shows the normalized joint torque vs. EMGσ during extension-dominant (top) and flexion-dominant (bottom) portions of the tracking task at seven different joint angles for subject WY04. The EMGσ-torque curves at different joint angles exhibit a similar shape but different gains. The EMGσ-torque curves were also generated for the other 11 subjects, and this observation was consistent across the subjects.

Table 11.1 provides the summary results of analysis of median errors between the predicted and actual torques from all subjects, at seven different joint angles, when the polynomial degree ranged from $1 \leq D \leq 5$, and using two distinct EMGσ processors. For each joint angle and polynomial degree, the four-channel whitened processor produced a lower median error than the signal-channel unwhitened processor.

Joint Angle/ EMGσ Processor	Polynomial Degree (D) $D = 1$	$D = 2$	$D = 3$	$D = 4$	$D = 5$
45°					
Single, Unwhite	6.79%	5.27%	4.87%	4.71%	4.70%
Multiple, White	5.35%	4.65%	4.22%	4.32%	4.33%
60°					
Single, Unwhite	6.53%	5.14%	5.09%	4.96%	4.73%
Multiple, White	5.69%	4.23%	3.96%	4.08%	3.88%
75°					
Single, Unwhite	5.76%	4.39%	4.19%	4.21%	4.10%
Multiple, White	4.80%	3.36%	3.07%	2.88%	2.88%
90°					
Single, Unwhite	5.06%	4.60%	4.18%	3.98%	3.91%
Multiple, White	4.59%	3.38%	3.15%	3.30%	3.29%
105°					
Single, Unwhite	4.78%	4.21%	4.23%	4.12%	4.02%
Multiple, White	4.18%	3.22%	3.16%	3.21%	3.26%
120°					
Single, Unwhite	4.86%	4.22%	4.19%	4.17%	4.17%
Multiple, White	3.33%	2.90%	2.86%	2.79%	2.69%
135°					
Single, Unwhite	4.13%	3.75%	3.73%	3.68%	3.66%
Multiple, White	2.46%	2.26%	2.24%	2.23%	2.26%

Table 11.1. EMG-torque error (percent of mean absolute MVC flexion at 90°). Each result is the median of 24 test trials (12 subjects × 2 trials/subject)

11.4 Discussion

First, advanced EMGσ estimation was applied to the EMG-torque problem at multiple joint angles for constant-posture, quasi-constant-torque contractions about the elbow. Results from 12 subjects showed that the multiple-channel whitened EMGσ processor consistently produced improved EMG-torque estimation. Depending on the joint angle, use of the multiple-channel whitened EMGσ processor with higher polynomial degrees produced a median error that was 50%-66% that found when using the single-channel, unwhitened EMGσ processor with a polynomial degree of D=1. Second, the EMGσ-torque curves of individual subjects, viewed across multiple joint angles, indicated that the relationship between EMGσ and joint torque might be multiplicative as a function of angle [Vredenbregt 1973]. Therefore, EMG-torque models might be calibrated at certain joint angles and then applied to other angles via only a change in model gain.

Chapter 12

Influence of joint angle on EMG-torque model during constant-posture, quasi-constant-torque contractions

Pu Liu[1], Lukai Liu[1], and Edward A. Clancy[1]

[1]ECE Dept., Worcester Polytechnic Institute, Worcester. MA, USA.

This chapter has been published: **Pu Liu**, **Lukai Liu** and **Edward A. Clancy**, "Influence of Joint Angle on EMG-Torque Model during Constant-Posture, Quasi-Constant-Torque Contractions," *IEEE Transactions on Neural Systems and Rehabilitation Engineering*, vol. 23 (6), pp. 1039-1046, 2015. Available: http://ieeexplore.ieee.org/xpls/abs_all.jsp?arnumber=7046403

Abstract—Relating the electromyogram (EMG) to joint torque is useful in various application areas, including prosthesis control, ergonomics and clinical biomechanics. Limited study has related EMG to torque across varied joint angles. We related the biceps-triceps surface EMG of 22 subjects to elbow torque at six joint angles (spanning 60^o to 135^o) during constant-posture, torque-varying contractions. Three nonlinear EMGσ-torque models, advanced EMG amplitude (EMGσ) estimation processors (i.e., whitened, multiple-channel) and the duration of data used to train models were investigated. When EMG-torque models were formed separately for each of the six distinct joint angles, a minimum "gold standard" error of 4.01 ± 1.2% MVC_{F90} resulted (i.e., error relative to maximum voluntary contraction at 90^o flexion). This model structure, however, did not directly facilitate interpolation across angles. The best model which did so, achieved a statistically equivalent error of 4.06 ± 1.2% MVC_{F90}. Results demonstrated that advanced EMGσ processors lead to improved joint torque estimation as do longer model training durations.

Keywords—Biological system modeling, electromyography, electromyogram (EMG) amplitude estimation, electromyogram (EMG) signal processing, joint angle influence.

12.1 Introduction

For several decades, the surface electromyogram (EMG) has seen extensive investigation as a non-invasive measure that can be used to estimate muscle tension and/or joint torque (see Staudenmann et al. [Staudenmann 2010] for a recent review) [An 1983, Clancy 2006, Clancy 1997, Clancy 2012, Doheny 2008, Gottlieb 1971, Hasan 1985, Hashemi 2012, Hashemi 2013, Heckathorne 1981, Hof 1981, Hogan 1980b, Inman 1952, Lawrence 1983, Liu 2013b, Messier 1971, Potvin 2004, Sanger 2007, Shin 2009, Solomonow 1986, Staudenmann 2009, Thelen 1994 and Vredenbregt 1973]. A common approach is to estimate the EMG standard deviation (EMGσ, a.k.a. EMG amplitude) from one or more sites on muscles about a joint, and then use system identification techniques to model an EMGσ-torque relationship. These non-invasive estimates are used in prosthesis control [Parker 2006], clinical biomechanics [Disselhorst-Klug 2009 and Doorenbosch 2003] and ergonomics analysis [Hagg 2004, Kumar 1996 and Mathissen 1995]. Numerous system identification approaches have been successfully applied, with most studies now accounting for agonist-antagonist co-activation [Solomonow 1986] and individual subject differences in the EMG-torque relationship [Hasan 1985]. Because EMG is a stochastic signal, methods which lower the variance of EMGσ estimates—e.g., whitening and multiple-channel combination—have been shown to lower EMG-torque errors, as have improved system identification methods [Clancy 1995, Clancy 1997, Clancy 2000, Clancy 2002, Clancy 2006, Clancy 2012, Hashemi 2012, Hashemi 2013, Hogan 1980a, Hogan 1980b, Potvin 2004, Sanger 2007, Staudenmann 2010 and Thelen 1994].

A topic with more limited investigation is the role of joint angle. The EMG-torque relationship changes with angle, at least due to the length-tension relationship [Rack 1969 and Zajac 1989], changes in muscle moment arms [Messier 1971] and the movement of electrodes with respect to underlying muscle tissue and the innervation zone [Martin 2006 and Rainoldi 2000]. Vredenbregt and Rau [Vredenbregt 1973], as well as more recent studies [Doheny 2008, Hashemi 2013 and Liu 2013b], found evidence of a multiplicative influence of angle on EMG-torque, at least during constant-torque contractions at various torque levels. That is, the EMG-torque curve has the same shape at each angle, but is scaled by a gain factor that is distinct for each angle.

In this study, we report on continued improvements to EMG-torque processing, with an emphasis on the influence of joint angle. Our primary contribution focuses on extending the experimental conditions to *force-varying* contractions conducted over a range of fixed joint angles. We specifically investigated the appropriateness of extending the multiplicative model vs. joint angle to force-varying contractions. We also compared standard EMGσ processing to advanced processors that include signal whitening and multiple channel combination. Finally, two areas of system identification were contrasted. First, we contrasted linear dynamic models to nonlinear dynamic models. Second, the duration of data available for model training has seen limited evaluation [Clancy 2012 and Hahne 2014]. Hence, we also evaluated this modeling variant.

12.2Methods

12.2.1 Experimental data and methods

Experiments were approved and supervised by the WPI IRB. Experimental data were acquired from 22 healthy subjects (12 male, 10 female; aged 18–56 years), each of whom provided written informed consent. Subjects were seated and strapped into a custom-built straight-back chair (see Fig. 1 of [Liu 2013b]) with their right shoulder abducted 90^{o}, their forearm oriented in a parasaggital plane, and their supinated wrist (palm perpendicular to the floor) tightly cuffed to a load cell (Vishay Tedea-Huntleigh Model 1042, 75 kg full scale). The angle between the upper arm and the forearm was fixed, but selectable. Skin above the biceps and triceps muscles was cleaned with an alcohol wipe and a bead of electrode gel was massaged into the overlying skin. Six bipolar EMG electrode-amplifiers were applied in a row, transversely across each of the biceps and triceps muscle groups, midway between the elbow and the midpoint of the upper arm (to avoid the innervation zone proximally and the tendon distally). Only the middle four of each set of six were analyzed. Subjects were instructed to tense their muscles at both angular extremes (60^{o}, 135^{o}) to aid in visualizing the distal tendon and the muscle midpoint locations. EMG recording over the tendon is discouraged because the tissue is not electrically active and prone to motion artifacts. Recording over the innervation zone (typically located near the muscle mid-point) can lead to large variations in EMGσ values with small changes in location [Rainoldi 2000]. The center of the row of electrodes was aligned with the muscle midline, to best avoid crosstalk from adjacent muscles. Each

electrode-amplifier had a pair of 8 mm diameter, stainless steel, hemispherical contacts separated by 1 cm edge-to-edge, oriented along the muscle's long axis. The distance between adjacent electrode-amplifiers was ~1.75 cm. A ground electrode was gelled and secured on the upper arm. Custom electronics amplified and filtered each EMG signal (CMRR > 90 dB at 60 Hz; 8th-order Butterworth highpass at 15 Hz; 4th-order Butterworth lowpass at 1800 Hz) before being sampled at 4096 Hz with 16-bit resolution. The RMS EMG signal level at rest (representing equipment noise plus ambient physiological activity) was on average 2.4 ± 2.5% of the RMS EMG at 50% maximum voluntary contraction (MVC) at 90^o, using the full available frequency range. For comparison to a more common bandwidth found in commercial EMG electrodes, the resting signal was digitally lowpass filtered at 500 Hz (2nd-order Butterworth), and this RMS noise measure was 2.2 ± 2.5% of RMS EMG at 50% MVC.

All contractions were constant-posture, with the elbow angle selectable. Subjects were provided a warm-up period, then rested three minutes. Separate extension and flexion MVCs were then measured at a joint angle of 90^o. Subjects took 2–3 seconds to slowly ramp up to MVC and maintained that force for two seconds. The average load cell value during the contraction plateau was taken as the MVC. Five second duration, constant-force contractions at 50% MVC extension, 50% MVC flexion and at rest (arm removed from the wrist cuff) were next recorded at 90^o. These contractions were used to calibrate advanced EMGσ estimation algorithms [Clancy 2000 and Prakash 2005]. Then, a sequence of constant-posture, torque-varying contractions was conducted at randomized elbow angles (the included angle between the forearm and upper arm) of 60^o, 75^o, 90^o, 105^o, 120^o and 135^o. At each angle (other than 90^o), MVC torque was measured in both elbow extension and flexion. Then, four tracking trials of 30 s duration were recorded during which the subjects used the load cell as a feedback signal to track a computer-generated torque target. The target moved on the screen in the pattern of a bandlimited (1 Hz) uniform random process, spanning 50% MVC extension to 50% MVC flexion. Two minutes of rest were provided between trials to avoid cumulative fatigue. A total of 24 tracking trials were recorded (four trials for each of six angles).

12.2.2 Methods of analysis

Analysis was performed offline in MATLAB. The sampled EMG signals were notch

filtered at the power line frequency and its harmonics (2nd-order IIR comb filter designed, notch bandwidth ≤ 0.5 Hz each, dual-pass filtered—filter applied in the forward, then reverse time directions to achieve zero phase), since whitening at high frequencies is particularly susceptible to signal interference; and then each signal was highpass filtered (15 Hz cutoff, 5th-order Butterworth filter designed; duel-pass filtered). Next, two distinct EMGσ variations were created for each of the extension and flexion muscle groups for each 30 s trial. Estimators were either single-channel, unwhitened (using a centrally located electrode) or four-channel whitened (using the four centrally located electrodes). Whitened channels used the non-causal adaptive whitening algorithm of Clancy and Farry [Clancy 2000] and Prakash et al. [Prakash 2005]. After optional whitening, each processor utilized a first-order demodulator (rectifier). Thereafter, signals were lowpass filtered at 16 Hz then downsampled by a factor of 100 to 40.96 Hz. The torque signal was similarly decimated, producing an EMG data set with a bandwidth approximately 10 times that of the torque signal being estimated. This decimated sampling rate is best for system identification, being large enough to capture the system dynamics and small enough to avoid noise existing out of the signal band [Clancy 2006 and Ljung 1999]. The first and last 2 s of data were excluded from each 30 s trial to account for filter startup and tail transients.

The decimated extension and flexion EMGσ inputs were related to joint torque (output), comparing three dynamic nonlinear polynomial model structures. First, a dynamic model was fit separately at each joint angle, providing the *angle-specific model*:

$$T[m] = \sum_{d=1}^{D} \sum_{q=0}^{Q} f_{d,q,\theta} \sigma_F^d[m-q] - \sum_{d=1}^{D} \sum_{q=0}^{Q} e_{d,q,\theta} \sigma_E^d[m-q] \qquad (12.1)$$

where m was the decimated discrete-time sample index; $T[m]$ the measured torque; D the EMGσ polynomial degree (varied from D=1–4, where D=1 produced a linear model); Q the number of time lags (Q=20) [Clancy 2012]; θ the elbow joint angle; $f_{d,q,\theta}$ and $e_{d,q,\theta}$ the flexion and extension fit parameters, respectively (which specified the *shape* of the EMGσ-torque relationship); and $\sigma_{F[m]}$ and $\sigma_{E[m]}$ the flexion and extension EMGσ estimates, respectively. This model was fit using linear least squares, regularized via the pseudo-inverse; if the ratio of the largest to a given singular value in the design matrix was less than 0.0056, that singular value was omitted [Clancy 2012 and Press 1994]. This angle-specific model served as the performance "gold standard."

Second, a model which incorporated the hypothesized gain variation in the form of polynomial gain vs. angle functions (one for flexion and another for extension) provided the *polynomial-gain model*:

$$T[m] = \left(\sum_{a=0}^{A} g_{a,F}\theta^{a}[m]\right)\left(\sum_{d=1}^{D}\sum_{q=0}^{Q} f_{d,q}\sigma_{F}^{d}[m-q]\right) - \left(\sum_{a=0}^{A} g_{a,E}\theta^{a}[m]\right)\left(\sum_{d=1}^{D}\sum_{q=0}^{Q} e_{d,q}\sigma_{E}^{d}[m-q]\right) \quad (12.2)$$

where $g_{a,F}$ and $g_{a,E}$ were the flexion and extension angle fit parameters, respectively (which specified the multiplicative gain vs. joint angle). The angle polynomial degree was varied from A=1–4. Note that the dynamic fit coefficients, $f_{d,q}$ and $e_{d,q}$, were fixed across angle (i.e., *not* a function of angle). This model was fit using nonlinear least squares. The initial dynamic parameters ($f_{d,q}$ and $e_{d,q}$) were those of the angle-specific model at 90°. The initial angle parameters were then found by fixing the dynamic parameters and solving for the $g_{a,F}$ and $g_{a,E}$ parameters via linear least squares (*simultaneously* across all angles). The full nonlinear model was then minimized across all angles. The inclusion of both angle and EMGσ polynomials resulted in one redundant overall scaling parameter. Anecdotally, this additional degree of freedom seemed to aid the least squares minimization, thus was retained. However, for consistency across models, the angle polynomial was rescaled to a gain of one at 90° after the fit was complete, with a compensatory inverse scaling applied to the EMGσ polynomial. This model immediately interpolates the gain function across all joint angles.

The third model simplified the gain vs. angle relation by utilizing distinct flexion and extension gains at each angle. This *piece-wise-gain model* is:

$$T[m] = g_{\theta,F}\left(\sum_{d=1}^{D}\sum_{q=0}^{Q} f_{d,q}\sigma_{F}^{d}[m-q]\right) - g_{\theta,E}\left(\sum_{d=1}^{D}\sum_{q=0}^{Q} e_{d,q}\sigma_{E}^{d}[m-q]\right) \quad (12.3)$$

where gain parameters $g_{\theta,F}$ and $g_{\theta,E}$ were designated at each of the six angles (total of 12 angle parameters). Again, note that the dynamic fit coefficients were fixed across angle. This model was fit using nonlinear least squares. The initial dynamic parameters ($f_{d,q}$ and $e_{d,q}$) were those of the angle- specific model at 90°. The initial angle parameters could then be found by fixing the dynamic parameters and solving for the $g_{\theta,F}$ and $g_{\theta,E}$ parameters via linear least squares (each pair fit *separately* at each angle). The full nonlinear model (angle parameters and dynamic parameters) was then simultaneously minimized across all angles, and then normalized to a gain of one at 90°. This model did *not* facilitate immediate gain interpolation across angle. However, gain vs. angle interpolations which preserve the exact gain values at the measured angles (e.g., spline

functions) can be fit *post hoc* to provide EMG-torque at any angle.

Each subject completed four tracking trials at six distinct angles. Six trials, one per angle, were combined to form an analysis record (four per subject). Initially, one record was used for training and a second record for testing. The mean absolute difference between the test torque and that predicted by the EMG-torque model was computed. This difference excluded the first and last 2 s (due to filter startup and tail transients) as well as an additional 488 ms startup transient due to the Q=20 order dynamic filter. Error values were normalized to twice the torque at 50% flexion MVC at angle 90° (MVC_{F90}). The average test trial error from all 12 possible single-record train-test combinations (full cross-validation) was reported for each subject. Next, two records were used for training and two for testing, with full cross-validation (12 combinations). Finally, three records were used for training and one for testing (four combinations). For statistical analysis, test error values were subjected to a paired sign test [Miller 1977]. Twenty two paired values contributed to each sign test (22 subjects).

12.3 Results

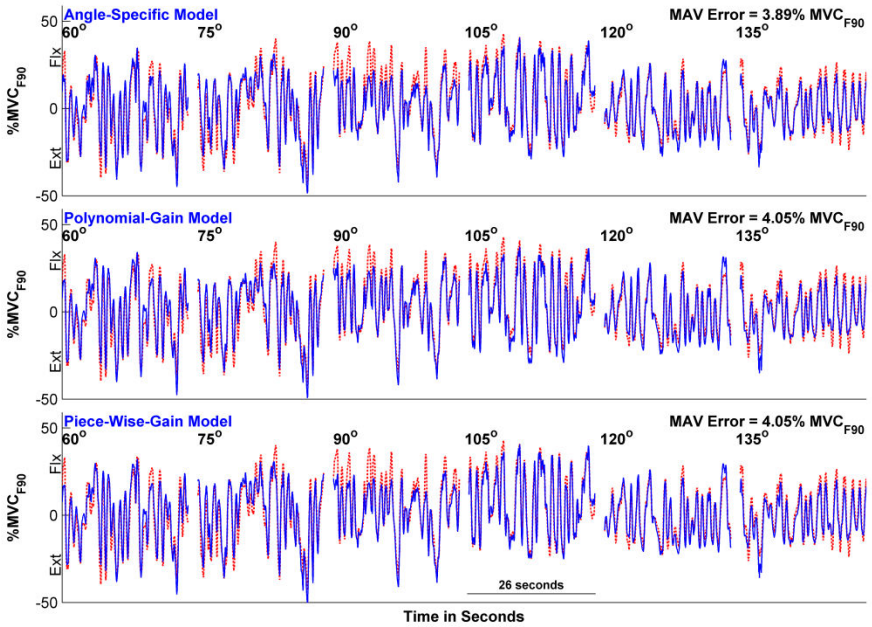

Figure 12.1. Sample EMGσ-torque estimation results for the three models. Estimated torque (solid blue line) and actual torque (dotted red line) vs. time. Data for each angle (26 s in duration, after exclusion of transients) were collected during distinct trials, then concatenated in the figure. Results use multiple-channel whitened EMGσ processing, three training records (78 s), and the D and A selections providing the lowest overall average errors (see Table 12.2).

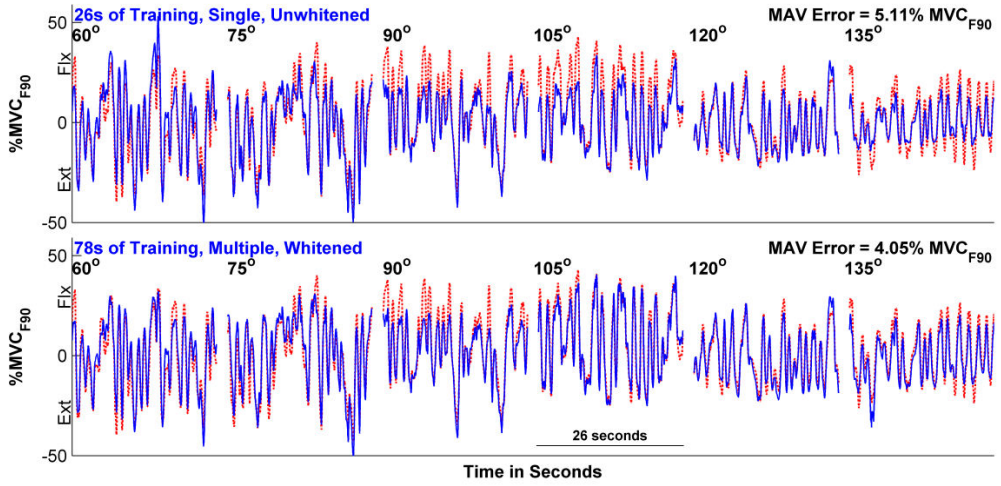

Figure 12.2. Top: Sample EMGσ-torque results for the shortest (26 s) training duration, piece-wise gain model, using single-channel unwhitened EMGσ processing and a D=2 nonlinear dynamic model (20th order). Bottom: Sample EMGσ-torque results for the longest (78 s) training duration, piece-wise gain model, using multiple-channel whitened EMGσ processing and a D=3 nonlinear dynamic model (20th order). In each plot, estimated torque shown in solid blue line, actual torque shown in dotted red line.

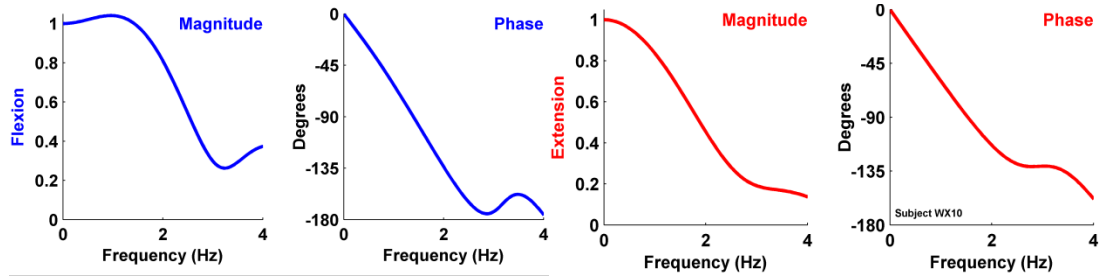

Figure 12.3. Sample frequency response from the flexion (left two) and extension (right two) portions of a linear (D=1) model fit. Piece-wise-gain model, using multiple channel whitened EMGσ and three training records (78 s). Model fit uses data from all joint angles.

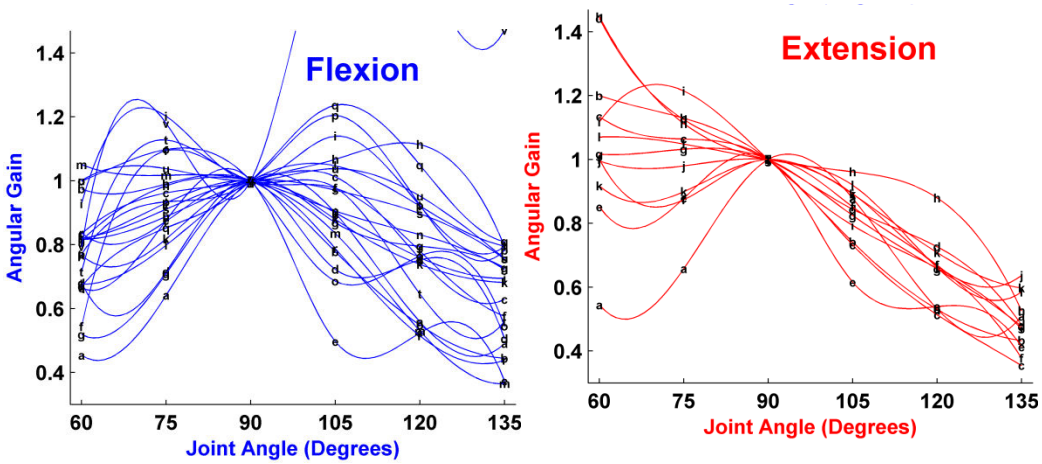

Figure 12.4. Flexion (top) and extension (bottom) angular gain functions vs. angle for the 22 subjects (different plot marker per subject), for the piece-wise-gain model, polynomial degree D=3, three training records (78 s). Markers show model gains at the measured angles, lines show cubic spline interpolations. Note that the model imposes a gain of one at joint angle 90°.

Records Used to Train	Angle Degree (A)	EMGσ Polynomial Degree (D)			
		$D = 1$	$D = 2$	$D = 3$	$D = 4$
Angle-Specific Model:					
One	N/A	6.36 ± 2.3	5.90 ± 2.0	6.17 ± 2.3	6.56 ± 2.6
Two	N/A	6.00 ± 2.1	5.44 ± 1.9	5.54 ± 2.0	5.71 ± 2.2
Three	N/A	5.87 ± 2.0	**5.28 ± 1.8**	5.30 ± 1.7	5.37 ± 1.7
Polynomial-Gain Model:					
One	1	6.59 ± 2.2	5.95 ± 2.1	5.92 ± 2.1	6.25 ± 2.2
	2	6.45 ± 2.4	5.86 ± 2.2	**5.81 ± 2.1**	6.06 ± 2.1
	3	6.48 ± 2.3	6.08 ± 2.3	6.13 ± 2.3	6.74 ± 3.1
	4	7.16 ± 2.4	6.50 ± 2.2	6.48 ± 2.2	6.64 ± 2.5
Two	1	6.48 ± 2.2	5.85 ± 2.1	5.75 ± 2.0	5.78 ± 2.0
	2	6.30 ± 2.2	5.71 ± 2.1	**5.62 ± 2.0**	5.68 ± 2.0
	3	6.30 ± 2.2	5.83 ± 2.1	6.16 ± 2.3	6.30 ± 2.4
	4	8.35 ± 5.2	6.88 ± 3.1	6.53 ± 2.5	6.35 ± 2.5
Three	1	6.44 ± 2.2	5.80 ± 2.1	5.72 ± 2.1	5.69 ± 1.9
	2	6.24 ± 2.2	5.66 ± 2.1	**5.61 ± 2.2**	**5.61 ± 2.0**
	3	6.22 ± 2.2	5.81 ± 2.1	5.91 ± 2.2	6.54 ± 2.8
	4	8.08 ± 3.5	6.20 ±2.2	7.06 ± 2.8	6.80 ± 3.0
Piece-Wise-Gain Model:					
One	N/A	6.41 ± 2.3	5.87 ± 2.2	6.12 ± 2.3	11.3 ± 20
Two	N/A	6.09 ± 2.1	5.53 ± 1.9	5.59 ± 1.9	5.74 ± 1.9
Three	N/A	5.95 ± 2.0	**5.41 ± 1.8**	5.44 ± 1.9	5.54 ± 1.9

Table 12.1. Mean ± std. dev. EMG-torque test error results from all three models, for *single-channel unwhitened* EMG processing. Errors expressed in percent mean absolute MVC flexion at 90^{o} from 22 subjects. Each training record was 26 s in duration.

Figure 12.1 shows an example of the estimated torque and actual torque vs. time for the six elbow angles using the three different model structures. The best performing parameters, as indicated in the caption, were selected for each model in the figure. The angle-specific model was considered the "gold standard," since it optimized the model coefficients at each particular joint angle. It does not interpolate across angles. Figure 12.2 shows example EMG-torque estimation vs. time, comparing training duration and EMGσ processing. Figure 12.3 shows an example flexion-portion and extension-portion frequency response from a linear model (D=1). As would be expected, the least squares fit produces a lowpass characteristic in the dynamic model with a cutoff frequency similar to the bandwidth of the input tracking bandwidth (1 Hz). Figure 12.4 shows angular gain vs. angle for each subject, using the piece-wise-gain model. The gains at the six tested angles are shown as well as cubic spline interpolation of gains between these angles. The flexion gains trend down at the two angular extremes, while the extension

gains trend down as joint angle increases. Table 12.1 gives the mean plus/minus standard deviation test error results for the three models when single-channel unwhitened EMGσ processing was used. The analysis dimensions enumerated are: EMGσ-torque model, number of training records used to fit a model, EMGσ polynomial degree (D) and angle polynomial degree (A; applicable to the polynomial gain model, only). Table 12.2 gives the corresponding results when multiple-channel whitened EMGσ processing was used. The general trends in these results were for lower errors due to multiple-channel whitened EMGσ processing, longer duration training and nonlinear dynamic models (D>1). The lowest errors in the polynomial-gain model always occurred when the angle polynomial equaled A=2.

Records Used to Train	Angle Degree (A)	EMGσ Polynomial Degree (D)			
		D = 1	D = 2	D = 3	D = 4
Angle-Specific Model:					
One	N/A	4.91 ± 1.8	4.66 ± 1.7	4.75 ± 1.7	5.01 ± 2.1
Two	N/A	4.60 ± 1.6	4.17 ± 1.3	4.17 ± 1.3	4.25 ± 1.4
Three	N/A	4.49 ± 1.5	4.04 ± 1.2	**4.01 ± 1.2**	4.05 ± 1.2
Polynomial-Gain Model:					
One	1	5.21 ± 1.6	4.74 ± 1.5	4.70 ± 1.4	4.80 ± 1.4
	2	4.90 ± 1.7	4.46 ± 1.5	**4.41 ± 1.3**	4.47 ± 1.3
	3	4.94 ± 1.7	4.57 ± 1.5	4.68 ± 1.4	4.77 ± 1.4
	4	6.28 ± 2.4	5.03 ± 1.6	5.03 ± 1.5	5.08 ± 1.7
Two	1	5.12 ± 1.6	4.65 ± 1.4	4.57 ± 1.3	4.56 ± 1.3
	2	4.77 ± 1.6	4.33 ± 1.4	4.25 ± 1.3	**4.23 ± 1.2**
	3	4.86 ± 1.6	4.39 ± 1.5	4.49 ± 1.4	4.47 ± 1.4
	4	6.22 ± 2.0	5.56 ± 3.2	5.11 ± 1.7	4.73 ± 1.5
Three	1	5.09 ± 1.6	4.61 ± 1.4	4.53 ± 1.3	4.47 ± 1.2
	2	4.73 ± 1.6	4.28 ± 1.4	4.19 ± 1.2	**4.16 ± 1.**2
	3	4.89 ± 1.6	4.35 ± 1.4	4.37 ± 1.3	4.52 ± 1.4
	4	5.84 ± 1.7	4.92 ± 1.8	4.94 ± 1.6	4.84 ± 1.5
Piece-Wise-Gain Model:					
One	N/A	4.96 ± 1.8	4.50 ± 1.5	4.53 ± 1.4	4.78 ± 1.7
Two	N/A	4.67 ± 1.6	4.23 ± 1.4	4.16 ± 1.2	4.23 ± 1.2
Three	N/A	4.57 ± 1.5	4.14 ± 1.3	**4.06 ± 1.2**	4.19 ± 1.3

Table 12.2. Mean ± std. dev. EMG-torque test error results from all three models, for *multiple-channel whitened* EMG processing.

Statistical analysis began by comparing single-channel unwhitened results (Table 12.1) to multiple-channel whitened results (Table 12.2). For each combination of EMGσ-torque model and training duration (nine combinations per table), the cell with the lowest

average error in Table 12.1 was compared to the corresponding cell with the lowest average error in Table 12.2. Each of the nine comparisons was statistically significant $\left(p < 10^{-5}\right)$, with multiple-channel whitened results demonstrating lower errors in each case. Hence, subsequent statistical analysis was limited to the multiple-channel whitened results (Table 12.2). Next, statistical comparison was made between the number of training records used to fit a model. Within each of the three models, the cell with the lowest average error for each training duration in Table 12.2 was compared pair-wise to the results from the other two durations (three combinations for each of the three models). Each of the nine comparisons was statistically different ($p<10^{-3}$), with two training records always producing lower errors than one training record and three training records always producing the lowest error. Hence, subsequent statistical analysis was further limited to the results using three training records in Table 12.2. Angle degree was next compared (polynomial gain model only). The lowest average error was identified for each of the four angle degrees. The data from the cell with the minimum overall error (A=2, D=4) was compared to that of each of the other three cells. All differences were significant ($p<10^{-3}$); angle degree A=2 produced the minimum error. Accordingly, subsequent statistical analysis with the polynomial-gain model limited the angle degree to A=2. Then, differences between polynomial degrees (D) were compared *within* each model. For each model, the data from one row in Table 12.2 were used (three training trials, A=2 for the polynomial-gain model) by comparing the cell with the minimum average error to each of the three other cells. For the angle-specific model, the cell with the minimum average error (D=3) differed only from D=1 ($p < 10^{-4}$). For the polynomial-gain model, D=4 differed significantly from D=1 and D=2 $\left(p \le 10^{-4}\right)$. And, for the piece-wise-gain model, D=3 differed from D=1 and D=2 ($p<0.01$). Finally, comparison was made *between* models. For each model, the cell with the lowest average error in Table 12.2 was compared pair-wise to the similar results from the other two models (three combinations). There was a weak difference when comparing the angle-specific model to the polynomial-gain model (p=0.026) and no difference for the other two model comparisons ($p>0.25$). Thus, the results from the piece-wise-gain model—which can be interpolated across angle—were not statistically different than results from the "gold standard" angle-specific model. The lowest EMGσ-torque error was 4.01 ± 1.3% MVC_{F90}.

12.4 Disussion

This study evaluated methods for relating EMG to joint torque across a range of angles, during constant-posture force-varying contractions. In general, the processing was conducted in two sequential stages: estimation of extension and flexion EMGσ, followed by system identification of torque from the extension and flexion EMGσ time-series. In the first stage, "standard" EMGσ estimation (single-channel unwhitened) was compared to advanced EMGσ estimation (multiple-channel whitened). As with past experimental studies [Clancy 1995, Clancy 1997, Clancy 2012, Hogan 1980b, Liu 2013b, Potvin 2004 and Prakash 2005], advanced EMGσ estimation resulted in a substantial decrease in torque estimation error. Herein, error was reduced on average by 25% for each of the three EMGσ-torque models studied. This performance improvement is attributed to a reduction in the variance of the EMGσ signal, due to whitening and channel combination [Hogan 1980a, Hogan 1980b and Liu 2013a]. Nonetheless, there may be some drawbacks to the use of multiple-channel EMGσ estimators, including: increased hardware cost; the increased risk of electrode malfunction and its associated precipitous degradation in the EMGσ estimate [Clancy 1995]; and the possibility that better models could be formed by including all channels directly in the EMGσ-torque model, rather than combining EMG channels at the amplitude estimation stage [Staudenmann 2009 and Vieira 2010].

In the second processing stage (relating EMGσ to torque), we studied three model structures. The angle-specific model was considered the "gold standard," since it provided a separate fit at each available angle. The other two models incorporated an angle-invariant EMGσ-relation that was multiplicatively scaled as a function of angle—as suggested by the work of Vredenbregt and Rau [Vredenbregt 1973] which studied slowly force-varying contractions. We found that the best angle-invariant models had an error that was not statistically different from the best gold standard/angle-specific model. These EMGσ-torque models account for (and cannot distinguish between) all variations due to changes in angle, including: the muscle length-tension relationship, variation in muscle moment arms and muscle movement under the skin with respect to electrode location. Our results provide further evidence that the constant-posture EMGσ-torque relationship maintains the same *shape* across elbow angles, and need only be scaled to account for different angles—extending the prior results to force-varying (constant-

posture) contractions. The angle-invariant models are simple and can be easily interpolated over all angles within the range studied.

Few studies have rigorously studied the role of training contraction duration on model performance. In a prior study of the elbow with a similar protocol, but limited to only the 90^o joint angle, training set durations of 26 s and 52 s were contrasted [Clancy 2012]. The longer duration consistently produced better results, particularly as the number of fit parameters increased. The best (lowest error) model formed using 26 s of data had an error of 5.55 ± 4.5% MVC_{F90}, while the best model using 52 s had an error of 4.65 ± 3.6% MVC_{F90}. Thus, average error decreased %16 due to the increased training duration. In the present study (across six angles), training durations of 26 s, 52 s and 78 s exhibited best-case average errors of 4.75 ± 1.7% MVC_{F90}, 4.17 ± 1.3% MVC_{F90} and 4.01 ± 1.2% MVC_{F90}, respectively, for the angle-specific model. Hence, increasing from 26 s to 52 s reduced average error by 12%, while increasing from 26 s to 78 s reduced average error by 16%. As might be expected, the relative rate of improvement diminishes as the training duration increases. Note that the overall lower average errors in the present study are likely due to the range of angles studied, as lower torques are generated when joint angle deviates from 90^o. These lower torques lead to lower errors, as all errors were referenced to torque at 90^o.

The optimal EMGσ polynomial degree ranged from D=2–4 when using single-channel unwhitened EMGσ processing and from D=3–4 when using multiple-channel whitened EMGσ processing. The number of dynamic fit parameters (compared to the D=1 linear model, which had 42 dynamic fit parameters) doubles for D=2, triples for D=3 and quadruples for D=4. Thus, the nonlinear dynamic models have a very large number of parameters, which can be a challenge for robust least squares estimation. For this reason, our fit parameter estimates were regularized using the pseudo-inverse approach whenever *linear* least squares fitting was applied [Clancy 2012 and Press 1994]. In particular, note that regularized *linear* least squares estimation was used to find the initial guess parameters that seeded each of the *nonlinear* least squares estimators. When regularization was not used for the initial guess, several of the nonlinear optimizations failed to converge. More generally, the conditioning of the linear least squares fit (or convergence of the nonlinear least squares minimization) is improved by

longer training durations, fewer parameters and data sets that excite all modes of the model [Ljung 1999]; hence our reason for using a broadband torque target in the experimental protocol. Of these factors, it is useful to note that our method of achieving a nonlinear dynamic model (raising EMGσ and its lag values to a power) does not use fit coefficients efficiently. Functions that facilitate a similar model shape, but utilize fewer fit coefficients—such as parallel cascade models [Hashemi 2012]—might be more parsimonious.

For the polynomial-gain model, the best angle polynomial degree was A=2 in all cases. Since only six distinct joint angles were examined, it is likely that overfitting began to occur for degrees above A=2. The piece-wise-gain model avoided this issue entirely by fitting gain only at the available joint angles, facilitating interpolation between angles as a *post hoc* processing step. Spline functions are an excellent choice for such processing, as they preserve the value of the function at the knots (i.e., at the joint angles at which measurements were made) and provide a smooth fit in-between.

The fixed postures imposed during these experiments facilitated study of the system identification methods, and may be representative of conditions experienced by prosthesis users whose remnant musculature may be fixed in orientation. But, fixed postures are not representative of the free movements made during most activities of daily living in non-amputees. Hence, future work should consider conditions during which the joint is dynamically changing angle. In doing so, models may need to consider differences in the EMGσ-torque relationship as a function of concentric vs. eccentric contraction [Komi 2000]. While three distinct models were studied in this work, we did not extensively study all possible model parameters (e.g., the number of dynamic model lags was fixed at Q=20, the pseudo-inverse tolerance was set at Tol = 0.0056), instead fixing these values based on a prior study [Clancy 2012]. Slight tuning of these values might provide some additional reduction in torque error estimation, albeit rather limited.

In summary, models were formed during constant-posture, torque-varying contractions ranging in joint angle from 60^o to 135^o, using advanced EMGσ estimation techniques and multiple training trials. With EMG-torque models formed separately at each of the six distinct joint angles, a minimum "gold standard" error of 4.01 ± 1.2% MVC_{F90} resulted [EMGσ polynomial degree of D=3, three training records (78 s) and

multiple-channel whitened EMGσ processing]. The piece-wise-gain model, which facilitates interpolation across angles, achieved a statistically equivalent error of 4.06 ± 1.2% MVC_{F90}. Compared to single-channel unwhitened EMGσ processing, multiple-channel whitened EMGσ processing reduced torque error by 25% on average. Increasing the training trial duration from 26 s to 52 s reduced average error by 12%, while increasing it from 26 s to 78 s reduced average error by 16%. These results further support the experimental observation, for both slowly torque varying and (herein) torque-varying contractions, that the shape of the constant-posture EMGσ-torque relationship is the same at each joint angle, but is scaled by a gain factor that is distinct at each angle.

Chapter 13

Appendices

13.1 Introduction to firing rate calculation models

This section describes the performance of various firing rate estimation methods when the firing rate is constant. Although physiologic firing rates are never constant, this simplified model is helpful in understanding the overall performance of the estimation methods. Methods for calculating continuous firing rates of various methods are listed in (6.1.1a)–(6.1.1e): instantaneous method [$r_{inst}(t)$], LeFever method [$r_{LeFever}(t)$] [DeLuca 1979], Berger method [$r_{Berger}(t)$] [Berger 1986], Berger variant method [$r_{BergerV}(t)$], Mateo-Laguna method [$r_{Lag}(t)$] [Mateo 1996] and instantaneous-spline method [$r_{inst.spline}(t)$]. The firing rate is calculated either in the continuous domain $t \in \mathbb{R}^+$ or in the uniformly sampled discrete domain $t_n = nT_s \in \mathbb{R}^+$. To facilitate processing and storage on digital computers, methods with firing rates in the continuous time domain are always discretized. However, for analytical results, continuous-domain results are analyzed in the continuous domain. By convention, rounded parentheses are used to denote continuous-time variables, while square-brackets are used to denote discrete-time variables.

The time of the k-th firing occurs at time t_k, satisfying $0 \le t_k < t_{k+1}$ and $k \in \mathbb{N}$. Some commonly used functions are:

- Indicator function: $1_{\Im}(x) = \begin{cases} 0, & x \notin \Im \\ 1, & x \in \Im \end{cases}$,
- The Hanning window function of length w defined on $\mathbb{Z}$ as:

$$\mathrm{Hann}_{\mathrm{w}}[n] = 0.5\left(1 - \cos\frac{2\pi n}{\mathrm{w}-1}\right),$$

- The rectangular window function of length X as a specialized indicator function:

$$\mathrm{Rect}_X(x) = \begin{cases} 0, & |x| \le X \\ 1, & |x| > X \end{cases},$$

- Convolution of continuous functions f and g with domains of $\mathbb{R}$

$$f(t) \otimes g(t) = \int_{-\infty}^{\infty} f(\tau) g(t-\tau)\, d\tau,$$

- Convolution of discrete functions f and g with domains of $\mathbb{Z}$

$$f[n] \otimes g[n] = \sum_{k=-\infty}^{\infty} f[k]g[n-k],$$

- Sinc function with domain of $\mathbb{R}$, at cutoff frequency f Hz is

$$\mathrm{sinc}_f(t) = \frac{\sin 2\pi f t}{\pi t},$$

- Its discrete counterpart with domain of $\mathbb{Z}$ at F_s Hz sample frequency

$$\mathrm{sinc}_f[n] = F_s \frac{\sin \pi f n/F_s}{\pi n},$$

- The Dirac-delta function can be loosely defined as

$$\delta(t) = \begin{cases} \infty, & t = 0 \\ 0, & t \neq 0 \end{cases},$$

  satisfying $\int_{-\infty}^{\infty} \delta(t)\, dt = 1$. Its discrete counterpart is

$$\delta[n] = \begin{cases} 1, & n = 0 \\ 0, & n \neq 0 \end{cases}.$$

- Spline interpolation process: given that $y = f(x)$ at a set of points $\{x_k : k \in \mathbb{N}, 1 \leq k \leq N, x_k < x_{k+1}\}$ (a.k.a. knots), the k-th degree spline interpolated function $g(k, x) \in \mathbb{C}^k$ satisfies $g(k, x_k) = f(x_k)$.

- The integral pulse frequency modulation (IPFM) model. Let the modulation process $-1 \leq m(t) < \infty$, $t \geqslant 0$ be an integrable stochastic process satisfying $Em(t) = 0$. The IPFM model gives

$$M(t) = \int_0^{\infty} \frac{1 + m(\tau)}{T} d\tau$$

  It's easy to see that $M(t)$ is another stochastic process that is non-negative, non-decreasing and bijective of t for $t>0$, and is linear of $m(t)$. The continuous rate function derived from $M(t)$, $\hat{r}(t) = M'(t) = \frac{1+m(t)}{T}$ is non-negative and continuous as an estimate of firing rate $r(t)$, satisfying $E\hat{r} = \frac{1}{T}$. The constant T is also the expectation of the renewal process $\{\Delta_k = t_k - t_{k-1} : k \in \mathbb{N}, t_k < t_{k+1}\}$: $T = E\Delta_k = \lim_{N\to\infty} \frac{t_N}{N}$. The inverse problem of calculating the firing rate under IPFM formulation seeks an estimate of $\hat{r}(t)$ based on t_k, the only measurement from lossy observation of $\{t_k : k \in \mathbb{N}, M(t_k) = k\}$.

  In practice, it's required that $m(t)$ be continuous, so that $M(t)$ is also continuous. Under that assumption, it can be decomposed as $M(t) = \lfloor M(t) \rfloor + \widetilde{M}(t)$, where $\lfloor M(t) \rfloor$ is a pure jump surjective function of $\mathbb{R}^+ \to \mathbb{N}$

taking integer values with discontinuity at t_k, and $\widetilde{M}(t) \in \mathbb{C}[t_{k-1}, \quad t_k) \to [0, \quad 1)$ is piecewise continuous.

Let T_s be the uniform temporal sampling interval, $r(t) \in \mathbb{R}^+$ be the underlying ground-truth continuous firing rate and $r[n] = \frac{s_n}{T_s} \in \mathbb{R}^+$ be the uniformly discretized firing rate, where s_n is the number of firings in interval $\left[\left(n - \frac{1}{2}\right)T_s, \quad \left(n + \frac{1}{2}\right)T_s\right)$. The continuous rate is non-negative, continuous and upper-bounded (usually below 100 pps). Note that $r[n] \neq r(nT_s)$ as $r[n]$ is an average measure. In physical measurements, however, it's often assumed that $x[n] = x(nT_s)$ due to temporal resolution and aliasing. It is straightforward to discretize a proper continuous function (and continuous rate) with this relation. Many of the subsequent analyses are carried out in the continuous domain because it is easier to apply proper continuous mapping than its discrete counterpart, and the result is trivially applicable to discrete cases.

Let $t_k \in \mathbb{R}^+$be the time of the k-th firing. With these definitions of commonly used functions, the firing rate estimators studied are defined as:

$$r_{\text{inst}}(t) = \frac{1}{t_k - t_{k-1}} \sum_{k=1}^{\infty} 1_{[t_{k-1}, \quad t_k)}(t) \tag{13.1.1a}$$

It is obvious that for any t value, only one interval in the summation takes value one (i.e., only one indicator function, $1_{[t_{k-1}, \quad t_k)}(t)$, is nonzero) and all others terms are zero.

$$r_{\text{LeFever}}[n] = x[n] \otimes \text{Hann}_{\text{w}}[n] \tag{13.1.1b}$$

$$r_{\text{Berger}}(t) = r_{\text{inst}}(t) \otimes \text{Rect}_{T_c}(t) \tag{13.1.1c}$$

$$r_{\text{BergerV}}[n] = r_{\text{inst}}[n] \otimes \text{sinc}_{f_c}[n] \tag{13.1.1d}$$

$$y_{\text{Lag}}(t) = \sum_{k=1}^{N} M(t)\delta(t - t_k) = \begin{cases} k, & t = t_k \\ 0, & \text{otherwise} \end{cases}$$

$$r_{\text{Lag}}(t) = g'\big(k = 3, y_{\text{Lag}}(t), \{t_k\}\big) \tag{13.1.1e}$$

$$r_{\text{inst.Lag}}(t) = g\left(k = 3, \sum_{k=2}^{n} \frac{\delta(t - t_k)}{t_k - t_{k-1}}, \{t_k\}\right) \tag{13.1.1f}$$

in the above, $M(t)$ is the stochastic integral process from IPFM model, and $g(k, f(t), \{t_k\})$ is spline interpolation of degree k of function $f(t)$ at time $\{t_k\}$.

LeFever [DeLuca 1982] applied a 400ms discrete Hanning window function to filter the impulse train. This method contains one parameter: odd number of taps of the Hanning window.

The Berger method analytically convolves a rectangular temporal window of duration T_c seconds with the continuous instantaneous heart rate (13.1.1a) before it is sampled. The temporal rectangular window is a sinc(*f*) function in the frequency domain that attenuates high-frequency components introduced by jumps in the instantaneous rate that occur at each firing time. The resulting rate is piecewise linear in the continuous domain $t \in \mathbb{R}^+$, with joints at $t_k \pm T_c/2$ (edges of windows centered at t_k where the influence of a previous impulse vanishes and/or the next impulse starts to affect $r_{\text{Berger}}(t)$). The continuous rate (13.1.1c) is then sampled to its discrete equivalent. Alternatively, the discrete firing rate can be calculated only at sampling instants. The Berger method has the window taps, odd likewise, as its only method parameter. Berger also corrected for the *sinc* shape in the frequency domain, which we did not do.

For implementation/simulation purposes of all these methods on a digital computer, the continuous functions are first discretized as described before operations in discrete counterparts are carried out. The Berger-variant method (13.1.1d) replaces the discrete rectangular window in the implementation of Berger method with a discrete $\text{sinc}_{fc}(t)$ function with cut-off frequency f_c Hz. As the firing sequence always has finite duration, an infinite duration *sinc* function can be used to convolve with the sampled instantaneous rate. Alternatively, we can truncate the *sinc* function with N_c taps, with $sinc_{Tr}[n]=0$ for $n < \frac{1-N_c}{2}$ or $n > \frac{N_c-1}{2}$.

To see this, let $x[n]$ be a sequence with N_{cx} non-zero terms, then $y[n] \coloneqq x[n] \otimes \text{sinc}_{f_c}[n]$ has infinite non-zero terms because of $\text{sinc}_{fc}[n]$, but out of which only N_{cx} terms at the same location as $x[n]$ are interesting to us. Let the leftmost non-zero term of $x[n]$ be indexed n_L, and rightmost non-zero term indexed $n_R=n_L+N_{cx}-1$; then we have $y[n] = \sum_{k=-\infty}^{\infty} x[k]\text{sinc}_{f_c}[n-k] = \sum_{k=n_L}^{n_R} x[k]\text{sinc}_{f_c}[n-k]$, and only $n_L-n_R=1-N_{cx} \leq n \leq n_R-n_L=N_{cx}-1$ terms of $\text{sinc}_{fc}[n]$ are needed in the computation. Thus $N_c=2N_{cx}+1$ terms are needed from $\text{sinc}_{fc}[n]$.

The Maeto-Laguna method [Maeto 1996] samples from the continuous IPFM result $M(t)$ (which cumulatively sums the rate process) at instants t_k and spline interpolates to obtain the continuous function $\hat{y}_{\text{Lag}}(t)$ with the approximation that $x[n] = x(nT_s)$ (i.e. discrete rate at nT_s equals continuous rate at that time), then takes its derivative to obtain rate. Note that discretization of integral and differential are performed via summation and

difference given that step size (resolution) is high enough, and convolution by summation of discrete products.

The spline interpolation process can be viewed as a time-varying filter whose frequency response depends on the duration between interpolated samples. For an *l*-th order spline, the cutoff frequency of the impulse response for uniformly spaced spline interpolation is inversely proportional to the interpolated sample duration. A cubic spline has a cutoff frequency of $\frac{0.44}{T_0}$ Hz and a 14-th order spline has a cutoff frequency of $\frac{0.48}{T_0}$ Hz [Maeto 2000]. The cubic spline is a good candidate because of its negligible dependence on the interpolation factor, and because higher orders barely improve the filtering performance due to numerical precision limits [Mateo 2000]. This method has the interpolation factor (spline order) as its method parameter.

13.2 Analysis of constant firing rate estimations

For most analysis of firing rates in this chapter, it is implicitly assumed that the firing sequence starts from zero and extends to infinity, so that the tail transient of filtering processes is absent from the analysis. Often, for the sake of further simplicity, it is stated that the sequence also has infinite history, i.e. it starts from -∞. Under that assumption, both start up transients and tail transients are safely ignored.

13.2.1 Instantaneous method

It is trivial to mention that the instantaneous rate (13.1.1a) gives constant output when presented with a constant firing rate input, assuming an infinite time sequence. The Fourier transform of the instantaneous rate is

$$R_{inst}(\omega) = \sum_{k=1}^{\infty} \frac{\operatorname{sinc}\left[\frac{\omega}{2}(t_k - t_{k-1})\right]}{t_k - t_{k-1}} e^{-j\frac{\omega}{2}(t_k + t_{k-1})} \qquad (13.2.1)$$

13.2.2 Berger method

The temporal filter in the continuous time domain is a rectangular window of duration $2T_0$: $\mathrm{w}(t) = \frac{1}{2T_0}\mathbf{1}_{[-T_0,\ \ T_0]}(t)$ with Fourier transform $\mathrm{W}(\omega) = \frac{\sin \omega T_0}{\omega T_0}$. The filtered output is:

$$r_{\mathrm{Berger}}(t) = r_{\mathrm{inst}}(t) \otimes \mathrm{w}(t) = \frac{1}{2T_0}\sum_{k=1}^{\infty} \frac{l_k(t)}{t_k - t_{k-1}} \qquad (13.2.2)$$

where $l_k(t)$ is the overlap coverage of the two intervals $[t_{k-1}, t_k)$ and $[t - T_0,\quad t + T_0)$ for each k.

For an infinite-duration constant firing rate with t_k=kT, (13.2.2) reduces to $r_{\mathrm{Berger}}(t) = \frac{\sum_{k=1}^{\infty} l_k(t)}{T} = \frac{1}{T}$, the reciprocal of the constant firing interval. In a more general

setting, when firing times are non-negative, $l_k(t)$ can be classified into five cases illustrated in Fig 13.1:

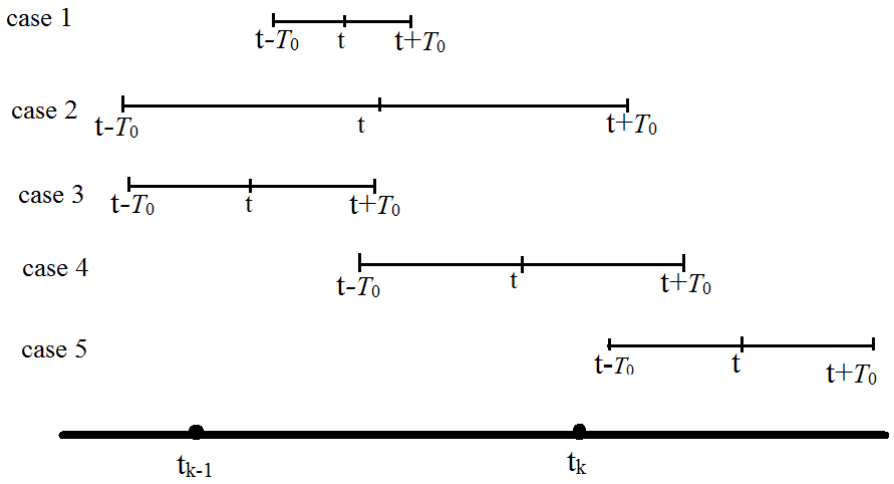

Figure 13.1. Interval intersection cases. This plot shows all five possible cases of a rectangle window's coverage of an interval between (k-1)-th and k-th firing.

$$l_k(t) = \int_{-\infty}^{\infty} 1_{[t_{k-1},t_k)}(\tau)\, 1_{[t-T_0,\ \ t+T_0)}(\tau)\, d\tau$$

$$= \begin{cases} 2T_0 & t \in [t_{k-1}+T_0,\ \ t_k - T_0) \quad \text{(case 1)} \\ t_k - t_{k-1} & t \in [t_k - T_0,\ \ t_{k-1}+T_0) \quad \text{(case 2)} \\ t + T_0 - t_{k-1} & t \in (t_{k-1} - T_0,\ \ \min\{t_k - T_0, t_{k-1} + T_0\}) \quad \text{(case 3)} \\ -t + T_0 + t_k & t \in (\min\{t_k - T_0, t_{k-1} + T_0\},\ \ t_k + T_0) \quad \text{(case 4)} \\ 0 & t \in (-\infty,\ \ t_{k-1} - T_0) \cap (t_k + T_0,\ \ \infty) \quad \text{(case 5)} \end{cases} \tag{13.2.3}$$

It is non-zero for only finite many terms because of finite time support of the rectangular window function. Case-1 occurs only when $2T_0 \le t_k - t_{k-1}$, when an interval between two adjacent firings is long enough to contain the rectangle window centered at t; case-2 occurs only when $2T_0 > t_k - t_{k-1}$, or when the interval is too short so that it is contained by the rectangle window centered at t. These two cases are exclusive depending on the window duration and where t locates. Case 3 occurs when only (k-1)-th firing is covered by the window; case-4 when only k-th firing is covered, and case-5 when the left edge of window is to the right of k-th firing.

We see from case-5 that $r_{\text{Berger}}(t) = 0$ before $t_0 - T_0$. When k=1, either case-4 or case-1 must be present in (13.2.2) to make interval $[t - T_0,\ \ t + T_0]$ completely covered by $[t_{k-1}, t_k)$, implying that $t > t_0 + T_0$. This gives a start-up transient of $2T_0$ for (13.2.2).

Find indices L and U into overlapping coverage function (13.2.3) such that $t_{L-1} < t - T_0 \le t_L$ and $t_U \le t + T_0 < t_{U+1}$. Note that $U + 2 \ge L$ includes all five cases in (13.2.3), then (13.2.2) can be written as:

$$r_{\text{Berger}}(t) = \begin{cases} \frac{1}{t_L - t_U} & L > U \\ \frac{1}{2T_0}\left(\frac{t_L - t + T_0}{t_L - t_{L-1}} + \frac{t - t_U + T_0}{t_{U+1} - t_U} + u - l\right) & L \le U \end{cases} \tag{13.2.4}$$

For constant rate $t_k = kT + \xi$, extend the uniform point process to $-\infty$ to avoid finite start-up transients: $\{t_k \in \mathbb{R}, k \in \mathbb{Z}: t_k < t_{k+1}\}$, then (13.2.3) reduces to

$$l_k(t) = \begin{cases} 2t_0 & t \in kT + \xi - [T_0, \quad T - T_0) \\ T & t \in kT + \xi - [T - T_0, \quad T_0) \\ t + T_0 - (k-1)T - \xi & t \in kT + \xi - (T + t_0, \quad \max\{t_0, T - T_0\}) \\ -t + T_0 + kT + \xi & t \in kT + \xi + (-\min\{t_0, T - T_0\}, \quad t_0) \\ 0 & t \in (-\infty, \quad kT + \xi - T - T_0) \cap (kT + \xi + T_0, \quad \infty) \end{cases} \tag{13.2.5}$$

When case-1 occurs, at most two $l_k(t)$'s are non-zero for any given t. When only one $l_k(t)$ is non-zero, (13.2.2) gives $R_{\text{Berger}}(t) = \frac{1}{T}$; when two adjacent $l_k(t)$'s are non-zero, they correspond to case-4: left partial-cover of interval $[t_{k-1}, \ t_k)$ and case-3: right partial-cover of interval $[t_{k-1}, \ t_k)$) respectively, so the output is $R_{\text{Berger}}(t) = \frac{1}{2T_0 T}[-t + T_0 + (k-1)T + \xi + t + T_0 - kT - \xi + T] = \frac{1}{T}$.

When case-2 occurs, at least two l_k terms are non-zero. Let $s = \left\lceil \frac{t - T_0}{T} \right\rceil$, then there are $L = \left\lfloor \frac{t + T_0}{T} \right\rfloor - s \ge 0$ terms of $l_k(t)$ that correspond to case-2 (complete interval coverage), contributing to the filtered output $R_{\text{Berger}_c}(t) = \frac{LT}{2T_0 T} = \frac{L}{2T_0}$; one term of l_k that corresponds to case-4 and -3 respectively (partial coverage), together contributing to output $R_{\text{Berger}_p}(t) = \frac{1}{2T_0 T}\{[-t + T_0 + kT + \xi] + [t + T_0 - (k+L)T - \xi]\} = \frac{1}{T} - \frac{L}{2T_0}$. So the resulting output is still $R_{\text{Berger}}(t) = y_c(t) + y_p(t) = \frac{1}{T}$.

Thus, under constant-rate point process, the continuous output (13.2.2) of the Berger's method is constant and inversely proportional to the firing interval after finite initial transient time. An alternative approach to reach the same conclusion is to see that the instantaneous rate in this case is constant, thereby so is the continuous Berger rate as a rectangle window filtering output of the instantaneous rate. Subsequent sampling does not alter this property.

13.2.3 Berger-variant method

13.2.3.1 Time-domain approach

The Berger-variant method is calculated the same way as in Berger method from the renewal process $\{\Delta_k = t_k - t_{k-1}: k \in \mathbb{N}, t_k < t_{k+1}\}$ based on the point process $\{t_k \in \mathbb{R}: k \in \mathbb{N}, t_k < t_{k+1}\}$ of firing times. It is then filtered with a temporal *sinc* function $\mathrm{w}(t) = \mathrm{sinc}_{f_c}(t) = \frac{\sin \omega_c t}{\pi t}$ with Fourier transform $\mathrm{W}(\omega) = \mathbf{1}_{[-\omega_c, \omega_c]}(\omega)$ with $f_c = \frac{\omega_c}{2\pi}$, and is subsequently sampled.

For constant firing rate with t_k=kT and infinite duration and infinite past (i.e. $\inf\{k\} = -\infty$), the Berger-variant rate reduces to $\frac{1}{T}\int_{-\infty}^{\infty} \mathrm{w}(t)\,dt = \frac{1}{T}$.

More generally, when firing times are non-negative, the filtered output before sampling is:

$$r_{\mathrm{BergerV}}(t) = r_{\mathrm{inst}}(t) \otimes \mathrm{w}(t) = \int_{-\infty}^{\infty} \sum_{k=1}^{\infty} \frac{\mathbf{1}_{[t_{k-1},t_k)}(\tau)}{t_k - t_{k-1}} \cdot \frac{\sin \omega_c(t-\tau)}{\pi(t-\tau)} d\tau$$

$$= \frac{\omega_c}{\pi} \sum_{k=1}^{\infty} \frac{1}{t_k - t_{k-1}} \int_{t-t_k}^{t-t_{k-1}} \frac{\sin \omega_c \tau}{\omega_c \tau} d\tau \qquad (13.2.6)$$

The change of summation with integral is due to the Fubini-Tonelli theorem [Tonelli, 1909]. Introduce the sine integral function $S_i(x) = \int_0^x \frac{\sin t}{t} dt$ and the Dirichlet integral $S_i(\infty) = \frac{\pi}{2}$. We have $\int_{t_1}^{t_2} \frac{\sin \omega_0 \tau}{\omega_0 \tau} d\tau = \frac{S_i(\omega_0 t_2) - S_i(\omega_0 t_1)}{\omega_0}$. The resulting filtered output is:

$$r_{\mathrm{BergerV}}(t) = \frac{1}{\pi}\sum_{k=1}^{\infty} \frac{S_i(\omega_0(t-t_{k-1})) - S_i(\omega_0(t-t_k))}{t_k - t_{k-1}} = \frac{\omega_0}{\pi}\sum_{k=1}^{\infty} \frac{1}{t_k - t_{k-1}} \int_{t_{k-1}}^{t_k} \mathrm{sinc}(t-\tau)\,d\tau \qquad (13.2.7)$$

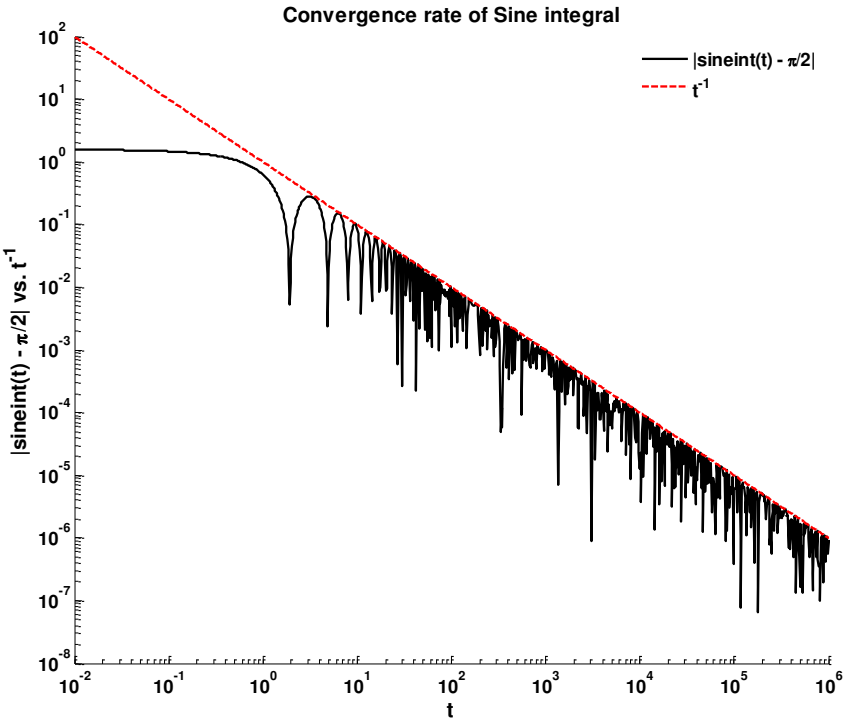

Figure 13.2. Convergence rate of sine integral. It shows the absolute difference between the sine integral and the Direchlet integral is shown in black and 1/t (red) in log-log scale. We can see that the absolute difference is upper-bounded by 1/t, and is negligible for t>1 second.

The convergence rate of $S_i(t)$ is shown in Figure 13.2. The bandwidth ω_0 of the filter $\mathrm{w}(t)$ scales with startup transient effects; doubling ω_0 halves the time needed to limit start-up effects to a given level.

For constant firing rates $t_k = kT + \xi$, the output becomes:

$$r_{\mathrm{BergerV}}(t) = \frac{1}{2T} + \frac{1}{\pi T} S_i\big(\omega_0(t-\xi)\big) \to \frac{1}{T}, t \to \infty \tag{13.2.8}$$

We can see that the calculated firing rate for a constant interval is non-constant due to the infinite start-up transients of the windowing function in the time domain, converging to the constant rate $\frac{1}{T}$ as $t \to \infty$.

13.2.3.2 Frequency approach

The conclusion (13.2.8) can also be reached by calculating (13.2.6) in the frequency domain. The output in the frequency domain is:

$$R_{\mathrm{BergerV}}(\omega) = R_{\mathrm{inst}}(\omega)\mathrm{W}(\omega) = \sum_{k=1}^{\infty} \frac{\mathrm{sinc}\left[\frac{\omega}{2}(t_k - t_{k-1})\right]}{t_k - t_{k-1}} e^{-j\frac{\omega}{2}(t_k + t_{k-1})} \mathbf{1}_{[-\omega_0, \omega_0]}(\omega) \tag{13.2.9}$$

For constant firing rate with $t_k = k\mathrm{T}$ and infinite duration and infinite past, $R_{\mathrm{inst}}(\omega) = \frac{\mathrm{sinc}\frac{\omega}{2}T}{T} \sum_{k=1}^{\infty} e^{-j\omega\left(k-\frac{1}{2}\right)T} = \frac{\delta(\omega)}{T}$ almost everywhere, so that (13.2.9) reduces to $R_{\mathrm{BergerV}}(\omega) = \frac{\delta(\omega)}{T}$, which gives $r_{\mathrm{BergerV}}(t) = \frac{1}{T}$.

Let $y_k(t) = \int_{-\omega_0}^{\omega_0} \mathrm{sinc}\left[\frac{\omega}{2}(t_k - t_{k-1})\right] e^{j\omega t}\, d\omega$ then when (13.2.9) is put in time domain, it becomes:

$$r_{\mathrm{BergerV}}(t) = \frac{1}{2\pi} \int_{-\omega_0}^{\omega_0} R_{\mathrm{BergerV}}(\omega) e^{j\omega t}\, d\omega = \frac{1}{2\pi} \sum_{k=1}^{\infty} y_k\left(t - \frac{t_k + t_{k-1}}{2}\right) \tag{13.2.10}$$

To simplify it, introduce the cosine integral function $C_i(t) = \int_0^t \frac{\cos\tau}{\tau} d\tau$, even; and an auxiliary function:

$$Z(\omega) = \int_0^{\omega} \mathrm{sinc}(\upsilon\tau) e^{j\upsilon t}\, d\upsilon$$

$$= \frac{1}{2\tau}\big[S_i\big(\omega(t+\tau)\big) - S_i\big(\omega(t-\tau)\big)\big] - \frac{j}{2\tau}\big[C_i\big(\omega(t+\tau)\big) - C_i\big(\omega(t-\tau)\big)\big]$$

with $Z(-\omega) = -\frac{1}{2\tau}\big[S_i\big(\omega(t+\tau)\big) - S_i\big(\omega(t-\tau)\big)\big] - \frac{j}{2\tau}\big[C_i\big(\omega(t+\tau)\big) - C_i\big(\omega(t-\tau)\big)\big]$ so that $y_k(t) = \frac{2}{t_k - t_{k-1}}\left[S_i\left(\omega_0\left(t + \frac{t_k - t_{k-1}}{2}\right)\right) - S_i\left(\omega_0\left(t - \frac{t_k - t_{k-1}}{2}\right)\right)\right]$. Substitute into (13.2.10) to arrive at (13.2.8).

13.2.3.3 Temporal truncated filter

When the Sinc window is truncated to $[-T_0, T_0]$: $\mathrm{sinc}_{\omega_0,T}(t) = \frac{\sin\omega_0 t}{\pi t} \mathbf{1}_{[-T_0,T_0]}(t)$, its Fourier transform becomes:

$$\mathrm{Sinc}_{\omega_0,T_0}(\omega) = \mathbf{1}_{[-\omega_0,\omega_0]}(\omega) * \frac{2\sin\omega T_0}{\omega} = 2\left[S_i\big((\omega+\omega_0)T_0\big) - S_i\big((\omega-\omega_0)T_0\big)\right] \quad (13.2.11)$$

It's easy to verify that $\mathrm{Sinc}_{\omega_0,T}(\omega)$ is even. Now the filtered output (6.2.8) becomes:

$$r_{\mathrm{BergerV}}(T_0,\ \ t) = \frac{\omega_0}{\pi}\sum_{k=1}^{\infty}\frac{1}{t_k - t_{k-1}}\int_{-T_0}^{T_0}\frac{\sin\tau}{\tau}\mathbf{1}_{[t_{k-1},\ \ t_k)}(t-\tau)\,d\tau = \frac{\omega_0}{\pi}\sum_{k=1}^{\infty}\frac{l_k^T(t)}{t_k - t_{k-1}} \quad (13.2.12)$$

With the same classification as (13.2.5):

$$l_k^T(t) = \int_{-\infty}^{\infty}\frac{\sin\omega_0\tau}{\omega_0\tau}1_{[t_{k-1},t_k)}(\tau)1_{[t-T_0,\ \ t+T_0)}(\tau)\,d\tau =$$

$$\begin{cases} \frac{1}{\omega_0}\left[S_i\big(\omega_0(t+T_0)\big) - S_i\big(\omega_0(t-T_0)\big)\right], & t \in [t_{k-1}+T_0,\quad t_k - T_0) \\ \frac{1}{\omega_0}\left[S_i(\omega_0 t_k) - S_i(\omega_0 t_{k-1})\right], & t \in [t_k - T_0,\quad t_{k-1}+T_0) \\ \frac{1}{\omega_0}\left[S_i\big(\omega_0(t+T_0)\big) - S_i(\omega_0 t_k)\right], & t \in (t_{k-1}-T_0,\quad \min\{t_k - T_0, t_{k-1}+T_0\}) \\ \frac{1}{\omega_0}\left[S_i(\omega_0 t_{k-1}) - S_i\big(\omega_0(t-T_0)\big)\right], & t \in (\min\{t_k - T_0, t_{k-1}+T_0\},\quad t_k + T_0) \\ 0, & t \in (-\infty,\quad t_{k-1}-T_0) \cap (t_k + T_0,\quad \infty) \end{cases} \quad (13.2.13)$$

where $l_k^T(t)$'s are nonzero for only finite terms at any time t as is in Berger's case. Finding indices l and u such that $t_{l-1} < t - T_0 \le t_l$ and $t_u \le t + T_0 < t_{u+1}$ as in (13.2.4), (13.2.12) reduces to

$$r_{\mathrm{BergerV}}(T_0,\ \ t)$$

$$= \begin{cases} \dfrac{S_i\big(\omega_0(t+T_0)\big) - S_i\big(\omega_0(t-T_0)\big)}{\pi(t_l - t_u)} & u < l \\ \dfrac{S_i(\omega_0 t_l) - S_i\big(\omega_0(t-T_0)\big)}{\pi(t_l - t_{l-1})} + \dfrac{S_i\big(\omega_0(t+T_0)\big) - S_i(\omega_0 t_u)}{\pi(t_{u+1} - t_u)} + \displaystyle\sum_{k=l+1}^{u}\frac{S_i(\omega_0 t_k) - S_i(\omega_0 t_{k-1})}{\pi(t_k - t_{k-1})} & u \ge l \end{cases} \quad (13.2.14)$$

For constant firing rate $t_k = kT + \xi$, we have $l = \left\lceil\frac{t-T_0-\xi}{T}\right\rceil$ and $u = \left\lfloor\frac{t+T_0-\xi}{T}\right\rfloor$ which makes it simplifies into

$$r_{\mathrm{BergerV}}(T_0,\ \ t) = \frac{S_i(\omega_0(t+T_0)) - S_i(\omega_0(t-T_0))}{\pi T} = \frac{\omega_0}{\pi T}\int_{-T_0}^{T_0}\mathrm{sinc}(t+\tau)\,d\tau \quad (13.2.15)$$

13.2.4 Continuous-time IPFM model and heart timing signal

A slightly more realistic and complicated scenario than constant-firing rate is the single-tone or multi-tone modulation, where the modulation function is the superposition of some sinusoidal rates with different amplitudes, frequencies and phases. Indeed, Fourier transformation enables us to decompose a stationary process into sinusoids. Analysis for the summation of finitely many sinusoids, however, becomes more difficult than the constant rate cases. We use the IPFM model to connect the underlying firing rate

and observed firing times, and try to establish an analytic relationship between firing times and modulation function when finite sinusoids are used in IPFM model.

Now that $t(x)$ is the time for the x-th pulse, the instantaneous firing rate (13.1.1a) from the IPFM model can be written as $t'(x)$. For uniform sampling in time $t[k] = kT_s$, the firing rate can be approximated as,

$$t'\big(x(t)\big) = \frac{dx^{-1}(t)}{dx} \cong \frac{T}{1+\frac{1}{T_s}\int_{-\infty}^{\infty} m(\tau)1_{[t_{k-1}\ \ t_k)}(\tau)\,d\tau} \tag{13.2.16}$$

The underlying zero-mean modulating function $m(t)$ is first modeled in a multitone form

$$m(t) = \sum_{k=1}^{L} a_k \cos(\omega_k t + \varphi_k) \tag{13.2.17}$$

with a_k , $\omega_k > 0$ and $\varphi_k \in [0,\ \ 2\pi)$ deterministic. The HT signal [Maeto 1996] is calculated as

$$ht(t) = T \cdot x(t) - t = \int_0^t m(\tau)\,d\tau \tag{13.2.18}$$

and is linear in the modulating signal $m(t)$. Let $HT(\omega)$ and $M(\omega)$ be the Fourier transforms of $ht(t)$ and $m(t)$, then perfect reconstruction of $m(t)$ from the spectrum of HT signal is possible from $HT(\omega) = \frac{M(\omega)}{j\omega} + \pi M(0)\delta(\omega)$ [Mateo 2000].

To obtain from $m(t)$ the underlying point process of firing times, we can solve N equations for t_k under the restriction that $0 < t_k \le NT, 1 \le k \le N$:

$$ht(t_k) = kT - t_k = \sum_{l=1}^{L} \frac{a_l}{\omega_l}[\sin(\omega_l t_k + \varphi_l) - \sin\varphi_l] \tag{13.2.19}$$

For each k, the existence of a solution t_k is guaranteed as $ht(t_k)$ is generated from the underlying $m(\tau)$. However, the uniqueness of t_k is not easily guaranteed. Apparently, the solution is unique if and only if $t + \int_0^t m(\tau)$ is strictly increasing, implying $|a_1| < 1$ for monotone modulation; for multi-tone modulation, sinusoids add up constructively or destructively and $\{t|m(t) < -1\}$ may not be empty. When $|m(t)| \ll 1$ (or $|a_k| \ll 1$), then the uniqueness can often be guaranteed as observed from the simulation results of Figure 13.3. A numeric solution to (13.2.19) may be found using the Newton method with an initial guess $t_k^0 = \frac{k}{N}t_N - \sum_{l=1}^{L}\frac{a_l}{\omega_l}\sin\varphi_l$.

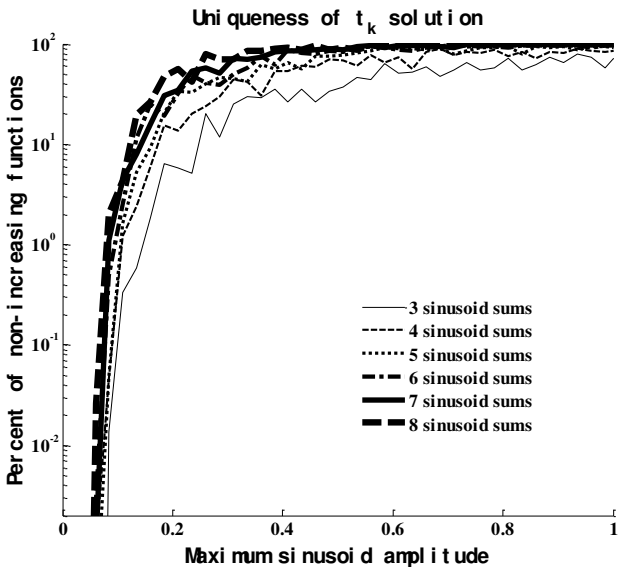

Figure 13.3. Simulation results for uniqueness of t_k solutions

In Figure 13.3, the simulated $ht(t_k)$ is generated from a given $\boldsymbol{L}$, and coefficients a_l, ω_l and φ_l, $1 \le l < L$, are randomly assigned. The a_l coefficients are uniformly distributed from $[0, \quad a_{\max}]$ with $a_{\max}$ below 1 and $a_L = a_{\max}$; the ω_l's are from a standard normal distribution and φ_l's from uniform distribution of $[-\pi, \quad \pi]$. A total of 5×10^5 realizations of $ht(t)$ are generated for each $a_{\max}$ for $t \in [0, \quad 5]$ with spacing of 0.02, and then we check if $ht[t]$ is increasing from its samples. The percent of non-increasing realizations for each $a_{\max}$ value are shown in the figure, and the process repeated for various L's. With 95% confidence, the $ht(t)$ sequence is increasing and thus t_k solutions of (13.1.25) are unique when $a_{\max} < 0.06$ for $L \le 10$.

It's straightforward to approximate $\sin t$ with a rational expression for $t \in [0, \quad \pi]$ by using the Bhaskara-I's sine approximation formula:

$$\begin{cases} \sin t \approx \mathrm{Sa}(t) := \frac{16t_r(\pi+t_r)}{5\pi^2+4t_r(\pi+t_r)} \\ \cos t \approx \mathrm{Ca}(t) := \frac{\sqrt{5}(\pi+2t_r)\sqrt{5\pi^2-12\pi t_r-12t_r^2}}{5\pi^2+4t_r(\pi+t_r)} \end{cases} \text{when } t - \left\lfloor \frac{t}{2\pi} \right\rfloor \in (\pi, \quad 2\pi) \quad (13.2.20a)$$

$$\begin{cases} \sin t \approx \mathrm{Sa}(t) := \frac{16t_r(\pi-t_r)}{5\pi^2-4t_r(\pi-t_r)} \\ \cos t \approx \mathrm{Ca}(t) := \frac{\sqrt{5}(\pi-2t_r)\sqrt{5\pi^2+12\pi t_r-12t_r^2}}{5\pi^2-4t_r(\pi-t_r)} \end{cases} \text{when } t - \left\lfloor \frac{t}{2\pi} \right\rfloor \in [0, \quad \pi) \quad (13.2.20b)$$

where $t_r = \begin{cases} t - \left\lfloor \frac{t}{2\pi} \right\rfloor, & t - \left\lfloor \frac{t}{2\pi} \right\rfloor \in [0, \quad \pi) \\ t - \left\lfloor \frac{t}{2\pi} \right\rfloor - 2\pi & t - \left\lfloor \frac{t}{2\pi} \right\rfloor \in (\pi, \quad 2\pi) \end{cases} \in [-\pi, \quad \pi]$. Replace t for t_r in (13.2.20) when $t \in (-\pi, \quad \pi)$.

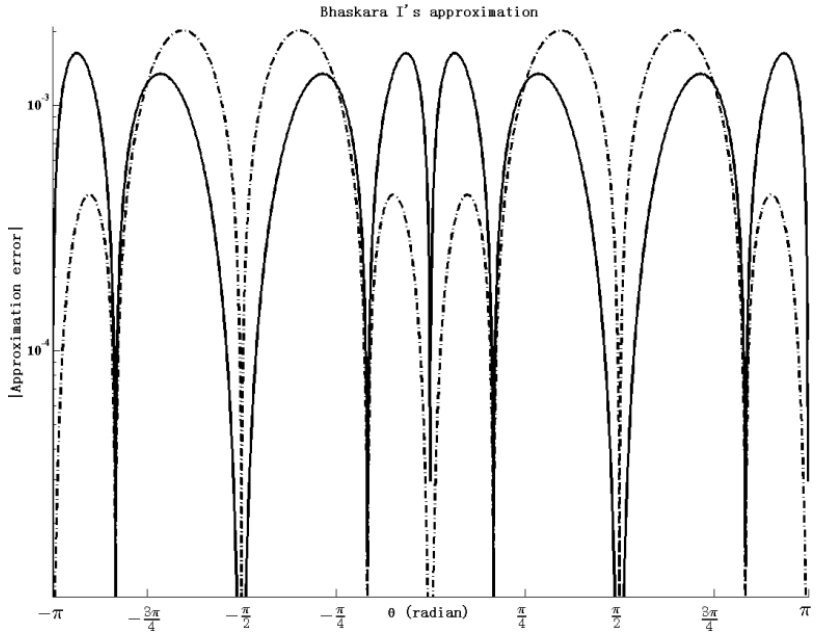

Figure 13.4. Approximation errors for Bhaskara I's formula. The solid line shows $|\sin t - \mathrm{Sa}(t)|$ and the dash-dotted line shows $|\cos t - \mathrm{Ca}(t)|$.

Figure 13.4 shows the Bhaskara I's approximation error $|\sin t - \mathrm{Sa}(t)|$ in solid line and $|\cos t - \mathrm{Ca}(t)|$ in dash-dotted line.

By imposing the constraint that $\omega_l \in \mathbb{Q}^+$, extending the greatest common divisor (GCD) to $\mathbb{Q}$, and letting $\omega_M = \frac{1}{\mathrm{GCD}\{\omega_l^{-1} | 1 \le l \le L\}}$, $R \triangleq \frac{k}{N} t_N + \sum_{l=1}^{L} b_l \sin \varphi_l$, $n \triangleq \left\lfloor \frac{\omega_l R}{2\pi} \right\rfloor$, $R_r \triangleq R - \frac{2n\pi}{\omega_M} \in \left[0, \quad \frac{2\pi}{\omega_M}\right)$ and $t_k^s \triangleq t_k - \frac{2n\pi}{\omega_M}$, $\omega_l t_k^s \in [0, \quad 2\pi)$ and (13.2.19) reduces to

$$\sum_{l=1}^{L} b_l \mathrm{Sa}(\omega_l t_k^s + \varphi_l) + t_k^s = R_r \tag{13.2.21}$$

with classification of quadrants of term $\omega_l t_k^s + \varphi_l$ for each l, it's *possible* to approximate (13.2.19) by solving a cubic equation, thereby determining analytically the firing times of finite sinusoids based on the IPFM model.

When *ht* is known at $\{t_k\}$ instants, a spline interpolation is used to obtain a continuous function with known value at irregularly spaced instants. Note that $h(t) \in \mathbb{C}^\infty$ is smooth, and the k-th derivative of $m(t)$ is

$$ht^{(k)}(t) = (-1)^{\left\lfloor \frac{k}{2} \right\rfloor} \sum_{l=1}^{L} \omega_l^{k-1} \cos\left\{\omega_l t + \varphi_l - \frac{\pi}{4}[1 + (-1)^k]\right\} \tag{13.2.22}$$

Let the L_p-th order spline be piecewise polynomials $P_j(t) = \sum_{l=0}^{L_p-1} p_j(l) t^l, \quad t \in [t_{j-1}, \quad t_j]$ satisfying $P_j^{(k)}(t_j) = P_{j+1}^{(k)}(t_j)$ for $0 \le k < L_p$. By substituting

$$P_j^{(k)}(t_j) = ht^{(k)}(t_j) = \sum_{l=0}^{L_p-k-1} \prod_{m=1}^{k} (m + l)\, p_j(l + k) t_j^l \tag{13.2.23}$$

we obtain L_p linear equations at each t_j for coefficients p_j's. In matrix notation:

$$\begin{pmatrix} 1 & t_j & t_j^2 & \cdots & t_j^{L_p-2} & t_j^{L_p-1} \\ 0 & 1 & 2t_j & \cdots & (L_p-2)t_j^{L_p-3} & (L_p-1)t_j^{L_p-2} \\ \vdots & \vdots & \vdots & \ddots & \vdots & \vdots \\ 0 & 0 & 0 & \cdots & 0 & (L_p-1)! \end{pmatrix} \begin{pmatrix} p_j(0) \\ p_j(1) \\ \vdots \\ p_j(L_p-1) \end{pmatrix} = \begin{pmatrix} ht(t_j) \\ ht'(t_j) \\ \vdots \\ ht^{(L_p-1)}(t_j) \end{pmatrix} \tag{13.2.24}$$

The solutions can be written in the recursive form:

$$\begin{cases} p_j(L_p-1) = \frac{ht^{(L_p-1)}(t_j)}{(L_p-1)!} \\ p_j(k) = \frac{1}{k!}\left[ht^{(k)}(t_j) - \sum_{l=1}^{L_p-k-1} \prod_{m=1}^{k}(m+l)\, p_j(k+l) t_j^l\right] \end{cases} \tag{13.2.25}$$

So that the analytic form of spline approximating finite sinusoidal summations is solved, an actual firing rate at any time can be approximated by substituting (13.2.25) into (13.2.22)–(13.2.23).

13.2.5 LeFever and DeLuca Method

LeFever and Deluca convolved a discrete Hanning function with the discrete impulse train $\{t_k = kT_s : k \in \mathbb{N}, t_k < t_{k+1}\}$ sampled at $\frac{1}{T_s}$ Hz to obtain an estimate of the average firing rate of EMG. The Hanning function may be replaced by any other commonly used window function.

The sampled input pulse sequence $x[n]$ for constant firing rate $t_k = kT$, extending to infinity in both directions; and the Hanning function $\mathrm{w}[n]$ of length $2N+1$ are:

$$x[n] = \sum_{l=-\infty}^{\infty} \delta(n - lT) \tag{13.2.26}$$

$$\mathrm{w}[n] = \frac{1}{2}\left(1 + \cos\frac{n\pi}{N}\right)\mathbf{1}_{[-N,\ \ N]}[n] \tag{13.2.27}$$

The filtered output is:

$$\begin{aligned} r_{\mathrm{LeFever}}[n] = x[n] \otimes \mathrm{w}[n] &= \frac{1}{2}\sum_{l=-\infty}^{\infty}\left(1 + \cos\frac{n-lT}{N}\pi\right)\mathbf{1}_{\left[\frac{n-N}{T}\ \ \frac{n+N}{T}\right]}[l] \\ &= \frac{l_2 - l_1 + 1}{2} + \frac{1}{2}\sum_{l=l_1}^{l_2}\cos\frac{n-lT}{N}\pi \end{aligned} \tag{13.2.28}$$

where $l_1 = \left\lceil\frac{n-N}{T}\right\rceil$ and $l_2 = \left\lfloor\frac{n+N}{T}\right\rfloor$. Note that $-1 < l_2 - l_1 - \frac{2N}{T} < 1$, so $\frac{l_2-l_1+1}{2} \in \left(\frac{N}{T},\ \ \frac{N}{T}+1\right)$ is approximately linear with $\frac{1}{T}$. Let $\hat{r}_{\mathrm{LeFever}}[n] = \frac{N}{T}$, then

$$E_{\mathrm{LeFever}}[n] = r_{\mathrm{LeFever}}[n] - \hat{r}_{\mathrm{LeFever}}[n] = \left(\frac{l_2-l_1+1}{2} - \frac{N}{T}\right) + \frac{1}{2}\sum_{l=l_1}^{l_2}\cos\frac{n-lT}{N}\pi \tag{13.2.29}$$

Use identity $1 - e^{j\theta} = 2\sin\frac{\theta}{2}e^{\frac{\theta-\pi}{2}j}$ to evaluate the second term:

$$\sum_{l=l_1}^{l_2} \cos\frac{n-lT}{N}\pi = \mathrm{Re}\left\{\sum_{l=l_1}^{l_2} e^{\frac{n-lT}{N}j\pi}\right\}$$
$$= \sqrt{1+\cot^2\frac{T}{2N}\pi}\cos\left(\frac{n}{N}-\frac{l_1+l_2}{2N}T\right)\pi\sin\left(\frac{l_2-l_1}{2N}T\pi+\alpha\right) \quad (13.2.30)$$

with α satisfying $\begin{cases} \sin\alpha = 1/\sqrt{1+\cot^2\frac{T}{2N}\pi} \\ \cos\alpha = \cot\frac{T}{2N}\pi/\sqrt{1+\cot^2\frac{T}{2N}\pi} \end{cases}$.

Observing from (13.2.21) that $\left|\sum_{l=l_1}^{l_2}\cos\frac{n-lT}{N}\pi\right| \le \sqrt{1+\cot^2\frac{T}{2N}\pi}$ and substituting it into (13.2.28) gives $|E_{\mathrm{LeFever}}[n]| < 1+\frac{1}{2}\sqrt{1+\cot^2\frac{T}{2N}\pi}$, which implies the upper bound of estimation error is determined by the Hanning function length N and firing period T. When $N \gg T \ge 1$ (trivially satisfied), we have $|E_{\mathrm{LeFever}}[n]| \le 1+\frac{1}{2}\sqrt{1+\cot^2\frac{T}{2N}\pi} \sim \frac{N}{T}$, when the upper bound becomes overly pessimistic as $\left|\frac{l_2-l_1}{2N}T\pi\right| < \frac{\pi}{2N} \ll 1$, $|\alpha| \approx |\sin\alpha| \approx \frac{T\pi}{2N} \ll 1$ so that in (13.2.30), $\left|\sin\left(\frac{l_2-l_1}{2N}T\pi+\alpha\right)\right| \sim \frac{T+1}{2N}\pi \ll 1$. Therefore, the perturbation term in (13.2.28) is negligible when the constant term $\frac{l_2-l_1+1}{2} = \frac{1}{T} \gg 1$.

13.3 Stochastic analysis of firing rate simulation

In a more realistic setting of the CNS encoding process, the modulation function of the IPFM model is stochastic and non-stationary. The physiological range of firing rate and bandwidth of variations, amongst other factors, determine how *m*(*t*) looks like.

To obtain a stochastic generator of families modulation functions and thus the firing rates from IPFM model whose resulting IPIs conform to known observations, we tried several methods. We started easy and observed the shortcomings of its outcome, and gradually evolved the design of modulation function generators. The goal was to produce IPI histograms consistent with those from experimental studies.

In a less ideal setting, i.e. in the presence of decomposition errors, various methods to calculate firing rates are more or less affected by missing and spurious firings. In the simplest case, we look at how much the RMSE deteriorates for the instantaneous method. For the continuous case (i.e. firing time can be arbitrary as opposed to uniform grids in the discrete case). Note that the precision of measurement is constrained by sampling frequency and the precise timing of an event, and the refractory period of neural firing

further imposes a "hard limit" on the attainable upper limit of firing frequency. These make such strict temporal analysis of this section in real domain of little practical value. We show that RMSE deterioration for either spurious or missed firings can be arbitrarily large. Then we give upper bounds for the two cases in the discrete case.

13.3.1 Stochastic approaches of firing rate simulation

One approach to a modulation function is to use a sinusoidal model as (13.2.17) with time-varying parameters coming from some stochastic process. This approach has the advantage of precisely knowing *a priori* variation of modulation once processes a_t and f_t are well known and satisfy certain conditions (bounded value, bounded total variation, etc.), and the disadvantage that its spectrum is hard to analyze even for constant a_t.

Another approach is to down-sample a discrete random process to the desired bandwidth and interpolate back to the higher sampling rate. Bendat [Bendat 2010] had shown that for a Gaussian process, the relationship between the bandwidth B_e of a spectrum with constant amplitude within B_e, and a degree of freedom n in given time T:

$$n = 2B_eT \tag{13.3.1}$$

From this relation the number of independent samples per second required to achieve a desired statistical bandwidth can be inferred. For a modulation frequency of 1 Hz (or 1pps/sec), two samples per second are required.

DeLuca [DeLuca 1979] has shown that the IPI histograms from a MUAPT for constant contraction assume a shifted Weibull distribution with PDF $f_x(x)$ and CDF $F_x(x)$:

$$f_x(x) = \frac{k}{\beta}\left(\frac{x-\alpha}{\beta}\right)^{k-1} \exp\left[-\left(\frac{x-\alpha}{\beta}\right)^{k}\right] \mathbf{1}_{[0,\ \infty)}(x-\alpha) \tag{13.3.2a}$$

$$F_x(x) = \left\{1 - \exp\left[-\left(\frac{x-\alpha}{\beta}\right)^{k}\right]\right\} \mathbf{1}_{[0,\ \infty)}(x-\alpha) \tag{13.3.2b}$$

$$EX = \beta\Gamma\left(1+\frac{1}{k}\right) \tag{13.3.2c}$$

with $k \in (0.97, 1.34)$, $\beta \in (31.19, 194.42)$ and $1.07 \le \alpha \le 6.71$ ms from his finding and Γ the Gamma function. Others have reported symmetric/skewed distributions.

It's straightforward from (13.1.2) and (13.1.22) that the relationship between instantaneous rate $r(t) = \frac{1+m(t)}{T}$ and the reciprocal relationship between instantaneous rate and inter-pulse interval as a time-varying continuous function, that when random variable y comes from the modulation process $m(t)$, then the random variable $1/y$ must follow the same distribution of IPI histogram as in (13.3.2) [Papoulis 2002]. This gives

$$f_y(y) = \frac{k\mathbf{1}_{[0,\ \infty)}(y-\alpha)}{\beta^k (y-\alpha)^{(k+1)} \exp\{[\beta(y-\alpha)]^{-k}\}} \tag{13.3.3a}$$

$$F_y(y) = \exp\{-[\beta(y-\alpha)]^{-k}\}\, \mathbf{1}_{[0,\ \infty)}(y-\alpha) \tag{13.3.3b}$$

$$Ey = \frac{1}{\beta}\Gamma\left(1-\frac{1}{k}\right) \tag{13.3.3c}$$

with parameters k, α and β in the aforementioned range. As this random variable has positive expectation, the requirement that the modulation process be zero-mean is addressed by

$$\check{x}(t) = \int_0^t \frac{1+m(\tau)}{T(1+Ey)}\, d\tau \tag{13.3.4}$$

so that the n-th firing instant occurs when the numerator of the integrand accumulates to $nT(1+Ey)$. Random variable y can be generated by transforming the standard uniform random variable u using $y = \alpha + \left[\beta(-\ln u)^{\frac{1}{k}}\right]^{-1}$.

To obtain an estimate of the PDF of the resulting IPI from different modulation functions, the modulation function is discretized at 4096 Hz using 100 second duration sequences. First, i.i.d. uniform random variables are transformed to the distribution of y. Then spline interpolation with the factor obtained from (13.4.1), followed by thresholding is used such that the resulting statistical bandwidth of $m(t)$ is roughly around the desired value (1Hz) satisfying $m(t) \geqslant -1$. For a summation to approximate the integral process of the IPFM, N=20 divisions per sampling interval are taken: $\int_{nT_s}^{(n+1)T_s} f(t)\, dt \approx \frac{T_s}{N}\sum_{k=0}^{N-1} f\left(\left(n+\frac{k}{N}\right)T_s\right)$. A total of 16 repetitions of realizations of the modulation function are taken and their result averaged to obtain a PDF estimate. When estimating the PDF of the resulting IPIs, 2048 samples along a uniform logarithmic scale spanning from 0.002 to 300 are taken and the Gaussian kernel for kernel density estimation is used with support of IPI>0.

Figure 13.5 shows the estimated density function of y and its reciprocal with a fixed set of parameters (k=1.2, β=130 and α=0), together with the theoretical density calculated from (13.3.2a) and (13.3.3a). The empirical results of IPIs from the given modulation are then used for kernel density estimation of IPIs, and a nonlinear regression to the Weibull PDF in (13.3.2a) with some reasonable initial values are used to check if it follows the Weibull distribution. A Kolmogorov-Smirnov test was also used to check y against (13.3.3b).

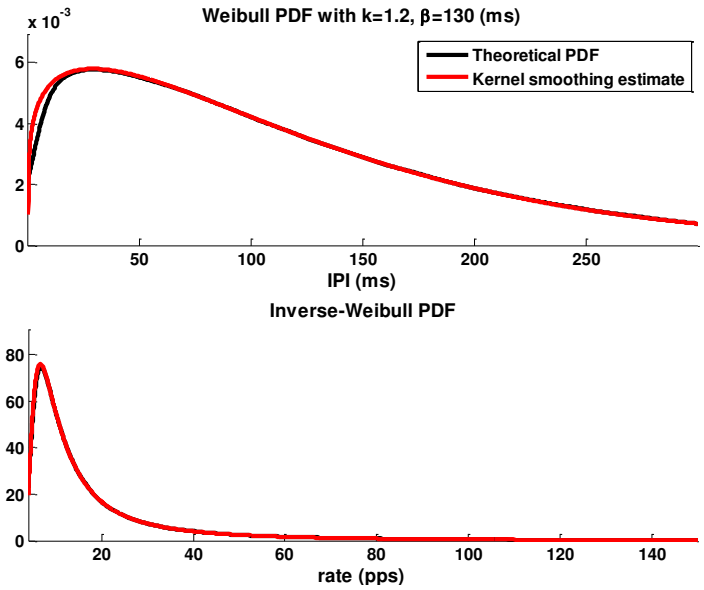

Figure 13.5. PDF estimates of Weibull distribution and instantaneous firing rate distribution. Theoretical and empirical distributions are shown in both plots.

Inspections of IPI distribution from simulation results using (13.3.3) show that the IPI histograms from (13.3.3) fail to follow the shifted Weibull distribution. There are several reasons for this disagreement: spline interpolation and thresholding after down-sampling of the modulation samples alter the distribution that is then fed to the IPFM model. Recall that spline interpolation can be viewed as a time-varying lowpass filtering process whose filter order is related to the interpolation factor (hereby from (13.3.1) the sampling frequency and statistical bandwidth) and, by the central limit theorem, filtering re-shapes most distributions towards the normal distribution. Due to this filtering effect, the expectation is for altered distribution changes when the original distribution is skewed. The discrete IPFM process approximates (13.3.1) by finite-step summation. The reset process that changes continuous output (3.3.2) to the point process $\{t_k\}$ also alters the IPI distributions. Amongst all these factors, we found that the filtering effect from spline interpolation turns out to be most contributive to distortion of IPI distribution, as shown in Figure 13.6 as the kernel density estimates of IPI measured from a MUAP recorded during an isometric contraction [DeLuca 1973].

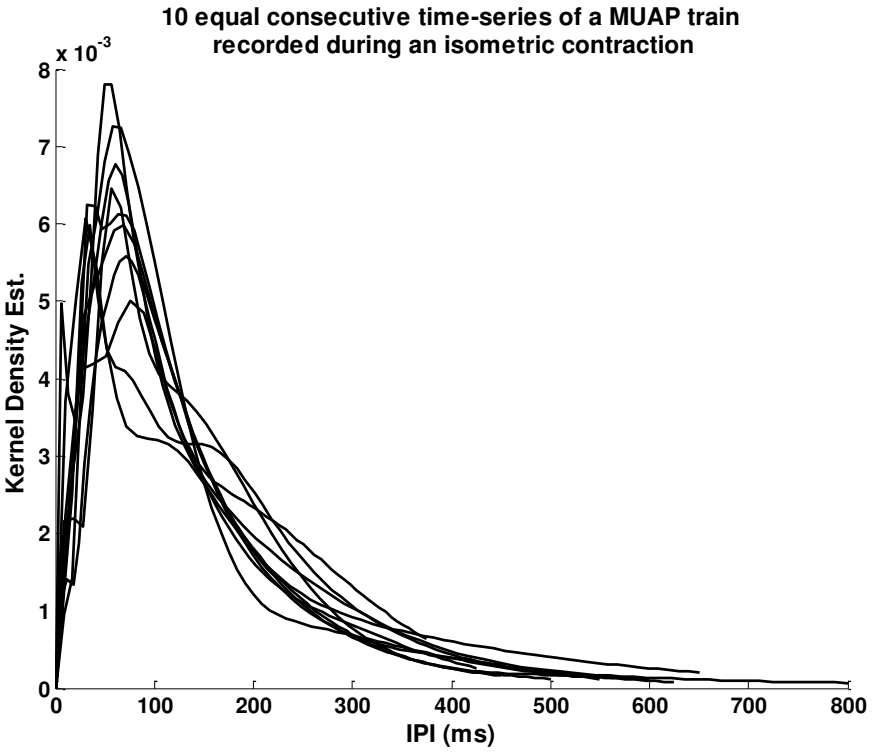

Figure 13.6. Kernel density estimates of 10 equal and consecutive time-series of a MUAP train that was recorded during an isometric contraction. Adapted from Figure 3 of [DeLuca 1973].

Other possible distributions for independent random variables as the modulation process $m(t)$ are described below.

Doubly-truncated zero-mean Gaussian with density function:

$$f_{x,m\sigma}(x) = \exp\left(-\frac{x^2}{2\sigma^2}\right) \Big/ \left[\sqrt{2\pi\sigma^2}\,\mathrm{erf}(m/\sqrt{2})\right] 1_{[-m\sigma,\ \ m\sigma]}(x) \qquad (13.3.5)$$

parameterized by standard deviation σ and truncation locations $\pm m\sigma$ (m>0), requiring that $m\sigma$ <1. A random number can be generated to fit the truncated distribution by simply discarding values that lie beyond the range of a Gaussian random number with the same mean and σ. The truncated distribution has discontinuities at the truncation locations with change related to m. The ensuing filtering and thresholding process makes the distribution of dependent samples of $m(t)$ more Gaussian. The spreading imposed on the resulting IPI distribution, though positively-skewed, is found to be densely packed around the mean value and does not attain the spread of the Weibull distribution of given parameter ranges in (6.4.2) or histograms of physiological measurements obtained by DeLuca and others. A plausible reason for this lack of spread is that the decay rate e^{-t^2} of a Gaussian is too fast so that too few samples fall away from the average IPI.

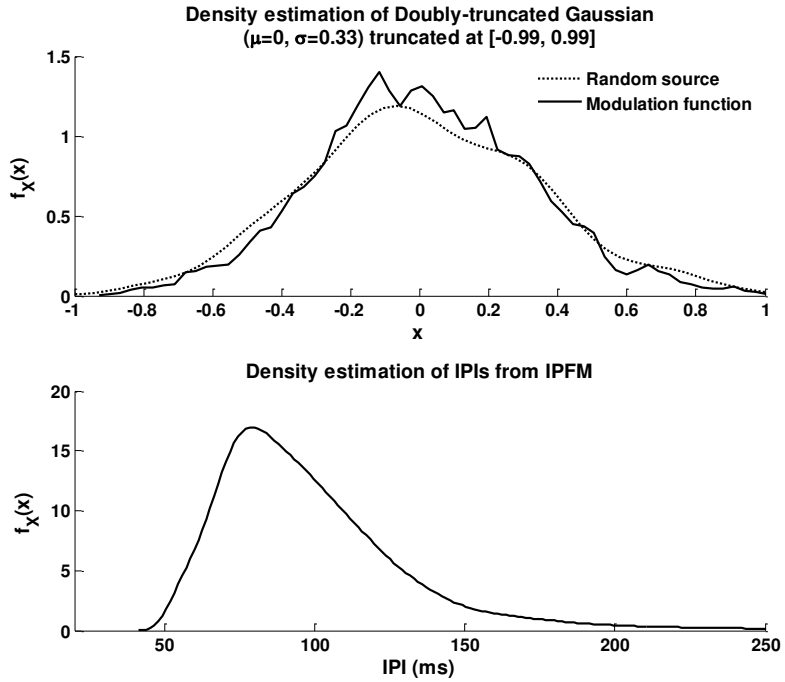

Figure 13.7. Kernel density estimations of the doubly-truncated zero-mean Gaussian model. The random number source (dash in upper plot), modulation function after interpolation and thresholding (solid in uppler plot) and the IPI from IPFM process

Figure 13.7 shows the shows the kernel density estimation of the doubly-truncated zero-mean Gaussian PRNG data source (dash in upper plot), spline-interpolated/thresholded modulation function (solid line in upper plot) and IPI distribution (lower) in a simulation. In this simulation, σ=0.33 and is truncated at ±3σ, the average IPI is chosen at 10 Hz and sEMG is generated at 4096 Hz with duration of 145 sec.

Piecewise-uniform with density $f_x(x) = \frac{b}{b-a}1_{[a,0)}(x) - \frac{a}{b-a}1_{[0,b]}(x)$ parameterized by $-1 \leq a < 0 < b$. It is zero-mean and has a discontinuity at 0 except when $a=-b$ (symmetric). The first term contributes to the right tail $\left(T,\ \frac{T}{1+a}\right)$, and second term the left portion $\left(\frac{T}{1+b},\ T\right)$ of the IPI distribution. Random numbers from a mixture model such as piecewise-uniform can be generated by assigning each sample to one of the distributions, which is generated from that pseudo random number generator (PRNG). The filtering effect broadens the density function so that the left/right bounds given above are larger/smaller than the bounds of $m(t)$. When $a+b \gg 1$ it causes a thump at x=0 due to the discontinuity in the density function and the filtering effect. The resulting IPI distribution exhibits a bimodal shape, which is unrealistic from a clinical point of view for the sEMG of constant-force contraction. When we set a~-1 and $a+b$~0 (typically $a \leqslant$ -0.8), the

distribution looks more Weibull-like but the spread is still tight as compared with physiological data.

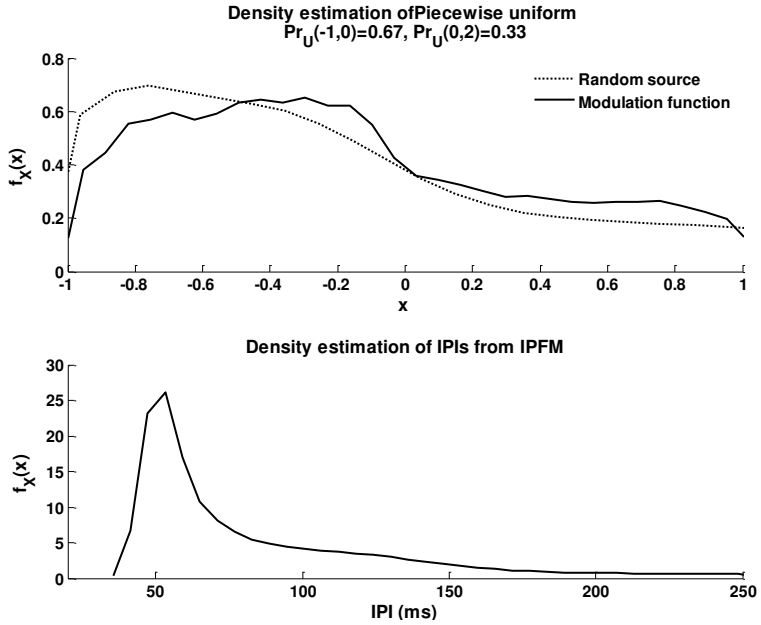

Figure 13.8. Kernel density estimations of the piece-wise uniform random model. The random number source (dash in upper plot), modulation function after interpolation and thresholding (solid in uppler plot) and the IPI from IPFM process (lower plot).

Figure 13.8 shows the kernel density estimation of the piecewise-uniform PRNG data source (dash in upper plot), spline-interpolated/thresholded modulation function (solid line in upper plot) and IPI distribution (lower) in a simulation. In this simulation, a=-1, b=2 are chosen.

Discrete uniform with $\Pr\{x = -1\} = \Pr\{x = 1\} = 0.5$. This gives sufficient samples at both low and high ends after interpolation (i.e. sufficient samples in $[-1-\varepsilon,\ \ -1+\varepsilon]$ and $[1-\varepsilon,\ \ 1+\varepsilon]$ for $\varepsilon \approx 0.1$). This yields sufficient data samples at both ends of IPFM firing rate in ranges $\left[\frac{1}{T_{max}}(1-\varepsilon),\ \ \frac{1}{T_{max}}(1+\varepsilon)\right]$ and $\left[\frac{1}{T_{min}}(1-\varepsilon),\ \ \frac{1}{T_{min}}(1+\varepsilon)\right]$; but the IPI distribution only remotely resembles the shifted Weibull distribution as shown in Figure 13.9.

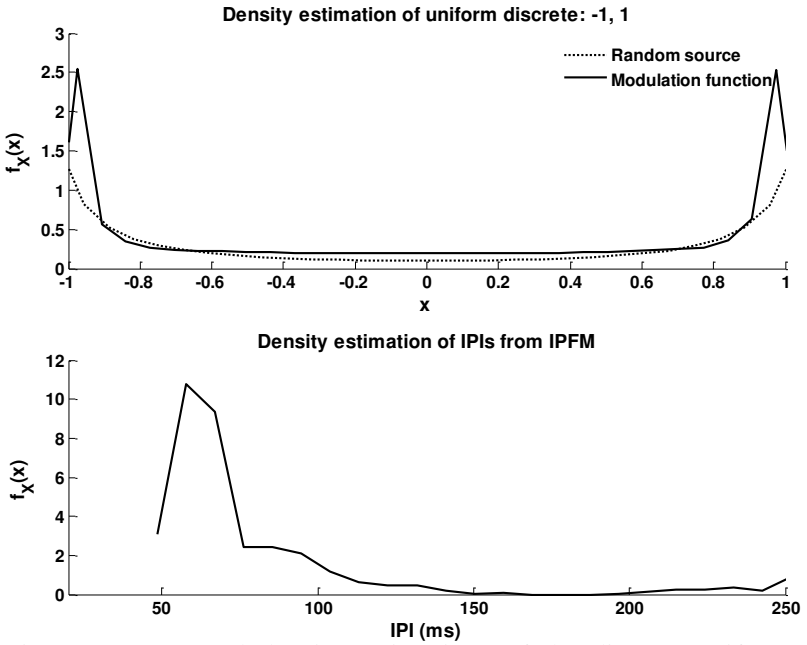

Figure 13.9. Kernel density estimations of the discrete uniform random model. The random number source (dash in upper plot), modulation function after interpolation and thresholding (solid in uppler plot) and the IPI from IPFM process (lower plot).

The truncated Gaussian-mixture model with density function:

$$f_x(x) = \left[\mathrm{w}\mathcal{N}_{-1,\sigma_1}(x) + (1-\mathrm{w})\mathcal{N}_{1,\sigma_2}(x)\right]1_{(-1,\ \ 1)}(x) \tag{13.3.6a}$$

$$\mathcal{N}_{\mu,\sigma}(x) = \exp\left[\frac{-(x-\mu)^2}{2\sigma^2}\right]\Big/\sqrt{2\pi\sigma^2} \tag{13.3.6b}$$

$$\mathrm{w} = \frac{\sigma_2 B - \frac{D}{\sqrt{2}} + \sqrt{\frac{\pi}{2}}}{\sigma_1 A + \sigma_2 B - \frac{C+D}{\sqrt{2}} + \sqrt{2\pi}} \tag{13.3.6c}$$

$$A = \Gamma\left(1, \frac{2}{\sigma_1^2}\right) - 1,\ B = \Gamma\left(1, \frac{2}{\sigma_2^2}\right) - 1,\ C = \Gamma\left(\frac{1}{2}, \frac{2}{\sigma_1^2}\right),\ D = \Gamma\left(\frac{1}{2}, \frac{2}{\sigma_2^2}\right) \tag{13.3.6d}$$

where $\Gamma(a,z) = \int_z^\infty t^{a-1}e^{-t}\,dt$ is the incomplete Gamma function. This distribution is zero-mean, continuous in (-1, 1) and is parameterized by the two standard deviations σ_1, σ_2>0 of the two truncated Gaussian distributions.

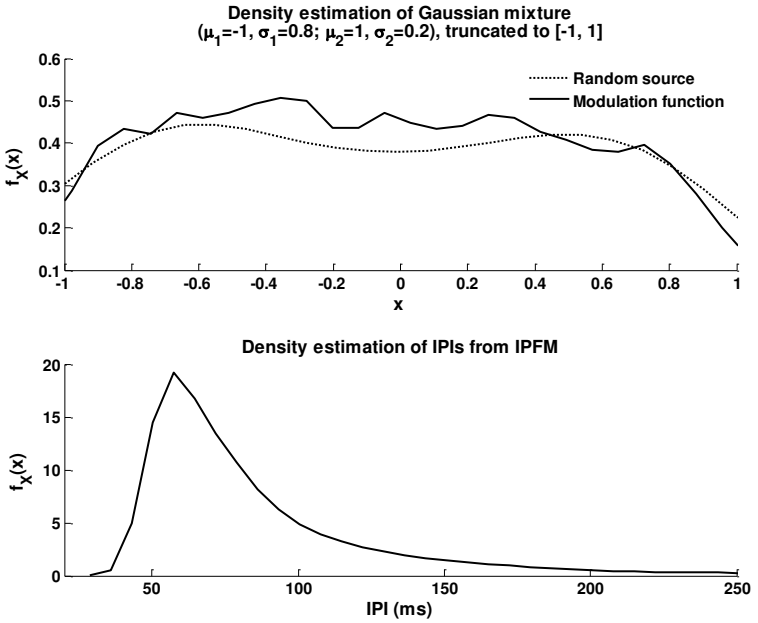

Figure 13.10. Kernel density estimations of the truncated Gaussian mixture model. The random source (dash in upper plot), modulation function after interpolation and thresholding (solid in uppler plot) and the IPI from IPFM process (lower plot).

Figure 13.10 shows the kernel density estimates of truncated Gaussian mixture model. Two Gaussian distributions from $\mathcal{N}_{-1,0.8}$ and $\mathcal{N}_{1,0.2}$. It is found that $\min(\sigma_1, \sigma_2) < 0.1$ violates the shifted Weibull shape of IPI distribution, and that the spread is still not attained in either polarity.

The uniform-truncated-Cauchy mixture model with density function

$$f_x(x) = \mathrm{w}1_{[-1,0]}(x) + \frac{1-\mathrm{w}}{\pi\gamma\left[1+\left(\frac{x}{\gamma}\right)^2\right]}1_{(0,T)}(x) \tag{13.3.8a}$$

$$T = \gamma\sqrt{\exp\left(\frac{1}{\gamma^2}\right) - 1}, \qquad \mathrm{w} = \left(1 + \gamma\,\mathrm{atan}\frac{T}{\gamma}\right)^{-1} \tag{13.3.8b}$$

and is parameterized by γ>0 that controls the decaying rate. It is zero-mean, continuous in $[-1, T]$ and the right-side truncated tail has even slower decay rate than the uniform-exponential mixture model. Simulation results show that the majority of resulting IPIs are typically >500ms and thus unacceptable.

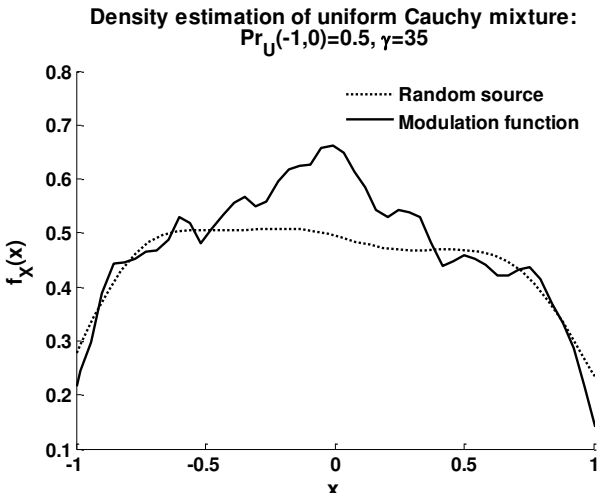

Figure 13.11. Kernel density estimations of the uniform-Cauchy mixture model. The random source (dash in upper plot), modulation function after interpolation and thresholding (solid in uppler plot) and the IPI from IPFM process (lower plot).

Figure 13.11 shows the density estimate of using uniform-Cauchy mixture model. The distribution of resulting IPI is not shown because its minimum value occurs at >500ms and therefore deviates far from the shifted Weibull distribution.

The uniform-exponential mixture model with density function

$$f_x(x) = \frac{1}{2a} 1_{[-a,0]}(x) + \frac{1}{2a} \exp\left(-\frac{x}{a}\right) 1_{(0,\infty)}(x) \qquad (13.3.7)$$

is zero-mean, continuous in $[-a, \infty)$ and is parameterized by $0 \leq a < 1$. The right tail enables the resulting IPIs to take 0 as their lower bound and parameter a controls the decay of both tails of the IPI distribution. The decay rate e^{-t} of the density is also slower than Gaussian. By varying parameter a, it's observed that (0.8, 1) seem to be a good range to give plausible IPI histograms that match both the shifted Weibull distribution and the physiological dataset.

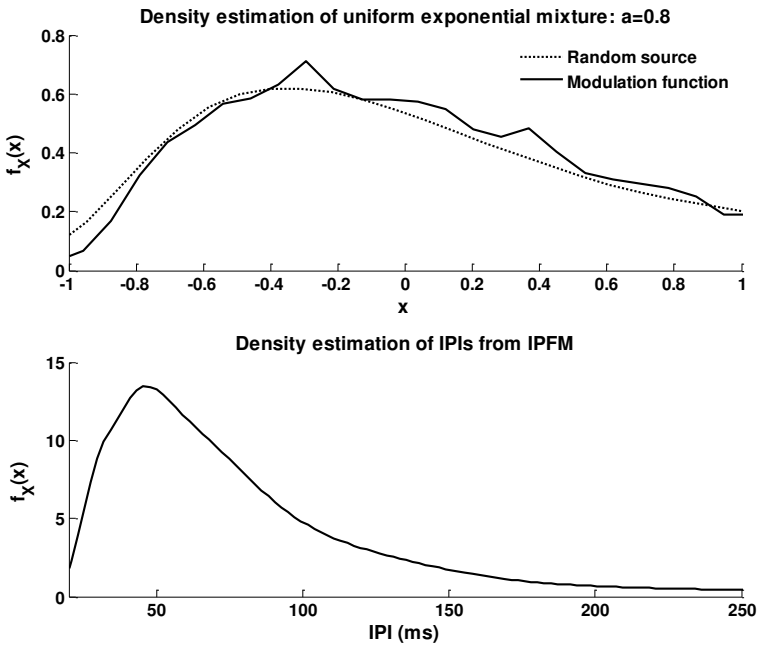

Figure 13.12. Kernel density estimations of the uniform-exponential mixture model. The random source (dash in upper plot), modulation function after interpolation and thresholding (solid in uppler plot) and the IPI from IPFM process (lower plot).

Figure 13.12 shows the density estimates using PRNG from this model when a=0.9. The IPI distribution matches closely to the ideal distribution from Figure 13.5 and measurement distribution from Figure 13.6. Therefore, this PRNG model with parameter a=0.9 is used to generate ground truth firing rate which is then used to obtain firing times for stochastic simulations.

13.3.2 Bounds for instantaneous RMSE due to decomposition error in firing rate

It is interesting to take a brief look at how much damage a "fly in the ointment" can bring or, in this context, how awry firing rate can become because of decomposition error. First we look at the continuous time-domain, where actual firing times as well as spurious ones are real and arbitrary. Then we march to the discretized domain. Note that due to frequency aliasing and the precision limit of temporal resolution (i.e. sampling frequency) of signal acquisition devices, and the neural refractory period that limits possible neural firing frequency, the analysis in the real domain is of little practical interest.

First we look at firing instants in the continuous time-domain. Let the IPI of a finite duration interval be the renewal process: $\Delta \triangleq \{0 < \Delta_k < T, \quad 1 \leq k \leq N\}$from the firing instants $\chi \triangleq \{0 < t_k < t_{k+1} < T, \quad 1 \leq k < N \quad t_k \in \mathbb{R}^+\}$, the false positive rate be ρ_+ and the false negative rate be ρ_-. Then there are on average a total of $N\rho_+$ spurious firings: $\chi_+ \triangleq \{0 < t_k^+ < T, \quad 1 \leq k \leq N\rho_+ \quad t_k \in \mathbb{R}^+\}$ satisfying $\chi_+ \cap \chi = \emptyset$; and a

total of $N\rho_-$ missed firings $\chi_- \triangleq \{\chi_k^- \in \chi, \quad 1 \le k \le N\rho_-\}$. In general, the RMSE between the two firing sequences of the same duration $0 \le t \le T$: $\chi_1 \triangleq \{0 < t_k < t_{k+1} < T, \quad 1 \le k < N_1 \quad t_k \in \mathbb{R}^+\}$, $\chi_2 \triangleq \{0 < \zeta_k < \zeta_{k+1} < T, \quad 1 \le k < N_2 \quad \zeta_k \in \mathbb{R}^+\}$ is:

$$\text{RMSE} = \left[\sum_{k=1}^{N_1}\sum_{j=1}^{N_2}\left(\frac{1}{t_{k+1}-t_k} - \frac{1}{\zeta_{j+1}-\zeta_j}\right)^2 \int_0^\infty 1_{[t_k,t_{k+1})}(t)1_{[\zeta_j,\zeta_{j+1})}(t)\,dt\right]^{1/2} \quad (13.3.9)$$

with $\{k\}=\{1 \le n \le N_1\}$ and $\{j\}=\{1 \le n \le N_2\}$ for both terms under the square root. Note that the integration represents the overlapping portion of two intervals $[t_k, \quad t_{k+1}]$ and $[\zeta_j, \quad \zeta_{j+1}]$.

It's easy to show that the RMSE due to a false positive event is unbounded (instantaneous rate can be arbitrarily when the false positive occurs at a time infinitesimally after/before an existing firing, thus error jumps unbounded in this region; similarly when a missing firing occurs infinitesimally close to another firing, the maximal instantaneous firing rate drastically drops in that region), which is equivalent to show that the RMS of Dirac delta function over a *finite* interval is infinite. The measureable Dirac delta function and its RMS are given below, thanks to the monotone convergence theorem (by letting $f_n(t) = \lim_{\tau\to 0}\frac{1_{(0,\tau)}(t)}{\tau+\varepsilon_n}$, $\lim_{n\to\infty}\varepsilon_n = 0$ in the theorem).

$$\delta(t) = \lim_{\tau\to 0}\frac{1_{(0,\tau)}(t)}{\tau} \quad (13.3.10)$$

$$\text{RMS}_{\delta(t)} = \sqrt{\frac{1}{T}\int_0^T \delta^2(\tau)\,d\tau} = \sqrt{\frac{1}{T}\lim_{\xi\to 0}\int_0^T \frac{1_{(0,\xi)}(\tau)}{\xi^2}d\tau} = \infty \quad (13.3.11)$$

Now let's see the effects of missing one firing event on RMSE. Assume that the *l*-th firing was missing, where $1<l<N$. Assume that $\lambda = \frac{\Delta_l}{\Delta_{l+1}}$ (note that Δ_l and Δ_{l+1} are interchangeable), then the RMSE becomes:

$$\text{RMSE}_{l-}^2 = \frac{1}{\Delta_l^2} + \frac{1}{\Delta_{l+1}^2} - \frac{1}{(\Delta_l+\Delta_{l+1})^2} = \frac{1}{\Delta_l^2}\left[1 + \frac{1}{\lambda} - \frac{1}{(1+\lambda)^2}\right] \to \infty, \lambda \to 0^+$$

Similar to a false positive, there is no upper-bound due to a single missed firing: (13.3.10)–(13.3.11) applies to missed firings in exactly the same way.

The upper bound of RMSE due to false negative occurs in similar condition as the upper bound of a false positive. Let $\Delta_{\max}(k)$ denote the *k*-th maximum firing interval and $\Delta_{\min}(k)$ the *k*-th minimum, then the lower bound of a false positives occurs when the $N\rho_-$ maximum firing intervals are adjacent and spurious firings occur in the middle point of $\Delta_{\max}(k)$:

$$\inf\left|\mathrm{RMSE}-\mathrm{RMSE}_{\rho_+}\right|=\sqrt{\sum_{k=1}^{1+Nm_-}\Delta_{\max}^{-2}(k)} \tag{13.3.11}$$

and the lower bound of false negative occurs when $\{t_{\min}(k),\quad 1\le k\le 1+N\rho_-\}$ are adjacent and missing:

$$\inf\left|\mathrm{RMSE}-\mathrm{RMSE}_{m_-}\right|=\sqrt{\sum_{k=1}^{1+Nm_-}\Delta_{\min}^{-2}(k)}-\frac{1}{\sum_{k=1}^{1+Nm_-}\Delta_{\min}(k)} \tag{13.3.12}$$

More generally, let the renewal process Δ follow the density function $f_\Delta(t)$, positive only for $t>0$, be independent, identically distributed, and its expectation $\mathrm{E}\Delta$ be finite. The probability that a false negative event occurs at time t_s and the expectation of RMSE difference due to a single false negative event are given below. The analysis for multiple false negative events is more cumbersome.

$$\Pr\left\{t_s^-\in\{\Delta=\Delta_1\}\cap t_s^+\in\{\Delta=\Delta_2\}\right\}=f_\Delta(\Delta_1)f_\Delta(\Delta_2) \tag{13.3.13}$$

$$\mathrm{E}\left|\mathrm{RMSE}-\mathrm{RMSE}_{\rho^-}\right|=\int_0^\infty\int_0^\infty f_\Delta(t)f_\Delta(\tau)\left(\sqrt{t^{-2}+\tau^{-2}}-\frac{1}{t+\tau}\right)dt\,d\tau \tag{13.3.14}$$

The probability that a false positive event occurs in an interval of duration t is $\frac{tf_\Delta(t)}{\mathrm{E}\Delta}$, and is by assumption uniformly distributed inside this interval. The expectation of RMSE difference due to a single false positive event is infinite:

$$\begin{aligned}\mathrm{E}\left|\mathrm{RMSE}-\mathrm{RMSE}_{\rho^+}\right|&=\int_0^\infty\frac{tf_\Delta(t)}{\mathrm{E}\Delta}\int_0^t\frac{\sqrt{t^{-2}+(\tau-t)^{-2}}-1/t}{t}d\tau\,dt\\&=\frac{1}{\mathrm{E}\Delta}\int_0^\infty f_\Delta(t)\left(\int_0^t\sqrt{t^{-2}+(\tau-t)^{-2}}\,d\tau-1\right)dt=\infty\end{aligned} \tag{13.3.15}$$

When the signal is sampled with F_s Hz, the upper bound of RMSE due to false positive occurs when each spurious event occurs at the next sampling time of a minimal event (not necessarily adjacent). With $\tilde{\Delta}_{\min}(k)$ be the k-th minimum elements of Δ that is larger than $\frac{1}{F_s}$, this gives

$$\sup\left|\mathrm{RMSE}-\mathrm{RMSE}_{\rho_+}\right|=NF_s\rho_++\sqrt{\sum_{k=1}^{N\rho_+}\left(\tilde{\Delta}_{\min}(k)-\frac{1}{F_s}\right)^{-2}}-\sqrt{\sum_{k=1}^{N\rho_+}\tilde{\Delta}_{\min}^{-2}(k)} \tag{13.3.16}$$

The other bounds are close to (13.3.3)–(13.3.5), except due to the fact that t_k is now discretized.

For the discrete case, let $f_\Delta[n] = \lim_{\tau\to 0^+}\int_{-\tau}^{\tau} f_\Delta(nT_s + t)\,dt$ be the discrete mass function of IPIs with expectation $\mathrm{E}\Delta = \sum_{n=1}^{\infty} n f_\Delta[n] < +\infty$. Then the expectations of RMSE difference due to a single false positive event or a single false negative event are:

$$\mathrm{E}\left|\mathrm{RMSE} - \mathrm{RMSE}_{\rho^+}\right| = \frac{F_s}{\mathrm{E}\Delta - 1}\sum_{n=2}^{\infty}(n-1)\,f_\Delta[n]\left(\sum_{m=1}^{n-1}\sqrt{m^{-2} + (n-m)^{-2}} - \frac{n-1}{n}\right) \tag{13.3.17}$$

$$\mathrm{E}\left|\mathrm{RMSE} - \mathrm{RMSE}_{\rho^-}\right| = F_s\sum_{n=1}^{\infty}\sum_{m=1}^{\infty} f_\Delta[n] f_\Delta[m]\left(\sqrt{n^{-2} + m^{-2}} - \frac{1}{n+m}\right) \tag{13.3.18}$$

It's straightforward that the set of rates calculated using the instantaneous method is a subset of rates calculated using the instantaneous spline method. Thus the bounds carry over to the instantaneous spline method.

In summary, for the continuous time-domain, the RMSE difference due to the presence of decomposition error is lower-bounded by the sum of (13.3.12) and (13.3.13), and its expectation is infinite; for periodically sampled time series, the RMSE is upper-bounded by approximately the sum of (13.3.11) and (13.3.17) and lower-bounded by approximately same amount as the continuous case. The RMSE differences for other calculating methods are bounded by the same settings but are harder to analyze.

13.4 Calculations of statistical bandwidth

In Chapters 4–7, we showed that application of signal whitening significantly improves sEMG classification accuracy for prosthesis control. There we showed that the CoV reduced as a result of reduction of the equivalent number of independent samples in a signal, based on the fact that signal whitening effectively makes the signal less correlated, thereby increasing the number of equivalent independent samples of the signal. The fact that the CoV decreases makes the classification task easier and justifies the improvement of classification accuracy observed there.

To quantify the amount of bandwidth change, it is necessary to estimate equivalent statistical bandwidth of a given signal. In this section, we introduce some empirical methods for the estimation and explain how they fit in the project of Chapters 4–7.

13.4.1 Background

[Bendat 2010] introduced the calculation of statistical bandwidth, B_s, from the power spectral density of energy signal $x(t) \in \mathcal{L}^2$ from the continuous-time power spectrum $P_{xx}(f)$, as

$$B_S \triangleq \frac{\left[\int_0^\infty P_{xx}(f)\,df\right]^2}{\int_0^\infty P_{xx}^2(f)\,df} \tag{13.4.1}$$

where f is frequency in Hz and $X(f) = X(-f)$ for $x(t) \in \mathbb{R}$.

When the continuous raw EMG signal $x(t)$ is sampled at F_s Hz whose discrete-time power spectrum is $G_d[k]$ using samples of $S_{xx}(e^{j\omega})$ of N_f-point discrete Fourier transform, its equivalent becomes:

$$B_S^d \triangleq \frac{\left(\sum_{k=0}^{N-1} P_{xx}[k]\right)^2}{\sum_{k=0}^{N-1} P_{xx}^2[k]}\Delta_f \tag{13.4.2}$$

where $N = \begin{cases} \frac{N_f}{2}+1 & N_f \text{ even} \\ \frac{1}{2}(N_f+1) & N_f \text{ odd} \end{cases}$ are the non-negative frequencies and $\Delta_f = \frac{F_s}{N_f}$ Hz is the frequency increment. The discrete-time power spectrum G_d can be estimated using a variety of methods, such as the Bartlett method and Welch method in the nonparametric methods family.

In a study [Hogan 1980], intact and amputee subjects were instructed to exert maximum force for 3–5 second durations, and subsequent recordings sampled at $F_s = 2048$ Hz were taken at 25%, 10% and 5% of maximum contraction level for 10 seconds, each repeated six times. Of these six repetitions, five were used with only the middle five-second portion of 10-second duration, giving a total of 25-seconds of data per contraction level. This 25-second segment was first divided into 50 non-overlapping sections, each 0.5s long, and spectrum estimation was performed on each section of data without windowing to obtain a 2 Hz resolution estimate using the Bartlett method (essentially using a 1024-point DFT), before the 50 estimates were averaged to obtain an estimate $\widehat{G_d}$ of the quantity G_d. The standard deviation of $\widehat{G_d}$ was reported to be 14% of its mean.

The power spectrum estimate for discrete-time Fourier transforms using the Bartlett method for an N_s-point sequence divided into K non-overlapping segments x_i, each of length M as in [Proakis 2006] is

$$P_{xx}^B(f) = \frac{1}{MK}\sum_{i=0}^{K-1}\left|\sum_{n=0}^{M-1} x_i[n]e^{-j2\pi fn}\right|^2 \tag{13.4.3}$$

The Welch method is similar to Bartlett's method except that overlapping and windowing before computing the periodigram are introduced (U is the normalization factor to account for the power of window function):

$$P_{xx}^W(f) = \frac{1}{MUK}\sum_{i=0}^{K-1}\left|\sum_{n=0}^{M-1} x_i[n]w[n]e^{-j2\pi fn}\right|^2. \tag{13.4.4}$$

For a given N_s value, smaller K (fewer segments) gives longer segments, or better frequency resolution at the cost of less averaging of estimated spectral values. In the context of P_{xx} in (13.4.3) and (13.4.4), segment length M substitutes N in (13.4.2).

The bias-variance tradeoff for the selection of K value for a given dataset states that larger K gives smaller variance with large $\widehat{B_s}$ values, while smaller values rough spectrum estimate and smaller $\widehat{B_s}$. There is no quantitative measurement of the goodness of K for bandwidth estimation, considering the amount of data, frequency content of the underlying data and windowing function as factors.

The quality of a spectral estimate (Bartlett, Welch, etc.) of the continuous-time $x(t)$ is defined as:

$$Q_A = \frac{\left\{\mathrm{E}\left[\widehat{P_{xx}^{A}}(f)\right]\right\}^2}{\mathrm{var}\left[\widehat{P_{xx}^{A}}(f)\right]} \tag{13.4.5}$$

Where the expectation and variance of continuous-time and discrete-time spectrum are:

$$\mathrm{E}P_{xx}(f) = \lim_{f_u\to\infty}\frac{1}{f_u}\int_0^{f_u} P_{xx}(f)\,df, \quad \mathrm{E}P_{xx}[n] = \frac{1}{N}\sum_{k=0}^{N-1} P_{xx}[k] \tag{13.4.6}$$

$$\mathrm{Var}[P_{xx}(f)] = \lim_{f_u\to\infty}\frac{1}{f_u}\left[\int_0^{f_u} P_{xx}^2(f)\,df - \frac{1}{f_u}\left(\int_0^{f_u} P_{xx}(f)\,df\right)^2\right],$$

$$\mathrm{Var}\{P_{xx}[n]\} = \frac{1}{N-1}\sum_{k=0}^{N-1}(P_{xx}[k] - \mathrm{E}P_{xx}[n])^2 \tag{13.4.7}$$

Given that total power $\sum_{k=0}^{N-1} P_{xx}[k] = \sum_{k=0}^{N-1}\widehat{P_{xx}}[k]$ is constant, we can see that smooth estimates with smaller variance give larger bandwidth values than rough estimates of the same spectrum.

13.4.2 Method description

The UNB dataset [Li 2010, Hargrove 2009] consists of ten intact subjects and five amputee subjects, each subject performing a sequence of 11 motions (including no-motion) recorded in a 10-channel surface electrode array, placed on the forearm of ten intact subjects and around the proximal portion of the forearm over the apex and distal end of the muscle bulge for five amputee patients. Recordings for each motion are four-seconds in duration sampled at 1 kHz and are repeated 16 times, and only the middle three-seconds are used, giving 16 three-second epochs. It was shown in Chapters 2–3 that whitening effectively decreases temporal correlation and improves subsequent motion classification results. Prior to whitening, power-line harmonics are notch filtered for each epoch. For each channel, we used "no-motion" recordings as the 0% MVC level (noise floor) and the motion with maximum mean absolute value (MAV) as a high signal level (typically 50% MVC in past whitening studies) to calibrate the whitener, and then

simultaneously whitened all electrodes for each motion. This technique gives us a new set of whitened EMG records for intact subjects and amputees.

For each electrode only two motions with maximum MAVs are used to calculate bandwidth, as they give higher SNR and are more representative of the current motion. It is observed in calculating the coefficient of variation that the moving-average envelope of EMG activity during each three-second epoch is not *quite* constant, and the level of activity for different epochs is different. Moreover, inter-subject differences for the same motion-electrode set are not negligible. We assumed and visually confirmed that the intra-subject spectra shapes for the 16 epochs (repetitions) are more similar than that of inter-subjects.

As the three-second data duration is deemed insufficient for a satisfactory spectrum estimate, an ensemble average is performed on the power-normalized spectrum of 16 epochs per electrode per subject to smooth the spectrum estimate, and statistical bandwidths using the Welch method with different K's in (13.4.3) are then estimated. In this way, we get a set of spectrum estimates with different frequency resolutions. The spectra are normalized so that the total power $\sum_{k=0}^{N-1} \widehat{P_{xx}}[k]$ are identical for all 16 epochs. At each resolution, this average spectrum estimate is then assumed to be ground truth and estimates with different K values are used on one three-second epoch to get a set of bandwidth values. When the bandwidth is plotted against window length M ("bandwidth-M" curve) in Figures 13.13–13.14, we see a decreasing trend.

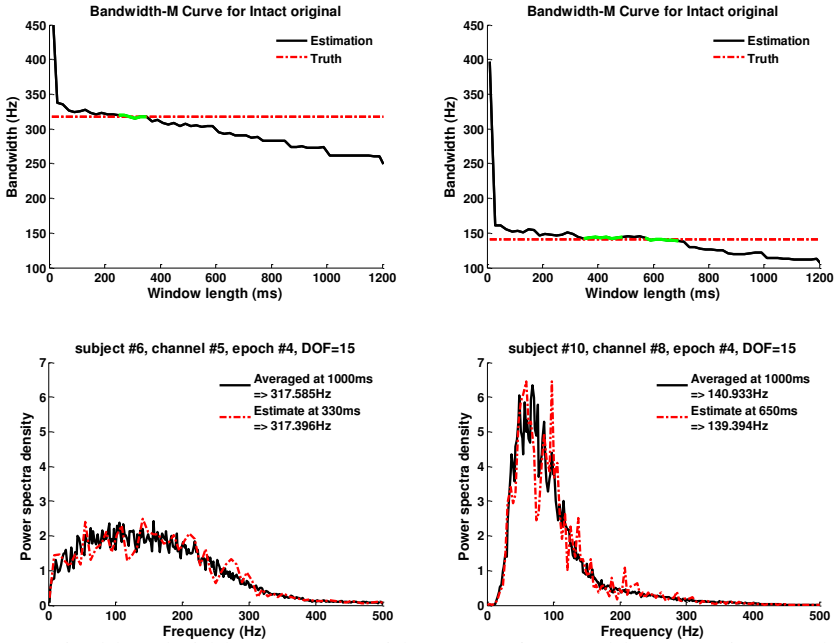

Figure 13.13. Typical bandwidth-M curves with DoF=15 ensemble averaging. In the upper plot, red dash-dot line shows the true bandwidth estimated using ensemble average with DoF=15, and black curve is the bandwidth-M curve of the selected subject, channel and epoch. Their intersection gives optimal window length which is used for PSD estimation of dash-dot in lower plots.

Figure 13.14 shows a representative plot: the upper-left shows the bandwidth-M of an overlapping segment for intact subject 6, channel 5 on the fourth epoch. The ensemble average of spectrum estimates is performed on all 16 epochs of that subject, as shown in black in the lower-left power spectrum estimates, with a frequency resolution of 0.976 Hz (M =1000, N_f =1024), which gives a bandwidth of 317.6 Hz from (13.2.2). We can see that the curve is rather steep when M<40 and then tapers off slowly (K=3 with 50% overlapping for truncated three-second recording). The intersection with ground truth bandwidth shows that when M=330 ms on the single epoch (with frequency resolution of 3.91 Hz), the bandwidth from that epoch approximates the true value. The right two plots show results for a different intact subject, where we found the ground truth to be 140.9 Hz and an optimal M around 630 ms.

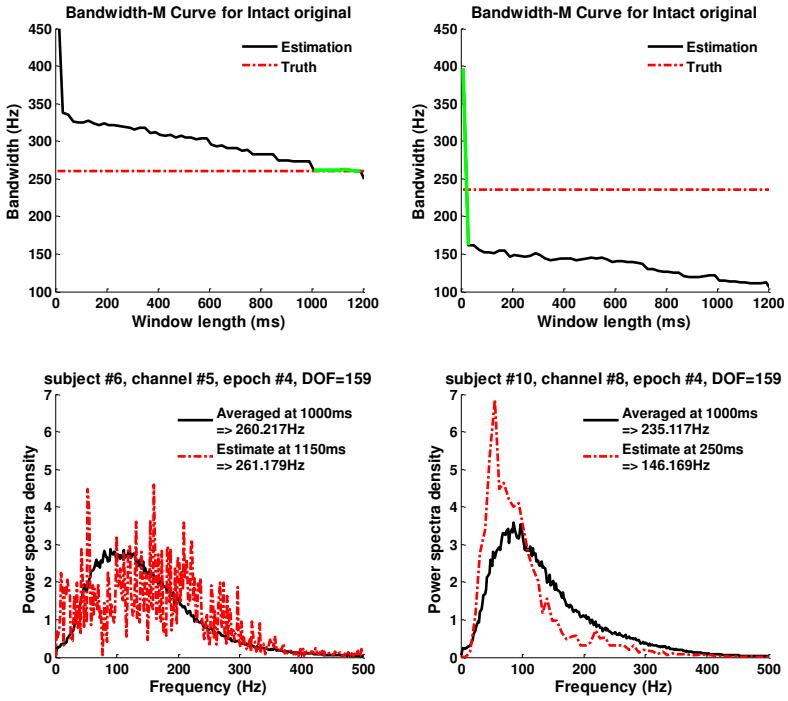

Figure 13.14. Typical bandwidth-M curves with DoF=159 ensemble averaging. In the upper plot, red dash-dot line shows the true bandwidth estimated using ensemble average with DoF=159, and black curve is the bandwidth-M curve of the selected subject, channel and epoch. Their intersection gives optimal window length which is used for PSD estimation of dash-dot in lower plots.

Figure 13.15 shows a different ensemble-averaging scheme for the same two cases as Figure 13.15: over all ten intact subjects and 16 epochs to give a 159 DoF evaluation. While the averaged spectra are smoother than Figure 1, both the calculated bandwidths and the shape/amplitude of two averaging schema are different. This implies that inter-subject variation of spectral content is too large to represent in a typical three-second

epoch, thus we prefer the first ensemble-averaging scheme and apply it to subsequent analysis.

I propose the following hypothesis to explain the relation between M and B_s^d observed in simulations: small M value gives smooth spectral estimates and larger bandwidth than large M values whose estimates are more variable. It is based on simulation observations and its discrete form is straightforward to describe.

Let $f(x)$, $g(x) \in C^1[a,b]$ be two Riemann-integrable functions of $[a,b] \to \mathbb{R}^+$ satisfying $\int_a^b f(x)\,dx = \int_a^b g(x)\,dx = M < \infty$. If the total variation of f is less than g, i.e. $\int_a^b |f'(x)|\,dx < \int_a^b |g'(x)|\,dx$, then it is hypothesized that $\int_a^b f^2(x)dx < \int_a^b g^2(x)dx$. There is yet no proof available for this hypothesis.

It is found that the optimal M value varies between subjects, channels and epochs, and M corresponding to 100–800 ms is a reasonable guess if one global value must be used for all subjects. Table 13.1 shows the average bandwidths for the four conditions: intact subject original EMG, intact subject whitened EMG, amputee original EMG and amputee whitened EMG. For each subject, two out of 11 motions are used per electrode and 16 bandwidths are calculated from each three-second epoch, giving 320 bandwidths per subject, or a DoF of 3199 for intact subjects and 1599 for amputees for the standard deviation.

Window length	150 ms	300 ms	450 ms	600 ms	750 ms
Intact-original	236.8±49.4	226.4±47.3	216.9±45.9	209.4±44.8	201.7±43.8
Intact-white	411.7±72.7	393.4±71.5	378.1±69.3	365.6±67.2	353.0±65.2
Amputee-original	252.4±53.8	240.9±54.1	230.4±53.4	222.4±52.6	214.4±51.5
Amputee-white	421.1±52.6	400.6±52.0	383.1±50.8	369.1±49.7	355.9±48.2

Table 13.1. Average bandwidths (Hz) with same window length for all subjects

To find an optimal window length for calculating the power spectrum of typical EMG data, simulated EMG data can be generated whose spectrum resembles that of real data. To do this, we calculate the Welch spectrum using the Hamming window of length N_1 for a 3-second epoch, and then design a FIR filter by Hamming-windowing the inverse-DFT of the frequency responses. The filter order N_2 controls smoothness of the designed filter: a small value overly smooths and may fail to follow the trend of the given spectrum while a large N_2 unnecessary follows all fluctuations of the spectrum estimate due to insufficient averaging. Then Matlab's "freqz" method is used with the designed FIR filter

coefficients, with N_3=1024 data points in [0, π), and bandwidth is calculated from the resulting power spectrum of the designed filter.

An N_1=500 ms window with 500 data samples with 50% overlap and a 512-point DFT with zero-padding is used to obtain the spectrum, and it's found that varying the window length N_1 from 100 to 800 ms gives less than 3% difference in terms of the bandwidth calculated. From several three-second trials, an N_2=200-order FIR filter follows the trend of the original power spectrum and gives sufficient smoothing; N_3 is relatively insensitive around 1000 for the final bandwidth result. This bandwidth is used as ground truth as the three parameters N_1, N_2 and N_3 give satisfactory spectrum approximation of real data with sufficient smoothing, and are insensitive in that range. These give an empirical estimate of the three parameters with the available dataset.

Then a three-second data segment is created from white Gaussian noise using the designed filter coefficients. By varying window lengths of the Welch method, a sequence of different bandwidths are obtained from generated data which follow a general decreasing trend similar as shown in Figure 13.5 and Figure 13.6. By finding the intersection of the curve with ground truth, we can establish an optimal window length to be used for calculating the bandwidth of simulated EMG signal.

13.4.3 Results

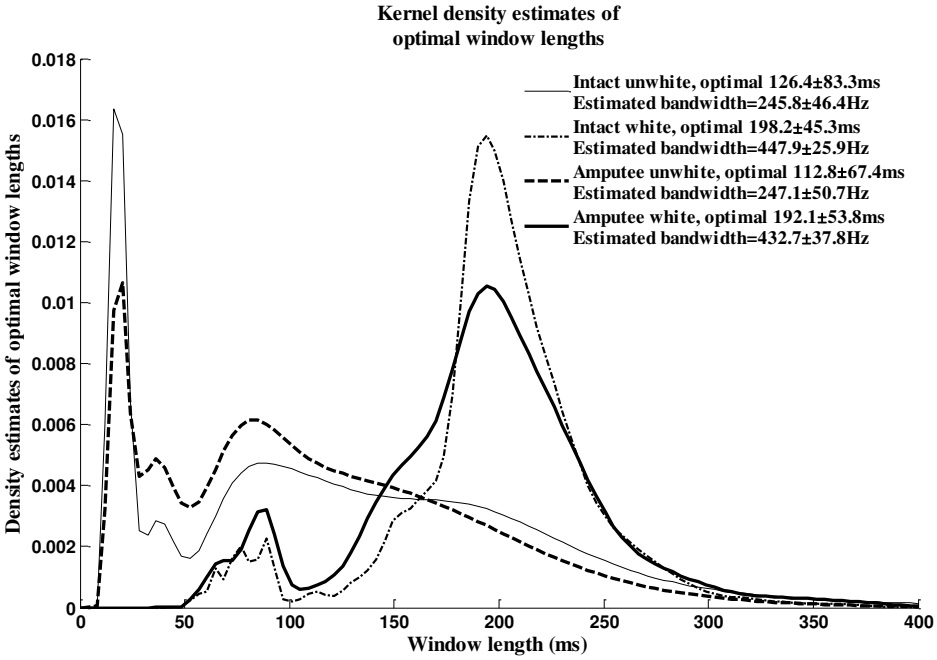

Figure 13.15. Kernel density estimates of optimal window lengths for bandwidth calculations of four subject types. The mean and standard deviations of optimal window lengths and estimated bandwidth in Hz are also shown.

Figure 13.15 shows the kernel density estimates of optimal windows found for the four types of subjects. The kernel density estimation is a method to estimate PDF from observation of data outcomes. We can see that the distributions for unwhite data are more skewed than whitened data. The two intact types have a DoF of 16×10×10-1=1599 each, and two amputee types have a DoF of 799. Their results are shown in the first column of Table 13.2.

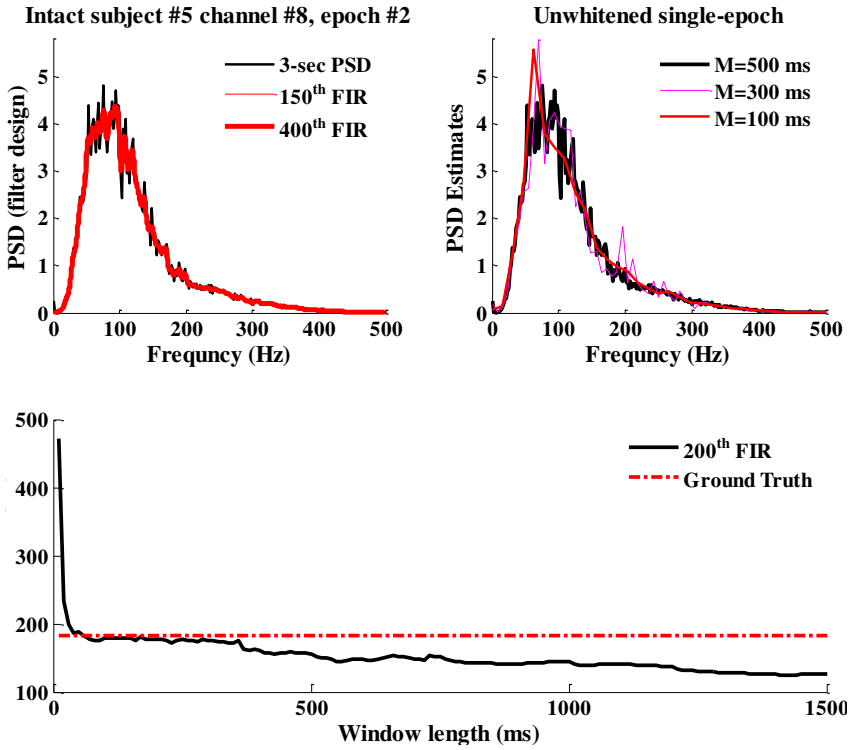

Figure 13.16. FIR Filter design with respect to filter order for intact unwhitened subject-5, channel-8, epoch-2, sampled at 1 kHz. The upper-left plot shows the ensemble-averaged spectrum in black and PSD of designed FIR filter with increasing order. Upper-right shows PSD of a single 3-second epoch with selected optimal window length in black and other window lengths. The lower plot shows the bandwidth-*M* curve of this 3-second epoch sEMG data.

The upper-left plot in Figure 13.8 shows the designed FIR filter frequency response (red) against partial underlying spectrum (black) with filter orders N_2 from 50 to 250 of one spectrum. A FIR filter of N_2=50 taps is incapable of following the fast increase portion around 50 Hz, and N_2=200 proves to be satisfactory in this case. The bandwidth-*M* curve in the lower plot intersects with ground-truth at 35 ms, where the bandwidth is 154.62 Hz. The upper-right plot shows PSD estimates of that three-second epoch with different window lengths *M*. Note that when the window length $\frac{M}{\Delta_f}$ (in units of seconds) is too small, the estimates have overly small frequency resolution (approximate triangle when *M*=50); when it is too large, too much variation arises due to noise. The optimal

window length for this epoch lies between 100–150 ms. It is expected that longer signal durations and more averaging of the spectral estimate would increase the optimal M to allow for better frequency resolution when the quality Q_A of the spectral estimate is fixed.

	Optimal M (ms)	Type-dependent bandwidths	Global bandwidths
Intact-original	105.55±75.21	241.37±50.89 Hz	238.81±50.10 Hz
Intact-white	174.6±41.50	408.72±72.66 Hz	413.63±72.35 Hz
Amputee-original	94.19±60.76	259.69±51.32 Hz	255.12±52.88 Hz
Amputee-white	167.08±48.08	419.33±52.36 Hz	424.30±52.01 Hz

Table 13.2. Average bandwidths (Hz) with optimal window lengths.

Table 13.2 shows the averaged bandwidths using the optimal window lengths described above. In the third column, each of the four EMG types uses its averaged optimal window length found in the first column; in the last column, each uses a "Global" optimal window length of 137ms. Paired t-tests between the bandwidth of intact groups (DoF=3199, two motions per electrode) and amputee groups (DoF=1599) for both optimal schema each reject the null hypothesis with p=0.

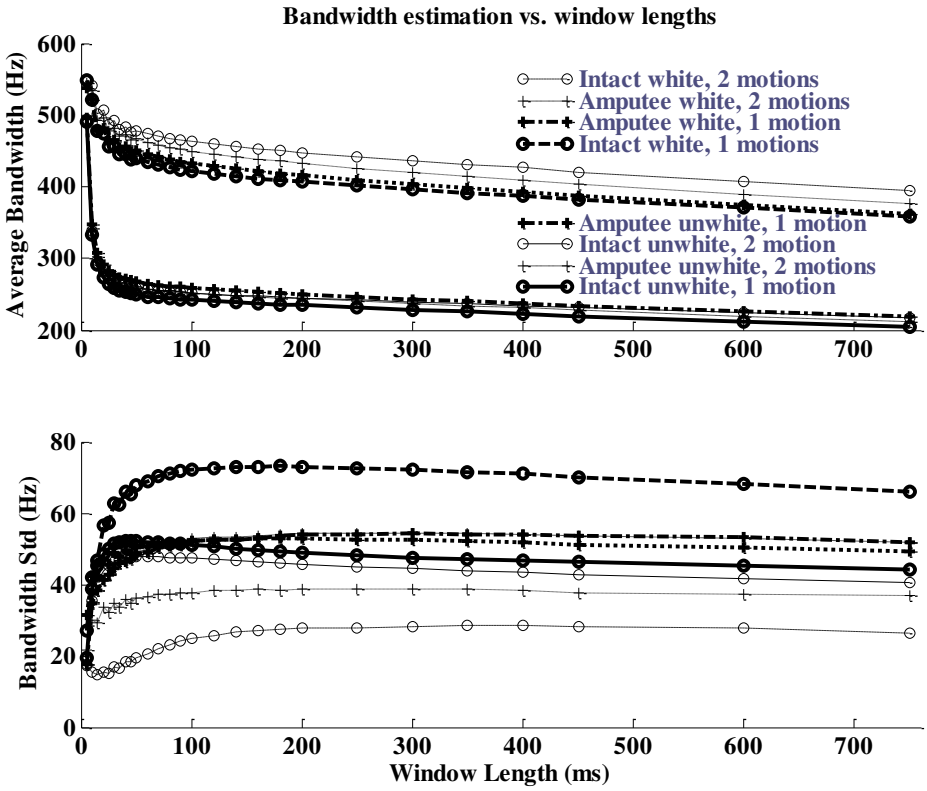

Figure 13.17. Averaged bandwidths and standard deviations vs. window lengths

For each electrode of a given subject, two out of 11 motions that yield maximum MAV values are selected. The bandwith-M curve is then evaluated using either one or

two motions with maximum MAV. When both motions are under use, average bandwidth is shown at each window length. Figure 13.17 shows the intra-subject ensemble-averaged bandwidth and their standard deviations against window lengths when all four types of subjects use the same window length and when one/two motions per electrode are used. Note that the unwhitened types suffer from a larger drop as the window length increases above 50 ms.

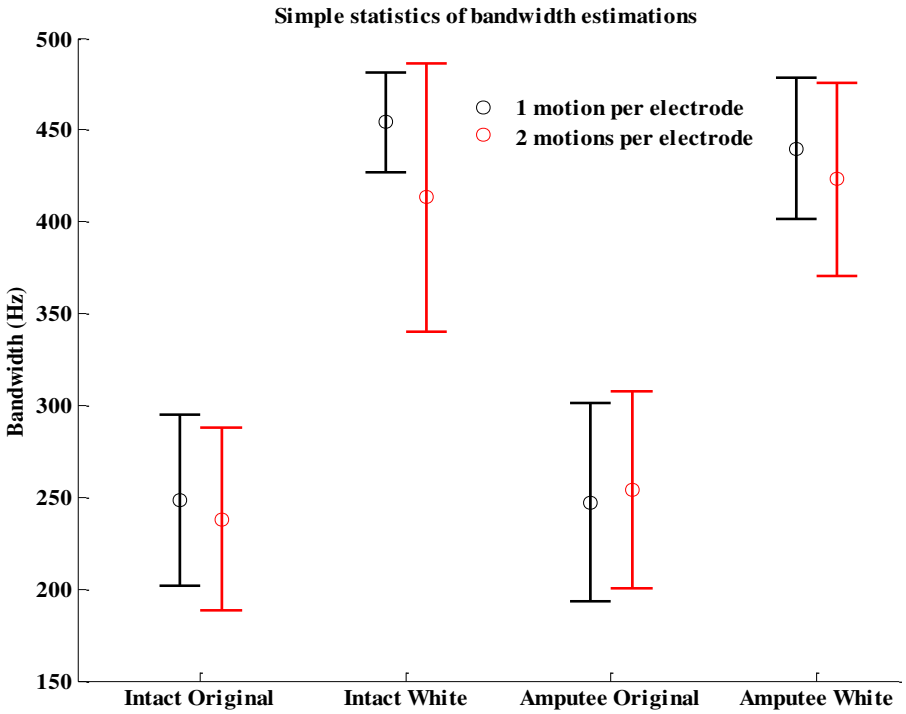

Figure 13.18. Simple statistics for bandwidth estimations

The mean and standard deviation of bandwidth of the four subject types are shown in Figure 13.18, when 150 ms is chosen as the global optimal window length. Paired *t*-tests for intact subjects with DoF=9 give $p=4.78\times10^{-10}$ / 5.36×10^{-9} for one/two motions per electrode, and for amputees with DoF=4 gives $p=6.17\times10^{-6}$ / 1.57×10^{-5}. Paired *t*-tests at all other *M* values are also significant.

Bibliography for Introduction and Appendices

[Adams 1999] P. F. Adams, G. E. Hendershot and M. A. Marona, "Current estimates from the national health interview survey, 1996," *National Center for Health Statistics, Vital Health Stat,* vol. 10, pp. 81–93, 1999.

[Aflalo 2007] T. N. Aflalo and M. S. Graziano, "Relationship between unconstrained arm movements and single-neuron firing in the macaque motor cortex," *Journal of Neuroscience*, vol. 27, pp. 2760–2780, 2007.

[Ahsan 2010] M. R. Ahsan, M. I. Ibrahimy and O. O. Khalifa, "Advances in electromyogram signal classification to improve the quality of life for the disabled and aged people," *Journal of Computational Science*, vol. 6, pp. 706–715, 2010.

[An 1983] K. N. An, W. P. Cooney, E. Y. Chao, L. J. Askew and J. R. Daube, "Determination of forces in extensor pollicis longus of thumb," *Journal of Applied Physiology*, vol. 54, pp. 714–719, 1983.

[Atkins 1996] D. Atkins, D. C. Y. Heard and W. H. Donovan, "Epidemiologic overview of individuals with upper-limb loss and their reported research priorities," *Journal of Prosthetic and Orthotics*, vol. 8, pp. 2–12, 1996.

[Azevedo 2005] C. Azevedo and K. Yoshida, "Towards a model–based estimator of muscle length and force using muscle afferent signals for real–time FES control," *International Conference on Computer as a Tool*, vol. 1, pp. 44–47, 2005.

[Bailón 2011] R. Bailón, G. Laouini, M. Orini and P. Laguna, "The integral pulse frequency modulation model with time-varying threshold: application to heart rate variability analysis during exercise stress testing," *IEEE Transactions on Biomedical Engineering*, vol. 58, pp. 642–652, 2011.

[Barbero 2011] M. Barbero, R. Gatti, L. L. Conte, *et al*. "Reliability of surface EMG matrix in locating the innervation zone of upper trapezius muscle," *Journal of Electromyograph and Kinesiology*, vol. 21, pp. 827–833, 2011.

[Barry 1990] D. T. Barry, K. E. Gordon and G. G. Hinton, "Acoustic and surface EMG diagnosis of pediatric muscle diseases," *Muscle & Nerve*, vol 13, pp. 286–290, 1990.

[Barton 1988] R. J. Barton and H. V. Poor, "Signal detection in fractional Gaussian noise," *IEEE Transactions on Information Theory*, vol. 34, pp. 943–959, 1988.

[Basmajian 1985] J. V. Basmajian and C. J. De Luca, *Muscle alive: their functions revealed by electromyogram*, William & Wilkins, 5ed, 1985.

[Bayly 1968] E. J. Bayly, "Spectral Analysis of Pulse Frequency Modulation in the Nervous System," *IEEE Transactions on Biomedical Engineering*, vol. 15, pp. 257–265, 1968.

[Bendat 1971] J. S. Bendat and A. G. Piesol, *Random data: analysis and measurement procedures*, New York: John Wiley and Sons Inc., 1971.

[Bendat 2010] J. S Bendat and A. G Piesol, *Random Data: Analysis and Measurement Procedures*. Wiley-Interscience, 4ed, pp. 276–281, 2010.

[Berger 1986] R. D. Berger, S. Akselrod, D. Gordon and R. J. Cohen. "An efficient algorithm for spectral analysis of heart rate variability," *IEEE Transactions on Biomedical Engineering*, vol. 33, pp. 900–904, 1986.

[Bigland-Ritchie 1983] B. Bigland-Ritchie, R. Johansson, O. C. Lippold, S. Smith and J. J. Woods, "Changes in motorneurone firing rates during sustained maximal voluntary contractions," *Journal of Physiology*, vol. 340, pp. 335–346, 1983.

[Bigland-Ritchie 2004] B. Bigland-Ritchie and J. J. Woods, "Changes in muscle contractile properties and neural control during human muscular fatigue," *Muscles & Alive*, vol. 7, pp. 691–699, 2004.

[Bolhuis 1997] B. M. Van Bolhuis, W. P. Medendorp and C. C. A. M. Gielen, "Motor-unit firing behavior in human arm flexor muscles during sinusoidal isometric contractions and movements," *Experimental Brain Research*, vol. 117, pp. 120–130, 1997.

[Boostani 2003] R. Boostani and M. H. Moradi, "Evaluation of forearm EMG signal features for the control of a prosthetic hand," *Physiological Measurement*, vol. 24, pp. 309–319, 2003.

[Burden 1999] A. Burden and R. Bartlett, "Normalisation of EMG amplitude: an evaluation and comparison of old and new methods," *Medical Engineer & Pyshics*, vol. 21, pp. 247–257, 1999.

[Burke 1971] R. E. Burke, D. N. Levine, F. E. Zajac III, P. Tsairis and W. K. Engel, "Mamalian motor units: physiological-histochemical correlation in three types in cat gastrocnemius," *Science*, vol. 174, pp. 709–712, 1971.

[Butts 2007] D. A. Butts, C. Wang, J. Jin, Chun–I Yeh, *et al*. "Temporal precision in the neural code and the timescales of natural vision," *Nature*, vol. 499, no.7158, pp 92–95, 2007.

[Christie 2009] A. Christie and G. Kamen, "Motor unit firing behavior during prolonged 50% MVC dorsiflexion contractions in young and older adults," *Journal of Electromyography and Kinesiology*, vol.19, pp. 335–346, 2009.

[Christova 1998] P. Christova, A. Kossev and N. Radicheva, "Discharge rate of selected motor units in human brachii at different muscle lengths," *Journal of Electromyogram and Kinesiology*, vol. 8, pp. 287–294, 1998.

[Clamann 1967] H. P. Clamann, "A quantitative analysis of the firing pattern of single motor units of a skeletal muscle of a man and their utilizations in isometric contractions," PhD dissertation, Johns Hopkins, 1967.

[Clamann 1969] H. P. Clamann, "Statistical analysis of motor unit firing patterns in a human skeletal muscle," *Biophysical Journal*, vol. 9, pp. 1233–1251, 1969.

[Clamann 1970] H. P. Clamann, "Activity of single motor units during isometric tension," *Neurology*, vol. 20, pp. 254–260, 1970.

[Clancy 1991] E. A. Clancy an N. Hogan, "Estimation of joint torque from the surface EMG," *Engineering in Medical and Biological Society*, vol. 13, pp. 877–878, 1991.

[Clancy 1994] E. A. Clancy and N. Hogan, "Single site electromyogram amplitude estimation," *IEEE Transactions on Biomedical Engineering*, vol. 41, pp. 159–167, 1994.

[Clancy 1995] E. A. Clancy and N. Hogan, "Multiple site electromyography amplitude estimation," *IEEE Transactions on Biomedical Engineering*, vol. 42, pp. 203–211, 1995.

[Clancy 1997a] E. A. Clancy and N. Hogan, "Relating angonist-antagonist electromyograms to joint torque during isometric, quasi-isotonic, non-fatiguing contractions," *IEEE Transactions on Biomedical Engineering*, vol. 44, pp. 1024–1028, 1997.

[Clancy 1997b] E. A. Clancy and N. Hogan, "Theoretic and experimental comparison of root-mean-square and mean-absolute-value electromyogram amplitude estimation," *Annual International Conference of IEEE Engineering in Medicine and Biological Society*, vol. 19, pp. 1267–1270, 1997.

[Clancy 1999a] E. A. Clancy, "Electromyogram amplitude estimation with adaptive smoothing window length," *IEEE Transactions on Biomedical Engineering*, vol. 46, pp. 717–729, 1999.

[Clancy 1999b] E. A. Clancy and N. Hogan, "Probability density of the surface electromyogram and its relationship to amplitude detectors," *IEEE Transactions of Biomedical Engineering*, vol. 46, pp. 730–739, 1999.

[Clancy 2000] E. A. Clancy and K. A. Farry, "Adaptive whitening of the electromyogram to improve amplitude estimation," *IEEE Transactions on Biomedical Engineering*, vol. 47, pp. 709–719, 2000.

[Clancy 2001] E. A. Clancy, S. Bouchard and D. Rancourt, "Influence of advanced electromyogram (EMG) amplitude during dynamic contractions," *IEEE EMBS Magzine*, vol. 20, pp. 47–54, 2001.

[Clancy 2002] E. A. Clancy, E. L. Morin and R. Merletti, "Sampling, noise-reduction and amplitude estimation issues in surface electromyography," Journal of Electromyogram and Kinesiology, vol. 12, pp 1–16, 2002.

[Clancy 2006] E. A. Clancy, O. Bida and D. Rancourt, "Influence of advanced electromyogram (EMG) amplitude processor on EMG-to-torque estimation during constant-posture, force-varying contractions," *Journal of Biomechanics*, vol. 39, pp. 2690–2698, 2006.

[Clancy 2010] E. A. Clancy, *EMG amplitude estimation toolbox: user's guide*, Alpha version 0.07, 2010. Available on-line at: http://www.wpi.edu/~ted/emg_tool.html. Accessed August 2010.

[Clancy 2012] E. A. Clancy, L. Liu, P. Liu and D. V. Moyer, "Identification of constant-posture EMG-torque relationship about the elbow using nonlinear dynamic models," *IEEE Transactions on Biomedical Engineering*, vol. 59, pp. 205–212, 2012.

[D'Alessio 1984] D'Alessio, "Some results on the optimization of a digital processor for surface EMG signals," *Electromyograms and Clinical Neurophysiology*, vol. 24, pp. 625–643, 1984.

[DeLuca 1973] C. J. DeLuca and W. J. Forrest, "Some properties of motor unit action potential trains recorded during constant force isometric contractions in man," *Kybernetik*, vol 12, pp. 160–168, 1973.

[DeLuca 1979] C. J DeLuca, "Physiology and mathematics of myoelectric signals," *IEEE Transactions on Biomedical Engineering*, vol. 26, pp. 313–325, 1979.

[DeLuca 1982] C. J. DeLuca, R. S. LeFever, M. P. McCue and A. P. Xenakis, "Control schem govening concurrently active human motor units during voluntary contraction," *Journal of Physiology*, vol. 329, pp. 129–142, 1982.

[DeLuca 1982] C. J. DeLuca, R. S. LeFever, M. P. McCue and A. P. Xenakis, "Behavior of human motor units in different muscle during linearly varying contractions," *Journal of Physiology*, vol. 329, pp. 113–128, 1982.

[DeLuca 1985] C. J. DeLuca, "Control properties of motor units", *Journal of Experimental Biology*, vol. 155, pp. 125–136, 1985.

[DeLuca 1994] C. J. DeLuca and Z. Erim, "Common drive of motor units in regulation of muscle force," *Trends in Neuroscience*, vol. 17, pp. 299–305, 1994.

[DeLuca 1996] C. J. DeLuca, P. J. Foley and Z. Erim, "Motor unit control properties in constant-force isometric contractions," *Journal of Neurophysiology*, vol. 76, pp. 1503–1516, 1996.

[DeLuca 2006] C. J. DeLuca, A. Adam, R. Wotiz, L. D. Gilmore and S. H. Nawab, "Decomposition of Surface EMG signals," *Journal of Neurophysiology*, vol. 96, pp. 1646–1657, 2006.

[DeLuca 2010] C. J. DeLuca and E. C. Hostage, "Relationship between firing rate and recruitment threshold of motorneurons in voluntary isometric contractions," *Journal of Neurophysiology*, vol. 104, pp. 1034–1046, 2010.

[Dietz 1974] V. Dietz, W. Hillesheimer and H. J. Freund, "Correlation between tremor, voluntary contraction, and firing pattern of motor units in Parkinson's disease," *Journal of Neurology, Neurosurgery and Psychiatry*, vol. 37, pp. 927–937, 1974.

[Dietz 1989] V. Dietz, G. A. Horstmann and W. Berger, "Interlimb coordination of leg-muscle activation during perturbation of stances in humans," *Journal of Neurophysiology*, vol. 62, pp. 680–693, 1989.

[Disselhort-Klug 2009] C. Disselhort-Klug, T. Schmitz-Rode and G. Rau, "Surface electromyography and muscle force: limits in sEMG-force relationship and new approaches for applications," *Clinical Biomechanics*, vol. 24, pp. 225–235, 2009.

[Drake 1967] A. W. Drake, "Fundamentals of Applied Probability Theory," New York: McGraw Hill Book Company, pp. 272, 1967.

[Dilingham 2002] T. R. Dilingham, L. E. Pezzin and E. J. MacKenzie, "Limb amputation and limb deficiency: epidemiology and recent trends in the United States," *South Medicine Journal*, vol. 95, pp. 875–883, 2002.

[Doheny 2008] E. P. Doheny, M. M. Lowery, D. P. FitzPatrick and M. J. O'Malley, "Effect of elbow joint angle on force-EMG relationships in human elbow flexor and extensor muscles," *Journal of Electromyogram and Kinesiology*, vol. 18, pp. 760–770, 2008.

[Doorenbosch 2003] C. A. M. Doorenbosch and J. Harlaar, "A clinically applicable EMG-force model to quantify active stabilization of knee after a leision of the anterior cruciate ligament," *Clinical Biomechanics*, vol. 18, pp. 142–149, 2003.

[Doorenbosch 2004] C. A. M. Doorenbosch and J. Harlaar, "Accuracy of a practicable EMG to force model for knee muscles," *Neuroscience Letter*, vol. 368, pp. 78–81, 2004.

[Dorfman 1989] L. J. Dorfman, J. E. Howard, K. C. McGill "Motor unit firing rates and firing rate variability in the detection of neuromuscular disorders," *Electroencephalography and Clinincal Neurophyisiology*, vol. 73, pp. 215–224, 1989.

[Duchateau 2006] J. Duchateau, J. G. Semmler and R. M. Enoka, "Training adaptations in the behavior of human motor units," *Journal of Applied Physiology*, vol. 101, pp. 1766–1775, 2006.

[Englehart 1994] K. B. Englehart and P. A. Parker, "Single motor unit myoelectric signal analysis with nonstationary data," *IEEE Transactions of Biomedical Engineering*, vol. 41, pp. 168–180, 1994.

[Erim 1996] Z. Erim, C. J. DeLuca, K. Mineo and T. Aoki, "Rank-ordered regulation of motor units," *Muscle & Nerve*, vol. 19, pp. 563–573, 1996.

[Erim 2008] Z. Erim and W. Lin, "Decomposition of intramuscular EMG signals using a heuristic fuzzy expert system," *IEEE Transactions on Biomedical Engineering*, vol. 55, pp. 2180–2189, 20 08.

[Farina 2000] D. Farina and R. Merletti, "Comparison of algorithms for estimation of EMG variables during voluntary isometric contractions," *Journal of Electromyography and Kinesiology*, vol. 10, pp. 337–349, 2000.

[Farina 2001] D. Farina, R. Colombo, R. Merletti and C. D. degli Oslen, "Evaluation of intra-muscular EMG signal decomposition algorithms," *Journal of Electromyography and Kinesiology*, vol. 11, pp. 175-187, 2001.

[Farina 2004] D. Farina, L. A. Nielsen, R. Merletti and T. G. Nielsen, "Effect of experimental muscle pain on motor unit firing rate and conduction velocity," *Journal of Neurophysiology*, vol. 91, 1250–1259, 2004.

[Farrell 2007] T. R. Farrell and R. F. Weir, "The optimal controller delay for myoelectric prosthesis," *IEEE Transactions on Neural System and Rehabilitation Engineering*, vol. 15, pp. 111–118, 2007.

[Ferri 2008] R. Ferri, C. Franceschini, G. Plazzi, *et al.* "A quantitative statistical analysis of the submentalis muscle EMG amplitude during sleep in normal controls and patients with REM sleep behavior disorder," *Journal of Sleep Research*, vol. 17, pp. 89–100, 2008.

[Fick 1855] A. Fick, "Ueber Diffusion", *Annalen der physic*, vol. 170, pp. 59–86, 1855.

[Fleischer 2008] C. Fleischer and G. Hommel, "A human exoskeleton interface utilizing electromyogram," *IEEE Transactions on Robotics*, vol. 24, pp. 872–882, 2008.

[Garrault 1987] G. Garrault, P. Toulouse and J. L. Coatrieux, "Lateral amytrophic sclerosis versus Guillain-Barré symdrome: an attempt of differentiation by automatic EMG classification," *Electromyography and Clinical Neurophysiology*, vol. 27, pp. 209–215, 1987.

[Gemperline 1995] J. J. Gemperline, S. Allen, D. Walker and W. Z. Rymer, "Characteristics of motor unit discharge in subjects with hemiparesis," *Muscle and Nerve*, vol. 18, pp. 1101–1114, 1995.

[Georgopoulos 1982] A. P. Georgopoulos, J. F. Kalaska, R. Carminiti and J. T. Massey, "On the relations between the direction of two-dimensional arm movements and cell discharge in primate motor cortex," *Journal of Neuroscience*, vol. 2, pp. 1527–1537, 1982.

[Georgopoulos 1988] A. P. Georgopoulos, R. E. Kettner and A. B. Schwartz, "Primate motor cortex and free arm movements to visual targets in three-dimensional space. II. Coding of the direction of movements and cell discharge in primate motor cortex," *Journal of Neuroscience*, vol. 8, pp. 2928–2937, 1988.

[Gerdle 2008] B. Gerdle, N. Ostlund, C. Gronlund, *et al*. "Firing rate and conduction velocity of single motor units in the trapezius muscle in fibromyalgia patients and healthy controls," *Journal of Electromyography and Kinesiology*, vol. 18, pp. 707–716, 2008.

[Gottlieb 1971] G. L. Gottlieb and G. C. Agarwal, "Dynamic relationship between isometric muscle tension and the electromyogram in man," Journal of Applied Physiology, vol. 30, pp. 345–351, 1971.

[Graupe 1975] D. Graupe and W. K. Cline, "Functional separation of EMG signals via ARMA identification methods for prosthesis control purposes," *IEEE Transactions on System, Man and Cybernetics*, vol. 5, pp. 252–259, 1975.

[Hagg 2004] G. M. Hagg, B. Melin and R. Kadefors, "Application in ergonomics" in *Electromyography: physiology, engineering and non-invasive applications*, R. Meletti and P. A. Parker (eds.) 2004.

[Hahne 2014] J. M. Hahne, F. Biebmann, N. Jiang, H. Rehbaum, D. Farina, F. C. Meinecke, K. R. Muller and L. C. Parra, "Linear and nonlinear regression techniques for simultaneous and proportional myoelectric control," *IEEE Transactions on Neural System and Rehabilitation Engineering*, vol. 22, pp. 269–279, 2014.

[Hargrove 2009] L. J. Hargrove, G. Li, K. B. Englehart, "Principle component analysis preprocessing for improved classification accuracies in pattern-recognition-based myoelectric control," *IEEE Transactions on Biomedical Engineering*, vol. 56, pp. 1407–1414, 2009.

[Hasan 1985] Z. Hasan and R. M. Enoka, "Isometric torque-angle relationship and movement-related activity of human elbow flexors: implications for the equilibrium-point hypothesis," *Experimental Brain Research*, vol. 59, pp. 441–450, 1985.

[Hashemi 2012] J. Hashemi, E. Morin, P. Mousavi, K. Mountjoy and K. Hashtudi-Zaad, "EMG-force modeling using parallel cascade identification," *Journal of Electromyogram and Kinesiology*, vol. 23, pp. 416–424, 2012.

[Heckathorne 1981] C. W. Heckathorne and D. S. Childress, "Relationships of the surface electromyogram to the force, length, velocity, and contraction rate of the cineplastic human biceps," *American Journal of Physical and Medicine*, vol. 60, pp. 1–19, 1981.

[Henneman 1965] E. Henneman, G. Somjen and D. O. Carpenter, "Functional significance of cell size in spinal motorneurons," *Journal of Neurophysiology*, vol. 28, pp. 560–580, 1965.

[Hoerl 1970] A. E. Hoerl and R. W. Kennard, "Biased estimation for nonorthogonal problems," *Technometrics*, vol. 12, pp. 55–67, 1970.

[Hof 1981] A. L. Hof and J. Van den Berg, "EMG to force processing I: an electrical analogue of the hill muscle model," *Journal of Biomechanics*, vol. 14, pp. 747–758, 1981.

[Hogan 1980a] N. Hogan and R. W. Mann, "Myoelectric signal processing: optimal estimation applied to electromyography–Part I: Deviation of the optimal myoprocessor," *IEEE Transactions on Biomedical Engineering*, vol. 27, pp. 382–395, 1980.

[Hogan 1980b] N. Hogan and R. W. Mann, "Myoelectric signal processing: optimal estimation applied to electromyogram–part II: experimental demonstration of optimal myoprocessor performance," *IEEE Transactions on Biomedical Engineering*, vol. 27, pp. 396–410, 1980.

[Holobar 2004] A. Holobar and D. Zazula, "Correlation-based decomposition of surface electromyograms at low contraction forces," *Medical and Biological Engineering and Computing*, vol. 42, pp. 487–495, 2004.

[Holobar 2007] A. Holobar and D. Zazula, "Multichannel blind source separation using convolution kernel compensation," *IEEE Transactions of Signal Processing*, vol. 55, pp. 4487–4496, 2007.

[Holobar 2009] A. Holobar, D. Farina, M. Gazzoni, R Merletti and D Zazula, "Estimating motor unit discharge patterns from high-density surface electromyogram," *Clinical Neurophysiology*, vol. 120, pp. 551–562, 2009.

[Holobar 2013] A. Holobar, M. A. Minetto and D. Farina, "A signal-based approach for assessing the accuracy of high-density surface EMG decomposition ," *2013 6th International IEEE/EMBS Conference on Neural Engineering*, pp. 585–588, 2013.

[Hudgins 1993] B. Hudgins, P. Parker and R. N. Scott, "A new strategy for multifunction myoelectric control," *IEEE Transactions on Biomedical Engineering*, vol. 40, pp. 82–94, 1993.

[Hyndman 1973] B. W. Hyndman, R. K. Mohn, "A pulse modulator model for pacemaker activity," *Proceedings of the Digest of the 10th International Conference on Medical and Biological Engineering*, 1973.

[Inman 1985] V. T. Inman, H. J. Ralston, J. B. Saunders, B. Feinstein and E. W. Wright, "Relation of human electromyogram to muscle tension," *Electroencephalogram and Clinical Neurophysiology*, vol. 4, pp. 187–192, 1985.

[Jamison 1993] J. C. Jamison and G. E. Caldwell, "Muscle synergies and isometric torque production: influence of supination and pronation level on elbow flexion," *Journal of Neurophysiology*, vol. 70, pp. 947–960, 1993.

[Jones 1972] T. A. Jones, "Multiple regression with correlated independent variables," *Journal of International Association for Mathematical Geology*, vol. 4, pp. 203–218, 1972.

[Kallio 2012] J. Kallio, K. Sogaard, J. Avela, P. Komi, H. Selanne and V. Linnamo, "Age-related decreases in motor unit discharge rate and force control during isometric plantar flexion," *Journal of Electromyography and Kinesiology*, vol. 22, pp. 983–989, 2012.

[Kamen 1995] G. Kamen, S. V. Sison, C. C. Du and C. Patten, "Motor unit discharge behavior in older adults during maximal-effort contractions," *Journal of Applied Physiology*, vol. 79, pp. 1908–1913, 1995.

[Karlsson 2001] S. Karlsson and B. Gerdle, “Mean frequency and signal amplitude of the surface EMG of the quadriceps muscles increase with increasing torque–a study using the continuous wavelet transform,” *Journal of Electromyography and Kinesiology*, vol. 11, pp. 131–140, 2001.

[Kasi 2009] P. K. Kasi, L. S. Krivickas, M. Meister *et al*. “Characterization of motor unit behavior in patients with amyotrophic lateral sclerosis,” *4th International IEEE/EMBS Conference on Neural Engineering*, pp. 10–13, 2009.

[Katsis 2006] C. D. Katsis, Y. Goletsis, A. Likas, D. I. Fortiadis and I. Sarmas, “A novel method for automated EMG decomposition and MUAP classification,” *Artificial Intelligence in Medicine*, vol. 37, pp. 55–64, 2006.

[Kern 2001] D. S. Kern, J. G. Semmler and R. M. Enoka, “Long-term activity in upper- and lower-limb muscles of human,” *Journal of Applied Physiology*, vol. 91, pp. 2224–2232, 2001.

[Khokhar 2010] Z. O. Khokhar, Z. G. Xiao and C. Menon, “Surface EMG pattern recognition for real-time control of a wrist exoskeleton,” *Biomedical Engineering Online*, vol. 9, pp. 41, 2010.

[Komi 2000] P. V. Komi, V. Linnamo, P. Silventoinen and M. Sillanpaa, “Force and EMG power spectrum during eccecntric and concentric actions,” *Medicine and Science in Sports and Exercies*, vol. 32, pp. 1757–1762, 2000.

[Koo 2005] T. K. K. Koo and A. F. T. Mak, “Feasibility of using EMG-driven neuromuscularskeletal model for prediction of dynamic moment of the elbow,” *Journal of Electromyogram and Kinesiology*, vol. 15, pp. 12–26, 2005.

[Kukulka 1981] C. G. Kukulka and H. P. Clamann, “Comparison of the recruitment and discharge properties of motor units in human brachial biceps and adductor pollicis during isometric contractions”, *Brain Research*, vol. 209, pp. 45–55, 1981.

[Kumar 1996] S. Kumar and A. Mital, *Electromyography in ergonomics*, Briston, PA: Taylor & Francis, 1996.

[Kuntzer 2004] T. Kuntzer and F. Ochsner, “Quantative EMG analysis and longitudinal nerve conduction studies in a Refsum’s disease patient,” *Muscle & Nerve*, vol. 18, pp. 857–863, 2004.

[Kwatny 1970] E. Kwatny, D. H. Thomas and H. G. Kwatny, "An application of signal processing techniques to the study of myoelectric signals," *IEEE Transactions on Biomedical Engineering*, vol. 17, pp. 303–313, 1970.

[Lawrence 1983] J. H. Lawrence and C. J. DeLuca, "Myoelectric signal versus force relationship in different human muscles," *Journal of Applied Physiology*, vol. 54, pp. 1653–1659, 1983.

[Lepora 2009] N. F. Lepora, C. H. Yeo, C. Evinger and P. Dean, "Recruitment in retractor bulbi muscle during eyeblinking condition: EMG analysis and common drive model," *Journal of Neurophysiology*, vol. 102, pp. 2498–2513, 2009.

[Li 2010] G. Li, E S. Aimee and T. A. Kuiken, "Quantifying pattern recognition-based myoelectric control of multifunctional transradial prostheses," *IEEE Transactions on Neural System and Rehabilitation Engineering*, vol. 18, pp. 185–192, 2010.

[Liu 2011] L. Liu, P. Liu, E. A. Clancy, E. Scheme and K. B. Englehart, "Signal whitening preprocessing for improved classification accuracies in myoelectric control," *IEEE 37th Northeast Bioengineering Conference*, 2011.

[Liu 2011] P. Liu, L. Liu, F. Martel, D Rancourt and E. A. Clancy, "EMG-torque estimation of constant-posture, quasi-constant torque contractions at varied joint angles," *IEEE 37th Northeast Bioengineering Conference*, 2011.

[Liu 2013a] L. Liu, P. Liu, E. A. Clancy, E. Scheme, and K. B. Englehart, "Electromyogram whitening for improved classification accuracy in upper limb prosthesis control," *IEEE Transactions on Neural System and Rehabilitation Engineering*, vol. 21, pp. 767–774, 2013.

[Liu 2013b] P. Liu, L. Liu, F. Martel, D. Rancourt and E. A. Clancy, "Influence of joint angle on EMG-torque model during constant-posture quasi-constant-torque contractions," *Journal of Electromyogram and Kinesiology*, vol. 23, pp. 1020–1028, 2013.

[Ljung 1999] L. Jung, *System identification: theory for the user*, Upper Saddle River NJ: Prentice-Hall, pp. 143–146, 444–452, 491–519, 1999.

[Lloyd 2003] D. G. Lloyd and T. F. Besier, "An EMG-driven musculoskeletal model to estimate muscle forces and knee joint moments in vivo," *Journal of Biomechanics*, vol. 35, pp. 765–776, 2003.

[Luh 1999] J. J. Luh, G. C. Chang, C. K. Cheng, *et al*. "Isokinetic elbow joint torques estimation from surface EMG and joint kinematic data: using an artificial neural network model," *Journal of Electromyography and Kinesiology*, vol. 9, pp. 173–183, 1999.

[Maeto 1996] J. Maeto and P. Laguna, "New heart rate variability time-domain signal construnction from the beat occurrence time and the IPFM model," *Computers in Cardiology*, pp. 185–188, 1996.

[Maeto 2000] J. Maeto and P. Laguna, "Improved heart rate variability signal analysis from the beat occurrence times according to the IPFM model," *IEEE Transactions on Biomedical Engineering*, vol. 47, pp. 985–997, 2000.

[Manns 1981] A. Manns, R. Miralles and F. Guerrero, "The changes in electrical acitivity of the postural muscles of mandible upon varying the vertical dimensions," *The Journal of Prosthesis Dentistry*, vol. 45, pp. 438–445, 1981.

[Marquardt 1975] D. W. Marquardt and R. D. Snee, "Ridge regression in practice," *The American Statistician*, vol. 29, pp. 3–20, 1975.

[Martin 2006] S. Martin and D. Maclsaac, "Innervation zone shift with changes in joint angle in the brachial biceps," *Journal of Electromyogram and Kinesiology*, vol. 5, pp. 197–226, 2006.

[Masland 1969] W. S. Masland, D. Sheldon and C. D. Hershey "Stochastic properties of individual motor unit interspike intervals," *American Journal of Physiology*, vol. 217, pp. 1384–1388, 1969.

[Masuda 1999] K. Masuda, T. Masuda, T. Sadoyama, *et al*. "Changes in surface EMG parameters during static and dynamic fatiguing contractions," *Journal of Electromyograph and Kinesiology*, vol. 9, pp. 39–46, 1999.

[Marthiassen 1995] S. E. Mathiassen, J. Winkel and G. M. Hägg, "Normalization of surface EMG amplitude from the upper trapezius muscle in ergonomic studies–A review," *Journal of Electromyography and Kinesiology*, vol. 5, pp. 197–226, 1995.

[Messier 1971] R. H. Messier, J. Duffy, H. M. Litchman, P. R. Parslay, J. F. Soechting and P. A. Stewart, "The electromyogram as a measure of tension in the human biceps and triceps muscles," *International Journal of Mechanical Science*, vol. 13, pp. 585–598, 1971.

[McGill 2005] K. C. McGill, Z. C. Lateva and H. R. Marateb, "EMGLab: an interactive EMG decomposition program," *Journal of Neuroscience Methodology*, vol. 105, pp. 700–710, 2005.

[Merletti 2004] R. Merletti and P. A. Parker, *Electromyography Physiology, engineering and noninvasive applications.* John Wiley & Sons, pp. 2–15, 2004.

[Miller 1977] I. Miller and J. E. Freund, *Probability and statistics for engineers*, Englewood Cliffs, NJ: Prentice-Hall Inc., pp. 272–275, 1977.

[Milner-Brown 1972] H. S. Milner-Brown, R. B. Stein and R. Yemm, "Mechanisms of increased force during voluntray contractions," *Journal of Physiology*, vol. 230, pp. 18P–19P, 1972.

[Milner-Brown 1973] H. S. Milner-Brown, R. B. Stein and R. Yemm, "The orderly recruitment of human motor units during voluntary isometric contractions," *Journal of Physiology*, vol. 230, pp. 359–370, 1973.

[Milner-Brown 1973] H. S. Milner-Brown, R. B. Stein and R. Yemm, "Changes in firing rate of human motor unit during linearly changing voluntary contractions", *Journal of Physiology*, vol. 230, pp. 371–390, 1973.

[Milner-Brown 1975] H. S. Milner-Brown, R. G. Lee, "Synchronization of human motor nerves: possible roles of exercise and supraspinal reflexes", *Electroencephalography and Clinical neurophysiology*, vol. 38, pp. 245–254, 1975.

[Morita 2000] S. Morita, K. Shibata, X. Z. Zheng and K. Ito, "Prosthesis hand control based on torque estimation from EMG signals," *2000 IEEE/RSJ International Conference on Intelligent Robots and System*, vol. 1, pp. 389–394, 2000.

[Moritani 1986] T. Moritani, M. Muro and A. Nagata, "Intramuscular and surface electromyogram changes during muscle fatigue," *Journal of Applied Physiology*, vol. 60, pp. 1179–1185, 1986.

[Moritz 2004] C. T. Moritz, B. K. Barry, M. A. Pascoe and R. M. Enoka, "Discharge rate variability influences the variation in force fluctuations across the working range of a hand muscle," *Journal of Neurophysiology*, vol. 93, pp. 2249–2259, 2004.

[Mosifrot 2013] J. Mosifrot, E. L. Carpentier and Y. Aoustin, "Online estimation of EMG signals model based on a renewal process," *IEEE International Conference on Acoustics, Speech and Signal Processing*, pp. 944–948, 2013.

[Mountjoy 2010] K. Mountjoy, E. Morin and K. Hashtrudi-Zadd, "Use of the fast orthogonal search method to estimate joint torque angle for upper-limb Hill-muscle models," *IEEE Transactions on Biomedical Engineering*, vol. 57, pp. 790–798, 2010.

[Navallas 2014] J. Navallas, A. Malanda and J. Rodriguez-Falces, "Maximum likelihood estimation of motor unit firing pattern statistics," *IEEE Transactions on Neural System and Rehabilitation Engineering*, vol. 22, pp. 460–469, 2014.

[Navallas 2015] J. Navallas, J. Rodriguez-Falces and A. Malanda, "Inter-discharge interval distribution of motor unit firing patterns with detection errors," *IEEE Transactions on Neural System and Rehabilitation Engineering*, vol. 23, pp. 297–307, 2015.

[Nawab 2008] S. H. Nawab, R. P. Wotiz and C. J. DeLuca, "Decomposition of indwelling EMG signals," *Journal of Applied Physiology*, vol. 105, pp. 700–710, 2008.

[Negro 2009] F. Negro, A. Holobar and D. Farina, "Fluctuations in isometric muscle force can be described by one linear projection of low–frequency componentsof motor unit discharge rates," *Journal of Physiology*, vol. 587.24, pp. 5925–5938, 2009.

[Neumaier 2001] A. Neumaier and T. Schneider, "Estimations of parameters and eigenmodes of multivariate autoregressive models," *ACM Transactions on Mathematical Software*, vol. 27, pp. 27–57, 2001.

[Nordander 2003] C. Nordander, J. Willner, G. Å. Hasson, B. Larsson, J. Unge, L. Granquist and S. Skerfving, "Influcne of subcutaneous fat layer, as measured by ultrasound, skinfold calipers and BMI, on the EMG amplitude," *European Journal of Applied Physiology*, vol. 89, pp. 514–519, 2003.

[Olson 1968] C. B. Olson, D. O. Carpenter and E. Henneman, "Orderly recruitment of muscle action potentials: motor unit threshold and EMG amplitude," *Archives of Neurology*, vol. 19, pp. 591–597, 1968.

[Ostry 2003] D. J. Ostry and A. G. Feldmann, “A critical evaluation of the force control hypothesis in motor control,” *Experimental Brain Research*, vol. 153, pp. 275–288, 2003.

[Pan 1985] J. Pan and W. J. Tompkins, “A real-time QRS detection algorithm,” *IEEE Transactions on Biomedical Engineering*, vol. 32, pp. 230–236, 1985.

[Papoulis 2002] A. Papoulis and S. U. Pillai, *Probability, random variable and stochastic process*, McGraw Hill, 4ed. ISBN 0073660116, pp. 125–127, 2002.

[Park 1995] E. Park and S. G. Meek, “Adaptive filtering of the eletromyographic signal for prosthetic control and force estimation,” *IEEE Transactions on Biomedical Engineering*, vol. 42, pp. 1048–1052, 1995.

[Parker 2006] P. Parker, K. Englehart and B. Hudgins, “Myoelectrical signal processing for control of powered lower limb prosthesis,” *Journal of Electromyogram and Kinesiolgy*, vol. 16, pp. 541–548, 2006.

[Perkel 1967] D. H. Perkel, G. L. Gerstein, G. P. Moore, “Neural spike trains and stochastic point process I. the single spike train”, *Biophysical Journal*, vol. 7, pp. 391–418, 1967.

[Persen 1972] R. S. Persen and L. P. Kudina, “Discharge frequency and discharge pattern of human motor units during voluntary contraction of muscle,” *Electroencephalography and Clinical Neurophysiology*, vol. 32, pp. 471–483, 1972.

[Petrofsky 1980] J. S. Petrofsky, and A. R. Lind, “The influence of temperature on the amplitude and frequency components of the EMG during brief and sustained isometric contractions,” *European Journal of Applied Physiology and Occupational Physiology*, vol. 44, pp. 189–200, 1980.

[Pfeifer 2012] S. Pfeifer, H. Vallery, M. Hardegger, R. Riener and E. J. Perreault, “Model-based estimation of knee stiffness,” *IEEE Transactions on Biomedical Engineering*, vol. 59, pp. 2604–2612, 2012.

[Pincivero 2000] D. M. Pincivero, R. C. Green, J. D. Mark and R. M. Campy, “Gender and muscle differences in EMG amplitude and median frequency, and variability during maximal voluntary contractions of the quadriceps femoris,” *Journal of Electromyogram and Kinesiology*, vol. 10, pp. 186–196, 2000.

[Potvin 2004] J. R. Potvin and S. H. M. Brown, "Less is more: high pass filtering, to remove up to 99% of the surface EMG signal power, improves EMG-based biceps brachii muscle force estimates," *Journal of Electromyography and Kinesiology*, vol. 14, pp. 389–399, 2004.

[Prakash 2005] P. Prakash, C. A. Salini, J. A. Tranquilli, D. R. Brown and E. A. Clancy, "Adaptive whitening in electromyogram amplitude estimation for epoch-based applications," *IEEE Transactions on Biomedical Engineering*, vol. 52, pp. 331–334, 2005.

[Press 1994] W. H. Press, S. A. Teukolsky, W. T. Vetterling and B. P. Flannery, *Numerical receipies in C (2ed)*, Cambridge University Press, 671–681, 1994.

[Proakis 2006] J. G Proakis and D. K. Manolakis, *Digital Signal Processing.* Prentice Hall, 4ed, 2006.

[Rack 1969] P. M. H. Rack and D. R. Westbury, "The effects of length and stimulus rate on tension in the isometric cat soleus muscle," *Journal of Physiology*, vol. 204, pp. 443–460, 1969.

[Rainoldi 2000] A. Rainoldi, M. Nazzaro, R. Merletti, D. Farina, I. Caruso and S. Gaudenti, "Geometric factors in surface EMG of the vastus medialis and lateralis muscles," *Journal of Electromyogram and Kinesiology*, vol. 10, pp. 327–336, 2000.

[Rainoldi 2003] A. Rainoldi, G. Melchiorri and I. Caruso, "A method for positioning electrodes during surface EMG recordings in lower limb muscles," *Journal of Neuroscience Methods*, vol. 134, pp. 37–43, 2003.

[Rancourt 2001] D. Rancourt and R. Hogan, "Stability in force-production tasks," *Journal of Motor Behavior*, vol. 33, pp. 193–204, 2001.

[Rice 1992] C. L Rice, T. L. Vollmer and B. Bigland–Ritchie, "Neuromuscular responses of patients with multiple sclerosis," *Muscle and Nerve*, vol. 15, pp. 1123–1132, 1992.

[Roeleveld 1997] K. Roeleveld, D. F. Stegeman, H. M. Vingerhoets and A. V. Oosterom, "Single motor unit potential contribution to surface electromyography," *Acta Physiologica Scandinavica*, vol. 160, pp. 175–183, 1997.

[Rosen 2001] J. Rosen, M. Brand, M. B. Fuchs and M. Arcan, "A myosignal-based powered exoskeleton system," *IEEE Transactions on System, Man and Cybernetics*, vol. 31, pp. 210–222, 2001.

[Ruijven 1990] L. J. Ruijven and W. A. Weijs, "A new model for calculating muscle forces from electromyograms," *European Journal of Applied Physiology and Occupational Physiology,* vol. 61, pp. 479–485, 1990.

[Sandercock 1985] T. G. Sandercock, J. A. Faulkner, J. W. Albers and P. H. Abbrecht, "Single motor unit and fiber action potentials during fatigue," Journal of Applied Physiology, vol. 58, pp. 1073–1079, 1985.

[Sanger 2007] T. D. Sanger, "Bayesian filtering of myoelectric signals," *Journal of Neurophysiology*, vol. 97, pp. 1839–1845, 2007.

[Saridis 1982] G. N. Saridis and T. P. Gootee, "EMG pattern analysis and classification for a prosthesis arm," *IEEE Transactions on Biomedical Engineering*, vol. 29, 1982.

[Semmler 1997] J. G. Semmler, M. A. Nordstrom and C. J. Wallace, "Relationship between motor unit shot-term synchronization and common drive in human first dorsal interosseous muscle", *Brain Research*, vol. 727, pp. 314–320, 1997.

[Shin 2009] D. Shin, J. Kim and Y. Koike, "A myokinetic arm model for estimating joint torque and stiffness from EMG signals during maintained posture," *Journal of Neurophysiology*, vol. 101, pp. 387–401, 2009.

[Sinex 1988] D. G. Sinex and L. P. McDonald, "Average discharge rate representation of voice onset time in the chinchilla auditory nerve," *The Journal of Acoustical Society of America*, vol. 83, pp. 1817–1827, 1988.

[Solomonow 1986] M. Solomonow, A. Guzzi, R. Baratta, H. Shoji and R. D'Ambrosia, "EMG-force model of the elbow's antagonistic muscle pair: the effect of joint position, gravity and recruitment," *American Journal of Physics and Medicine*, vol. 65, pp. 223–244, 1986.

[Song 2005] R. Song and K. Y. Tong, "Using recurrent artificial neural network model to estimate voluntary elbow torque in dynamic situations," *Medical and Biological Engineering and Computing*, vol. 43, pp. 473–480, 2005.

[Sörnmo 2005] L. Sörnmo and P. Laguna, *Bioelectrical signal processing in cardiac and neurological applications*, Academic Press, 1ed, 2005.

[St-Amant 1998] Y. St-Amant, Y. D. Rancourt and E. A. Clancy, "Influence of smoothing window length on electromyogram amplitude estimates," *IEEE Transactions on Biomedical Engineering*, vol. 45, pp. 795–799, 1998

[Stålberg 1991] E. Stålberg and P. Dioszeghy, "Scanning EMG in normal muscle and in neuromuscular disorders", *Electroencephalography and Clinical Neurophysiology*, vol. 81, pp. 403–416, 1991.

[Stålberg 1997] E. Stålberg and B. Falck, "The role of electromyography in neurology," *Electroencephalography and Clinical Neurophysiology*, vol. 103, pp. 579-598, 1997.

[Stashuck 1989] D. Stashuck and C. J. DeLuca, "Update on the decomposition and analysis of EMG signals," *Computer-Aided Electromyography and Expert Systems*, JE Desmedt (ed.), pp. 39–53, 1989.

[Stashuck 2001] D. Stashuck, "EMG signal decomposition: how can it be accomplished and used?" *Journal of Electromyogram and Kinesiology*, vol. 11, pp. 151–173, 2001.

[Staudenmann 2007] D. Staudenmann, J. R. Potvin, I. Kingma, D. F. Stegeman and J. H. van Dieen, "Effects of EMG processing on biomechanical models of muscle joint system: sensitivity of trunk muscle moments, spinal forces, and stability," *Journal of Biomechanics*, vol. 40, pp. 900–909, 2007.

[Staudenmann 2009] D. Staudenmann, I. Kingma, A. Daffertshofer, D. F. Stegeman and J. H. van Dieen, "Heterogeneity of muscle activation in relation to force direction: a multi-channel surface electromyography study on the triceps surae muscle," *Journal of Electromyogram and Kinesiology*, vol. 19, pp. 882–895, 2009.

[Staudenmann 2010] D. Staudenmann, K. Roleveld, D. F. Stegeman and J. van Dieen, "Methodological aspects of sEMG recordings for force estimation–A tutorial and review," *Journal of Electromyogram and Kinesiology*, vol. 20, pp. 375–387, 2010.

[Thelen 1994] D. G. Thelen, A. B. Shultz, S. D. Fassois and J. A. Ashton-Miller, "Identification of dynamic myoelectric signal-to-force models during isometric lumbar muscle contractions," *Journal of Biomechanics*, vol. 27, pp. 907–919, 1994.

[Tonelli 1909] L Tonelli, “Sull’integrazione per parti,” *Rend. Acc. Naz. Lincei*, vol. 5, pp. 246–253, 1909.

[Torbergsen 1996] T. Torbergsen, E. Stålberg and N. J. Brautaset, “Generator sites for spontaneous activity in neuromyotonia. An EMG study,” *Electroencephalography and Clinical Neurophysiology*, vol. 101, pp. 69–78, 1996.

[Varol 2010] H. A. Varol, F. Sup and M. Goldfarb, “Multiclass real-time intent recognition of a powered lower limb prosthesis,” *IEEE Transactions on Biomedical Engineering*, vol. 57, pp. 542–551, 2010.

[Vieira 2010] T. M. M. Vieira, R. Merletti and L. Mesin, “Automatic segmentation of surface EMG images: improving the estimation of neuromuscular activity,” *Journal of Biomechanics*, vol. 43, pp. 2149–2158, 2010.

[Vredenbregt 1973] J. Vredenbregt and G. Rau, “Surface electromyography in relation to force, muscle length and endurance,” *New Developments in Electromyogram and Clinical Neurophysiology*, vol. 1, pp. 607–622, 1973.

[Weber 2011] D. J Weber, B. M London, J. A Hokanson, C. A. Ayers, R. A. Gaunt, *et al.* “Limb–state information encoded by peripheral and central somasensory neurons: implications for an afferent interface,” *IEEE Transactions on Neural System and Rehabilitation Engineering*, vol. 19, pp. 501–513, 2011.

[Weidong 2004] Z. Weidong and J. Gotman, “Removal of EMG and ECG artifacts from EEG based on wavelet transform and ICA,” *Engineering in Medicine and Biology Society*, pp. 392–395, 2004.

[Weytjens 1984] J. L. F. Weytjens and D. van Steenberghe, “The effects of motor unit synchronization on the power spectrum of the electromyogram”, *Biological cybernetics*, vol. 51, pp. 71–77, 1984.

[Yang 1984] J. F. Yang and D. A. Winter, “Electromyographic amplitude normalization methods: improving their sensitivity as diagnostic tools in gait analysis,” *Archives of Physiology and Medical Rehabilitation*, vol. 65, pp. 517–521, 1984.

[Yang 1985] J. F. Yang and D. A. Winter, “Surface EMG profiles during different walking cadences in humans,” *Electroencephalography and Clinical Neurophysiology*, vol. 60, pp. 485–491, 1985.

[Zajac 1989] F. E. Zajac, "Muscle and tendon: properties, models, scaling, and application to biomechanics and motor control," *Critical Reviews in Biomedical Engineering*, vol. 17, pp. 359–441, 1989.

[Zhou 2004] P. Zhou and W. Z. Rymer, "MUAP number estimates in surface EMG: template-matching methods and their performance boundaries," Annals of Biomedical Engineering, vol. 32, pp. 1007–1015, 2004.